

**FLUORESCENCE ENHANCED OPTICAL TOMOGRAPHY ON BREAST
PHANTOMS WITH MEASUREMENTS USING A GAIN MODULATED
INTENSIFIED CCD IMAGING SYSTEM**

A Dissertation

by

ANURADHA GODAVARTY

Submitted to the Office of Graduate Studies of
Texas A&M University
in partial fulfillment of the requirements for the degree of
DOCTOR OF PHILOSOPHY

December 2003

Major Subject: Chemical Engineering

**FLUORESCENCE ENHANCED OPTICAL TOMOGRAPHY ON BREAST
PHANTOMS WITH MEASUREMENTS USING A GAIN MODULATED
INTENSIFIED CCD IMAGING SYSTEM**

A Dissertation

by

ANURADHA GODAVARTY

Submitted to Texas A&M University
in partial fulfillment of the requirements
for the degree of

DOCTOR OF PHILOSOPHY

Approved as to style and content by:

Eva M. Sevick-Muraca
(Chair of Committee)

Junuthula. N. Reddy
(Member)

Margaret. J. Eppstein
(Member)

Charles J. Glover
(Member)

Kenneth R. Hall
(Head of Department)

December 2003

Major Subject: Chemical Engineering

ABSTRACT

Fluorescence Enhanced Optical Tomography on Breast Phantoms Using an Intensified
CCD Imaging System. (December 2003)

Anuradha Godavarty, B.Tech., University of Madras;

M.S., University of Tennessee

Chair of Advisory Committee: Dr. Eva M. Sevick-Muraca

Fluorescence-enhanced optical imaging using near-infrared (NIR) light developed for *in-vivo* molecular targeting and reporting of cancer provides promising opportunities for diagnostic imaging. However, prior to the administration of unproven contrast agents, the benefits of fluorescence-enhanced optical imaging must be assessed in feasibility phantom studies.

A novel intensified charge-coupled device (ICCD) imaging system has been developed to perform 3-D fluorescence tomographic imaging in the frequency-domain using near-infrared contrast agents. This study is unique since it (i) employs a large tissue-mimicking phantom (~1087 cc), which is shaped and sized to resemble a female breast and part of the extended chest wall region, and (ii) enables rapid data acquisition in the frequency-domain by using a gain-modulated ICCD camera. Diagnostic 3-D fluorescence-enhanced optical tomography is demonstrated using 0.5-1 cc single and multiple targets contrasted from their surrounding by μM concentrations of Indocyanine green (ICG) in the breast-shaped phantom (10 cm diameter), under varying conditions of target-to-background absorption contrast ratios (1:0 and 100:1) and target depths (up to 3

cm deep). Boundary surface fluorescence measurements of referenced amplitude and phase shift were used along with the coupled diffusion equation of light propagation in order to perform 3-D image reconstructions using the approximate extended Kalman filter (AEKF) algorithm, and hence differentiate the target from the background based on fluorescent optical contrast.

Detection of single and multiple targets is demonstrated under various conditions of target depths (up to 2 cm deep), absorption optical contrast ratio (1:0 and 100:1), target volumes (0.5-1 cc), and multiple targets (up to three 0.5 cc targets). The feasibility of 3-D image reconstructions from simultaneous multiple point excitation sources are presented. Preliminary lifetime imaging studies with 1:2 and 2:1 optical contrast in fluorescence lifetime of the contrast agents is also demonstrated. The specificity of the optical imager is further assessed from homogeneous phantom studies containing no fluorescently contrasted targets.

While nuclear imaging currently provides clinical diagnostic opportunities using radioactive tracers, molecular targeting of tumors using non-ionizing NIR contrast agents tomographically imaged using the frequency-domain ICCD imaging system could possibly become a new method of diagnostic imaging.

*To Arvind, Amma, and Nana
whose love and support nurtured me throughout my doctoral program*

ACKNOWLEDGEMENTS

Acknowledgement is a small word for the amount of help, support, and encouragement that I received from many people around. First and foremost is Dr. Eva Sevick-Muraca who was not only my advisor, but also a role model for my academic growth in the last four years. I owe her more than just a *thank you*. Dr. Margaret Eppstein's co-advising in my research work added greatly to my research.

Help and support from Dr. Alan Thompson and Michael Gurfinkel during the instrumentation set-up is unforgettable. Discussions with Dr. Ranadhir Roy were useful and helpful. Jessica Houston's help in so many different ways were invaluable. Dr. Chaoyang Zhang was a great team player in our collaborative project and helped me incredibly in understanding the image reconstruction algorithms. Almost every member of the Photon Migration Laboratories, both past and present, including Daniel Hawrysz, Jangwoen Lee, Amit Joshi, Yingqing Huang, Feng Liang, Tianshu Pan, Sarabjot Dali, John Rasmussen, and Eddy Kuwana helped me at various stages of my doctoral research. Building the imaging system and performing experiments would not have been possible without the help of Randy Marek, Wayne, Virany Yowono, and Sangeeta Theru. To all these people, I am really thankful for their help.

Last but not least, I owe a great deal to my family (especially my brother, Vichu) and close friends (especially Malini), whose moral strength and support on an every day basis cannot be forgotten. Finally, I would like to acknowledge National Institutes of Health (NIH R01 EB002763 and R01 CA67176) for funding my research.

TABLE OF CONTENTS

	Page
ABSTRACT.....	iii
DEDICATION.....	v
ACKNOWLEDGEMENTS.....	vi
TABLE OF CONTENTS.....	vii
LIST OF FIGURES.....	xii
LIST OF TABLES.....	xxiii
NOMENCLATURE.....	xxvii
1. INTRODUCTION.....	1
2. BACKGROUND: MOLECULAR IMAGING MODALITIES.....	8
2.1. Molecular imaging modalities towards breast imaging.....	9
2.1.1. Contrast-enhanced x-ray computed tomography.....	10
2.1.2. Contrast-enhanced magnetic resonance imaging.....	11
2.1.3. Contrast-enhanced ultrasound	14
2.1.4. Radionuclide based imaging.....	15
2.1.5. Optical-based molecular imaging.....	18
2.2. Fluorescence-enhanced optical imaging.....	22
2.3. Measurement techniques in optical imaging.....	26
2.3.1. Continuous-wave imaging.....	26
2.3.2. Time-domain photon migration imaging.....	28
2.3.3. Frequency-domain photon migration imaging.....	29
2.4. Measurement geometries.....	32
2.4.1. Point illumination and point collection measurement geometry.....	33
2.4.2. Interstitial illumination measurement geometry.....	33
2.4.3. Area illumination and area collection measurement geometry.....	34
2.4.4. Point illumination and area collection measurement geometry.....	36
2.4.5. Area illumination and point collection measurement geometry.....	37
3. BACKGROUND: FLUORESCENCE-ENHANCED OPTICAL TOMOGRAPHY.....	38

	Page
3.1. Light propagation model using diffusion equation.....	39
3.2. Boundary conditions.....	42
3.2.1. Partial current boundary condition.....	42
3.2.2. Extrapolated boundary condition.....	44
3.2.3. Zero fluence boundary condition.....	45
3.3. Forward problem in fluorescence-enhanced optical tomography.....	46
3.4. Inverse problem in fluorescence-enhanced optical tomography.....	49
3.4.1. Localization or analytical approach	50
3.4.2. Backprojection.....	51
3.4.3. Numerical approach.....	52
3.5. Context of current research.....	59
 4. INSTRUMENTATION AND EXPERIMENTAL TOOLS.....	 63
4.1. Breast phantom.....	63
4.1.1. Collection optical fibers	65
4.1.2. Source optical fibers.....	65
4.1.3. Target.....	66
4.2. Instrumentation.....	66
4.2.1. Light source.....	67
4.2.2. Tissue phantom.....	69
4.2.3. Interfacing plates.....	70
4.2.4. Intensified CCD detection system.....	72
4.2.4.1. Focusing lens and lens assembly.....	72
4.2.4.2. Image intensifier.....	73
4.2.4.3. CCD camera.....	78
4.3. Data acquisition and processing technique	79
4.4. Referencing techniques.....	83
4.4.1. Referencing emission signal with respect to excitation signal Φ_m/Φ_x	85
4.4.2. Referencing emission signal with respect to emission signal at a given location Φ_m/Φ_{ref}	86
4.5. Reflectance versus fluence data.....	88
 5. FORWARD AND INVERSE FORMULATIONS.....	 92
5.1. Forward problem.....	92
5.1.1. Galerkin finite-element based formulation of the forward problem... ..	93
5.2. Inverse problem.....	98
5.2.1. Formulation of the inverse problem.....	99
5.2.1.1. Measurement type.....	100
5.2.1.2. Reconstructing parameter.....	101
5.2.1.3. Jacobian sensitivity matrices by adjoint formulation.....	103

	Page
5.2.1.4. Inversions using the approximate extended Kalman filter algorithm.....	108
5.3. Implementation of the inversion methodology.....	112
5.3.1. Parameter distribution using pseudo-beta transforms.....	112
5.3.2. Jacobian sensitivity matrix for referenced measurements.....	114
5.3.3. Computationally efficient version of the AEKF algorithm.....	118
5.3.4. Vectorization of the inverse formulation.....	120
5.4. Flowchart of the optical tomography process.....	120
6. DATA ANALYSIS AND EXPERIMENTAL PLAN.....	122
6.1. Experimental parameters.....	122
6.1.1. Fluorescence contrast agents.....	123
6.2. Data analysis methodology.....	126
6.2.1. Acquisition of excitation and fluorescence measurements.....	126
6.2.2. Determination of model match and model mismatch errors.....	128
6.2.3. Estimation of measurement error covariance, model error covariance, and parameter error covariance.....	130
6.2.4. Performance of image reconstructions using modified version of AEKF algorithm.....	132
6.3. Experimental plan.....	133
6.3.1. Absorption contrast studies.....	135
6.3.2. Lifetime contrast studies.....	137
6.3.3. Homogeneous phantom studies.....	138
6.3.4. Area illumination and area detection studies.....	138
7. MEASUREMENT PRECISION, ACCURACY, AND PRELIMINARY IMAGE RECONSTRUCTIONS.....	139
7.1. Measurement precision.....	139
7.2. Measurement accuracy (or model mismatch error) and effect of referencing schemes.....	144
7.2.1. Measurement accuracy using the first referencing scheme Φ_m/Φ_x ...	146
7.2.2. Measurement accuracy using the second referencing scheme Φ_m/Φ_{ref}	148
7.2.3. Effect of refractive index mismatch parameter on measurement accuracy.....	150
7.3. Image reconstructions.....	155
7.4. Summary.....	163
8. DEPTH STUDIES USING SINGLE AND DUAL POINT ILLUMINATION GEOMETRIES.....	165

	Page
8.1. Dual point illuminating imaging system.....	166
8.1.1. Instrumentation for the dual point illuminating imaging system.....	167
8.1.2. Experimental parameters.....	167
8.1.3. Image reconstructions using single and dual point illumination geometries.....	170
8.2. Results and discussion: Perfect uptake case.....	171
8.2.1. Effect on volume illuminated and signal strength.....	171
8.2.2. Model match between experiments and simulations	172
8.2.3. Measurement error.....	174
8.2.4. Image reconstructions.....	174
8.3. Results and discussion: Imperfect uptake case.....	179
8.3.1. Model match between experiments and simulations.....	179
8.3.2. Measurement error.....	182
8.3.3. Image reconstructions.....	183
8.4. Summary	187
9. SMALL VOLUME AND MULTIPLE TARGET STUDIES.....	190
9.1. Experimental parameters.....	190
9.2. Single small volume target study (Experiment # 1).....	191
9.2.1. Model match and measurement errors.....	193
9.2.2. Image reconstructions.....	193
9.3. Multiple small volume target study (Experiment # 2).....	199
9.3.1. Model match and measurement errors.....	201
9.3.2. Image reconstructions.....	201
9.4. Summary.....	207
10. PRELIMINARY LIFETIME STUDIES.....	210
10.1. Effect of the unstable DTTCI on lifetime studies.....	210
10.2. Experimental parameters for lifetime studies.....	211
10.3. Model match and measurement errors.....	213
10.4. Image reconstructions using μ_{axf} as the reconstructing parameter.....	216
10.5. Summary.....	219
11. HOMOGENEOUS PHANTOM STUDIES.....	221
11.1. Homogeneous phantom study (Experiment # 1).....	221
11.1.1. Model match and measurement errors.....	223
11.1.2. Image reconstructions.....	223
11.2. Homogeneous phantom study (Experiment # 2).....	226
11.2.1. Experimental parameters.....	228

	Page
11.2.2. Model match and measurement errors.....	229
11.2.3. Image reconstructions.....	231
11.3. Summary.....	234
12. PLANAR SOURCE STUDIES.....	236
12.1. Phantom details and instrumentation.....	238
12.2. Forward model formulation.....	240
12.3. Experimental parameters.....	241
12.4. Results and discussion.....	245
12.4.1. Effect of area source versus multiple point sources.....	245
12.4.2. Effect of finite-element discretization on the model match.....	247
12.5. Image reconstructions.....	249
13. CONCLUSIONS AND FUTURE WORK.....	251
13.1. Future work.....	254
13.1.1. Modifications in the current optical imaging system.....	254
13.1.2. Improvement in reconstruction algorithm.....	258
13.1.3. Analysis of specificity and sensitivity of the optical imager.....	259
13.1.4. Development of tumor-specific contrast agents.....	260
REFERENCES.....	261
APPENDIX A.....	280
APPENDIX B.....	284
APPENDIX C.....	288
APPENDIX D.....	295
APPENDIX E.....	299
VITA.....	303

LIST OF FIGURES

FIGURE	Page
2.1 Schematic of the principle of x-ray computed tomography (left) and its clinical set-up (right).....	11
2.2 Schematic of the principle of magnetic resonance imaging (left) and its clinical set-up (right).....	12
2.3 Schematic of the principle of ultrasound imaging (left) and its clinical application (right).....	15
2.4 Schematic of the principle of radionuclide based imaging, including (a) single photon emission computed tomography (SPECT) (left) and its clinical set-up (right), and (b) positron emission tomography (PET) (left) and its clinical set-up (right).....	17
2.5 Schematic of the principle of optical imaging (left) and its possible clinical application (right).....	19
2.6 Therapeutic optical window in tissue medium. Adapted from Ref [39]...	19
2.7 Jablonski diagram illustrating the principle of fluorescence.....	23
2.8 Schematic of the fluorescence-enhanced imaging process in a tissue medium (left) and its potential future clinical application (right).....	24
2.9 Schematic of the optical imaging process using different measurement techniques (a) continuous-wave imaging, (b) time-domain photon migration, and (c) frequency-domain photon migration. In each technique, the left hand plot represents input light intensity (I_o) launched onto the tissue surface, and the right hand plot represents the output light intensity (I) collected from the tissue surface.....	27
2.10 Fluorescence-enhanced optical imaging in the frequency-domain (a) detailed schematic of the FDPM principle using point illumination and point collection measurement geometry, (b) detailed schematic of the FDPM principle using area illumination and area collection measurement geometry, and (c) phase shift and amplitude attenuation observed during in any FDPM process.....	30
2.11 Schematic of different measurement geometries (a) point illumination and point collection geometry, (b) interstitial point illumination, where	

FIGURE	Page
the point of illumination is below the tissue-like surface, with collection via point or area detection, (c) area illumination and area collection geometry, (d) point illumination and area collection geometry, (e) area illumination and point collection geometry.....	32
3.1 Schematic of tissue boundary surface. n_1 is the refractive index of the tissue medium, n_2 is the refractive index of the outside medium, and \hat{n} is the normal to the tissue surface.....	43
3.2 Schematic of the forward problem (left) and the inverse problem (right) in optical tomography.....	47
4.1 (a) Tissue-mimicking phantom, (b) Actual phantom set-up with optical fibers for illumination and collection of light signal, (c) x-y location of all 27 point illumination (red asterisks) and 128 collection locations (black hollow circles) on the hemispherical portion of the phantom, (d) targets of varying size (i) $1 \times 1 \times 1$ cc cube, (ii) $1 \times 1 \times 0.5$ cc cuboid, and (iii) 0.5 cc spherical target, suspended into the phantom using the support of optical fibers.....	64
4.2 Schematic of the instrumentation set-up of the ICCD imaging system.....	68
4.3 Schematic of the principle of ICCD detection technique.....	68
4.4 Set-up of the laser diode mount and the fiber holder for input laser light..	70
4.5 Phantom set-up including collection fibers, which are interfaced to the hemispherical surface of the phantom on one end, and to either of the two interfacing plates on the other end.....	71
4.6 Resistor-capacitor circuit for modulating the photocathode of the image intensifier. Adapted from reference [100].....	75
4.7 Schematic of the homodyne detection technique in the ICCD imaging system.....	78
4.8 Data acquisition technique in a homodyned frequency-domain imaging system. Reproduced with permission from reference [51].....	81
4.9 Schematic of different referencing schemes used in the current study (a) referencing emission signal with respect to excitation signal at each pixel	

FIGURE	Page
(<i>i</i>), (<i>b</i>) referencing emission signal at each pixel (<i>i</i>) with respect to emission signal acquired at a fixed location (<i>ref</i>).....	86
5.1 Three-dimensional finite element mesh (consisting of tetrahedral elements) of the breast-shaped phantom.....	93
5.2 Flowchart of the image reconstruction algorithm.....	121
6.1 Excitation and emission spectra of ICG dissolved in water, plotted as normalized intensity versus the wavelength range. The excitation peak (between 600 nm to 800 nm) was obtained for a constant emission wavelength of 850 nm, and the emission peak (between 800 nm and 900 nm) was obtained for a constant excitation wavelength of 780 nm.....	124
6.2 Excitation and emission spectra of DTTCI dissolved in DMSO, plotted as normalized intensity versus the wavelength range. The excitation peak (between 650 nm to 780 nm) was obtained for a constant emission wavelength of 800 nm, and the emission peak (between 750 nm to 900 nm) was obtained for the constant excitation wavelength of 730 nm.....	125
6.3 Schematic of the data analysis process (a) acquiring repeated measurements at each pixel (<i>i</i>), (b) averaging the data from repeated measurements at each pixel (<i>i</i>), (c) referencing the averaged data using either of the two referencing schemes at each pixel (<i>i</i>), (d) determining the model mismatch error between experiments and simulations at each pixel (<i>i</i>), (e) determining the measurement error from the repeated measurements at each pixel (<i>i</i>), and (f) performing image reconstructions using all the required input parameters as shown.....	127
6.4 Outline of the broad research experimental plan.....	134
6.5 Experimental plan for absorption contrast studies.....	136
6.6 Experimental plan for lifetime contrast studies.....	137
7.1 Schematic of the measurement precision analysis (a) acquiring repeated measurements and averaging the data at each pixel (<i>i</i>), (b) repeating the complete data acquisition procedure of (a) using the same point of illumination, and (c) determining the measurement precision between the two data sets at each pixel (<i>i</i>).....	140

FIGURE	Page
7.2 Measurement precision as variance between repeated AC measurements. Frequency (on y-axis) is defined as the probability distribution of the data points, μ is the mean and σ^2 is the variance of precision in AC.....	142
7.3 Measurement precision as variance between repeated phase measurements. Frequency (on y-axis) is defined as the probability distribution of the data points, μ is the mean (in deg) and σ^2 is the variance of precision in phase.....	143
7.4 Schematic of the measurement accuracy analysis (a) acquiring repeated measurements (typically 5) at each pixel (i), (b) averaging the repeated measurements at each pixel (i), (c) referencing the averaged data at each pixel (i), and (d) determining the model mismatch errors between experimental and simulated data at each pixel or location (i).....	145
7.5 Comparison of model predictions with measurements for ln(ACR) and RPS, shown for a representative subset of source-detector pairs in the imperfect uptake case, using first referencing scheme Φ_m/Φ_s (a,b) and second referencing scheme $\Phi_m/\Phi_{m,ref}$ (c,d).....	147
7.6 Histograms of model mismatch error for the two experiments, using the second referencing method $\Phi_m/\Phi_{m,ref}$, for a) ln(ACR), imperfect uptake, b) RPS, imperfect uptake (in radians), c) ln(ACR), perfect uptake, d) RPS, perfect uptake (in radians). Frequency is the probability distribution of the measurements, μ is the mean and σ^2 is the variance in ACR and RPS model mismatch errors.....	149
7.7 Different cases of R_{eff} approximations in the partial current boundary condition of the coupled diffusion equations (a) actual phantom with air-tissue interface at circular boundary surface, and Liposyn-PVC interface at the remaining boundary surfaces, (b) Case 1: approximating all boundary surfaces with air-tissue interface, (c) Case 2: approximating all boundary surfaces with Liposyn-PVC interface, and (d) Case 3: using the actual phantom case described in (a).....	151
7.8 Effect of refractive index parameter in perfect uptake data at emission wavelength. (a), (b) correspond to Case 1; (c), (d) correspond to Case 2; and (e), (f) correspond to Case 3 of the three different R_{eff} cases. Frequency is the probability distribution of the data points, μ is the mean and σ^2 is the variance of ACR and RPS model mismatch errors.	152

FIGURE	Page
7.9 Effect of refractive index parameter in imperfect uptake data at emission wavelength. (a), (b) correspond to Case 1; (c), (d) correspond to Case 2; and (e), (f) correspond to Case 3 of the three different R_{eff} cases. Frequency is the probability distribution of the data points, μ is the mean and σ^2 is the variance of ACR and RPS model mismatch errors. Reproduced with permission from reference [119]	153
7.10 Model match of $\ln(\text{ACR})$ between experiments and simulations obtained using the three cases of the R_{eff} values in the slab phantom studies. Reproduced with permission from reference [104].....	154
7.11 Histograms of measurement error variances for all measurements (referenced as shown in Equation (4) with modulation depth > 0.025 for a) $\ln(\text{ACR})$, imperfect uptake, b) RPS, imperfect uptake (in radians), c) $\ln(\text{ACR})$, perfect uptake, d) RPS, perfect uptake (in radians). Frequency is the probability distribution of the data points, μ is the mean and σ^2 is the variance of ACR and RPS measurement errors.....	156
7.12 Flowchart for filtering out low signal-to-noise measurements at three levels: source level, detector level, and parameter update level.....	157
7.13 Model plot of the effect of modulation depth on model mismatch between experiments and simulations of AC data.....	158
7.14 Histograms of differences in model predictions with and without the fluorescent target, assuming background fluorescence absorption of 0.003 cm^{-1} , for a) $\ln(\text{ACR})$, b) RPS (in radians). Frequency is the probability distribution of the data points, μ is the mean and σ^2 is the variance.....	159
7.15 Convergence curves of sum of squared prediction errors for the two reconstructions.....	159
7.16 (a) The true fluorescence absorption distribution in the 3-D phantom containing the actual target. In both experiments, the value of the absorption coefficient due to fluorophore (μ_{axf}) in the actual target was 0.30 cm^{-1} . The background μ_{axf} value was 0.003 cm^{-1} and 0.000 cm^{-1} in the imperfect and perfect uptake case, respectively. (b) The fluorescence absorption distribution in the 3-D reconstructed phantom for the imperfect uptake case, with iso-surface shown at $\mu_{axf}=0.2 \text{ cm}^{-1}$. (c) The fluorescence absorption distribution in the 3-D reconstructed phantom	

FIGURE	Page
for the perfect uptake case, with iso-surface shown at $\mu_{axf}=0.2 \text{ cm}^{-1}$...	161
8.1 Instrument setup for dual point illuminating ICCD imaging system.....	168
8.2 Modulation depth of an interfacing plate for (a) single point illumination and (b) dual point illumination, for perfect uptake of 2cm deep and 1cc volume target.....	172
8.3 Convergence curves from 3-D image reconstructions using the dual and single point illumination geometries for (a) 1 cm target depth, and (b) 2 cm target depth cases under 1:0 absorption optical contrast ratio.....	176
8.4 Actual and reconstructed targets in x-y and x-z planes: (a) actual 1 cc target located 1 cm deep under 1:0 absorption optical contrast ratio, (b) reconstructed target using single point illumination measurement geometry, and (c) reconstructed target using dual point measurement geometry. All the reconstructions were performed with the initial guess of $\mathbf{P}=0.001$, and $\mu_{axf}=0.003 \text{ cm}^{-1}$	176
8.5 Actual and reconstructed targets in x-y and x-z planes: (a) actual 1 cc target located 2 cm deep under 1:0 absorption optical contrast ratio, (b) reconstructed target using single point measurement geometry, and (c) reconstructed target using dual point measurement geometry. All the reconstructions were performed with the initial guess of $\mathbf{P}=0.001$, and $\mu_{axf}=0.003 \text{ cm}^{-1}$	177
8.6 (a) Histogram of the reconstructed parameter, μ_{axf} (absorption coefficient due to the fluorophore) cm^{-1} in the experimental case containing the 1 cc target located ~ 1 cm deep with 1:0 absorption optical contrast ratio and using single point illumination geometry, (b) Histogram of the same experimental case zoomed in the y-axis and plotted using 500 bins.	178
8.7 Model match between experiments and simulations of the 3 cm deep target using the single point illumination measurement geometry (a) $\ln(\text{ACR})$ for 1:0 case, (b) RPS for 1:0 case, (c) $\ln(\text{ACR})$ for 100:1 case, and (d) RPS for 100:1 case. The model match is plotted for a subset of the total number of acquired measurements.....	181
8.8 Convergence plots for (a) 1-cm deep target case, (b) 2-cm deep target case, and (c) 3-cm deep target case with 100:1 absorption optical contrast	

FIGURE	Page
ratios, using both the illumination geometries. Reconstructions were performed with initial guess in $\mu_{axf}=0.003 \text{ cm}^{-1}$	184
8.9 Actual and reconstructed targets in x-y and x-z planes for: (a) actual 1 cc target located ~ 1 cm deep under 100:1 absorption optical contrast ratio cases, (b) reconstructed target using single point illumination measurement geometry, when initial guess of $\mathbf{P}=0.01$, and (c) reconstructed target using dual point illumination measurement geometry, when initial guess of $\mathbf{P}=0.001$	185
8.10 Actual and reconstructed targets in x-y and x-z planes for: (a) actual target 1 cc target located ~ 2 cm deep under 100:1 absorption optical contrast ratio cases, (b) reconstructed target using single point illumination measurement geometry, when initial guess of $\mathbf{P}=0.01$, and (c) reconstructed target using dual point illumination measurement geometry, when initial guess of $\mathbf{P}=0.001$	185
8.11 Actual and reconstructed targets in x-y and x-z planes for: (a) actual target 1 cc target located ~ 3 cm deep under 100:1 absorption optical contrast ratio cases, (b) reconstructed target using single point illumination measurement geometry, when initial guess of $\mathbf{P}=0.01$, and (c) reconstructed target using dual point illumination measurement geometry, when initial guess of $\mathbf{P}=0.001$	186
9.1 Measurement filtration process to remove data representing excitation leakage (at source level) or noise (at detector level)	192
9.2 Model match between experiments and simulations in terms of $\ln(\text{ACR})$ and RPS (in degrees), plotted for a subset of total acquired measurements. The mean and variance of errors in $\ln(\text{ACR})$ were estimated as -0.305 and 0.422, respectively, and the mean and variance of errors in RPS (in radians) were estimated as 0.068 and 0.149, respectively	194
9.3 Convergence plot for the single 0.5 cc target experimental case under perfect uptake case. Based on the convergence criterion, the reconstructions terminated after the 2 nd iteration (dotted vertical line) due to an increase in the errors, and the reconstructions were carried out until 20 iterations were reached	195
9.4 Contour slices in the y-plane of the (a) actual phantom containing a single 0.5 cc target, with no ICG in the background (b) reconstructed	

FIGURE	Page
phantom using the first convergence criterion of $< 1\%$ RMSE or a maximum iterations of 50, and (c) reconstructed phantom using the second convergence criterion of maximum 20 iterations. In both the reconstruction cases, $\mathbf{P}=0.001$, $\mu_{axf}=0.001\text{ cm}^{-1}$	197
9.5 (a) Histogram of the reconstructed parameter, μ_{axf} (absorption coefficient due to the fluorophore) cm^{-1} for the experimental case containing a 0.5 cc target at 1:0 absorption optical contrast ratio and located ~ 2 cm deep, (b) Histogram of the same experimental case zoomed in the y-axis and plotted using 500 bins.....	198
9.6 Actual targets used in the experimental studies (a) $1\times 1\times 1\text{ cm}^3$ target made from clear plastic. It was used in depth studies, (b) $0.5\times 1\times 1\text{ cm}^3$ target made from clear plastic. It was used in single small volume target study, and (c) ~ 0.5 cm radius spherical target made from Pyrex glass. (d) Suspension of the three targets in multiple target detection experiment, using optical fibers for support. The plate holding the targets helps position the targets precisely in the xyz coordinates.....	200
9.7 Comparison plots between referenced measurements and simulations (using coarse finite element mesh) in terms of $\ln(\text{ACR})$ and RPS (in degrees), plotted for a subset of the total measurements acquired. The mean and variance of errors in $\ln(\text{ACR})$ were 0.108 and 0.558, respectively. Similarly, the mean and variance of errors in RPS (in radians) were 0.062 and 0.080, respectively.....	202
9.8 Convergence plots of the multiple target experiment, using coarse and fine mesh during image reconstructions.....	203
9.9 y-x and y-z planar views of the actual breast phantom (a,d), reconstructed breast phantom using coarse mesh (b,e) and reconstructed breast phantom using fine mesh (c,f). Three targets of 0.5~0.6 cc volume were used in the actual breast phantom of ~ 1087 cc volume and illuminated using single point illumination geometry. All the reconstructions were performed using initial guess of $\mathbf{P}=0.001$ and $\mu_{axf}=0.001\text{ cm}^{-1}$	203
9.10 Histograms of reconstructed parameter, μ_{axf} (absorption coefficient due to the fluorophores) for the multiple small volume target experiment, under perfect uptake conditions. μ_{axf} distribution obtained in the finely discretized phantom is plotted separately for regions (a,b) $x<0$ & $y<0$, (c,d) $y>0$, and (e,f) $x>0$ & $y<0$. (b,d,f) are the same histograms of	

FIGURE	Page
(a,c,e), respectively, but zoomed in y-axis and plotted using 500 bins.....	205
10.1 x-y and x-z planar views of the actual breast phantom (a,c), and the reconstructed breast phantom using coarse mesh (b,d). A single target of 1.0 cc volume was used in the actual breast phantom of $\sim 1087 \text{ cm}^3$ volume and illuminated using single point illumination geometry. Reconstructions shown here are for μ_{axf} as unknown parameter performed with initial guess of $\mathbf{P}=0.001$, $\mu_{axf}=0.001 \text{ cm}^{-1}$. The iso-surface cut-off value was chosen as $\mu_{axf}=0.1 \text{ cm}^{-1}$	212
10.2 Comparison plot of $\ln(\text{ACR})$ and RPS (in deg) for the experiment with 150:1 absorption optical contrast and 2:1 lifetime optical contrast (i.e. DTTCI in target). A random subset of the total number of detections is presented here.....	214
10.3 Comparison plot of $\ln(\text{ACR})$ and RPS (in deg) for the experiment with 150:1 absorption optical contrast and 1:2 lifetime optical contrast (i.e. ICG in target). A random subset of the total number of detections is presented here.....	214
10.4 Convergence plots in reconstructions performed using μ_{axf} as the unknown parameter in both the lifetime studies. During reconstructions, initial guess of μ_{axf} and \mathbf{P} was assumed equal to 0.001 cm^{-1} and 0.001 , respectively.....	217
10.5 Contour slices in the x-plane (between $\langle -5, 5 \rangle \text{ cm}$) of the (a) actual phantom, and (b) reconstructed phantom when DTTCI was present in the target and ICG was present in the background. During reconstructions, $\tau = 0.56 \text{ nsec}$, $\phi = 0.016$ was assumed constant for the entire phantom.....	218
10.6 Contour slices in the x-plane (between $\langle -5, 5 \rangle \text{ cm}$) of the (a) actual phantom, and (b) reconstructed phantom when ICG was present in the target and DTTCI was present in the background. During reconstructions, $\tau = 1.18 \text{ nsec}$, $\phi = 0.034$ was assumed constant for the entire phantom.....	218
11.1 x-y plot of the homogeneous phantom study (Experiment # 1) in the absence of targets.....	222
11.2 Model match between experiments and simulations in terms of $\ln(\text{ACR})$	

FIGURE	Page
and RPS (in deg) for Expt # 1 in the homogeneous studies, plotted for a subset of measurements from the total number of acquired measurements	224
11.3 Convergence plot for homogeneous phantom study (Experiment # 1).....	225
11.4 Contour slices in y-plane of the reconstructed image corresponding to the homogeneous phantom (Experiment # 1).....	226
11.5 x-y plot of the homogeneous phantom study (Experiment # 2), containing a single 1 cc target (red square) located in zone 2 ($y < 0$) region. Zone 1 ($y > 0$), which is the region above the dotted line, is considered homogeneous. Zone 2 ($y < 0$), which is the region below the dotted line, is considered heterogeneous (that is, target present case).....	227
11.6 Model match between experiments and simulations in terms of $\ln(\text{ACR})$ and RPS for zone 1 of the homogeneous phantom study (Expt # 2), plotting a subset of measurements from the total number of acquired measurements.....	230
11.7 Convergence curves for the homogeneous phantom study (Experiment # 2) for both cases using initial $\mathbf{P} = 0.001$ and initial $\mu_{axf} = 0.001 \text{ cm}^{-1}$. Case 1 was reconstructed using data only from zone 1 and case 2 was reconstructed.....	232
11.8 Contour slice in y-plane of the reconstructed μ_{axf} distribution in experiment # 2 for (a) case 1, where only measurements from zone 1 were used in the reconstructions, and (b) case 2, where measurements from entire phantom were used in the reconstructions.....	233
11.9 Contour slices in y-plane of reconstructed μ_{axf} distribution in experiment # 2 for reconstruction case 1 (a,c), and reconstruction case 2 (b,d). The contour limits for (a,b) was $[0.0001 \ 0.0456] \text{ cm}^{-1}$ and contour limits for (c,d) was $[0.0001 \ 0.4736] \text{ cm}^{-1}$	234
12.1 Different measurement geometries (a) Sequential point illumination of single excitation sources using optical fibers, (b) Simultaneous point illumination of two excitation sources using optical fibers, (c) Simultaneous point illumination of multiple excitation sources using optical fibers, and (d) Area illumination using an expanded beam of excitation source. (c) and (d) are equivalent, if each point of illumination in the area illumination is assumed to be an individual optical fiber.....	237

FIGURE	Page
12.2 Instrumentation set-up for area illumination/area detection measurement geometry, using a cubical phantom of 8×8×8 cc volume.....	239
12.3 Discretized cubical phantom using tetrahedral finite elements (Mesh 1 of Table 12.2) (a) Entire phantom (b) top surface of the phantom, where the interior square is the region of area illumination and area detection.....	244
12.4 Effect of plane source versus multiple point sources in forward model simulations, in comparison to the experimental data, in terms of (a) ln(ACR), (b) Relative error in ACR (%), (c) Zoomed ACR error plot for a subset of detectors, (c) RPS (deg), (e) Absolute error in RPS (deg), and (f) Zoomed ACR error plot for a subset of detectors.....	246
12.5 Model match comparison plots between two finite-element meshes (of varying discretization) and the experimental data, in terms of (a) ln(ACR), (b) Relative error in ACR (%), (c) Zoomed ACR error plot for a subset of detectors, (c) RPS (deg), (e) Absolute error in RPS (deg), and (f) Zoomed ACR error plot for a subset of detectors.....	248
12.6 (a) Contour slices along the y-plane of actual cubical phantom, representing the true location of the 1cc target located 1cm deep from the top surface. (b) Contour slices along the y-plane of the reconstructed phantom, representing the reconstructed location of the target.....	250
13.1 Flowchart of the future direction of the current work towards clinical translation of the technology.....	255
13.2 Different methods to illuminate the phantom surface using simultaneous multiple point excitation sources using (a) an optical switch that splits the input laser beam into multiple optical fibers, or using (b) expanded laser beam focused onto a fiber bundle of optical fibers.....	258
13.3 Future set-up of the ICCD imaging system towards clinical translation of the technology.....	259

LIST OF TABLES

TABLE	Page
2.1 Comparison of conventional diagnostic imaging modalities.....	9
3.1 Fluorescence-enhanced optical tomography: Literature of image reconstructions using synthetic data.....	60
3.2 Fluorescence-enhanced optical tomography: Literature of image reconstructions using experimental data.....	61
4.1 Different referencing schemes employed in fluorescence-enhanced optical tomography.....	84
6.1 Fluorescent properties of ICG and DTTCl.....	125
7.1 Optical properties of the target and the background in the 1:0 and 100:1 target:background absorption contrast experiments. One μM ICG was present in the single 1 cc target located 1 cm deep from the phantom surface Reproduced with permission from ref [118].....	145
7.2 Centroid locations and integrated values of areas where fluorescence absorption (μ_{axf}) was greater than 0.2 cm^{-1} for the imperfect and perfect uptake experiments using a 1 cc target located ~ 1 cm deep from phantom surface.....	162
8.1 Experimental conditions towards target depth studies at various absorption optical contrasts and using two different measurement geometries.....	169
8.2 Optical properties of target and background for different contrast ratio experiments and for all the target depth studies. One μM of ICG was used in the target, with 0 and $0.001 \mu\text{M}$ ICG in the background, for the perfect and imperfect uptake cases, respectively, and for all the target depths.....	169
8.3 Model mismatch error in $\ln(\text{ACR})$ and RPS for different target depths with 1:0 absorption optical contrast ratio.....	173
8.4 Measurement error (in terms of mean of variance) in $\ln(\text{AC})$ and phase shift (θ) for different target depths with 1:0 absorption contrast ratio.....	175

TABLE	Page
8.5 Reconstructed image quality for the 1 cm-target depth case with 1:0 absorption optical contrast ratio, using both the point illumination geometries.....	177
8.6 Reconstructed image quality for the 2 cm-target depth case with 1:0 absorption optical contrast ratio, using both the point illumination geometries.....	178
8.7 Model mismatch error in ln(ACR) and RPS for different target depths with 100:1 absorption optical contrast ratio.....	180
8.8 Measurement error (in terms of mean of variance) in ln(AC) and phase shift for different target depths with 100:1 absorption optical contrast ratio of a single 1 cc target located from 1-3 cm deep.....	183
8.9 Reconstructed targets under different target depths for 100:1 absorption optical contrast ratio cases. The cut-off μ_{axf} was chosen based on the break between modes in the histogram of the reconstructed μ_{axf} ...	186
9.1 Experimental parameters for small volume and multiple target studies....	191
9.2 Acquired measurements for the single 0.5 cc target experimental case (Expt #1).....	194
9.3 Details of the reconstructed images using both the convergence criteria (for $\mathbf{P}=0.001$) for a single 0.5 cc target located 2 cm deep under perfect uptake case.....	198
9.4 Acquired measurements for the multiple target experimental case (Expt # 2).....	200
9.5 Details of the reconstructed images in the multiple small volume target study, using the coarsely discretized phantom (for $\mathbf{P}=0.001$).....	206
9.6 Details of the reconstructed images in the multiple small volume target study, using the finely discretized phantom (for $\mathbf{P}=0.001$).....	206
10.1 Experimental conditions in lifetime studies using ICG and DTTCl fluorescing contrast agents.....	212
10.2 Optical properties in the fluorescence lifetime contrasted experimental studies.....	213

TABLE	Page
10.3 Mean and variance of errors in the model match comparison of $\ln(\text{ACR})$ and RPS in both the lifetime studies.....	215
10.4 Measurement error (mean of variance) in $\ln(\text{ACR})$ and RPS for both the lifetime studies.....	215
10.5 Image quality of the actual and reconstructed phantoms for both the lifetime experiments, when $\mathbf{P} = 0.001$ and $\mu_{axf} = 0.001 \text{ cm}^{-1}$ are the initial guesses during reconstructions.....	219
11.1 Optical properties of the background phantom during the homogeneous phantom study (Experiment # 1).....	222
11.2 Experimental conditions of the homogeneous phantom study (Experiment # 1).....	223
11.3 Model mismatch errors in $\ln(\text{ACR})$ and RPS for the homogeneous phantom study.....	224
11.4 Measurement errors for the homogeneous phantom study (Experiment # 1).....	224
11.5 Experimental conditions of homogeneous phantom studies (Experiment # 2).....	229
11.6 Optical properties of the target and the background in the homogeneous phantom study (Experiment # 2).....	229
11.7 Model mismatch errors in $\ln(\text{ACR})$ and RPS for zone 1 of homogeneous phantom study (Experiment # 2).....	230
11.8 Measurement errors for zone 1 of homogeneous phantom study (Experiment # 2).....	230
12.1 Optical parameters for imperfect uptake absorption contrast ratio (100:1) experiment using ICG as the contrast agent.....	243
12.2 Finite-element (FE) and finite difference (FD) mesh details for the cubical phantom ($8 \times 8 \times 8$ cc volume).....	244
12.3 Model mismatch errors in $\ln(\text{ACR})$ and RPS between measurements and simulations obtained using two different finite-element meshes and a	

TABLE	Page
finite-difference mesh.....	248

NOMENCLATURE

Abbreviations

2-D	Two-dimension
3-D	Three-dimension
AC	Alternating current
ACR	AC ratio
AEKF	Approximate extended Kalman filter
BIM	Born iterative method
CCD	Charge coupled device
CGD	Conjugate gradient descent
CT	Computed tomography
CW	Continuous-wave
DBIM	Distorted Born iterative method
DC	Direct current
DTTCI	3-3, Diethyltriacyanine iodide
ECT	Emission computer tomographic
FD	Finite difference
FDA	Food and drug administration
FDG	¹⁸ F-2-fluoro-deoxyglucose
FDPM	Frequency-domain photon migration
FE	Finite element
FEM	Finite element method
FFT	Fast Fourier transform
GPIB	General purpose interface bus
ICCD	Intensified charge coupled device
ICG	Indocyanine green
II	Image intensifier
MCP	Multi-channel plate
MFD	Multi-grid finite difference
MRI	Magnetic resonance imaging
N/A	Not applicable
NA	Numerical aperture
NIR	Near-infrared
NS	Not specified
OD	Optical density
PC	Photocathode
PET	Positron emission tomography
PML	Photon Migration Laboratories
POCS	Projection onto convex sets
PVC	Polyvinyl chloride

RF	Radio frequency
RPS	Relative phase shift
RSME	Root mean square output error
	Simultaneous algebraic reconstruction
SIRT/SART	techniques
SNR	Signal-to-noise ratio
	Single photon emission computed
SPECT	tomography
SSE	Sum of square of errors
TDPM	Time-domain photon migration
US	Ultrasound

Symbols

A, B	Constants that vary depending on the numerical aperture of the collection fibers
$AC_{precision}$	Measurement precision in amplitude
b	Boundary term at a given wavelength
B_{lower}	Lower bound of the pseudo-beta distribution
B_{upper}	Upper bound of the pseudo-beta distribution
c_x	Velocity of light at excitation wavelength (m/sec)
c_m	Velocity of light at emission wavelength (m/sec)
C	Concentration of the fluorescing agent
D_x	Optical diffusion coefficient at excitation wavelength
D_m	Optical diffusion coefficient at emission wavelength
E	Objective function in differential approach
f	Frequency (sec^{-1})
F	Jacobian matrix
F_{AC}	Wavelength-dependency factor in amplitude
F_{θ}	Wavelength-dependency factor in phase shift
F_{skew}	Skewness of the pseudo-beta distribution
g	Anisotropy coefficient
G_{AC}	AC component of the gain of the image intensifier
G_{DC}	DC component of the gain of the image intensifier
G_f	Green's function
I_{AC}	Amplitude or AC intensity
I_{DC}	Mean intensity or DC intensity
I_{max}	Current corresponding to the maximum optical power of the laser diode
I_{th}	Threshold current of the laser diode
$Imag(I(f_{max}))$	Imaginary component of the FFT output
J	Jacobian matrix
k	Decay coefficient at a given wavelength
k_{nr}	Rate of non-radioactive decay

K	Gain matrix in the AEKF pseudo-code (repeat)
K	Global stiffness matrix
K_i	Elemental stiffness matrix
L_j	Natural coordinates of the tetrahedron
L_{AC}	AC component of the intensity-modulated fluorescent signal at the photocathode
L_{DC}	DC component of the intensity-modulated fluorescent signal at the photocathode
M	Number of tetrahedral elements
n	Modulation depth
n₁	Refractive index of the tissue medium
n₂	Refractive index of the outside medium
n_{rel}	Relative refractive index
N	Number of nodes or the total number of unknowns
N_η	Number of phase delays
p	Unknown parameter during reconstructions
P_{max}	Maximum desired power of the laser diode
P_{optical}	Optical power from the laser diode
P_{RF}	rf output power
P_{th}	Threshold power of the laser diode
P	Parameter error covariance matrix
Q	Model error covariance matrix
\bar{r}	Positional vector at a given point
\bar{r}_d	Positional vector at the collection point
\bar{r}_s	Positional vector at the illumination point
r	Local vector in FE formulation
R	Diffuse reflectance
R_{eff}	Effective refractive index
R_{fresnel}	Fresnel reflection coefficient
R_j	Fresnel's reflections
R_m	Reflection coefficients at emission wavelengths
R_x	Reflection coefficients at excitation wavelengths
R_φ	Fresnel's reflections
Re(I(f_{max}))	Real component of the FFT output
R	Measurement error covariance matrix
S	Source intensity at excitation wavelength (units ???)
S_m	Source term for emission
t	time
w	Weighting function
x	Distributed predictions of the measurable state variables ln(ACR) and RPS
Y or y	Optical properties
y_o	Initial guess of the optical properties

y	Uncertain or unknown parameters
z_b	Extrapolated boundary distance outside domain
z	Vector of measurements
Z	Measurements

Greek Symbols

α	Coupling efficiency of fibers from the phantom surface to the interfacing plate
β	Quantum efficiency of phosphor screen of the image intensifier
γ	Index mismatch parameter
Γ	Rate of radioactive decay (repeat)
Γ	Surface of integration
δ	Dirac-delta function
Δ	Area or volume of each element
$\underline{\Delta}_d$	Dirac-delta function in vectorized notation
ΔY	Small perturbation in the optical properties
\mathcal{E}_{am}	Extinction coefficient at emission wavelength ($M^{-1}cm^{-1}$)
\mathcal{E}_{ax}	Emission coefficient at emission wavelength ($M^{-1}cm^{-1}$)
θ	Phase shift (deg)
θ_{instr}	Phase delay owing to the instrument response time (deg)
$\theta_{precision}$	Measurement precision in phase shift (deg)
Θ	Angle of incidence within the medium (deg)
Θ'	Refracted angle in the outside medium (deg)
Θ_c	Critical angle for total internal reflection
η_d	Phase delay introduced between the two phase locked oscillators
η_{slope}	Slope efficiency of the laser diode
λ	Wavelength
μ_a	Absorption coefficient (1/cm)
μ_{amf}	Absorption coefficient due to fluorophores at emission wavelength
μ_{ami}	Absorption coefficient due to chromophores at emission wavelength
μ_{axf}	Absorption coefficient due to fluorophores at excitation wavelength
μ_{axi}	Absorption coefficient due to chromophores at excitation wavelength
$\mu_{ax \rightarrow m}$	Absorption coefficient due to fluorophores at excitation wavelength
μ_s	Scattering coefficient (1/cm)
μ_s	Isotropic scattering coefficient (1/cm)
ξ	Pseudo-beta distribution of parameters (X)
ρ	Phase of the fluorescent signal
σ	Standard deviation

σ^2	Variance
τ	Fluorescence lifetime (sec)
ϕ	Quantum efficiency
Φ	AC component of fluence
Φ_x	AC component of fluence at excitation wavelength
Φ_m	AC component of fluence at emission wavelength
$\underline{\Psi}$	Adjoint or Green matrix
ω	Modulation frequency (radians)
Ω	Volume of integration in a 3-D domain
$\partial\Phi/\partial n$	Flux at the boundary surface of the domain
∇	Gradient operator

Subscripts

<i>expt</i>	Experimental data
<i>f</i>	Fluorophores
<i>i</i>	Chromophores or corresponding pixel
<i>m</i>	Emission wavelength (cm ⁻¹)
<i>reim</i>	Real and imaginary terms together
<i>ref</i>	Reference pixel location
<i>sim</i>	Simulated data
<i>x</i>	Excitation wavelength (cm ⁻¹)

Superscripts

<i>m</i>	Measured data
<i>s</i>	Simulated data from the forward model
<i>el</i>	element

1. INTRODUCTION

Imaging plays a major role in the diagnosis, therapy, and prognosis¹ of cancer, with primary focus in detecting anatomical² abnormalities in the tissue. With the current emerging areas of genomics³ and proteomics,⁴ molecular targeting of early stage cancer holds a promise in contrast-enhanced diagnostic imaging, in comparison to the conventional, anatomical imaging that lacks sensitivity and specificity for early cancer detection [1]. Molecular imaging approaches foresee a promising future in improving cancer diagnostic imaging, thus impacting the quality of cancer patient care. Currently, most of the conventional imaging modalities such as magnetic resonance imaging (MRI), nuclear imaging, x-ray computed tomography (CT), and ultrasound (US) attempt to molecularly image tissues with exogenous agents. Typically, molecular imaging requires sufficient signal arising from minute quantities of the exogenous targeting agents in order to detect early stage and metastatic⁵ cancer. However, MRI and x-ray CT techniques require substantial (~millimolar) amounts of the contrast agents to generate sufficient signal in clinical imaging, and are thus challenged by nuclear and optical imaging techniques, which generate sufficient signal using orders of magnitude smaller levels (~ nanomolar) of the contrast agents. In addition, contrast agents delivered to the tissue in substantial (~ millimolar) amounts accumulate in excess at the

This dissertation follows the style and format of Optics Express.

¹ Prediction of the future course and likely outcome of a disease

² Related to morphological structure of tissues

³ Branch of genetics that studies genomes or full DNA sequences

⁴ Study of structure and function of proteins

⁵ Cancer that spreads from primary tumor cells

cell surface during the receptor mediated molecular targeting, thus challenging the concept of molecular imaging in contrast-enhanced MRI and x-ray CT techniques.

Diagnostic imaging of early stage breast cancer is essential for decreasing the death rate caused by cancer in the United States. The conventional anatomical based screening techniques are neither comprehensive nor infallible, especially in women with dense breast tissues. Molecular imaging using nuclear and optical techniques is the current alternative for diagnostic imaging of early stage breast cancer. While both nuclear and optical techniques require only small amounts (\sim nanomolar) of the contrast agents, near-infrared fluorescent contrast agents have a potential to generate a strong signal (at least 10^{23} events/sec) in comparison to the signal generated by the radioactive tracers ($< 10^4$ events/sec) in the nuclear imaging. In addition, the use of non-ionizing near-infrared radiation in optical techniques holds a promise for safe human imaging, with emphasis on quality patient care, in comparison to the use of ionizing gamma radiation in nuclear techniques.

Near-infrared (NIR) light between the wavelengths of 700-900 nm propagates deeply through tissues and provides a unique approach for molecularly-based diagnostic imaging. Over the past 15 years, near infrared (NIR) optical imaging approaches have been developed for breast cancer screening based upon the endogenous absorption contrast owing to the non-specific process of angiogenesis⁶ in order to discriminate normal from diseased tissues [2-8]. However, for diagnostic detection of early metastatic lesions wherein the angiogenesis induced contrast is non-existent or

⁶ Growth of blood vessels from surrounding tissue to a solid tumor

insufficient for tomographic⁷ NIR imaging of the breast, exogenous contrast based upon targeting and reporting fluorophores will be necessary [9-12].

In the Photon Migration Laboratories (PML), we have sought to develop fluorescence-enhanced optical tomography towards breast cancer diagnosis via molecular imaging techniques. The approach depends upon delivering molecularly targeting NIR excitable fluorescent contrast agents, which specifically target metastatic cancer cells within the breast tissue or, for prognostic indication of the extent of disease, within the lymph system draining the breast. Detection of cancer cells within the subsurface axillary lymph nodes, the internal mammary lymph nodes located beneath the medial sternum, or within the sentinel lymph node (or the lymph node closest to the primary breast tumor) is typically performed via biopsy following surgical resection,⁸ and in the case of sentinel lymph nodes, it is performed following anatomical mapping using nuclear imaging and detection techniques, and prior to surgical resection and pathology.⁹

Yet, before clinical feasibility trials involving the administration of a fluorescence contrast agent for diagnostic and prognostic imaging can commence, the efficacy of tomographic fluorescence-enhanced optical imaging must be demonstrated in clinically relevant phantom volumes. In addition, owing to the current lack of availability of a fluorescent contrast agent with a record of non-toxicity and patient safety, the translation of fluorescence-enhanced optical imaging into the clinic has been

⁷ Retrieval of information about the tissue interiors from boundary surface data

⁸ Removal of tissue or part or all of an organ by surgery

⁹ Study of tissues and cells under a microscope

limited and must be preceded by tissue phantom¹⁰ studies (mimicking the breast geometry), which may enable the assessment of detecting the multi-focality¹¹ of the disease. To date, three-dimensional fluorescence-enhanced optical tomography has been limited to *in-vivo* measurements in small animal models [13-14] or phantoms with unrealistic volumes/geometries [15-17] in comparison to what would be expected clinically in non-compressed tissues.

In the current work, we present the development of a fluorescence-enhanced optical imaging system, which interrogates clinically relevant tissue phantoms using rapid data acquisition schemes. Three-dimensional tomographic imaging results obtained under varying experimental conditions pertinent to diagnostic breast imaging within clinically relevant volumes is the highlight of the present work.

In the following background sections, we outline the various molecular-based imaging modalities, with emphasis on fluorescence-enhanced optical imaging, which can be performed using various measurement techniques and measurement geometries (Section 2). The light propagation model for fluorescence-enhanced optical imaging and the different approaches for tomographically reconstructing the tumor location in 2-D or 3-D tissue media are presented in the background section (Section 3). Details of the clinically relevant phantoms employed, the unique instrumentation involved in both measurement geometries, and a brief description of tomographic algorithm employed in the current work are described in the “Instrumentation and experimental tools” (Section 4) and “Simulations” sections (Section 5), respectively. The method of data analysis and

¹⁰ Model that mimics the required tissue or any substance of interest

¹¹ Multiple focal points of the spread tumor

a detailed experimental plan are presented in Section 6. The experimentally obtained images that demonstrate the feasibility for state-of-the-art 3-D fluorescence-enhanced optical tomographic reconstructions on clinically relevant tissue phantoms are presented for various target depths and target:background optical contrast ratios (Sections 7 and 8). Detection of multiple small targets in the breast phantom is demonstrated in order to assess the ability to detect the multi-focality of lesions using tomographic imaging (Section 9).

Optical imaging using fluorescent contrast agents has a unique opportunity to differentiate diseased lesions from normal tissue based on the changes in the lifetime of the fluorescing agent with respect to its environment [9]. Preliminary work towards fluorescence lifetime imaging is presented in Section 10. Experimental studies describing the specificity of the optical imaging system are explained by performing homogeneous (no target present) tissue phantom studies (Section 11). Finally, parallel ongoing clinical feasibility studies, performed as a group effort at PML, towards fluorescence-enhanced optical imaging for sentinel lymph node mapping in breast cancer patients is demonstrated (Section 12). The organization of the entire dissertation is provided in Figure 1.1.

When combined with novel targeting and reporting contrast agents, NIR tomographic imaging has the opportunity to augment or even replace the clinically applied nuclear imaging technique such as gamma, PET (Positron Emission Tomography) or SPECT (Single-Photon Emission Computer Tomography) imaging. Yet the added challenge for near-infrared (NIR) fluorescence enhanced imaging over

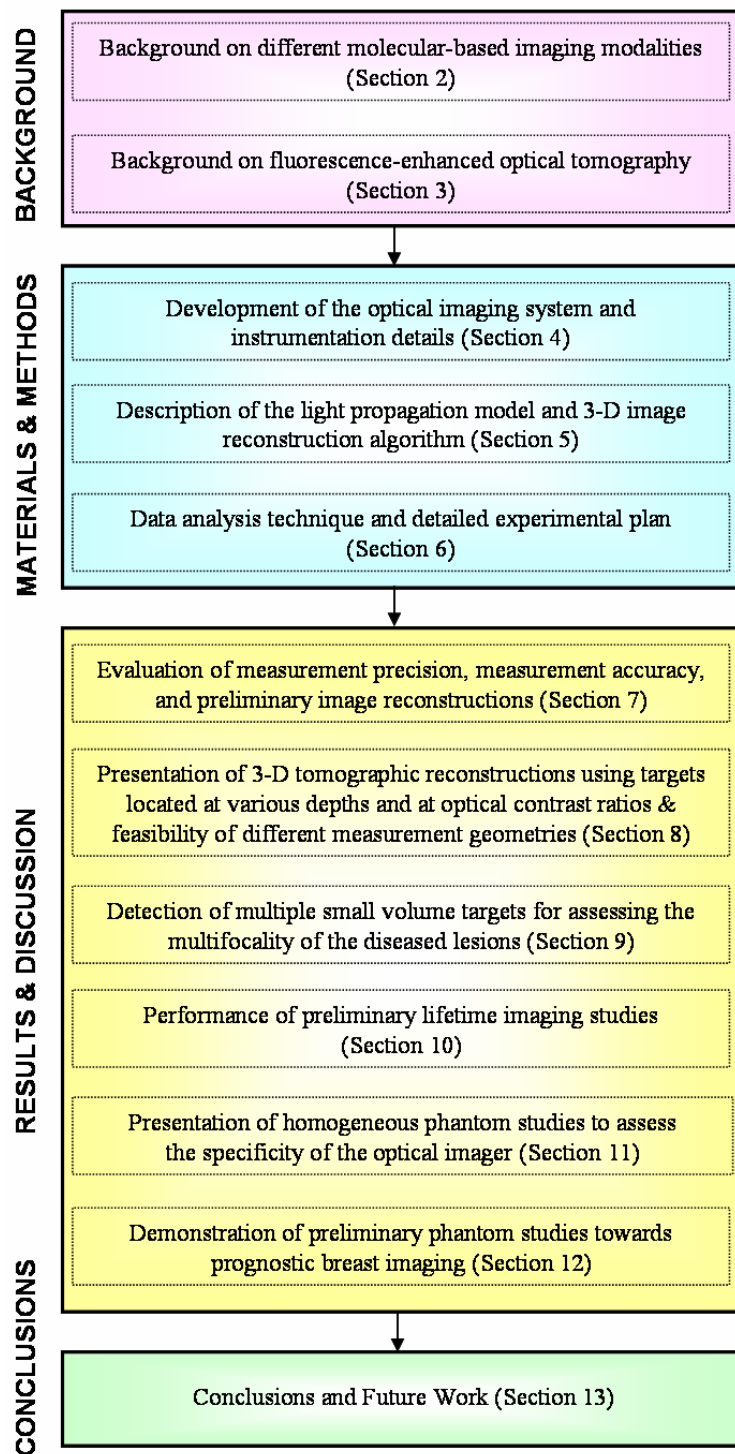


Figure 1.1 Organization of the dissertation.

nuclear imaging is that, unlike nuclear techniques, an activating or excitation signal must first be delivered to the contrast agent before there is registration of the emission signal from the tissue. However, since fluorescent contrast agents are not radioactive, their use in clinical imaging has significant advantages over radiocolloids and radionucleotides. Another opportunity for optical imaging is the ability for tomographic reconstruction and additional diagnostic information based upon the fluorescence decay kinetics of smartly designed probes. The current work will demonstrate preliminary investigations using an FDA (Food and Drug Administration) approved fluorescent agent, which may enable clinical translation of tomographic NIR techniques.

2. BACKGROUND: MOLECULAR IMAGING MODALITIES

Diagnostic imaging for assessment of breast cancer is typically based on the anatomical changes associated with the disease. The classical and *anatomically based* diagnostic procedures that perform soft and bony tissue imaging include x-ray mammography, ultrasound (US), magnetic resonance imaging (MRI), and computed tomography (CT) [18]. A comparison of the different conventional imaging modalities is provided in Table 2.1. Except MRI, these conventional imaging modalities are limited by their low contrast resolution for detecting early stage or small tumors. Direct imaging of molecular changes, which truly define the molecular basis of the disease, is the next frontier in diagnostic imaging research involving *in vivo* characterization and non-invasive mapping of cellular and sub-cellular molecular events towards early stage tumor diagnosis [1].

Molecular imaging techniques use molecular probes or contrast agents in small quantities (~ nanomolar concentrations) to examine integrative functions of molecules, cells, and organs, and also examine the structure and regulatory mechanisms of their organized functions, by molecularly targeting the cell receptors. Large quantities (~ millimolar concentrations) of the contrast agents do not molecularly target the cell receptors, but accumulate in the region of interest, thus challenging the concept of molecular imaging.

Successful *in-vivo* imaging at molecular levels requires (i) development of high affinity probes or contrast agents that can overcome the biological barriers,

Table 2.1 Comparison of conventional diagnostic imaging modalities.

Imaging Modality	Principle	Advantages	Disadvantages
X-ray	Uses x-rays of ~ 50 KeV photons to detect the x-rays attenuated by tissues of differing densities	Excellent resolution Good penetration depth	Ionizing radiation Poor contrast among soft tissues Overlooks 10% of breast cancer in non-calcified lesions
Computer Tomography (CT)	Uses x-rays in different angles for cross-sectional views	Same as x-ray technique, but provides more information	Greater exposure to x-ray radiation
Ultrasound (US)	Uses high frequency sound waves to detect the reflectance and transmittance from acoustically dissimilar tissues	Non-ionizing radiation Inexpensive Portable, safe, and versatile	Poor imaging quality Poor contrast
Magnetic resonance imaging (MRI)	Uses strong magnetic fields and rf waves to detect the emitted rf waves and relaxation of spin state of nuclei in tissues	Non-ionizing radiation Functional imaging Soft-tissue contrast Good resolution Good penetration depth	Strong magnetic field Expensive Not portable Slow process

(ii) improvement in the imageable signal for an increased contrast between normal and diseased cells and tissues, and (iii) development of fast, sensitive, cost-effective, and robust imaging systems with high resolution, specificity, and sensitivity.

2.1 Molecular imaging modalities towards breast imaging

Molecular imaging modalities towards breast imaging can be broadly categorized as (i) contrast-enhanced x-ray computed tomography, (ii) contrast-enhanced magnetic resonance imaging, (iii) contrast-enhanced ultrasound, (iv) radionuclide based (or nuclear) imaging, and (v) optical-based molecular imaging.

2.1.1. Contrast-enhanced x-ray computed tomography

X-ray computed tomography (CT) is based on the principle of launching x-rays (another form of electromagnetic radiation) onto the tissue surface and detecting the attenuated x-ray signals that geometrically propagate across the tissue volume. A schematic of the x-ray CT technique is provided in Figure 2.1. Based on the tissue type, tissue thickness, and its densities, different attenuation of x-rays occurs during passage through the tissue. If a tissue structure contains a greater number of atoms or heavier atoms x-rays are preferentially absorbed, thereby differentiating the tissue structures from one another. The x-rays are passed through the tissues in different angles and cross-sections along the path. The resulting attenuated x-ray signals are used to locate the tumors using simple image reconstruction techniques. X-ray CT is employed for breast imaging, but is limited by (i) its poor contrast in early stage or small tumors and (ii) its longer exposure to the ionizing x-ray radiation.

Contrast-enhanced x-ray CT has developed in the past few years towards improving contrast and hence detecting smaller lesions. Typically high molecular weight elements such as iodine, barium or xenon are used as contrast agents for x-ray CT. Due to their high molecular weight, these x-ray CT contrast agents absorb more x-rays, thus improving the contrast in the tissue regions. X-ray CT contrast agents are typically used in large concentrations (~millimolar) and are also toxic in nature. CT enhanced imaging with contrast-agents was employed in the prediction of residual breast

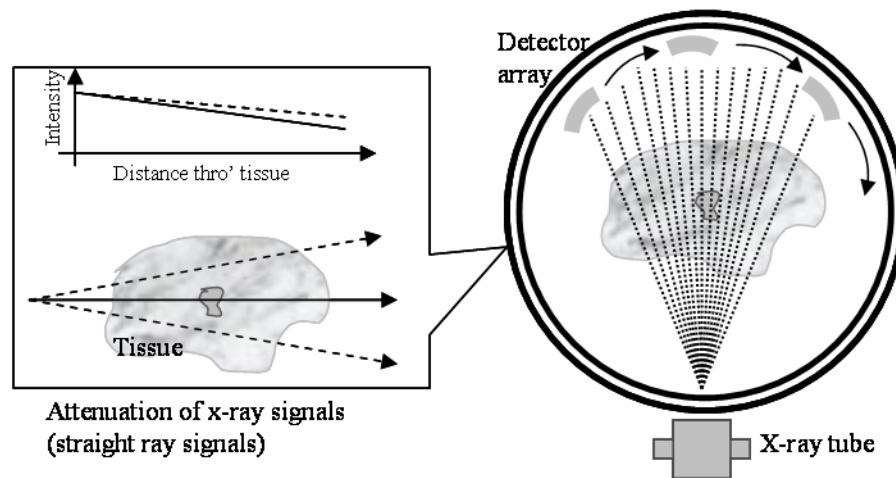


Figure 2.1 Schematic of the principle of x-ray computed tomography (left) and its clinical set-up (right).

cancer after chemotherapy [19] and for *in vivo* drug delivery [20], but has not been clinically applied towards breast cancer diagnosis.

2.1.2. Contrast-enhanced magnetic resonance imaging

Magnetic resonance imaging (MRI) is based on the principle of imaging the proton density and the radiofrequency (RF) waves of the spinning atomic nuclei in response to a magnetic field. A schematic of the MRI technique is given in Figure 2.2. In the presence of a strong, uniform magnetic field, a relatively greater number of protons in the nuclei align with the magnetic field in comparison to that in the absence of the magnetic field. This difference in alignment produces a net magnetization in the nucleus of the atoms, which allows them to precess (spin rotate) about the axis of the applied magnetic field, at a frequency depending on the strength of the magnetic field.

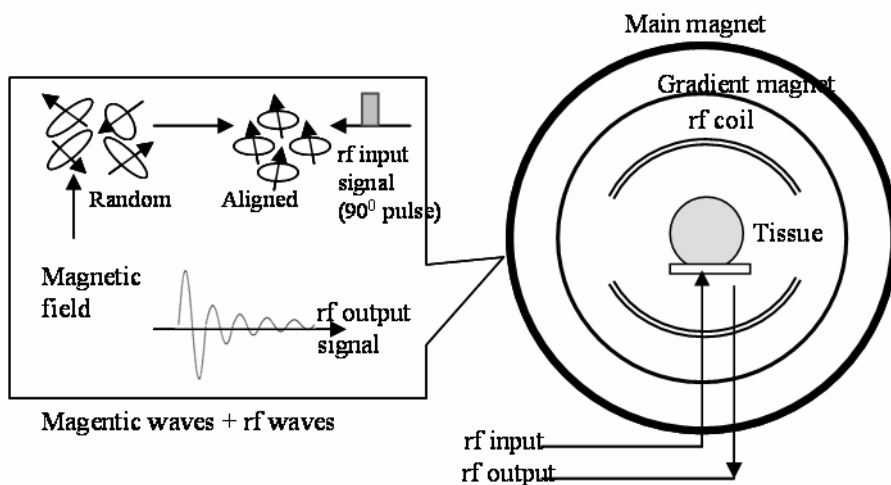


Figure 2.2 Schematic of the principle of magnetic resonance imaging (left) and its clinical set-up (right).

Upon perturbing the precessing nuclei using a pulsed RF wave, the nuclei precess in phase and emit a detectable, coherent RF signal at the precision frequency (termed the Larmor frequency). Gradient coils of weak magnetic field are used to provide spatial localization of the signal. The strength of the response and the time until which the signal fades are governed by: (i) the proton density, which is a measure of the free hydrogen constituting the water and lipids of various tissues; (ii) the T_1 and T_2 relaxation times (physical properties), which are defined by the way protons in the nucleus revert back to their equilibrium states after the initial RF pulse; and (iii) the T_2^* , which is a property of the MRI equipment and is defined as the time it takes for a real MRI signal to disappear. The average T_1 relaxation times for different organs in the body varies, thus differentiating between the normal and diseased organs based on the T_1 times. Unlike radionuclide imaging technologies, conventional MRI provides high resolution

anatomical imaging [18]. However, the use of intrinsic contrast agents for detecting breast cancer based on the relaxation times is less helpful [21].

Contrast-enhanced MRI is currently under development for enhanced imaging of breast cancer [22-24]. MRI contrast agents affect the relaxation times of the free hydrogen in different tissues, providing an enhanced contrast between different tissues based on difference in the relaxation times of the tissues. Gadolinium III (Gd(III)) complexes are considered as excellent contrast agents for advanced molecular imaging applications, although the current technology is at its developmental research phase [25]. The gadolinium chelates (metal Gd encapsulated within a substance that easily forms chemical complexes) are freely diffusible and serve as markers for detecting tumor angiogenesis, differentiating benign from malignant tumors, and also detecting tumors that were not visible in x-ray mammography [23-24]. Gadolinium chelates are less toxic than contrast agents used in contrast-enhanced x-ray CT, although large quantities (~millimolar) of the agent are still required for obtaining an enhanced-contrast during the imaging process. Despite the high sensitivity of the MRI technique, its cost-intensiveness and availability limits the clinical application of the technology. In addition, there are many unresolved issues in the clinical application of the contrast-enhanced MRI technique, which include (i) no defined standard technique or interpretation criteria, and (ii) unclearly defined clinical indications of applying the technology [22]. Recent studies involve dynamic contrast-enhanced MR imaging for detecting malignancies of the breast, where the tumors are evaluated with respect to their state of functional microcalcification [26-27]. Although the sensitivity of the technique

in breast imaging was the highest in comparison to mammography and ultrasound, MRI fails to depict every carcinoma of the breast.

2.1.3. Contrast-enhanced ultrasound

Ultrasound is based on the principle of detecting the reflected and transmitted acoustical impedance from the tissue medium in response to a short pulse of high frequency ultrasound waves between 1 to 15 MHz. A schematic of the ultrasound imaging technique is given in Figure 2.3. The high frequency sound (ultrasound) waves cause mechanical high frequency longitudinal vibration of the molecules, which reflect back the ultrasound waves in specific ways, based on the tissue type. Transducers are used for transmitting as well as collecting these ultrasound waves that are assumed to be straight ray waves in a tissue medium. Although conventional ultrasound is appealing by virtue of its low cost, portability, its millimeter-range resolution, and non-ionizing radiation, ultrasound is still limited in its application towards breast, heart or brain imaging due to its inherent low contrast and poor imaging quality [18].

Ultrasound imaging using microbubble contrast agents is under development for assessing molecular or genetic signatures for disease [28]. The microbubble contrast agents are tiny gas bubbles ($< 10 \mu\text{m}$ in size), which are stabilized within biodegradable shells. Each tiny bubble reflects sound waves and when these contrast agents are injected in the blood stream, the overall reflections from blood filled tissues increase significantly. Currently, the technology is focused towards non-invasive pathological detection with molecular targeting of thrombus, endothelial cells, and leukocytes [28].

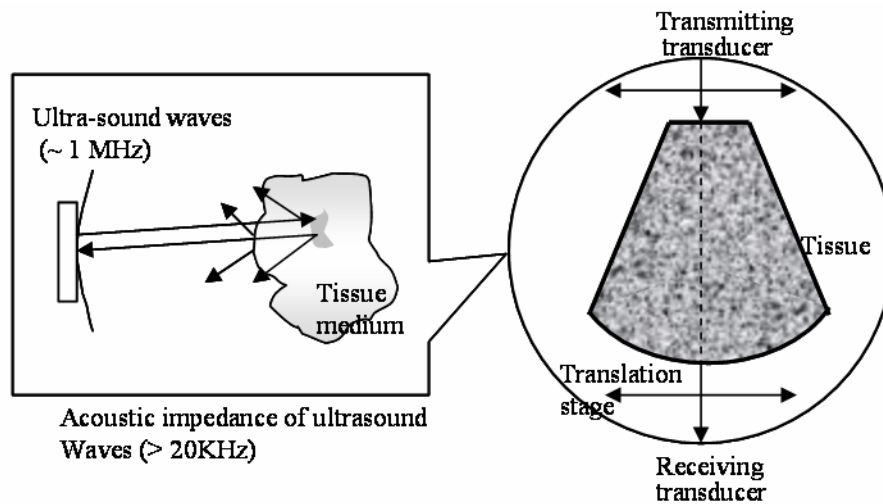


Figure 2.3 Schematic of the principle of ultrasound imaging (left) and its clinical application (right).

Preliminary studies in assessing the angiogenesis in small animals such as mice have been performed using the microbubble contrast agents [29] and extensive studies are yet to be performed on human breast tissues [30] before determining the clinical applicability of the technology.

2.1.4. Radionuclide based imaging

Radionuclide based imaging or nuclear imaging is based on the principle of injecting radioisotopes and detecting the emitted gamma rays from the tissues. Nuclear imaging technique includes single photon emission computed tomography (SPECT) and positron emission tomography (PET). Both SPECT and PET have the ability to label almost any chemical species with a suitable radionuclide, enabling the development of radioactive probes capable of imaging at molecular levels.

In SPECT imaging, the injected radionuclide attains stability by the γ decay process, where a single high-energy photon (~ 140 keV) is emitted. The single high-energy photon is detected using a gamma camera (a special camera to detect radioactive energy emitted by a radionuclide), and a collimator is used to acquire the detected signal from multiple views. A schematic of the SPECT imaging technique is given in Figure 2.4a. The radionuclides used in SPECT are relatively long-lived γ emitters such as Technetium-99m, Iodine-123, Xenon-133, Thallium-201, and Gallium-67. However, these radionuclides alter the biochemical activity of the pharmaceutical compound they are tagged to, thus altering the uptake rate and organ specificity of the tagged compound with respect to the untagged compound [18]. In addition, the image quality of SPECT can only be improved at the expense of its resolution and vice-versa. Thus SPECT is still at its developmental stages towards breast cancer imaging in human subjects.

In PET imaging, the injected radionuclide attains stability by the β^+ decay process, where β^+ particles (or positrons) are released. Each emitted positron from the proton-rich nuclei interacts with an electron and annihilates. During this process, the mass of proton and electron combines to give two gamma rays (~ 511 keV each) that travel $\sim 180^\circ$ apart, that is, outwardly in opposite directions from the annihilation site. These two gamma rays are in turn detected using a gamma camera [18]. A schematic of the PET imaging technique is given in Figure 2.4b. The radioisotopes used in PET are short-lived positron emitters such as ^{15}O , ^{11}C , ^{13}N , and ^{18}F . In PET, the radionuclide is not tagged on to pharmaceutical compounds (as in SPECT imaging), but incorporated in

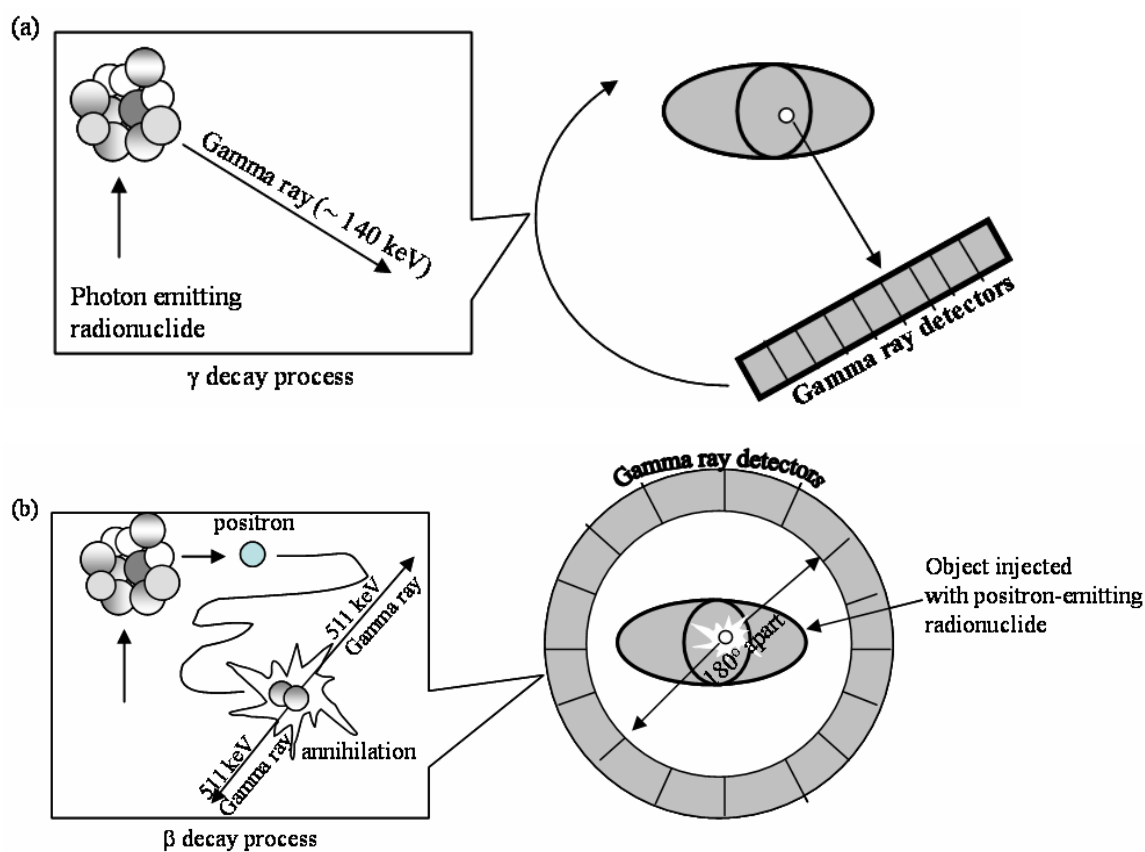


Figure 2.4 Schematic of the principle of radionuclide based imaging, including (a) single photon emission computed tomography (SPECT) (left) and its clinical set-up (right), and (b) positron emission tomography (PET) (left) and its clinical set-up (right).

the chemical structure of the compound. This helps prevent the alteration of the biological or biochemical activity of the compound, making it advantageous over SPECT imaging. In comparison to SPECT, PET better quantifies the radionuclide concentration, and provides greater resolution and sensitivity due to the production of two gamma rays that better localize the annihilation site.

Typically micro to milli- Curie quantities of radioactive material are injected into the whole body during nuclear imaging. These quantities correspond to a decay rate of $\sim 10^6$ to 10^8 disintegrations/sec (also termed as Bequerel) of the radioactive material ($1\mu\text{Cu} = 3.7 \times 10^4$ Bequerels). The various radiopharmaceuticals used in PET imaging are based on (i) glucose metabolism (^{18}F -2-fluoro-deoxyglucose (FDG)), (ii) amino acid metabolism (^{11}C L-methionine), or (iii) progesterin and estrogen receptors [31]. In the case of tumor diagnosis where the tumor cells have enhanced glucose metabolism, FDG-PET imaging technique can help (i) differentiate benign from malignant lesions, (ii) identify biological changes in early stage cancers, and also (iii) study the metastatic spread of the tumor in the whole body [32-34]. Although FDG-PET has an appropriate application in the evaluation of distant metastases, it is limited by (i) its sensitivity to detect or define small breast lesions (< 4 mm diameter), and by (ii) incompletely or partially determined specificity [35-36]. PET technology in general is limited not only by its cost and imaging time but also by its inability to detect lesions in patients with small risk of metastases [35-37].

2.1.5. Optical-based molecular imaging

Optical imaging is based on the principle of launching near-infrared (NIR) light (between the wavelengths of 700-900 nm, which corresponds to ~ 2 eV photons) on to the tissue surface and detecting the scattered and attenuated NIR signal. A schematic of the optical imaging technique is given in Figure 2.5. The normal tissues are

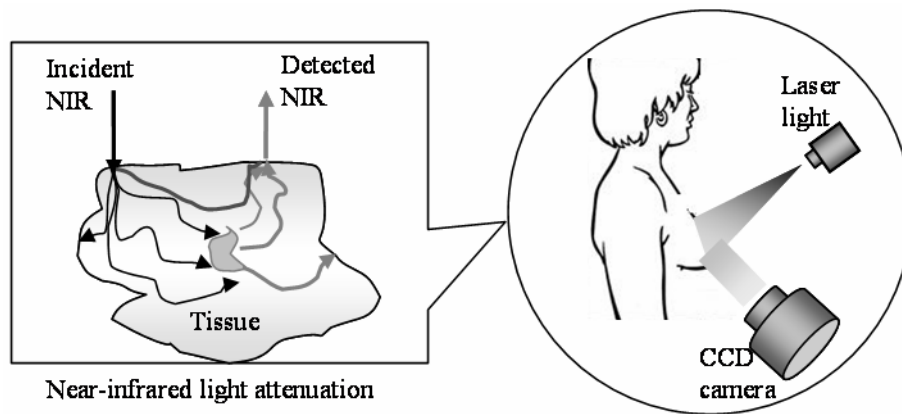


Figure 2.5 Schematic of the principle of optical imaging (left) and its possible clinical application (right).

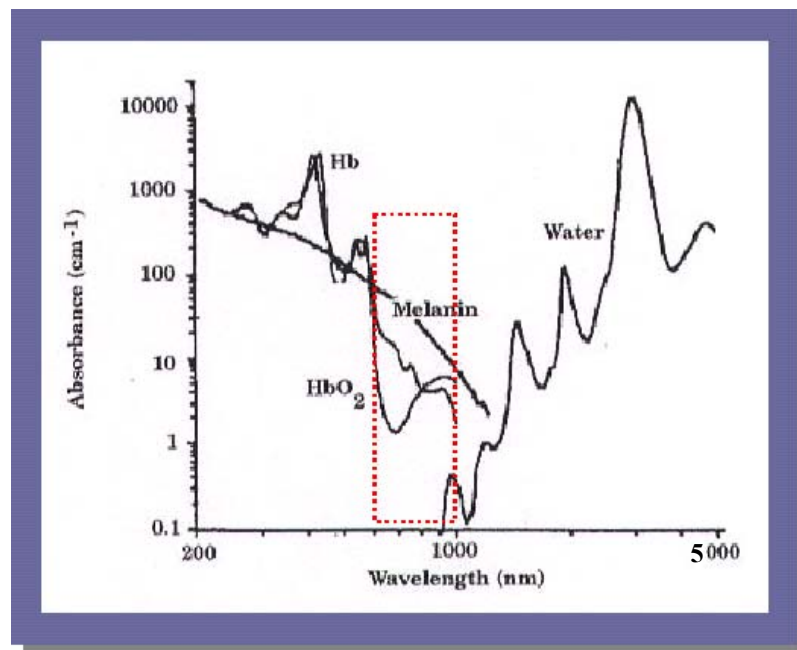


Figure 2.6 Therapeutic optical window in tissue medium. Adapted from Ref [39].

differentiated from the diseased tissues based on the inherent differences (termed as endogenous contrast) in the optical properties (in terms of absorption and scattering coefficient, as defined below) of the tissue medium [38]. Figure 2.6 shows the therapeutic optical window, where the blood components of oxy- and deoxy-hemoglobin exhibit low absorption and enhanced scattering, thus allowing deeper tissue penetration of the NIR light at 700-900 nm wavelength [39]. Measurements of the time-dependent photon density on the tissue surface (described in Section 2.3) can determine the average tissue absorption, which can be related to oxygenation hemoglobin saturation or blood volume, and the average scattering to the cell density. In other words, physiological information about the tissue can be inferred from optical imaging technique (or the photon migration technique).

When optical techniques using coherent light have been used for microscopic studies in the past, optical techniques using diffusely propagating light for deep tissue imaging is emerging as a new technology. One example of diffuse optical imaging in deep tissues is the breast imaging performed by various researchers using the non-invasive near-infrared light optical techniques [2-8]. The smallest detectable tumor so far detected through endogenous contrast mechanism was ~ 0.5 cm diameter, obtained by Franceschini *et al.* [2]. Although the endogenous contrast occurring due to the heterogeneous distribution of water, lipids, and hemoglobin in the diseased breast tissue helps in detecting late stage angiogenesis (growth of blood vessels from surrounding tissue to a solid tumors) in the breast, it does not help in detecting smaller tumors (i.e. < 0.5 cm diameter) or breast cancer at its early stages.

Hence, recent advances in optical imaging include the development of optical probes or contrast agents for molecularly targeting the diseased cells, thus enhancing the optical contrast ratio towards improved detection. Molecular imaging using optical probes or contrast agents provides: (i) high sensitivity due to the specificity of fluorescing molecules, (ii) cancer detection at the molecular onset of the tumor cells and before the tumor cells are apparent by their anatomical changes, and (iii) details of specific cancer types without altering the tumor environment. Optical probes or contrast agents currently used in *in-vivo* imaging are either tumor specific receptors [40], protease-activatable [41-42], or activated by transferred gene expression [43]. Various other contrast agents are under development towards enhanced specificity to tumor cells, and the reader is referred to reviews focused on the developments in contrast agents [10-11, 44-45].

Diffuse optical imaging is limited by its poor spatial resolution relative to x-ray, CT, and MRI; potentially long computation times for the development of a three-dimensional image; and instability and non-uniqueness of the image reconstruction problem (details of image reconstruction problem are explained in Section 3). Nonetheless, as a non-invasive and non-ionizing imaging technique, optical imaging with its high sensitivity feature can complement the conventional breast imaging techniques. This is especially true with the recent developments towards contrast-enhanced optical imaging that has generated considerable interest for breast cancer diagnosis and detection [10-12, 44-45]. One good example of the sensitivity feature of contrast-enhanced optical imaging is the work performed by Houston *et al.*, where ~100

femtomoles of the contrast agent located ~ 4 cm deep generated a signal at the tissue surface [12]. In addition, contrast-enhanced optical imaging has the potential to compete with the clinically available radionuclide imaging techniques, based on its non-ionizing radiation as well as the enhanced contrast it can provide using minimal quantities (nanomolar concentrations) of the optical contrast agent. When radionuclide imaging generates a maximum of 10^8 disintegrations/sec (or events/sec) upon injecting milli-Curie of radionuclides, fluorescence-enhanced optical imaging can generate almost $\sim 10^{23}$ events/sec even using nanomolar concentrations of the fluorescing agents that exhibit a nanosecond fluorescence lifetime. Since the radionuclides are already used in clinical studies towards breast imaging, the potential for fluorescence-enhanced optical imaging towards clinical application is high.

With focus on fluorescence-enhanced optical imaging in the current work, the physics behind this emerging molecular imaging technique is discussed in the rest of the chapter, providing details of the various measurement techniques and measurement geometries employed in the current imaging process.

2.2 Fluorescence-enhanced optical imaging

Fluorescence-enhanced optical imaging involves the use of fluorescent contrast agents in order to enhance the optical contrast between normal and diseased tissues. The process of emission of a photon, when a molecule relaxes from its excited state to the ground state is termed as *fluorescence*. In this process, a molecule of significant aromaticity absorbs light corresponding to a transitional energy level and becomes

activated into a “singlet” state, from which it can relax radiatively. Due to the loss of energy associated with the fluorescence process, the released energy of the light (i.e. emission light) is of lower energy (or higher wavelength) than the incident light (i.e. excitation light) [38]. The Jablonski diagram illustrating the electronic transitions associated with absorption and fluorescence is given in Figure 2.7.

The rate of radiative decay, Γ , and the rate of non-radiative decay, k_{nr} , from the “singlet state” to the ground state is mediated by the local environment of the activated dye molecule. The fluorescent lifetime, τ (or the mean time that the fluorophore resides in the activated “singlet” state), is influenced by the relative rates of radiative and non-radiative decays and is given by, $\tau = \frac{1}{\Gamma + k_{nr}}$. The quantum efficiency of the fluorescent

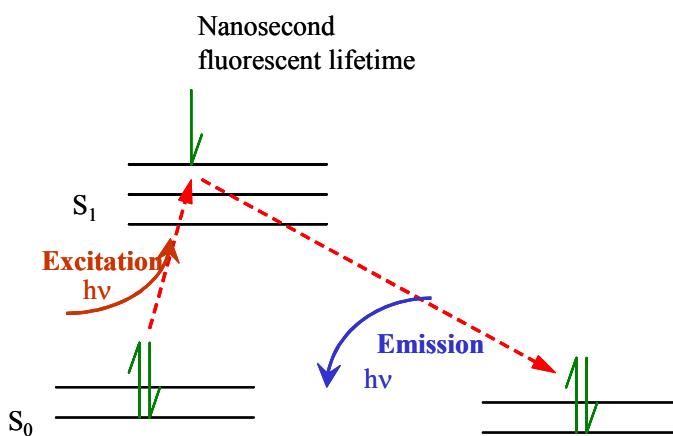


Figure 2.7 Jablonski diagram illustrating the principle of fluorescence.

emission (ϕ) is the fraction of excited dye molecules, or activated fluorophores, which relax radiatively and is given by $\phi = \frac{\Gamma}{\Gamma + k_{nr}}$.

In fluorescence-enhanced optical imaging process, when NIR light at the excitation wavelength is launched onto the tissue surface, the photons propagate into deep tissues, during which they are minimally absorbed and preferentially scattered (Figure 2.8). Upon encountering a fluorescent molecule, the photons excite the fluorescent molecules from their ground state to a higher orbital level. After residing at the higher energy orbital for a period defined as the *fluorescence lifetime*, the fluorescent molecule emits fluorescent signal of greater wavelength than the incident NIR light. The emitted fluorescent signal along with the perturbed excitation signal propagates in the tissue, before they are detected at the tissue surface.

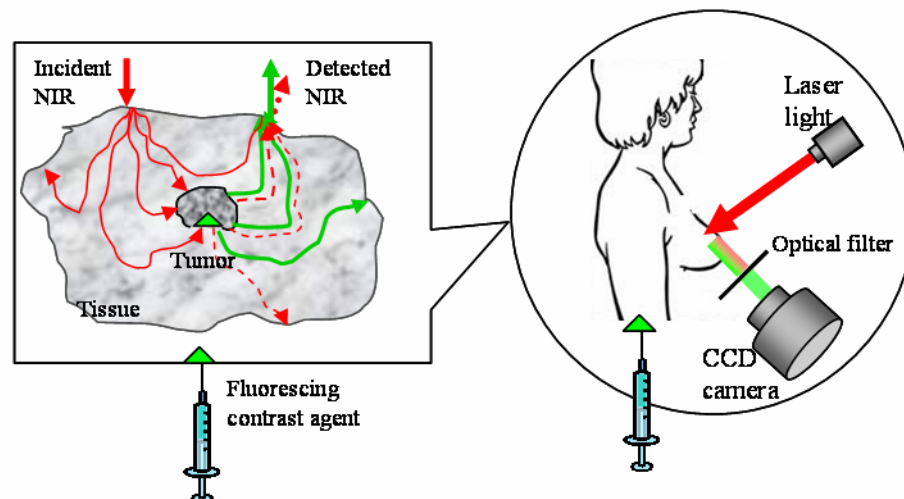


Figure 2.8 Schematic of the fluorescence-enhanced imaging process in a tissue medium (left) and its potential future clinical application (right).

The optical contrast in fluorescence-enhanced optical imaging can arise from absorption contrast or lifetime contrast. Absorption contrast is generally expressed in terms of the absorption coefficient (μ_a), defined as the inverse of the mean distance a photon will travel before being absorbed. In endogenous or intrinsic optical contrast, absorption occurs primarily from the tissue chromophores of oxy- and deoxy-hemoglobin, fat, melanin, and water. Upon using fluorescent contrast agents, the absorption contrast due to the fluorophore is the parameter of interest and it is based on the concentration of the fluorophore accumulated in the target and background. Scattering is typically due to refractive index differences of extracellular and intracellular structures causing reflection, refraction, and diffraction of photons. For fluorescence-enhanced imaging, optical contrast in terms of scattering is assumed negligible. Lifetime contrast is based on the difference in the lifetime of the fluorescing dye within the target and the background. This is achieved by using a single fluorescing dye whose lifetime varies with respect to the surrounding environment, such that the fluorophore in diseased tissue exhibits a differing lifetime than that within the background. Another method of obtaining a lifetime contrast is by using two fluorescing dyes of varying lifetimes, that excite and emit at similar wavelengths but each of the fluorescing dye has an affinity to different targets.

In either of the optical contrast approaches, the differences in the characteristics of the illuminating incident light signal and the detected signal are measured using time-dependent or time-independent measurement techniques (described in Section 2.3). From the collected signal the location of the fluorescent molecule, and in turn the

location of the diseased tissue is determined. Details of the different measurement techniques employed in fluorescence-enhanced optical imaging process are described in the following section.

2.3 Measurement techniques in optical imaging

Fluorescent light is launched and detected at the tissue surface using either time-independent techniques, such as continuous-wave (CW) imaging, or using time-dependent techniques such as time-domain photon migration (TDPM) and frequency-domain photon migration (FDPM). Details of each measurement technique are described below.

2.3.1 Continuous-wave imaging

In continuous-wave (CW) imaging, time-invariant steady-state NIR light at the excitation wavelength is launched onto the tissue surface and the emitted steady-state fluorescent light is detected at the tissue surface (Figure 2.9a). The NIR excitation light attenuates due to absorption and scattering in the tissue medium. Upon encountering the fluorescent molecule, steady-state fluorescent signal is emitted, which attenuates before it is detected at the tissue surface. CW imaging technique employs using photon multiplier tubes (PMTs) or charge coupled device (CCD) cameras for the detection of the time-invariant steady-state fluorescent signals.

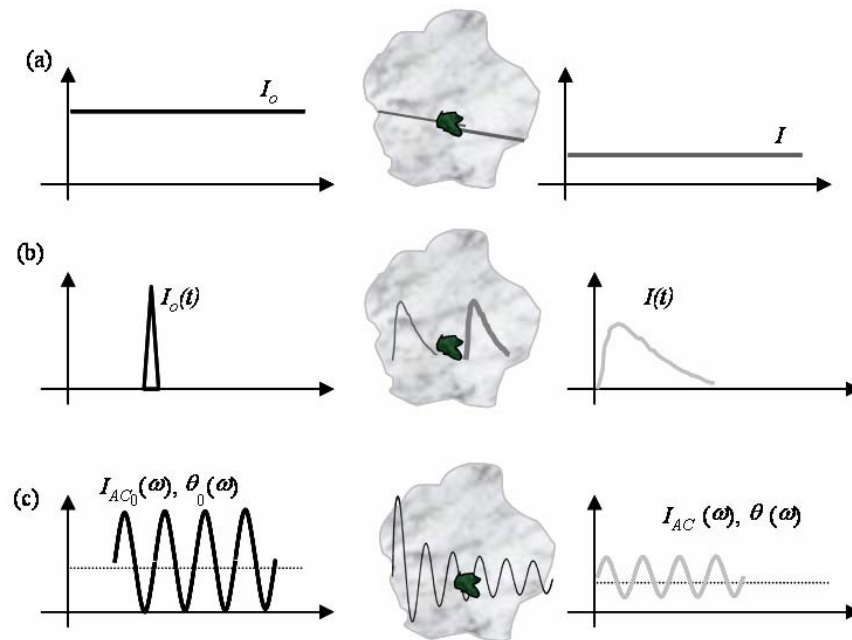


Figure 2.9 Schematic of the optical imaging process using different measurement techniques (a) continuous-wave imaging, (b) time-domain photon migration, and (c) frequency-domain photon migration. In each technique, the left hand plot represents input light intensity (I_o) launched onto the tissue surface, and the right hand plot represents the output light intensity (I) collected from the tissue surface.

Due to the highly scattering nature of the tissue medium, light travels in different paths between the point of illumination and the point of detection. Since CW imaging employs steady-state light signals, the distribution of path lengths between the illumination and detection points are not detected, thus limiting the information required to map the interior optical properties of the tissue required in order to locate the diseased tissue. In addition, the detected fluorescent signal depends on the fluorophore concentration, its decay kinetics, as well the optical properties of the tissue. Yet, the CW technique is unable to differentiate between changes in the fluorescent intensity arising from the fluorophore concentration or from its decay kinetics [46-49]. However, the

CW technique is widely employed for fluorescence-enhanced optical imaging owing to the simplicity of the technique.

2.3.2 Time-domain photon migration imaging

In time-domain photon migration (TDPM), a picosecond or femtosecond impulse of light is launched onto the tissue surface and the intensity of the detected light is recorded at some distance away from the point of illumination (see Figure 2.9b). The excitation light pulse broadens and attenuates as it travels through the scattering medium. Upon encountering a fluorescent molecule, a fluorescent light pulse is emitted, which broadens and attenuates as it propagates in the tissue medium. This broadened pulse of fluorescent light is further broadened and attenuated due to absorption and scattering in the tissue medium, before it is detected at the tissue surface. The time span between the launch of an excitation pulse and the detection of the emission pulse light represents the photon “times-of-flight” and the fluorescence decay kinetics, and is measured using photon counting techniques or streak camera detectors with picosecond or greater resolution [9,38].

TDPM is performed using single-photon counting or gated integration techniques. In the single-photon counting technique, the first fluorescent photon emitted after each incidence of excitation pulse is collected. However, collection of statistically significant photon counts in a reasonable amount of data acquisition time is not feasible using the single-photon counting technique. This poses a potential drawback to this detection technique. In the gated integration technique, the data acquisition time is

enhanced by recording the total number of photons arriving at the detector (within a small temporal window at varying times), following an incident excitation pulse. In either of these techniques, the photon collection times depend on the incident excitation photon “time-of-flights” associated with the kinetics of absorption and radiative relaxation of the fluorophore molecule, and photon “time-of-flights” of the emitted fluorescent pulse. The temporal discrimination of the excited and emitted pulse helps differentiate between the decay kinetics, fluorophore concentration, and the tissue optical properties.

Although TDPM measurements provide a wealth of information in order to map the optical properties of the tissues and are used by few researchers, it is still limited by its large dynamic range of signal-to-noise ratio (SNR), requiring significant data acquisition times compared to CW or FDPM techniques (as will be shown below).

2.3.3 Frequency-domain photon migration (FDPM) imaging

In FDPM, modulated excitation light at a single frequency is launched onto the tissue surface and the modulated fluorescent signal is detected at the tissue surface (Figure 2.9c). The incident excitation light intensity is sinusoidally modulated at frequencies varying between 10 MHz to 1 GHz. The optimal frequencies in the physiological range of optical properties vary between 30-200 MHz.

The modulated excitation light or “photon density wave” propagates as a spherical wave (when illuminated at a single point) (Figure 2.10). Owing to the absorption and scattering properties of the tissue, the excitation wave is amplitude

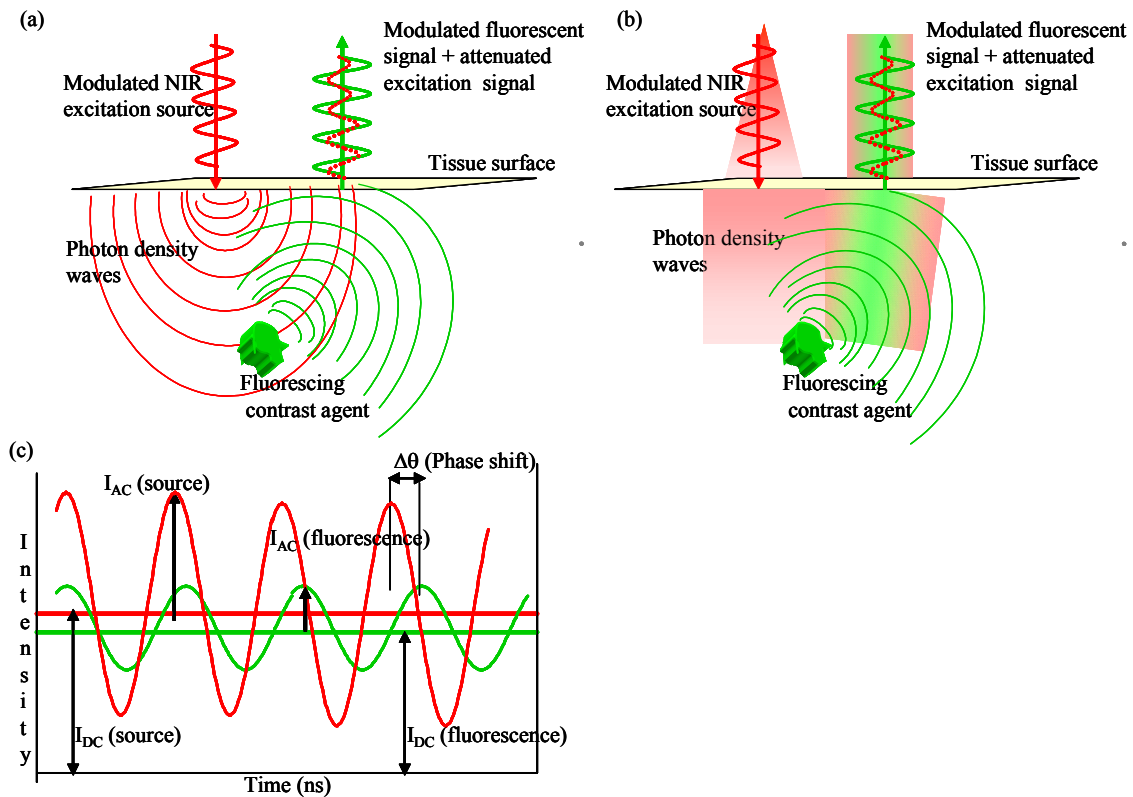


Figure 2.10 Fluorescence-enhanced optical imaging in the frequency-domain (a) detailed schematic of the FDPM principle using point illumination and point collection measurement geometry, (b) detailed schematic of the FDPM principle using area illumination and area collection measurement geometry, and (c) phase shift and amplitude attenuation observed during in any FDPM process.

attenuated and phase shifted relative to the incident wave [9,38]. Upon encountering the fluorescent molecules within the tissue, a fluorescent “photon density wave” is generated with additional amplitude attenuation and phase lag owing to the fluorescence decay kinetics of the fluorophore. This fluorescent photon density wave then propagates throughout the tissue and during transit, experiences additional amplitude attenuation and phase lag owing to the tissue optical properties until it reaches the tissue boundaries and is detected using modulated photon multiplier tubes (PMTs) or gain-modulated

intensified charge coupled device (CCD) cameras. The detected phase shift (θ) and AC amplitude, given by the fluence, Φ ($\Phi = I_{AC} \exp(i\theta)$), (that is, intensity of detected light) are related to the optical properties of the tissue and are used to map the optical properties of the tissues in order to locate the diseased tissues (see Section 3.1 for further details).

The FDPM technique is a Fourier analog of the TDPM technique, which can differentiate between the decay kinetics, fluorophore concentration, and the tissue optical properties, similar to TDPM. However, FDPM is preferable over TDPM due to its inexpensive instrumentation and improved signal-to-noise ratio (SNR). In addition, the steady-state FDPM measurements in terms of amplitude and phase are minimally corrupted by the ambient light, since the instrument detects only modulated signals. Thus the FDPM instrument automatically acts as a filter for ambient light rejection, which is not only an advantage for FDPM over CW or TDPM techniques, but favored for clinical application in a non light-proof environment.

Thus, fluorescence-enhanced optical imaging can be performed using either of the above measurement techniques in order to acquire surface boundary measurements. Measurements can be acquired at discrete points or over a given area, based on the mode of detection, as well as on the type of excitation illumination (point or area) of the tissue surface. The different feasible measurement geometries that describe the mode of illumination of excitation signal and detection of emission signal are described in the following section.

2.4 Measurement geometries

The incident excitation light can be launched onto the tissue surface and the emission light collected using various measurement geometries (see Figure 2.11) such as (i) point illumination and point collection, (ii) interstitial illumination and collection, (iii) area illumination and area collection, (iv) point illumination and area collection, and (v) area illumination and point collection.

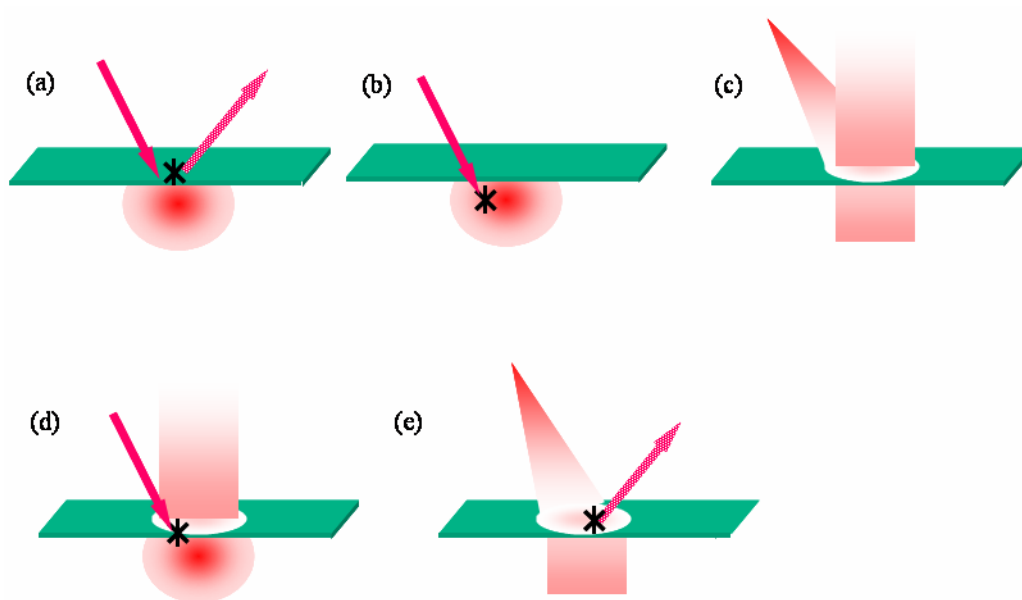


Figure 2.11 Schematic of different measurement geometries (a) point illumination and point collection geometry, (b) interstitial point illumination, where the point of illumination is below the tissue-like surface, with collection via point or area detection, (c) area illumination and area collection geometry, (d) point illumination and area collection geometry, (e) area illumination and point collection geometry.

2.4.1 Point illumination and point collection measurement geometry

The method of point illumination and point collection is achieved by illuminating at a single point using the excitation light source and detecting the emitted fluorescent signal at a distance away from the point of illumination. Point illumination of excitation light from lasers or laser diodes is typically launched onto the tissue surface via optical fibers (which range from μm - mm in diameter) and the emitted fluorescent signal is collected via optical fibers and detected using photon multiplier tubes (PMTs) or avalanche photo diodes (APD). The point of incident excitation light results in propagation of light that attenuates exponentially along tissue depths, thus probing minimal tissue volumes (Figure 2.11a). Hence dense boundary surface measurements are required using this measurement geometry in order to locate a tumor in an otherwise unknown location. Due to the nature of the measurement geometry illuminating and detecting point locations on tissue surface, the probability of missing the tumor location or the region of interest are high during imaging. Yet, the point illumination and point collection measurement geometry has been employed by various researchers in order to locate tumors in 2-D and 3-D tissue phantoms [38] probably because of point illumination and collection are traditionally used in tomography and geophysical imaging.

2.4.2 Interstitial illumination measurement geometry

The method of interstitial illumination is achieved by invasively illuminating the tissue medium below its surface and near the region of interest (or the tumor location).

Illumination is typically performed by launching the excitation source via optical fibers embedded in the tissue. This illumination geometry increases the chances of exciting the fluorophores near the region of interest, but requires *a priori* knowledge of the target's location. Interstitial illumination has been used in coordination with area detection technique towards imaging drug distribution in tumors present in mice [50], but has not been applied to optical imaging towards tumor diagnosis due to the invasive nature of the illumination technique.

2.4.3 Area illumination and area collection measurement geometry

The method of area illumination and area collection is achieved by illuminating a given area of the tissue surface and detecting the same or different area of the tissue surface. Area illumination is achieved using an expanded beam of excitation source light attained from lasers or laser diodes, and the area detection is typically achieved using charge coupled device (CCD) cameras or by photography. In *in-vivo* fluorescence-enhanced optical imaging of small animals, area detection is accomplished using incident powers typically ranging from $\mu\text{W}/\text{cm}^2$ – mW/cm^2 (review of this work is provided in reference [38]). The area illumination and area collection technique not only increases the density of acquired boundary surface measurements, but also enhances the data acquisition rates, since a greater area of the tissue is scanned in a given time in comparison to the area scanned using point illumination and point collection geometry.

In general, CCD cameras are used for area detection, along with or without image intensifiers for enhancing the weak fluorescent signal, and along with or without a spectrograph for spectral discrimination. In either of the different combinations of area detection, the SNR depends not only on the sensitivity of the photodetector, but also on its integration time and the amount of fluorescent signal emitted and collected. In spite of using a very sensitive detector, the imaging system is usually limited by excitation light leakage. The excitation leakage occurs if the difference between the excitation and emission wavelength maxima (obtained from the absorption and emission spectra) of the fluorescence contrast agent is very small. The excitation leakage problem is also due to the inefficiency of the optical filters to reject the excitation light completely and detecting only the weak fluorescent signal. In the case of area illumination and area detection geometry, apart from the excitation leakage problem, the specular reflection from the tissue surface further enhances the difficulty in collecting the weak fluorescent signal. The method of area illumination and area detection is widely used for optical imaging in small animal models [38], where the tumor is qualitatively located from 2-D images which are acquired from the animal's tissue surface. However, this measurement geometry has not been employed in quantifying the 2-D images in order to locate the tumors in 3-D tissue medium. Work is currently performed at PML employing area illumination and area collection measurement geometry for locating tumors in 3-D tissue phantoms [51-52]. Some of this work is presented as a portion of the current project in Section 12.

2.4.4 Point illumination and area collection measurement geometry

The method of point illumination and area collection is achieved by illuminating the excitation light at a single point and collecting the emitted fluorescent signal over a given area on the tissue surface. Point illumination is achieved by launching the excitation light from laser or laser diodes via optical fibers, and area detection is achieved using CCD cameras or by photography. A few fluorescence imaging studies have been performed using point illumination and area collection geometries, with modifications to the mode of illumination (fiber optics through an endoscope [53], or fiber optics on the surface [54]) and detection (fiber bundles interfaced to be detected by a CCD [54] or area detection by photography [53]).

Detection geometry employing intermediate fiber bundles that are imaged using CCD camera or by photography is effectively a point collection geometry, where the data acquisition rates are enhanced by detection of multiple collection points on the tissue surface simultaneously. Hence, the measurement geometry can be considered as a *hybrid measurement geometry* that is based on point illumination and point collection measurement geometry, with improvement in data acquisition rates achieved by performing area detection over the multiple collection points.

In recent years, Ntziachristos *et al.* has employed this *hybrid measurement geometry* in small animal studies, in order to quantitatively locate the 3-D tumor location using CW imaging technique [13-14]. Most of the currently available mathematical tools to quantitatively estimate the 3-D tumor location are based on the point illumination and point collection geometry. By employing the hybrid measurement

geometry, not only is the tumor located in 3-D, but the data acquisition rates are also enhanced. The current work also employs this hybrid measurement geometry, by interfacing multiple collection points for area detection using a CCD camera. Implementation of this measurement geometry for our current research using time-dependent techniques is described in Section 4.

2.4.5 Area illumination and point collection measurement geometry

The method of area illumination and point collection is achieved by illuminating the excitation light as an expanded beam of given area and collecting the emitted fluorescent signal at a given point on the tissue surface. Although this measurement geometry is theoretically feasible, there is no practical application for this measurement geometry and it has not been employed in optical imaging studies.

In summary, fluorescence-enhanced optical imaging can be performed using various measurement techniques and measurement geometries. Each of these geometries have their respective advantages and disadvantages as described above. Using either of these methods, boundary surface measurements of the emitted fluorescence signal are acquired and used in tomographic reconstructions of the target's location and size. The different methods of tomographic reconstructions are described in detail in the following chapter.

3. BACKGROUND: FLUORESCENCE-ENHANCED OPTICAL TOMOGRAPHY

In any imaging modality, mathematical tools are applied to the acquired boundary surface measurements, in order to obtain a 2-D or 3-D image of the interior tissue medium. The process of solving this boundary-value problem in imaging techniques is termed as *tomography*. Tomography is performed in every imaging modality using mathematical tools that are based on the physics of the imaging process. Imaging modalities such as x-ray CT, ultrasound, MRI, and nuclear imaging generating x-rays, ultrasound waves, magnetic waves, and gamma rays, respectively are assumed to minimally scatter in a tissue medium. Hence the incident and detected signals in all these imaging modalities are assumed as *straight-ray signals*, thus simplifying the mathematics behind the imaging process. Two-dimensional or three-dimensional images can be generated by performing simple back-projection techniques.

The technique of *backprojection* is typically applied through Fourier transforms in reconstructing images from the given imaging modality. In this method of backprojection, it is assumed that there is a single definite path between the source and the detector, along which the radiating signal attenuates. By changing the orientation of the source-detector pair along different angles on the domain surface, or by using multiple source-detector pairs located in different orientation angles, the tissue densities can be mapped and the target location backprojected. However, the backprojection technique becomes erroneous when scattering increases in a tissue medium. Hence, the

technique cannot generate accurate 2-D or 3-D images in optical imaging of large tissues, since optical imaging is based on the principle of minimal absorption and preferential scattering, where the assumption of *straight-ray signals* is incorrect. Tomographic reconstruction of NIR light in optical imaging is thus performed by employing mathematical formulations, which describe the principle of light propagation in a highly scattering tissue medium.

3.1 Light propagation model using diffusion equation

Propagation of light can be modeled using either a microscopic (discrete) approach or a continuum approach [55]. In a microscopic approach, which uses Maxwell equations, the approach is more fundamental and exact. However, modeling light propagation in a biological tissue at microscopic levels becomes computationally expensive.

Alternately, the continuum approach describes the light propagation using the transport phenomenon of light and is given by the radiative transport equation [56]. Several assumptions have been made to this transport equation for computational ease in biological media and to obtain the *photon diffusion equation*. These assumptions are: (i) the source is isotropic in nature (in other words, the source emits light with uniform angular distributions); (ii) the scattering length is much smaller than the mean free absorption length or $\mu_s' \gg \mu_a$ in the medium; and (iii) the distance between the point of illumination and collection is at least ten times the scattering length. With these assumptions, the *photon diffusion equation* can be derived and used to predict the light

propagation in random media as well as in tissues [56]. To predict the fluorescent light generation and its propagation in tissues, we employ a coupled diffusion equation to predict the fluence, or the concentration of the photons times the speed of light. The coupled diffusion equation for light propagation at a given modulation frequency of light, f ($\omega=2\pi f$ radians) is given by [57-59]:

$$-\nabla \cdot [D_x(\vec{r})\nabla\Phi_x(\vec{r},\omega)] + \left[(\mu_{axi} + \mu_{axf})(\vec{r}) + \frac{i\omega}{c_x} \right] \Phi_x(\vec{r},\omega) = S\delta(\vec{r} - \vec{r}_s) \quad (3.1)$$

$$-\nabla \cdot [D_m(\vec{r})\nabla\Phi_m(\vec{r},\omega)] + \left[(\mu_{ami} + \mu_{amf})(\vec{r}) + \frac{i\omega}{c_m} \right] \Phi_m(\vec{r},\omega) = \phi\mu_{a_{x \rightarrow m}} \frac{1}{1 - i\omega\tau} \Phi_x(\vec{r},\omega) \quad (3.2)$$

In the above equations, Φ_x and Φ_m are the AC components of the excitation and emission fluence (photons/sec.cm²) respectively; μ_{axi} is the absorption coefficient due to the chromophores (cm⁻¹) (i.e. the endogenous chromophores in tissues); μ_{axf} is the absorption coefficient due the fluorophores or the exogenous fluorescing agents (cm⁻¹); μ_{am} represents the absorption coefficient of the emission light due to the chromophores (cm⁻¹); and ϕ and τ denote the quantum efficiency and lifetime (nsec) of the fluorophore, respectively. The terms c_x and c_m represent the velocity of light at excitation and emission wavelengths (cm/sec); ω corresponds to the modulation frequency of propagating light ($=2\pi f$ radians); and r and r_s are the positional vectors at a given point and source illumination point, respectively. The excitation fluence, Φ_x , couples the

diffusion equations (3.1) and (3.2). In the frequency-domain, fluence at excitation and emission wavelengths are given by $\Phi_x = I_{AC,x} \exp(i\theta_x)$ and $\Phi_m = I_{AC,m} \exp(i\theta_m)$, respectively. Here I_{AC} is the amplitude and θ is the phase shift at excitation(suffix 'x') and emission (suffix 'm') wavelengths, respectively.

The optical diffusion coefficients, D_x and D_m for the excitation and emission light (cm) are given by

$$D_{x,m} = \frac{1}{3}(\mu_{ax,m} + \mu_{sx,m}(1-g)) \quad (3.3)$$

where μ_{sx} and μ_{sm} are the scattering coefficients at excitation and emission wavelengths (cm^{-1}), respectively. Here, g represents the anisotropy coefficient, which is defined as the average cosine of the scattering angle, and varies from 0 for an isotropic medium to 1 for a forward scattering medium (typically, $g > 0.9$ for biological tissues). The term $\mu_s(1-g)$ is also defined as the reduced scattered coefficient μ_s' .

Simulated studies have been performed comparing the accuracy of the diffusion approximation with respect to the full radiative transport equation [60]. It was observed that the diffusion equation was not accurate near boundaries of the medium and near source locations. Also, when the anisotropy coefficient, g was greater than 0.85 (typically observed in biological tissues), the errors were large in a CW imaging system [61]. However, when the source detector distance was maintained at least ten times the transport length, the effect of anisotropy coefficient on the errors in the diffusion

approximation was minimal [62]. The coupled diffusion equations are solved using one of the boundary conditions described in the following section.

3.2 Boundary conditions

Several boundary conditions have been suggested to represent the tissue boundaries (Figure 3.1), including, (i) the partial current boundary condition, (ii) the extrapolated boundary condition, and (iii) the zero-boundary condition.

3.2.1 Partial current boundary condition

The partial current boundary condition, which is representative of the physics, states that the photon leaving the tissue surface never returns and the Fresnel reflections at the air-tissue interface are determined using a reflection parameter [63-64].

$$\Phi_{x,m}(r, \omega) + 2\gamma D_{x,m}(r) \frac{\partial \Phi_{x,m}(r, \omega)}{\partial n} = 0 \quad (3.4)$$

where γ is the index-mismatch parameter, which is a function of the effective refractive index (R_{eff}) at the boundary surface.

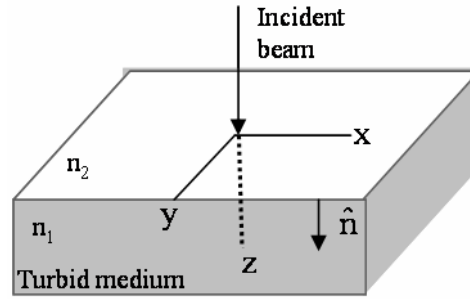


Figure 3.1 Schematic of tissue boundary surface. n_1 is the refractive index of the tissue medium, n_2 is the refractive index of the outside medium, and \hat{n} is the normal to the tissue surface.

$$\gamma = \left(\frac{1 + R_{eff}}{1 - R_{eff}} \right) \quad (3.5)$$

R_{eff} is determined directly from Fresnel's reflections, R_j and R_ϕ and is in turn related to relative refractive index, n_{rel} [59].

$$R_{eff} = \frac{1 + R_j}{1 - R_\phi} \quad (3.6)$$

where

$$R_j = \int_0^{\pi/2} 2 \sin \Theta \cos \Theta R_{Fresnel}(\Theta) d\Theta \quad (3.7)$$

$$R_{\Phi} = \int_0^{\pi/2} 3 \sin \Theta \cos^2 \Theta R_{Fresnel}(\Theta) d\Theta \quad (3.8)$$

and $R_{Fresnel}$ is the Fresnel reflection coefficient for light incident upon the boundary at an angle of incidence, Θ [63].

$$R_{Fresnel}(\Theta) = \frac{1}{2} \left(\frac{n_1 \cos \Theta' - n_2 \cos \Theta}{n_1 \cos \Theta' + n_2 \cos \Theta} \right)^2 + \frac{1}{2} \left(\frac{n_1 \cos \Theta - n_2 \cos \Theta'}{n_1 \cos \Theta + n_2 \cos \Theta'} \right)^2 \quad \text{when } 0 \leq \Theta \leq \Theta_c \quad (3.9)$$

$$R_{Fresnel}(\Theta) = 1 \quad \text{when } \Theta_c \leq \Theta \leq \pi/2 \quad (3.10)$$

where n_1, n_2 are the refractive index of the turbid (or tissue) medium and the outside medium ($n_{rel} = n_2 / n_1$), respectively; Θ and Θ' are the angle of incidence within the turbid medium and the refracted angle in the outside medium, respectively, which satisfies $n_1 \sin \Theta = n_2 \sin \Theta'$. The critical angle Θ_c for total internal reflection is given by $n_1 \sin \Theta_c = n_2$. The value of R_{eff} varies for different interfaces. Consequently the γ term varies within the partial current boundary condition.

3.2.2 Extrapolated boundary condition

The extrapolated boundary condition is a simplified form of the partial current boundary condition [65-67]. Here, the fluence rate is set to zero at an extrapolated boundary located at a distance, z_b outside the domain.

$$\Phi_{x,m}(r, \omega) = 0 \quad \text{at } z = z_b \quad (3.11)$$

An approximate value for z_b was estimated to include the Fresnel reflection at the surface and is given in terms of the index mismatch parameter and diffusion coefficient as [63]

$$z_b = 2\gamma D_{x,m}(r) \quad (3.12)$$

3.2.3 Zero fluence boundary condition

In the zero fluence boundary condition, the fluence Φ is set to zero on, as well as, outside the boundary.

$$\Phi_{x,m}(r, \omega) = 0 \quad \text{at } z = 0 \quad (3.13)$$

Although the zero fluence boundary condition is mathematically simpler and yields an analytical solution to the diffusion equation in homogeneous scattering media, it does not represent the real system accurately [63,65].

The coupled diffusion equations are used along with one of the above boundary conditions, in order to solve for the parameter of interest. In any feasibility studies, the optical tomography problem is solved in three steps. As a first step in optical tomography, the interior optical property map of the tissue medium is assumed known and the coupled diffusion equations are solved for the fluence at either wavelengths

(termed as *forward problem*) (Figure 3.2). As a second step, the fluence obtained from the forward model is compared to the acquired boundary surface measurements, in order to validate the light propagation model employed for fluorescence-enhanced optical tomography; in other words, model validation is performed on known phantoms. As a third and final step, the acquired boundary surface measurements are used in the coupled diffusion equations in order to estimate the interior optical property map (termed as *inverse problem*); in other words, inversions are performed assuming that the phantom properties are unknown. In a practical situation containing unknown phantoms, the acquired boundary surface measurements are used along with the light propagation model in order to solve the *inverse problem* (third step in feasibility studies) directly. Details of the forward and inverse problem in fluorescence-enhanced optical tomography are described in the following sections.

3.3 Forward problem in fluorescence-enhanced optical tomography

In the forward problem of fluorescence-enhanced optical tomography, the optical properties are assumed known for the entire tissue medium (or domain) and the fluence is evaluated using analytical or numerical methods over the entire tissue medium (Figure 3.2). Analytical methods are employed for infinite or semi-infinite media by making suitable assumptions and approximations. For a finite medium, it is difficult to solve the coupled equations analytically, and hence numerical methods such as the finite difference or the finite element methods are employed.

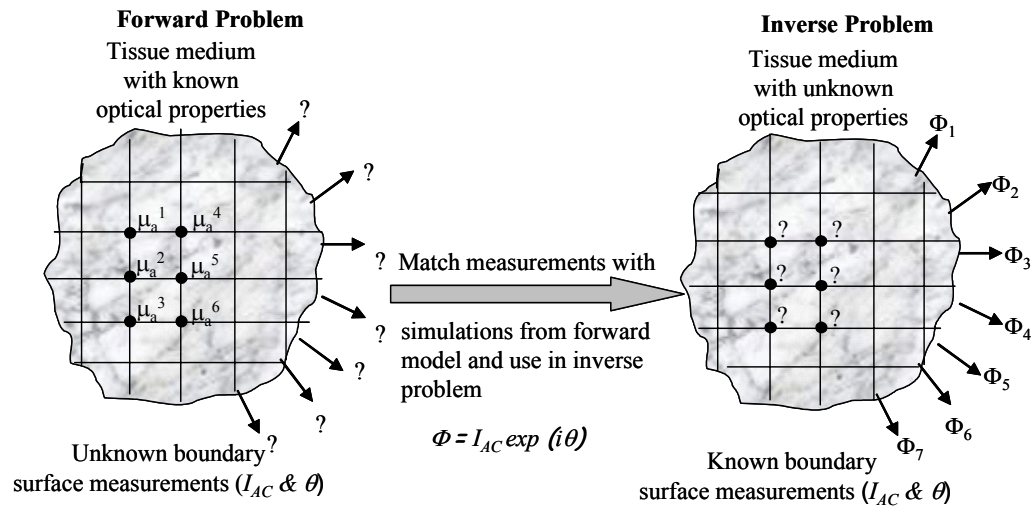


Figure 3.2 Schematic of the forward problem (left) and the inverse problem (right) in optical tomography.

In the finite difference (FD) method, the entire 2-D or 3-D domain is discretized into square or cubic elements, respectively and the unknown parameter is estimated at each node of every element. The mesh is finely resolved in order to minimize the discretization error at the cost of increasing in the dimensionality of the problem. Hence, the forward problem becomes computationally intense in the case of large 3-D domains. This problem can be overcome by using multigrid finite difference methods over single grid methods [68-71]. In the multigrid FD method, the problem is solved initially on a coarse mesh and the results are used as an initial guess on successive finer meshes. The process is continued until the desired resolution is reached. Not only is the multigrid method faster than the single grid method, but also reduces the discretization errors while maintaining resolution [68, 72-73].

The finite element (FE) method involves the discretization into triangle elements in 2-D domains, or tetrahedral, pyramidal, and hexahedral elements in the 3-D domain. In this method, if the mesh is not finely discretized, then errors in the numerical solution of the coupled equations result. However, unlike the finite difference methods, FE methods can be employed on curvilinear domains, such as the physiological tissue shapes, with minimum discretization errors and better computational efficiency in the inverse problem upon appropriate coding [74-76], and applicable to the coupled diffusion equations in both the time- and frequency-domain. Typically, the finite element method is formulated using the Galerkin approximation, where the second-order coupled diffusion equation is converted to first-order differential equations. The solution of these first-order differential equations are in turn approximated as a linear function in space within each finite element. Details of this method are discussed in Section 5.

Using either the analytical or numerical methods, the forward problem has a unique solution even for large 3-D domains, since the number of unknown variables (that is, fluence at each point) is less than or equal to the number of known parameters (that is, optical properties at each point) in the 3-D discretized domain. The fluence obtained at both the wavelengths is thus compared to the boundary surface measurements acquired at both the respective wavelengths in a known 3-D domain. Having validated the light propagation model with respect to the acquired boundary surface measurements, the inverse problem can be tackled.

3.4 Inverse problem in fluorescence-enhanced optical tomography

In the inverse problem of fluorescence-enhanced optical tomography, the boundary surface measurements are used along with the coupled diffusion equations in order to reconstruct the optical property map of the entire 3-D domain, using analytical or numerical techniques. Unlike the forward problem, where the number of unknowns (fluence at each node of the discretized) is less than or equal to the number of known parameters (optical properties at each node) in the system of equations to be solved, the inverse problem is a more complicated problem to solve. Here, the boundary surface measurements (represented in terms of amplitude and phase shift of the fluence, Φ) are the known quantities that are sparsely obtained on the boundary surface of the 3-D domain. These sparse numbers of known boundary surface measurements are used to reconstruct the unknown parameters or optical properties (that is, μ_a , τ , or ϕ) at every point of the entire 3-D domain. Typically the number of unknown parameters far exceeds the number of known parameters. Hence, the solution to the inverse problem is not unique and may also be unstable, especially in the presence of measurement error. In other words, the inverse problem is highly ill-posed.

Various approaches are attempted to solve the inverse problem in optical tomography, although none of them have been proven to be very effective or consistent for actual systems. Techniques employed by various researchers are quite varied, but they can be broadly categorized as analytical methods and numerical methods. Based on whether an analytical solution or a numerical method was employed to solve the system

of equations, the various approaches are classified into: (i) localization or analytical, (ii) backprojection, and (iii) numerical approach.

3.4.1 Localization or analytical approach

In the localization or analytical approach, the inversion is based on the analytical solutions of the homogeneous semi-infinite and infinite tissue medium. Here, the position and size of the tumor are predetermined and the difference between the acquired raw measurements and the analytical solutions of the semi-infinite or infinite medium is minimized using non-linear least squares optimization routines, such as Levenberg-Marquardt method.

The optical properties of the background can be roughly determined *a priori*, but the optical properties of the tumor are not known in reality, making it difficult to predetermine the tumor position and size. In the case of perfect uptake of the fluorescing agent into the tumor (that is, no fluorescence in the background tissue), the strength of the re-radiating fluorescent target can be used to determine the centroid of the tumor. However, in the case of imperfect uptake of the fluorescing agent into the tumor (that is, fluorescence is also present in the background), detection of the tumor using localization schemes becomes difficult. In addition, modeling of human tissues as semi-infinite or infinite medium geometries is also not accurate. Yet, the simplicity of the localization approach with its reduced computational speed as well as computational intensiveness pose as an advantage to this inversion approach.

Hull *et al.* [77] and O’Leary *et al.* [78] have employed localization schemes to reconstruct 2-D images in large phantoms, using CW and FDPM fluorescence measurement techniques, respectively. When Hull used Monte-Carlo simulations to minimize the model mismatch and locate the target, O’Leary used the power of the re-radiating photon density waves from the fluorescing target in order to locate the target. Unlike the 2-D studies, Wu *et al.* [79] and Chernomordik *et al.* [80] performed 3-D reconstructions on phantoms using TDPM and CW measurements, respectively in order to locate up to two fluorophore targets.

3.4.2 Backprojection

In the backprojection approach, Fourier transforms are applied to the boundary surface measurements in order to obtain 2-D or 3-D image reconstructions. However, representing the attenuating signal as a single path in a highly scattering tissue medium is erroneous. Yet, the backprojection approach is advantageous due to its simplified formulation (without incorporating the coupled diffusion equations), thus increasing the computational speed and reducing the computational intensiveness of the inverse problem. Schotland developed an analytical solution using Radon transforms (or Fourier transforms) in order to backproject the target’s location in a CW imaging system [81]. However, the backprojection approach has not been applied so far in fluorescence-enhanced optical tomography.

3.4.3 Numerical approach

In the numerical approach, the coupled diffusion equations are solved using numerical techniques in order to reconstruct the optical property maps. Small changes in the predicted measurements (Z) are directly expressed in terms of small changes in the optical properties (Y) using a Jacobian sensitivity matrix, J , which is in turn used to update the estimates of the optical properties in the entire domain typically using gradient-based inversion approaches such as Newton's method.

The computationally intense Jacobian sensitivity matrices can be evaluated using a first-order finite-difference method, a second-order finite difference method, or an approximate adjoint method. The matrix is termed computationally intense since in large 3-D geometries the unknown parameter is spatially resolved in three dimensions and needs to be evaluated at each location coordinate of the 3-D geometry. Typically a first-order approximation is computed as a backward difference,

$$\frac{\partial \Phi}{\partial p} \cong \frac{\Phi(p + \delta p) - \Phi(p)}{\delta p} \quad (3.14)$$

or a forward difference approach. Although computationally intense, finite-difference methods are easy to implement and obtain accurate results.

The integral formulation of the Jacobian matrix, J is based on the organization of the diffusion equation to represent an inhomogeneous differential equation and analytically solving for the fluence Φ_m using the Green's function. In a physical sense,

small perturbations in the optical properties of the tissue cause small perturbations on the boundary surface measurements as well. These perturbations are additive in nature, thus contributing to an integrated effect on the signal acquired on the surface. Initially, the background optical properties are assumed to be known *a priori* from homogeneous measurements. The change in the background optical properties (p) due to the presence of a tumor, causes a perturbation (δ) in the fluence at both the wavelengths

$$p \rightarrow p + \delta p \Rightarrow \Phi \rightarrow \Phi + \delta\Phi \quad (3.15)$$

By reorganising the emission diffusion equation (equation (3.2)) to represent an inhomogeneous differential equation, the emission fluence can be solved analytically using the Green's function, G_f .

$$\nabla^2 \Phi_m(\vec{r}, \omega) + k_m^2(\vec{r}, \omega) \Phi_m(\vec{r}, \omega) = -\frac{S_m(\vec{r}, \omega)}{D_m(\vec{r})} - \left(\frac{\nabla D_m(\vec{r})}{D_m(\vec{r})} \right) \nabla \Phi_m(\vec{r}, \omega) \quad (3.16)$$

where the complex diffusion wave number can be expressed as

$$k_m^2(\vec{r}, \omega) = -\frac{1}{D_m(\vec{r})} \left(\mu_{ami}(\vec{r}) + \mu_{amf}(\vec{r}) + i \frac{\omega}{c} \right) \quad (3.17)$$

The source term, S_m is the excitation fluence lumped with the decay kinetic parameters of the fluorescing dye and is given by

$$S_m(\vec{r}, \omega) = \frac{\phi \mu_{\text{axf}}}{D_m(\vec{r})(1 - i\omega\tau)} \Phi_x(\vec{r}, \omega) \quad (3.18)$$

The term $\left(\frac{\nabla D_m(\vec{r})}{D_m(\vec{r})}\right) \nabla \Phi_m(\vec{r}, \omega)$ in Equation (3.18) is assumed negligible, since there is little or no variation of the isotropic scattering coefficient, the component that overwhelmingly contributes to the diffusion coefficient at the emission wavelength (D_m) (termed as Born approximation). The corresponding Green's function consequently satisfies

$$\nabla^2 G_f(\vec{r}, \vec{r}') + k_m^2(\vec{r}) G_f(\vec{r}, \vec{r}') = -\delta(\vec{r} - \vec{r}') \quad (3.19)$$

By using Green's theorem,

$$\int_V (\mathbf{U} \nabla^2 \mathbf{G} - \mathbf{G} \nabla^2 \mathbf{U}) d^3 \mathbf{r} = \oint_S (\mathbf{U} \nabla \mathbf{G} - \mathbf{G} \nabla \mathbf{U}) \cdot d\mathbf{S} \quad (3.20)$$

Equation (3.16) can be re-written as a spatial convolution of the Green's function, G_f and the source term (Equation (3.18)), in order to analytically solve for the emission fluence,

Φ_m .

$$\Phi_m(\vec{r}_d, \vec{r}') = \int_{\Omega} G_f(\vec{r}_d, \vec{r}') \frac{\phi \mu_{axf}(\vec{r}')}{D_m(\vec{r})(1-i\omega\tau)} \Phi_x(\vec{r}', \vec{r}_s) d\Omega \quad (3.21)$$

where, Ω is the volume of integration in a three-dimensional domain; \vec{r}_d is the point of collection (i.e. detector); and \vec{r}_s is the point of illumination (i.e. source). In a discretized 2-D or 3-D domain, the emission fluence in Equation (3.21) is given by

$$\Phi_m(\vec{r}_d, \vec{r}_s) = \sum_{j=1}^N G_f(\vec{r}_j, \vec{r}_d) \Phi_x(\vec{r}_j, \vec{r}_s) \frac{\phi \mu_{axf}(\vec{r}_j) \Delta}{D_m(\vec{r})(1-i\omega\tau)} \quad (3.22)$$

where N is the total number of nodes in the 2-D or 3-D domain, and the term Δ is the area or the volume of each element in the 2-D or 3-D domain, respectively. The integral formulation is thus discretized by linearizing the perturbation term (containing the unknown optical properties) and hence obtaining a matrix of equations of the form $\Phi_m = JY$, when multiple source-detector measurements are acquired. Here the Jacobian matrix, J_j , and the unknown optical parameters, Y_j , at each node, j , are given by

$$J_j = G_f(\vec{r}_j, \vec{r}_d) \Phi_x(\vec{r}_j, \vec{r}_s) \frac{\phi \Delta}{D_m(\vec{r})(1-i\omega\tau)} \quad (3.23)$$

$$Y(\vec{r}_j) = \mu_{axf}(\vec{r}_j) \quad (3.24)$$

Thus, the boundary surface measurements of fluence are used to solve for the unknown optical properties contained in the perturbation term. The inversions are carried out iteratively under the chosen objective function is minimized (as described at the end of the current section) and the system has converged.

During the iterative inversion scheme, when the Green's function solution is kept a constant (i.e. G_f is not updated in each iteration in Equation (3.21)), the integral method becomes Born Iterative Method (BIM); and when the Green's function is updated after each iteration (i.e. G_f is updated constantly in Equation (3.21)), the integral method becomes Distorted Born Iterative Method (DBIM). In both the cases, by applying the Born approximation in the above integral formulation of the Jacobian matrix in the inverse problem, the ability to detect more than one target in a tissue medium becomes difficult [82].

In fluorescence-enhanced optical tomography, the above described Jacobian formulation for solving the inverse problem has been used by O'Leary *et al.* [83], Hawrysz *et al.* [15], Eppstein *et al.* [16], Lee *et al.* [17, 84], and Ntziachristos *et al.* [13-14]. Unlike the 2-D simulated studies performed by O'Leary, Ntziachristos *et al.* performed experimental studies using a CW imaging system and modifying O'Leary's integral formulation for obtaining 3-D image reconstructions. However, Ntziachristos *et al.*'s studies were limited to measurements obtained from small volume cylindrical phantoms (~76 ml), which were clinically irrelevant, although the work is significant as a first step towards 3-D reconstructions using experimental data. Three-dimensional reconstructions on large tissue phantoms (256 ml) were first demonstrated by Hawrysz

et al. [15], Eppstein *et al.* [16], and Lee *et al.* [17, 84] using FDPM measurements and employing the DBIM integral approach.

The objective functions, chosen differently by various researchers, are minimized during the iterative inversion scheme as described above. For example, using the least-squares objective function (E)

$$E(Y) = \sum_{i=1}^M \left[(\Phi_i)^{(m)} - (\Phi_i)^{(s)} \right]^2 = \sum_{i=1}^M [f_i(Y)]^2 \quad (3.25)$$

where, f_i is referred to as a residual, superscript s is the simulated data from the forward model and superscript m correspond to the measured data from experiments.

The gradient of the error function with respect to the optical properties (Y) is given by

$$\nabla E(Y) = 2J^T f(Y) \quad (3.26)$$

$$\nabla^2 E(Y) = 2 \left[J^T J + \sum_{i=1}^M f_i(Y) \nabla^2 f_i(Y) \right] \quad (3.27)$$

Expanding the function E as a Taylor's series expansion around a small perturbation of the optical properties, ΔY , we obtain

$$E(Y + \Delta Y) = E(Y) + \nabla E(Y) \cdot \Delta Y + \frac{1}{2} \Delta Y^T \cdot \nabla^2 E(Y) \cdot \Delta Y \quad (3.28)$$

The function to be minimized, $\Phi(\Delta Y)$, can thus be written as

$$\Phi(\Delta Y) = E(Y + \Delta Y) - E(Y) = \nabla E(Y) \cdot \Delta Y + \frac{1}{2} \Delta Y^T \cdot \nabla^2 F(Y) \cdot \Delta(Y) \Rightarrow 0 \quad (3.29)$$

In the case of first order Newton's methods, the second order term in Equation (3.29) is neglected, whereas in the case of gradient based Truncated Newton's method, the second order term is retained. The optical property map is iteratively updated until a minimum error is obtained, or in other words, until the function $\Phi(\Delta Y)$ approaches zero or a small pre-described value. Some of the common updating techniques employed in fluorescence-enhanced optical tomography include Newton-Raphson, truncated Newton's, conjugate gradient descent, and approximate extended Kalman filtering methods.

A great deal of work has been performed using various updating techniques on synthetic data, both in 2-D and 3-D domains, using CW and FDPM measurement techniques [69, 71, 85-92]. Chang *et al.* performed 2-D studies on large phantoms using CW techniques and employing differential approach (conjugate gradient descent method) [85, 93-94] as well as integral approach [93-94], as mentioned earlier. However, three-dimensional image reconstructions on phantoms were first presented by Hawrysz *et al.* [15], and Eppstein *et al.* [16] using FDPM measurements and approximate extended Kalman filter (AEKF) inversion algorithms.

To summarize, a listing of literature studies that contribute to fluorescence-enhanced tomography using synthetic data (Table 2.1) and experimental data (Table 2.2) and employing one of the inversion approaches is tabulated [13-17, 69, 71, 77-80, 83-96]. Based on the fluorescence-enhanced tomographic studies performed to date, the context of the current research is described in the following section.

3.5 Context of current research

Various investigators have demonstrated fluorescence-enhanced optical tomography in 2-D and 3-D synthetic or real domains using CW, TDPM, and FDPM measurement techniques as described above. Of all these studies, only a few employ actual experimental data to reconstruct three-dimensional images [13-17, 79-80, 84]. Furthermore, the experimental studies with 3-D reconstructions performed to date are limited either to (i) smaller volume phantom models ($< 100 \text{ cm}^3$) or *in vivo* studies on small rodent models that are not clinically relevant [13-14]; (ii) compressed tissue-mimicking phantom geometries of large volumes ($\sim 260 \text{ cm}^3$) [15-17, 84], where information at the nipple region and the chest wall may be lost; (iii) large volume studies employing simplified localization schemes for reconstructing the targets [79]; or (iv) phantom studies with shallow target depths (1-6 mm from the surface) [80].

In addition, previous studies at PML involved slow and laborious data acquisition and calibration procedures owing to single source-detector detection schemes that employ multiplexed or individual detectors [15-17, 84]. Recently a CCD scanner was used by Ntziachristos *et al.*, [13-14] for rapid acquisition of CW measurements in order to

Table 3.1 Fluorescence-enhanced optical tomography: Literature of image reconstructions using synthetic data.

Reference	Noise	Contrast agent	Uptake ratio	Measurement method	2D or 3D	Forward method	Inverse formulation
O'Leary <i>et al.</i> (1996) [83]	0.1° in θ , 1% in AC	ICG	1:0, 20:1	FDPM	2D	Analytical	SIRT
Paithankar DY <i>et al.</i> (1997) [69]	0.1-1° in θ , 0.01 in log(AC) (Gaussian)	ICG	20:1	FDPM	2D	MFD	Newton-Raphson
Chang J <i>et al.</i> (1998) [85]	1-10% white noise	N/A	100:1	CW/FDPM	2D/3D	NS	Conjugate gradient
Jiang H (1998) [86]	0-5 %	N/A	2:1 ϕ , τ	FDPM	2D	FEM	Newton's iterative method
Eppstein MJ <i>et al.</i> (1999) [71,87]	0.1° in θ , 1% in log AC (Gaussian)	N/A	1:0, 100:1 10:1 in ϕ , τ , μ_a	FDPM	2D/3D	MFD	AEKF
Roy R & Sevick-Muraca EM (1999, 2000) [88-89]	0.1° in θ , 1% in log AC (Gaussian)	N/A	2.5:1 5:1	FDPM	2D	FEM	Gradient-Based & Truncated Newton
Roy R & Sevick-Muraca EM (2001) [90-91]	55dB in excitation; 35 dB in emission	N/A	10:1	FDPM	2D/3D	FEM	Gradient-Based Optimization & Truncated Newton's method
Roy <i>et al.</i> (2003) [[92]	55dB in excitation; 35 dB in emission	N/A	100:1	FDPM	3D	FEM	Constrained Truncated Newton's

Abbreviations

AEKF: Approximate extended Kalman filter

CW: Continuous-wave imaging

FDPM: Frequency-domain photon migration

FEM: Finite Element Method

MFD: Multi-grid Finite Difference

N/A: Not Applicable

NS: Not Specified

SIRT or SART: Simultaneous algebraic reconstruction techniques

TDPM: Time-domain photon migration

 ϕ , τ : Quantum efficiency and lifetime of the contrast agent

Table 3.2 Fluorescence-enhanced optical tomography: Literature of image reconstructions using experimental data.

Reference	Data Type	Noise	Contrast agent	Uptake ratio	Measurement method	2D or 3D	Forward method	Inverse formulation
O'Leary <i>et al.</i> (1994) [78]	Phantom (large glass fish tank)	Yes	ICG	1:0	TDPM	2D	None	Localization
Wu <i>et al.</i> (1995) [79]	Phantom (7-cm dia. glass beaker)	Yes	Diethylthiatricarbocyanine	1:0	TDPM	3D	None	Localization
Chang <i>et al.</i> (1995) [93]	Phantom (8-cm dia. cylinder)	Yes	Rhodamine 6G	1:0, 1000:1	CW	2D	NS	POCS, CGD, SART
Wu <i>et al.</i> (1997) [95]	Phantom (6.4-cm dia. glass beaker)	Yes	HITCI iodide dye	1:0	TDPM	2D	NS	Laplace transform
Chang J <i>et al.</i> (1997) [94]	Phantom (8-cm dia. cylinder)	Yes	Rhodamine 6G	500:1	CW	2D	NS	POCS, CGD, SART
Hull <i>et al.</i> (1998) [77]	Phantom (6630.125 cm ³)	Yes	Nile Blue A	1:0	CW	2D	Monte-Carlo	Localization
Chernomordik <i>et al.</i> (1999) [80]	Phantom	Yes	Rhodamine	1:0	CW	2D/3D	Random Walk theory	Analytical
Yang <i>et al.</i> (2000) [96]	<i>In vivo</i> (rats)	Yes	ICG & DTTCI	1:0 & imperfect uptake	FDPM	2D images	FEM	Marquardt & Tikhonov regularization
Hawrysz <i>et al.</i> (2001) [15]; Eppstein <i>et al.</i> (2002) [16]	Phantom (256cm ³)	Yes	ICG	50:1, 100:1	FDPM	3D	MFD	AEKF
Ntziachristos <i>et al.</i> (2001, 2002) [13-14]	Phantom (74 cm ³)	Yes	ICG in background; Cy5.5 as contrast tumor	1:0	CW	3D along z-planes	FD	Normalized Born expansion
Lee <i>et al.</i> (2001, 2002) [84,17]	Phantom (256cm ³)	Yes	ICG	100:1	FDPM	3D	MFD	Distorted BIM

Abbreviations

CGD: Conjugate Gradient Descent, FD: Finite Difference, POCS: Projection onto convex sets

reconstruct images of small cylindrical volumes ($\sim 74 \text{ cm}^3$) containing a rodent. Nonetheless to date, there remains a need for a time-dependent fluorescence imaging measurement approach that can interrogate large volumes that mimic female breast geometries with appropriately fast data acquisitions while maintaining sufficient signal to noise for 3-D tomographic reconstructions. Time-dependent measurement techniques such as frequency- and time-domain approaches provide enhanced optical contrast over time-independent continuous-wave (CW) imaging techniques [12, 97].

In the current work, a 3-D frequency-domain (time-dependent) imaging system is developed for imaging large clinically relevant phantom models, which mimic the female breast geometry. Enhanced data acquisition rates were achieved using an ICCD (image-intensified charge coupled device) camera to simultaneously detect all the signals collected by the fiber optics surrounding the phantom surface. This work is unique in that it not only enables a rapid data acquisition scheme, but it also uses clinically relevant phantom volumes.

4. INSTRUMENTATION AND EXPERIMENTAL TOOLS

Fluorescence-enhanced optical imaging studies were performed using large tissue-mimicking phantoms and rapid data acquiring intensified CCD detection system. In this chapter, details of the breast-shaped phantom, instrumentation set-up, and data acquisition procedures using frequency-domain measurement techniques will be described in detail.

4.1 Breast phantom

A 3-D tissue-mimicking hollow cup-shaped model was constructed (at Riverside Campus, Texas A&M University) using white PVC (refractive index = 1.5 to 1.55 as obtained from manufacturer) in order to mimic the shape of the breast tissue. The model consists of a hemispherical portion (10-cm inner diameter) representing the breast geometry and a cylindrical portion (10-cm inner diameter and 10-cm height) representing the extended chest wall region and the underlying tissues around the breast (see Figure 4.1a). A wall thickness of 0.5 cm of the hollow phantom was used to enable the firm placement of source and collection fibers. Holes of 1 mm diameter were drilled symmetrically at various points on the surface of the hemisphere, in order to pre-fix the location of the multimode optical fibers [(model FT-1.0-EMT, Thorlabs Inc., NJ) of 1000 μm diameter and numerical aperture (NA) of 0.39], which illuminate and collect the light signal from the phantom's boundary surface.

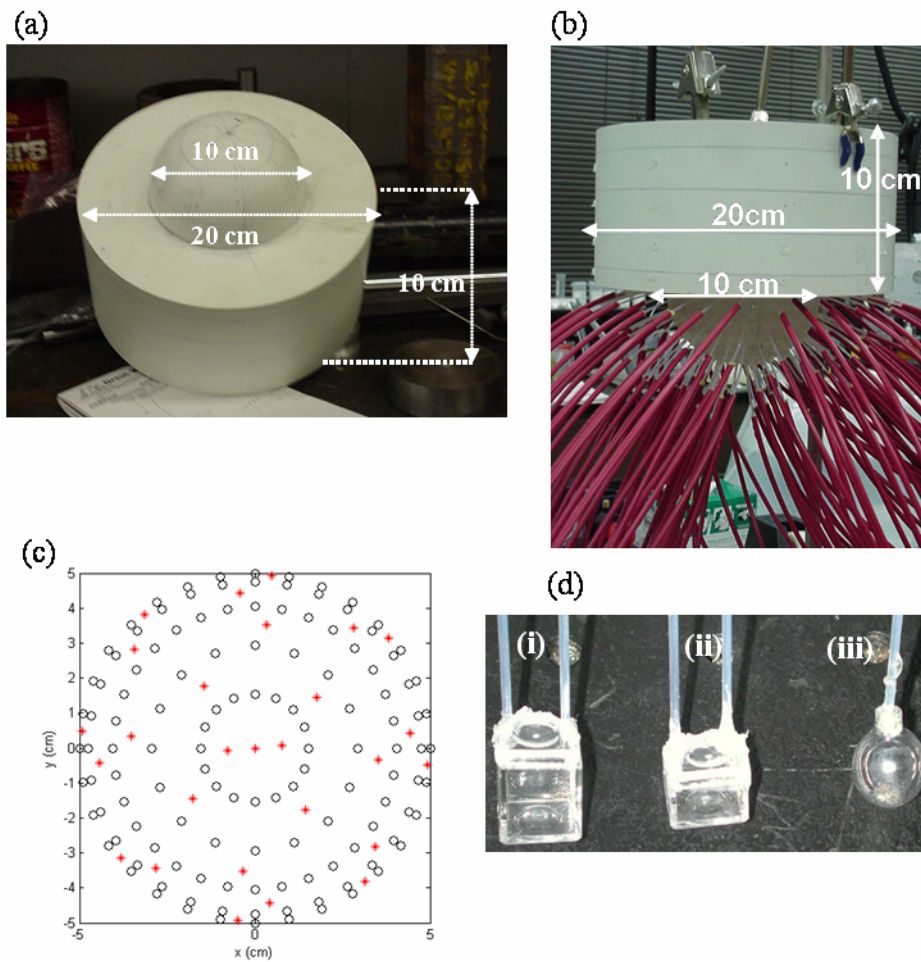


Figure 4.1 (a) Tissue-mimicking phantom, (b) Actual phantom set-up with optical fibers for illumination and collection of light signal, (c) x-y location of all 27 point illumination (red asterisks) and 128 collection locations (black hollow circles) on the hemispherical portion of the phantom, (d) targets of varying size (i) 1x1x1 cc cube, (ii) 1x1x0.5 cc cuboid, and (iii) 0.5 cc spherical target, suspended into the phantom using the support of optical fibers.

In the current work, the hemispherical portion of the phantom model was the region of interest, and hence no optical fibers were pre-fixed on the cylindrical portion of the phantom model for incident illumination and collection measurements from the cylindrical region. The optical fibers were polished on either ends using 5 μm lapping

film (LFG5P, Thorlabs Inc., NJ) and placed in a protective sheath (FT038, Thorlabs Inc., NJ) in order to prevent any light loss from the cladding of the fiber.

4.1.1 Collection optical fibers

A total of 128 optical fibers (each of ~ 1.3 m length) that collect the acquired signal (collection fibers) were symmetrically positioned along alternate concentric rings on the hemispherical portion of the phantom as shown in Figures 4.1b and 4.1c. The other end of the collection fibers were positioned on a 2-D interfacing plate in an array for facilitating simultaneous data acquisition from multiple collection fibers using the ICCD imaging technique described in Section 4.2.3).

4.1.2 Source optical fibers

Between the concentric rings of the collection fibers, a total of 27 fibers (each of ~ 1 m length) that illuminated the phantom (source fibers) were positioned on the same hemispherical surface. The free end of the source fibers were fitted with SMA connectors (SMA 11040A, Thorlabs Inc., NJ) in order to align the input laser light onto the source fibers via a fiber holder that was affixed with SMA couplings. The coordinates of the source and collection fibers in the 3-D phantom are given in Appendix A.

Unlike studies involving phantom geometries mimicking a compressed breast or a conical-shaped tissue [15-17, 84, 98], the use of the cup-shaped phantom enables assessment of imaging information around the nipple and chest-wall regions. The use of

a liquid phantom (1% Liposyn solution, Abbott Laboratories, North Chicago, IL) to fill the hollow phantom structure enabled ease in handling target positioning. Solid or gel-like phantoms are disadvantageous in that the target geometry is permanently fixed for each phantom.

4.1.3 Target

A *target* represents a tumor or diseased tissue targeted by fluorescent contrast agents. Here, the targeted diseased tissue was mimicked using acrylic cuvettes or glass spheres of varying sizes (see Figure 4.1d) that were filled with 1% Liposyn solution and the fluorescent contrast agent in required concentrations. The acrylic cuvette allowed ~82.5% light transmission and the glass spheres allowed ~90% of light transmission, and these values were accounted in the mathematical models to predict the forward and inverse problems (see Section 4). Two 1 mm fibers of equal length were glued to the cubical target or a single 1 mm optical fiber was glued to the spherical target in order to suspend them into the inverted breast phantom (Figure 4.1d). A plastic lid with 1 mm drilled holes on its x-y plane facilitated the positioning of the target accurately in the 1% Liposyn phantom.

4.2 Instrumentation

The main components of the instrumentation include: (i) a laser diode, (ii) an image intensifier, (iii) a CCD camera, and (iv) frequency synthesizers (or oscillators). The accessories include temperature and power controller for the laser diode, laser diode

mount, fiber holder, power supply to laser diode and image intensifier, interfacing plates, Nikon lens, lens assembly, and amplifiers. A schematic of the instrumentation set-up is given in Figure 4.2 and the principle of the ICCD imaging system is given in Figure 4.3. Details of the instrument are described based on the principle of the imaging technique, highlighting the major components and the corresponding accessories at each stage.

4.2.1 Light source

Near-infrared light at 785 nm excited the fluorophores, which emit a fluorescence signal at 830 nm (details in Section 2.2). A high power laser diode was used in these studies in order to improve photon budget in large phantoms with greater penetration depths (up to 10 cm), and because the final sensitivity of the detector was uncertain. The phantom was illuminated using modulated light (~ 783 nm), which was delivered at a point on the phantom surface through a 1 mm diameter multimode optical fiber. The high power laser diode (HPD1105-9mm-D-78505 model, High Power Devices Inc., NJ) of ~ 783 nm wavelength and maximum power of 530 mW was mounted onto a customized laser diode mount (model TCLDM9, Thorlabs Inc. NJ). Unlike the regular laser mounts whose maximum RF input (or AC) was 200 mW, the laser mount for the current study was customized to incorporate an RF input of ~ 1.7 W, such that a greater modulation depth (AC/DC) can be achieved using the high power laser diode having a DC power. The laser mount was driven using a laser diode driver (LDC500, Thorlabs Inc., NJ) and its temperature was controlled at 15°C using a temperature controller (TEC500, Thorlabs Inc., NJ).

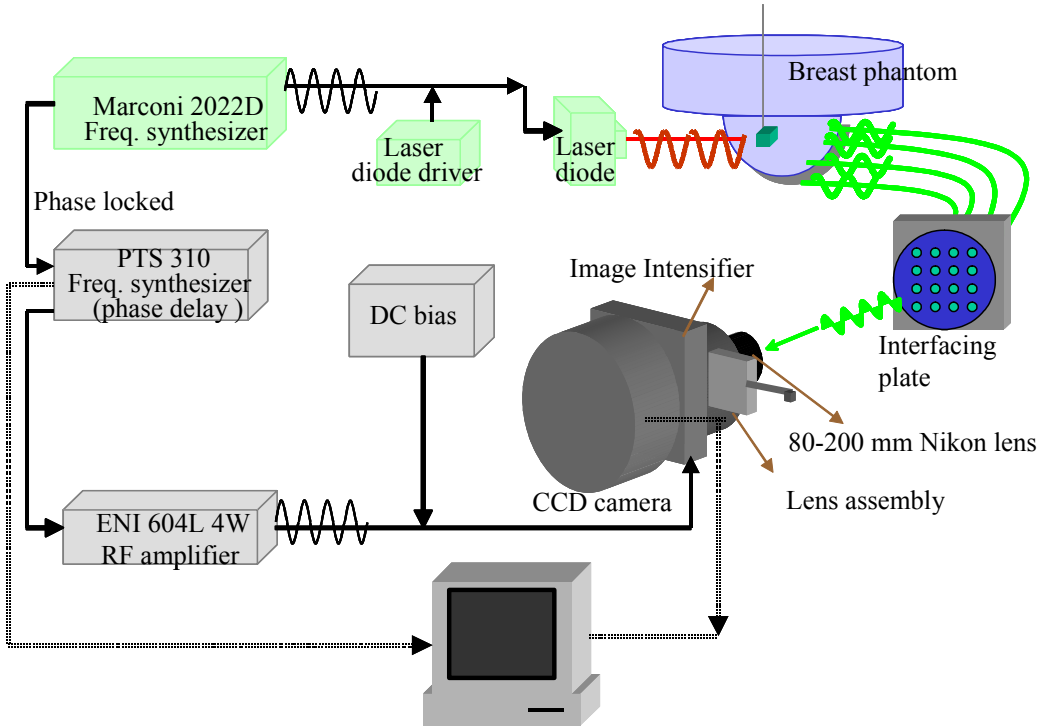


Figure 4.2 Schematic of the instrumentation set-up of the ICCD imaging system.

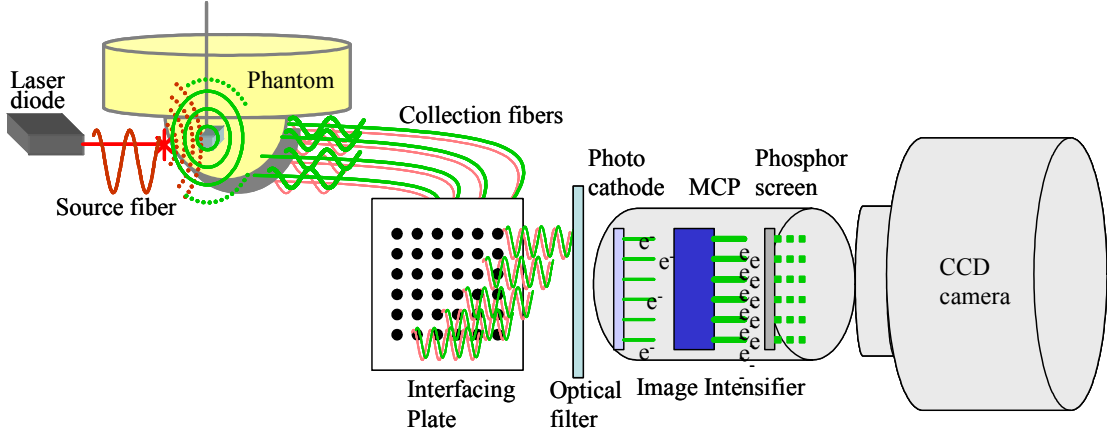


Figure 4.3 Schematic of the principle of ICCD detection technique.

The source light was modulated at 100 MHz by superimposing the RF (radiofrequency) signal from a frequency synthesizer (model 2022D, Marconi Instruments, UK) onto the constant DC bias from the laser diode at its RF input. Based on the required modulation depth (AC/DC) at the illuminating fiber end, the electrical power requirements of the high power laser diode were estimated along with the optical power of the modulated light from the laser diode (see Appendix B). The modulated light source from the laser mount was collimated using a collimating aspheric lens (Model C240TM-B, NA=0.5, Thorlabs Inc., NJ), and focused onto the fiber mount, which held a coupling/collimation package (Model F220SMA-B, Thorlabs Inc., NJ) (see Figure 4.4). The source illumination fiber was SMA coupled to the collimation package of the fiber mount, and the fiber launched the modulated light onto the tissue phantom's surface.

4.2.2. Tissue phantom

The modulated NIR light at ~ 783 nm was launched onto the phantom surface through the source optical fibers. The phantom details are described in Section 4.1. The emitted fluorescence signal and the attenuated excitation signal generated from the phantom volume were collected from different locations on the hemispherical surface of the phantom using the 128 collection fibers, which were interfaced onto two interfacing plates.

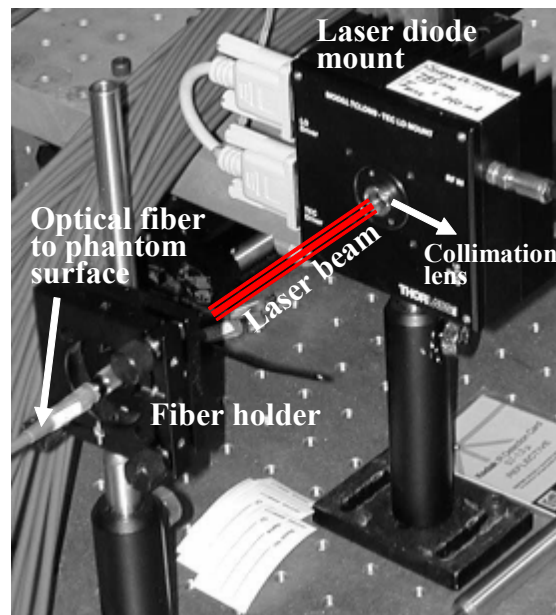


Figure 4.4 Set-up of the laser diode mount and the fiber holder for input laser light.

4.2.3. Interfacing plates

An interfacing plate was used to couple all the collection fibers as 2-D arrays, such that multiple collection fibers could be imaged simultaneously using the intensified CCD (ICCD) camera. The interfacing plate was made of black nylon of $7 \times 7 \text{ cm}^2$ surface area and 0.5 cm thickness. The collection fibers were permanently fixed (using a five-minute epoxy) into the 1 mm diameter holes that were drilled 1 cm apart from each other on the interfacing plate (see Figure 4.5). All the fibers were not spatially accommodated onto one plate as the current ICCD system had lower resolution when a larger area was focused. Hence, the 128 collection fibers were evenly distributed between two interfacing plates and separate images were acquired of each interfacing plate. In the future clinical work, the CCD camera of the ICCD imaging system will be replaced with

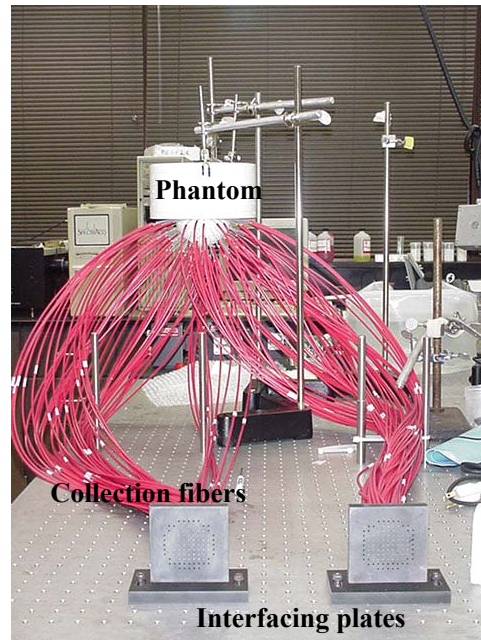


Figure 4.5 Phantom set-up including collection fibers, which are interfaced to the hemispherical surface of the phantom on one end, and to either of the two interfacing plates on the other end.

the latest generation cameras, which can image all the collection fibers accommodated onto one interfacing plate or within a fiber bundle without losing the image resolution.

The two interfacing plates were aligned with respect to the ICCD camera in order to acquire the excitation and emission signal from the phantom surface. The signal at the surface of the interfacing plate was not collimated, which could possibly cause a loss in the detected signal. However, future clinical studies may incorporate collimating lens at the end of the interfacing plate, or the optical fibers may be directly coupled via a fiber bundle onto the ICCD camera in order to minimize any loss in the detected signal.

4.2.4. Intensified CCD detection system

The intensified CCD (ICCD) detection system primarily consisted of an image intensifier (FS9910C, ITT Night Vision, VA), which is optically coupled to the 12-bit CCD camera (TE/CCD-512-EFT Photometric CH12, Roper Scientific, Trenton, NJ). A lens assembly containing a Nikon lens and optical filters was used to focus and filter the excitation and emission signal. Accessories included in the detection system were the focusing lens and lens assembly, power supplies, frequency synthesizers that were used to drive and modulate the image intensifier, respectively, and amplifiers and attenuators to control the RF power at the detection end. Details of each component are described below.

4.2.4.1. Focusing lens and lens assembly

The light signal from each interfacing plate was focused onto the 18 mm diameter image intensifier tube (see next section for details on the image intensifier), using a variable focal length Nikon lens (80-200mm f/2.8D AF-S model, Nikon, NY). The diameter of focus in each plate was adjusted to ~ 4.6 cm, such that all the 64 fibers in each plate were within the image plane.

A lens assembly made of anodized aluminum housed various optical filters in order to separate light the excitation and emission signals. The lens assembly was placed between the variable focal length Nikon lens (80-200mm, f/2.8D AF-S model, Nikon, NY) and the image intensifier. The weak fluorescent signal was acquired using a combination of (i) a holographic notch filter (HNPF-785.0-2.0 model, Kaiser Optical

Systems Inc., Ann Arbor, MI), and (ii) an 830-nm interference filter (F10-830.0-4-2.0 model, CVI Laser Corp., NM) of 53% average transmission, in order to minimize the excitation light leakage as well as reject light outside the bandwidth of the 830 nm emission wavelength [12]. For acquisition of the strong excitation signal, absorptive neutral density filters (FSQOD series, Newport Corp., CA) of varying optical density (OD) were employed in order to attenuate the excitation signal and hence prevent any damage to the image intensifier, which is sensitive to strong light. During the acquisition of excitation signal, a 785-nm interference filter was not used in order to filter the emission signal, since the emission signal was at least 3-4 orders of magnitude smaller than the excitation signal [12]. More details on the characteristics of different filters used and their transmission dependence with wavelength are described in Appendix C.

4.2.4.2. Image intensifier

The image intensifier is considered the heart of time-dependent measurements acquired by the ICCD imaging system. The image intensifier used in the current studies was a Generation III type device of 18 mm diameter and was made of three main components namely, the photocathode (PC), multichannel plate (MCP), and the phosphor screen. The Gen III image intensifier uses gallium arsenide (Ga As) as the photocathode, allowing for a more efficient conversion of light energy to electrical energy at extremely low levels of light [99].

A detailed schematic of the image intensifier along with the bias-T circuit that aids in modulation of the image intensifier is given in Figure 4.6 [51, 100]. A resistor-capacitor based circuit was built to modulate the image intensifier at its photocathode using a ~ -65 V of DC voltage and 53 dBm of RF signal. The multichannel plate operated at a variable voltage of 0 to 1000 V between its input and output leads and the phosphor screen was maintained at a constant voltage of 4000 V. A GBS Micro Power Supply (model PS20060500, San Jose, CA) provided the required DC voltages to the photocathode (PC), multichannel plate (MCP), and phosphor screen of the image intensifier. The GBS Micro Power supply also provided DC voltage to a phosphor screen current limiting protection circuit, which would shut down the image intensifier when the incident light reached potentially damaging levels [100]. The DC voltages at each component of the image intensifier increased from the photocathode to the phosphor screen, in order to control the direction of current flow.

A sinusoidally modulated ± 22 V RF signal at 100 MHz that was generated using a PTS-310 frequency synthesizer (Programmed Test Sources model 10M201GYX-53, Littleton, MA) was superimposed along with the DC voltage supplied to the photocathode of the image intensifier, in order to modulate the intensifier at $\sim 50\%$ modulation depth. The 13 dBm RF power generated by the frequency synthesizer (or oscillator) was amplified to 53 dBm or ± 22 V RF voltage using a 40 dBm amplifier (ENI model 604L-01, Rochester, NY) (see Figure 4.2). The oscillators driving the laser

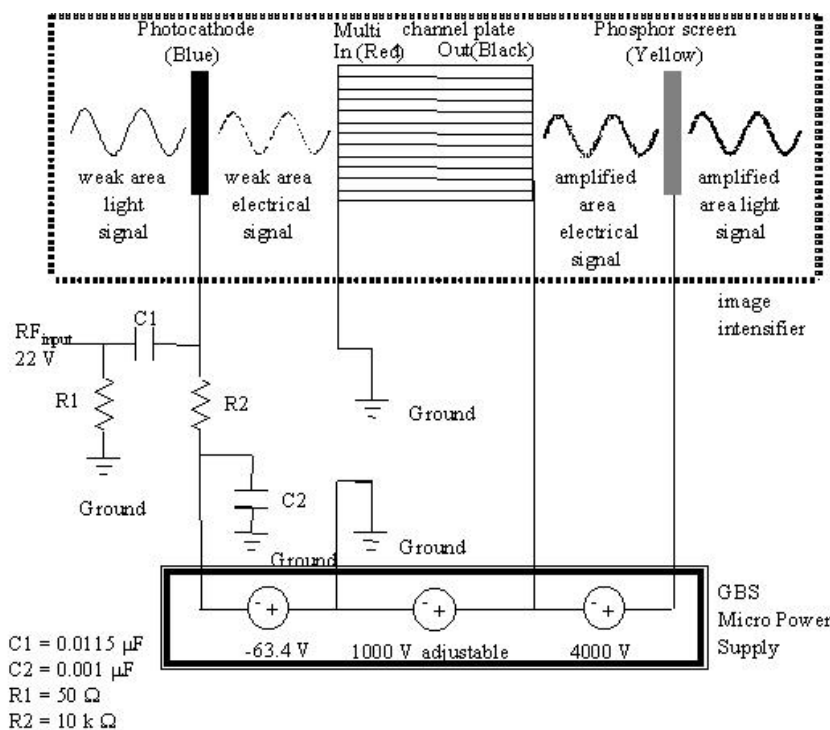


Figure 4.6 Resistor-capacitor circuit for modulating the photocathode of the image intensifier. Adapted from reference [100].

diode and the photocathode of the image intensifier were phase locked with a reference phase of 10 MHz in order to operate these oscillators at a consistent phase difference.

The principle behind the operation of the image intensifier in the ICCD imaging system is shown in Figure 4.3. At the photocathode, the diffuse light signal collected through the 80-200 mm Nikon lens and the lens assembly is converted into electrical energy (or electrons). This electrical signal is amplified at the MCP by varying the gain setting on the power supply of the image intensifier. The amplified signal is converted back to a light signal of $\sim 500 \text{ nm}$ wavelength at the phosphor screen and is imaged onto the CCD camera. Thus, the modulated light signal at the photocathode is converted to a steady-state signal (with no modulation) at the phosphor screen and is thus imaged onto

the CCD array, which is optically coupled to the phosphor screen using an optical couplant (Q2-3067, Dow Corning, Midland, MI), in order to minimize the refractive-index mismatch between the two surfaces.

Mathematically, the collected fluorescent light signal reaching the photocathode of the image intensifier, from the interfacing plate via the Nikon lens and optical filters, has an amplitude intensity of $L_{AC}(r)$, average intensity of $L_{DC}(r)$, and phase delay of $\rho(r)$, which vary with respect to the location of the collection fiber on the phantom surface and consequently with respect to its corresponding location on the photocathode face.

$$L(r) = \alpha [L_{DC}(r) + L_{AC}(r) \cos(\omega t + \rho(r))] \quad (4.1)$$

Here, α represents the coupling efficiency of the fibers from the phantom surface to the interfacing plate and from the lens to the image intensifier; ω is the frequency at which both the phase-locked oscillators are modulated; and t is the time. Similarly, the gain of the image intensifier has an amplitude, G_{AC} ; an average amplitude, G_{DC} ; and a possible phase delay owing to the instrument response time, θ_{instr} , at the same modulation frequency as the source.

$$G = G_{DC} + G_{AC} \cos(\omega t + \theta_{instr}) \quad (4.2)$$

The modulated photocathode converts the NIR photons from the interfacing plate into electrons, which are multiplied to more electrons at the MCP before they are focused

onto the phosphor screen (Figure 4.7). The resulting signal at the photocathode is a mixed homodyne signal, S_{mixed} , which is a product of the above two signals, $L(r)$ and G . The mixed signal contains all the amplitude, DC, and phase information of the optical signal collected by the collection fiber.

$$S_{mixed} = \alpha\beta \left[\begin{aligned} &G_{DC}L_{DC}(r) + G_{AC}L_{DC}(r)\cos(\omega t + \theta_{instr}) + G_{DC}L_{AC}(r)\cos(\omega t + \rho(r)) \\ &+ \frac{G_{AC}L_{AC}(r)}{2}\cos(\theta_{instr} - \rho(r)) + \frac{G_{AC}L_{AC}(r)}{2}\cos(2\omega t + \theta_{instr} + \rho(r)) \end{aligned} \right] \quad (4.3)$$

Here, β represents the quantum efficiency of the phosphor screen of the image intensifier, which is a function of the wavelength of the light signal (see Appendix C for details on wavelength dependency of the image intensifier).

The phosphor screen has response times on the order of sub milliseconds, and hence acts as a low pass filter [101] by eliminating the high frequency components of equation (4.3). In other words, the decay rate of the phosphor screen is much slower than the rate at which electrons are bombarded from the MCP onto the phosphor screen, knocking down the high frequency terms to reduce the equation to the form

$$S_{mixed} = \alpha\beta \left[G_{DC}L_{DC}(r) + \frac{G_{AC}L_{AC}(r)}{2}\cos(\theta_{instr} - \rho(r)) \right] \quad (4.4)$$

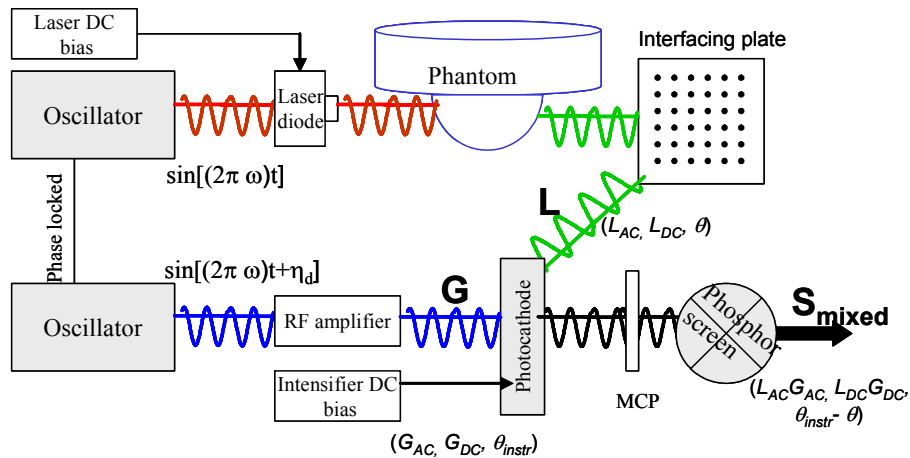


Figure 4.7 Schematic of the homodyne detection technique in the ICCD imaging system.

The time-invariant, phase-sensitive image on the phosphor screen is then imaged by the CCD camera (512x512 pixelated array), which is optically coupled to the phosphor screen of the image intensifier.

4.2.4.3. CCD camera

A 512×1024 frame transfer array (TE/CCD-512-EFT Photometric CH12, Roper Scientific, Trenton, NJ) CCD camera that was thermoelectrically cooled to -35°C and had a 12-bit A/D (analog-to-digital) converter was coupled to the phosphor screen of the image intensifier. Details of the architecture of the CCD camera used are provided in Appendix D.

The steady-stage phase sensitive images from the phosphor screen of the image intensifier was imaged by the CCD camera, where the photons were converted to electrons, and the electrons were multiplied based on the exposure time of the CCD

camera and the efficiency of the photon-to-electron conversion (termed as the quantum efficiency of the CCD camera). The 512×512 pixelated images were binned twice to 128×128 pixelated images during charge read out and before signal digitization, and the output intensity signal from the CCD camera obtained as a 128×128 pixelated image is given by

$$I(i, j) = \alpha\beta\gamma \left[G_{DC} L_{DC}(i, j) + \frac{G_{AC} L_{AC}(i, j)}{2} \cos(\theta_{instr} - \rho(i, j)) \right] \quad (4.5)$$

where γ represents the quantum efficiency of the CCD camera and gain of the CCD output amplifier (ratio of digitized units per electron received). The magnitude of these steady-state phase-sensitive signals depended on the introduced phase delay, η_d introduced between the two phase-locked oscillators, as described in the following section.

4.3. Data acquisition and processing technique

Rapid multipixel FDPM data acquisition was carried out using the homodyne detection technique. The phase of the photocathode modulation was stepped, or delayed with respect to the laser diode modulation, at regular intervals varying from 0 to 2π . The phase delay introduced between the two oscillators (PTS-310 and Marconi-2022D) was digitally controlled using the Labview via an IEEE-488 GPIB instrument control bus (National Instrumentations Corp. Austin, TX). At each phase delay, η_d the phosphor

screen and eventually the CCD camera captured the phase-sensitive steady-state (or time-invariant) image for a given exposure time of the camera, using a Labview data acquisition program (National Instruments Corp., Austin, TX) at each phase delay for the given exposure time. The introduced phase delay caused a difference in the phase-sensitive intensity at each pixel on the CCD camera (see Figure 4.8). Upon varying the phase delay (η_d) over the entire cycle of 0 to 2π , the phase-sensitive intensity at different pixel locations on the image varied in a sinusoidal manner. The phase sensitive images were stacked as a function of the phase delay in their third dimension, creating sine-curves at each pixel along the dimension of the varying phase delay (see Figure 4.8).

A Matlab (version 6.1, The Mathworks, Inc., Natick, MA) routine was used to extract the modulated amplitude (AC) and phase information from the sinusoidal data obtained at each pixel by performing a Fast Fourier Transform (FFT) of the phase-sensitive images that were arranged in the order of their phase delay. Thus, rapid FDPM measurements in terms of amplitude and phase can be obtained from phase-sensitive steady-state images using the homodyne technique in our ICCD imaging system, by carrying out the following steps in the Matlab routine.

- (i) Stacking of the 128×128 pixelated images with respect to the number of phase delays (N_η) in its third dimension.
- (ii) Computing the mean intensity, I_{DC} , at each pixel (i,j)

$$I_{DC}(i,j) = \frac{1}{N_\eta} \sum_{k=1}^{N_\eta} I(i,j,k) \quad (4.6)$$

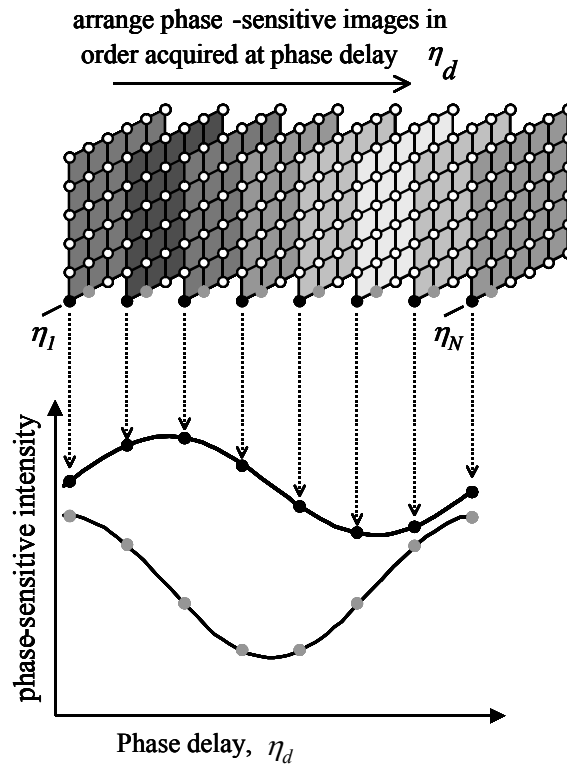


Figure 4.8 Data acquisition technique in a homodyned frequency-domain imaging system. Reproduced with permission from reference [51].

(iii) Subtracting the mean DC intensity, $I_{DC}(i,j)$ at each pixel from the phase sensitive AC intensity at each pixel, $I(i,j,k)$ in order to normalize the sine curve. This process of subtraction reduced the number of unknowns from AC, DC, and phase shift to only AC and phase shift, during the FFT.

(iv) Performing FFT to the phase sensitive intensity data (after subtracting the DC component), in order to obtain the modulated intensity, $I_{AC}(i,j)$, and phase, $\theta(i,j)$ at each pixel [100].

$$I_{AC}(i,j) = \frac{[\{\text{Im}[I(f_{\max})_{ij}]\}^2 + \{\text{Re}[I(f_{\max})_{ij}]\}^2]^{1/2}}{N_{\eta} / 2} \quad (4.7)$$

$$\theta(i,j) = \arctan\left(\frac{\text{Im}[I(f_{\max})_{ij}]}{\text{Re}[I(f_{\max})_{ij}]}\right) \quad (4.8)$$

where, $\text{Im}[I(f_{\max})_{ij}]$ and $\text{Re}[I(f_{\max})_{ij}]$ are the imaginary and the real components of the FFT output (power spectrum), respectively, of the modulated intensity that best describes the sinusoidal data at each pixel (i,j) .

Typically, five to ten frames of $I(i,j, \eta_d)$ were obtained at each phase delay and averaged across the total number of phase delays (N_{η}) and evaluated in order to obtain a mean value of amplitude, $I_{AC}(i,j)$ and phase shift, $\theta(i,j)$. Based on the prior work performed at PML, introducing 32-phase delays equally spaced between 0 and 2π provided greater measurement precision and accuracy of the phase-sensitive detected signal in terms of their amplitude and phase [51,102].

Image acquisition rate by the ICCD system can be controlled by the integration time of the CCD camera. The overall data acquisition rate during measurements can also be controlled by choosing the number of repeated steady-state images acquired at

each phase delay, and the number of phase delays introduced during the acquisition of frequency-domain data. The weak fluorescent signal collected from the phantom surface can be amplified by the ICCD imaging system by using one or all of the different methods: (i) adjusting the aperture (i.e. F-stop) of the Nikon lens at the cost of image resolution, (ii) increasing the gain setting on the power supply to the image intensifier (G_{AC} and G_{DC}), and/or (iii) increasing the exposure time of the CCD camera.

The detected fluorescent signal in terms of amplitude (I_{AC}) and phase shift (θ) do not reflect the actual fluorescent signal collected at the phantom surface due to various instrument effects (described in Equations (4.1), (4.2) and (4.5)), in terms of the coupling efficiency of the optical fibers, quantum efficiency of the image intensifier and the CCD camera. Hence, the acquired FDPM measurements are referenced in order to eliminate the instrument effects, as described in the following section.

4.4 Referencing techniques

The measured $I_{AC}(i,j)$ is proportional to the actual intensity signal, L_{AC} , originating from the phantom surface (as shown in Equation (4.1)). The proportionality constant is a function of (i) the individual fiber lengths that are interfaced onto the interfacing plate, (ii) the coupling efficiency of the Nikon lens, (iii) the transmission efficiencies of the optical filters used, (iv) the gain and quantum efficiency of the image intensifier, (v) quantum efficiency of the CCD camera, and (vi) the gain of the CCD output amplifier. Normalizing or referencing the measured signal eliminates the effect of most of the factors mentioned above. In other words, referencing of the measured

data was performed in order to account for the instrument effects and the effect of unknown source strength.

Two different methods to eliminate the instrument effects include: (i) referencing the fluorescent signal with respect to the excitation signal at each pixel; and (ii) referencing the fluorescent signal at each pixel with respect to the fluorescent signal at a reference pixel at the same wavelength. Apart from the two referencing schemes employed in the current study, various other referencing schemes have been employed by other researchers during their experimental or simulated studies in fluorescence-enhanced optical tomography [13-14, 17, 84, 92] (see Table 4.1).

Table 4.1 Different referencing schemes employed in fluorescence-enhanced optical tomography.

Referencing scheme	Description	Reference	Study
$\left(\frac{\Phi_m}{\Phi_x}\right)_i$	Emission fluence with respect to excitation fluence at each pixel (i)	Current study	Experimental
$\frac{\Phi_{m,i}}{\Phi_{m,ref}}$	Emission fluence at each pixel (i) with respect to emission fluence at a particular location (ref)	Hawrysz <i>et al.</i> [15] Eppstein <i>et al.</i> [16]	Experimental Experimental
$\frac{\Phi_{m,i}}{\Phi_{x,ref}}$	Emission fluence at each pixel (i) with respect to excitation fluence at a particular location (ref)	Lee <i>et al.</i> [17,84] Roy <i>et al.</i> [92]	Experimental Simulated
$\left(\frac{\Phi_{fluorescence}}{\Phi_{incidence-excitation}}\right)_i$	Emission or fluorescence fluence at each pixel (i) with respect to fluence obtained before fluorescence injection.	Ntziachristos <i>et al.</i> [13-14]	Experimental

4.4.1 Referencing emission signal with respect to excitation signal Φ_m/Φ_x

In the first referencing method, the fluorescent signal was referenced with respect to the excitation signal at each corresponding pixel (i) (Figure 4.9a). The referenced fluence at each pixel or collection fiber location (i), is given by $\left(\Phi_m/\Phi_x\right)_i$ where

$\Phi_{x,m} = I_{ACx,m} \exp(i\theta_{x,m})$. In terms of amplitude and phase shift,

$$ACR_i = \left(\frac{I_{ACm}}{I_{ACx}} \right)_i \quad (4.9)$$

$$RPS_i = (\theta_m - \theta_x)_i \quad (4.10)$$

where, ACR_i is the referenced AC or AC ratio at each pixel (i), and RPS_i is the referenced phase shift or relative phase shift at each pixel (i). It was assumed that the amplitude loss and phase shift in each of the fibers remain constant and independent of the wavelength of the detected signal. The coupling efficiency of the Nikon lens was also assumed independent of the wavelength of the signal. However, in order to employ this referencing technique, the wavelength dependency of the filters, image intensifier and the CCD camera need to be accounted for (for details, refer to Appendix C).

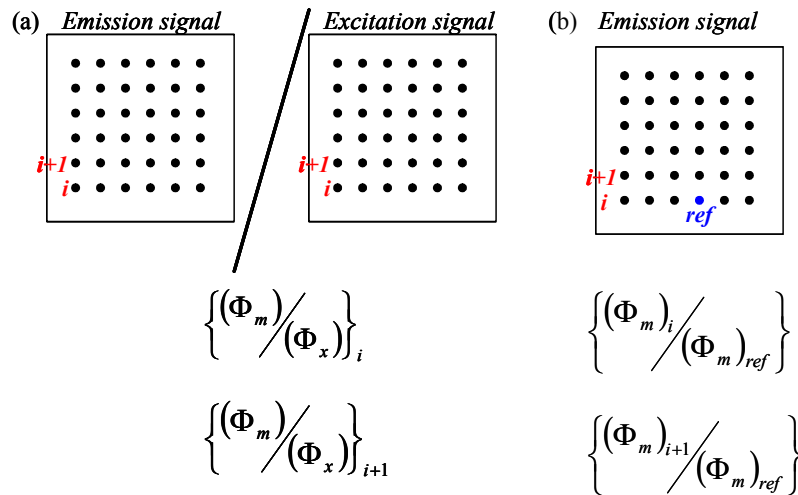


Figure 4.9 Schematic of different referencing schemes used in the current study (a) referencing emission signal with respect to excitation signal at each pixel (i), (b) referencing emission signal at each pixel (i) with respect to emission signal acquired at a fixed location (ref).

4.4.2 Referencing emission signal with respect to emission signal at a given location

$$\frac{\Phi_m}{\Phi_{m,ref}}$$

In the second referencing method, the fluorescent signal obtained at each pixel (i) was referenced with respect to the fluorescent signal at a particular pixel chosen as the reference location (ref), considering it an arbitrary location for present (Figure 4.9b). The referenced fluence at each pixel location (i) is given by $\left(\frac{\Phi_m}{\Phi_{m,ref}}\right)_i$, and in terms of referenced AC and phase shift,

$$(ACR_i)_{x,m} = \left(\frac{I_{AC,i}}{I_{AC,ref}} \right)_{x,m} \quad (4.11)$$

$$(RPS_i)_{x,m} = (\theta_i - \theta_{ref})_{x,m} \quad (4.12)$$

where the suffix ‘ x ’ and ‘ m ’ correspond to excitation and emission wavelength. In this case, since the measurements in terms of amplitude and phase shift are referenced with respect to the measurement acquired at the same wavelength, the instruments effects that arise due to the wavelength-dependency of the acquired signal (that is, the effect of wavelength on the quantum efficiency of the image intensifier, on the transmission efficiencies of the filters used) are eliminated. In addition, since the measurements were acquired under similar settings on the ICCD imaging system (such as the gain settings on the image intensifier and the CCD camera, and the coupling efficiency of the Nikon lens), all the instrument effects are automatically accounted for in the current referencing scheme. The only parameter of concern was the differing fiber lengths that need to be accounted for since fluorescence signal collected by each collection fiber was referenced with respect to the fluorescence signal collected at a particular reference fiber of possibly varying fiber length. However, the referencing scheme was employed in experimental studies based on the assumption that the collection fibers were of the same length, such that the differences in time-dependent light propagation arose within the random medium, and not due to the transit within the fibers.

The absolute (non-referenced) measurements do not truly reflect the fluence, which is described in the light propagation model given by the coupled diffusion equations (Equations (3.1) and (3.2)), but are in turn related to the reflectance of the diffuse light signal collected at the phantom surface. However, referencing the absolute measurements of amplitude and phase shift (as described above) helps in comparing the reflectance with respect to fluence as presented in the following section.

4.5. Reflectance versus fluence data

The measured phase-sensitive intensity (I) acquired by the ICCD imaging system corresponds to the diffuse reflectance of the signal collected at the phantom surface, rather than the fluence or flux. The phase-sensitive intensity at each pixel (i,j) was in turn used to determine the amplitude attenuation (I_{AC}) phase-shift (θ) of the diffuse excitation and emission reflectance.

The diffuse reflectance, $R(r, \omega)$, is a function of the distance, r , between the detected area and the incident beam and includes contributions from the fluence as well as flux at the boundary surface of the phantom. The diffuse reflectance also depends on the numerical aperture of the detector and contributions arising from the refractive-index mismatch at the interface. For FDPM reflectance measurements, $R(r, \omega)$ is given by the following empirical equation [103]:

$$R(r, \omega) = A\Phi(r, \omega) + B \frac{\partial}{\partial n} \Phi(r, \omega) \quad (4.13)$$

where A , B are constants that vary depending on the numerical aperture of the detector and the R_{eff} value at the interface, and are wavelength independent. The terms $\Phi(r, \omega)$ and $\partial\Phi(r, \omega)/\partial n$ are the fluence and the flux at the surface boundaries respectively, and are related by the partial current boundary condition applied at the phantom or tissue boundary surface.

$$\Phi(r, \omega) + 2\gamma D(r) \frac{\partial\Phi(r, \omega)}{\partial n} = 0 \quad (4.14)$$

The diffusion coefficient, $D(r)$ in the above equation is given by

$$D(r) \cong \frac{1}{3\mu'_s} \text{ when } \mu'_s \gg \mu_a \quad (4.15)$$

where μ'_s is the isotropic scattering coefficient (cm^{-1}) and μ_a is the absorption coefficient (cm^{-1}). In a given tissue medium, μ'_s is assumed constant with respect to distance, but a function of wavelength. Combining equations (4.13) and (4.14), we obtain

$$R(r, \omega) = A\Phi(r, \omega) - \frac{B}{2\gamma D(r)} \Phi(r, \omega) \quad (4.16)$$

In other words,

$$R(r, \omega) = \left(A - \frac{B}{2\gamma D(r)} \right) \Phi(r, \omega) \quad (4.17)$$

stating that the diffuse reflectance, $R(r, \omega)$ is directly proportional to the fluence. Upon referencing the measured diffuse reflectance, $R(r, \omega)$ to that measured at a reference point $R(r_{ref}, \omega)$, that is assuming the referencing scheme $\Phi_m / \Phi_{m,ref}$, the term $A - \frac{B}{2\gamma D(r)}$ cancels out leaving behind the relationship

$$\frac{R(r, \omega)}{R(r_{ref}, \omega)} = \frac{\Phi(r, \omega)}{\Phi(r_{ref}, \omega)} \quad (4.18)$$

where, the suffix *ref* refers to the location of the reference measurement [104]. Thus, referencing the measurements not accounts for the instrument effects (described earlier), but also accounts for the coefficients, A and B given in Equation (4.13). In terms of amplitude attenuation and phase shift,

$$\frac{R(r, \omega)}{R(r_{ref}, \omega)} = \frac{I_{AC}}{I_{AC,ref}} \exp(\Delta\theta) = \frac{\Phi(r, \omega)}{\Phi(r_{ref}, \omega)} \quad (4.19)$$

where, $I_{AC}/I_{AC,ref}$ is the referenced AC (AC ratio, ACR) and $\Delta\theta$ is the referenced or relative phase shift (RPS) ($\Delta\theta = \theta - \theta_{ref}$) at each location r , and modulation frequency ω .

In summary, although diffuse reflectance data in terms of amplitude and phase shift is acquired using the frequency-domain ICCD imaging system, the acquired data is equivalent to fluence (or amplitude and phase corresponding to the fluence term) upon referencing. The referenced measurements in terms of amplitude and phase shift under obtained varying experimental conditions are compared to the simulated amplitude and phase shift, which are obtained by solving the forward problem of the coupled diffusion equations (described in the next major section).

5. FORWARD AND INVERSE FORMULATIONS

In this chapter, the mathematical details of the solution to the forward and inverse imaging problem are discussed.

5.1 Forward problem

To solve the forward problem, the interior optical property map of the 3-D phantom is assumed known and the fluence (at both the emission and excitation wavelengths) of the entire phantom is predicted using numerical techniques to solve the coupled diffusion equations in finite volume domains. Details of the coupled diffusion equations and the boundary condition used have been described earlier (Section 3.5). The fluence data determined from the forward model simulations is compared to the measured fluence data (in terms of AC and phase shift), in order to validate the light propagation model that is employed in the current studies.

A finite-element based approach (using Galerkin approximation) was employed to solve the forward problem of the coupled diffusion equations [76, 105-106]. A three-dimensional finite-element mesh of the phantom consisting of tetrahedral elements (see Figure 5.1) was generated using GAMBIT 2.0.4 software (Fluent Inc, New Hampshire), prefixing nodes corresponding to the actual source and collection fiber locations. The mesh consisted of 34413 tetrahedral elements and 6956 nodes distributed along the entire phantom.

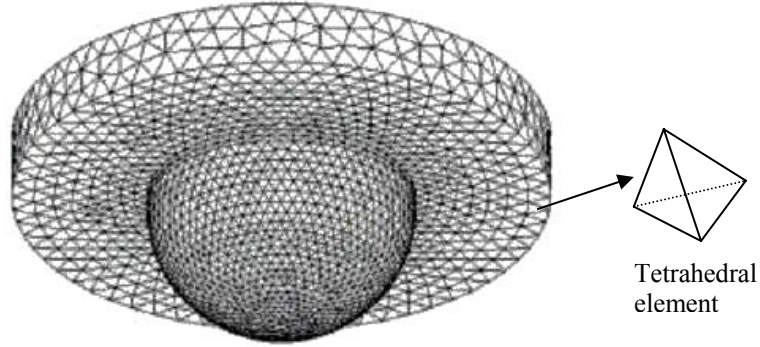


Figure 5.1 Three-dimensional finite element mesh (constituting of tetrahedral elements) of the breast-shaped phantom.

5.1.1 Galerkin finite-element based formulation of the forward problem

The Galerkin formulation of the finite-element method is employed to solve for the fluence, Φ_{ex} and Φ_{em} over the finite element domain, Ω using the coupled diffusion equations (Equations (3.1) and (3.2)) and the partial current boundary condition (Equation (3.4)) [105-106]. The formulation for the diffusion equation at excitation is described in detail here, and a similar procedure is employed to obtain the formulation of the diffusion equation at the emission wavelength.

In the Galerkin formulation of the finite element method, the first equation of the coupled diffusion equation (Equation (3.1)) is multiplied with a weighting function, w_j , and integrated over the entire 3-D domain, Ω .

$$\int_{\Omega} \left[-\nabla \cdot (D_x \nabla \Phi_x) + \left(\mu_{axi} + \mu_{axf} + \frac{i\omega}{c_x} \right) \Phi_x \right] w_j d\Omega = 0 \quad (5.1)$$

where, w_j $\{w_j: j = 1, \dots, N\}$ is a set of linearly independent weighting functions and N is the number of unknowns. Upon applying Green's theorem to the above equation and employing the chain rule, which is given by

$$-(D\Phi)'w = D\Phi'w - (D\Phi'w)' \quad (5.2)$$

we obtain,

$$\int_{\Omega} \left[D_x (\nabla \Phi_x) \cdot (\nabla w_j) + \left(\mu_{axi} + \mu_{axf} + \frac{i\omega}{c_x} \right) \Phi_x w_j \right] d\Omega - \int_{\Gamma} D_x \frac{\partial \Phi_x}{\partial n} w_j d\Gamma = 0 \quad (5.3)$$

The first term in Equation (5.3) is the volume integral over the domain, Ω , the second term is the surface integral along the external boundary; and w_j is assumed to be continuous over the entire domain, Ω . Applying the partial current boundary condition at excitation wavelength to the surface integral term of Equation (5.1),

$$\int_{\Gamma} D_x \frac{\partial \Phi_x}{\partial n} w_j d\Gamma = \frac{1}{2\gamma} \int_{\Gamma} (\Phi_x + S) w_j d\Gamma \quad (5.4)$$

and upon simplifying Equation 5.3 using Equation 5.4, we obtain

$$\int_{\Omega} \left[D_x (\nabla \Phi_x) \cdot (\nabla w_j) + \left(\mu_{axi} + \mu_{axf} + \frac{i\omega}{c_x} \right) \Phi_x w_j \right] d\Omega - \frac{1}{2\gamma} \int_{\Gamma} \Phi_x w_j d\Gamma = \frac{1}{2\gamma} \int_{\Gamma} S w_j d\Gamma \quad (5.5)$$

The phantom domain, Ω in our studies is divided into M tetrahedral elements and the elemental form of the above equation can be represented as

$$\sum_{el=1}^M \left[\int_{\Omega^{el}} \left[D_x^{el} (\nabla \Phi_x^{el}) \cdot (\nabla w_j) + \left(\mu_{axi}^{el} + \mu_{axf}^{el} + \frac{i\omega}{c_x} \right) \Phi_x^{el} w_j \right] d\Omega - \frac{1}{2\gamma} \int_{\Gamma^{el}} \Phi_x^{el} w_j d\Gamma \right] = \sum_{el=1}^M \left[\frac{1}{2\gamma} \int_{\Gamma^{el}} S w_j d\Gamma \right] \quad (5.6)$$

Assuming that the Φ_x^{el} , D_x^{el} , and μ_{axf}^{el} vary linearly within each tetrahedral element, el , and μ_{axi} is constant over the whole domain, Ω , the above terms can be expressed in their nodal forms, shown here for Φ_x^{el} as an example.

$$\Phi_x^{el} = \sum_{j=1}^4 L_j (\Phi_x)_j \quad (5.7)$$

where, L_j are the natural coordinates of the tetrahedron. According to Galerkin's method, the weighting function, w_j 's are chosen such that these are similar to the approximation function used to represent the elemental form of terms such as Φ_x^{el} , D_x^{el} , and μ_{axf}^{el} . In other words,

$$w_j = L_j \quad \text{for } j = 1, 2, \dots, N \quad (5.8)$$

Equation 5.6 can now be represented as

$$\begin{aligned} & \sum_{el=1}^M \left[\int_{\Omega^{el}} \left[D_x^{el} \left(\frac{\partial \Phi_x^{el}}{\partial x} \frac{\partial L_j}{\partial x} + \frac{\partial \Phi_x^{el}}{\partial y} \frac{\partial L_j}{\partial y} + \frac{\partial \Phi_x^{el}}{\partial z} \frac{\partial L_j}{\partial z} \right) + \left(\mu_{axi}^{el} + \mu_{axf}^{el} + \frac{i\omega}{c_x} \right) L_j \right] \Phi_x^{el} d\Omega + \frac{1}{2\gamma} \int_{\Gamma^{el}} \Phi_x^{el} L_j d\Gamma \right] \\ & = \sum_{el=1}^M \left[\frac{1}{2\gamma} \int_{\Gamma^{el}} S L_j d\Gamma \right] \end{aligned} \quad (5.9)$$

Upon integrating Equation 5.9 and rearranging the terms, the resulting elemental stiffness equation is represented as

$$\sum_{el=1}^M \left[\mathbf{K}_{stiff,1}^{el} + \mathbf{K}_{stiff,2}^{el} + \mathbf{K}_{stiff,3}^{el} \right] \Phi_x^{el} = \sum_{el=1}^M \mathbf{r}_{stiff}^{el} \quad (5.10)$$

where, $\mathbf{K}_{stiff,i}^{el}$ and \mathbf{r}_{stiff}^{el} are the elemental stiffness matrices and the local vector, respectively, constituting of complex numbers. A global stiffness matrix \mathbf{K}_{stiff} is formed by combining these local elemental stiffness matrices (shown in the above equation). The forward solution is obtained by solving the complex equation given by

$$\mathbf{K}_{stiff} \bar{\Phi}_{x,m} = b_{stiff} \quad (5.11)$$

where b_{stiff} is the global vector corresponding to the global stiffness matrix formulation.

The excitation and emission fluence data obtained at each node of the phantom is

converted to phase and AC data and further referenced using one of the referencing schemes (Φ_m/Φ_x or $\Phi_m/\Phi_{m,ref}$) that was described in (Section 4.5).

$$\theta_{X,M} = \tan^{-1} \left(\frac{IMAG(\Phi_{X,M})}{REAL(\Phi_{X,M})} \right) \quad (5.12)$$

$$I_{AC_{X,M}} = \sqrt{IMAG^2(\Phi_{X,M}) + REAL^2(\Phi_{X,M})} \quad (5.13)$$

The simulated referenced phase shift (also termed as relative phase shift or RPS) and referenced AC (also termed as AC ratio or ACR) for all the source-detector pairs are compared to the measurements acquired from the various experimental conditions (described in the forthcoming chapters).

Two different implementations of the FE method are employed in the current studies. The first implementation is the finite-element based forward simulator, programmed in Fortran language, which was initially developed by Dr. Roy in order to perform simulated tomographic studies [76, 105-106]. The simulator was modified for the current experimental studies, in order to incorporate the actual phantom optical properties and also account for the boundary condition parameters (i.e. the refractive-index mismatch parameter). The computational efficiency of the forward simulator was also improved significantly using HSL2000 package (AEA Technology Engineering Software, Oxon, UK) and optimized BLAS (Basic Linear Algebra Subprograms) routines, which were employed to perform large matrix factorizations. The current

Fortran-based forward model was developed at PML in order to verify the model match between measurements and simulations obtained using the light propagation model, which is further employed during image reconstructions.

The second implementation is the finite-element based forward simulator, programmed in Matlab V. 6.1, which was developed and employed by our collaborators at the University of Vermont, along with their image reconstruction algorithm. The computational efficiency of the forward solver was improved by employing a high degree of vectorization in the code, often at the expense of added memory requirements (Section 5.3.4). The source code for the inverse problem or image reconstructions was developed by Dr. Eppstein's laboratory and applied for the current measurements in order to reconstruct the target location and size. Details of the inverse problem and the technique employed to solve the inverse problem are described in the following section.

5.2 Inverse problem

The inverse problem involves the estimation of the optical property map of the three-dimensional phantom, in order to determine the location and size of the target, using surface measurements. Various analytical and numerical approaches are attempted by researchers in order to solve for the inverse problems (Section 3.7). Usually, in all these approaches, the number of unknowns is much greater than the total number of surface measurements acquired during experimentation, reducing the inverse problem to a solution of an underdetermined system of linear equations ($Ax=b$). The problem is also 'ill-posed,' meaning that the solutions are non-unique and inconsistent. In addition,

the measurement error arising either from random sampling uncertainties or from model mismatch makes the inverse problem non-trivial.

Solution to any inverse problem requires the usage of appropriate mathematical models that represent the physics of the process (here, the optical imaging process). The optical tomography problem in general is highly non-linear and attempts to linearize the problem results in solution instabilities and often intractably long computational times, especially if the update step is to remain within the range of accuracy of the linearization. In our studies, the fluorescence-enhanced optical tomography problem is solved using the approximate extended Kalman filter (AEKF) algorithm, where the problem is linearized in order to perform computationally expensive calculations. Details of the image reconstruction formulation and the AEKF algorithm are thus described herein.

5.2.1 Formulation of the inverse problem

Before attempting to solve the inverse problem, four steps are involved in formulating the measurements and the coupled diffusion equations. These steps include: (i) measurement type, (ii) reconstructing parameter, (iii) Jacobian sensitivity matrices by adjoint formulation, and (iv) inversions using the approximate extended Kalman filter algorithm.

5.2.1.1 Measurement type

The first step in the formulation of the inverse problem is to determine the nature of the measurements (termed as *measurement type*) that will be incorporated into the inversion algorithm. One method is to choose the logarithm of fluence, Φ ($\Phi = I_{AC} \exp(i\theta)$), which would directly reflect the I_{AC} and θ obtained from the measurements. An alternate method for measurement type is to employ the real and imaginary components of the fluence. Here, the acquired measurements are not directly reflected in the measurement type used during inversions, but are embedded as $I_{AC} \cos(\theta)$ and $I_{AC} \sin(\theta)$, the real and imaginary components of fluence. Mathematically representing the two methods,

$$\text{Method 1:} \quad \ln(\Phi) = \ln(I_{AC}) + i\theta \quad (5.14)$$

$$\text{Method 2:} \quad \Phi = I_{AC} \cos(\theta) + iI_{AC} \sin(\theta) \quad (5.15)$$

In both the cases, the measurement type needs to be referenced for maintaining consistency with respect to the referenced measured data. In the current studies, the first method of the data type, that is the I_{AC} and θ , is used in the inverse algorithm since it reflects the actual measured data. The second method was not attempted in the current reconstruction studies.

5.2.1.2 Reconstructing parameter

The second step in the formulation of the inverse problem is to determine the unknown (or reconstructing) parameter to be reconstructed using the coupled diffusion equations. The unknown optical parameter, p can be one of the following optical parameters or a transformation of the parameter

$$p \in \left\{ \mu_{axf}, \mu_{axi}, \mu'_{sx}, \mu_{amf}, \mu_{ami}, \mu'_{sm}, \tau, \phi, R_x, R_m \right\} \quad (5.16)$$

where, R_x and R_m are the reflection coefficient at excitation and emission wavelengths, respectively; and range from 0 (no reflectance condition) to 1 (total reflectance condition) at the phantom surface. In our studies, the two important parameters that were considered for reconstruction include the absorption coefficient due to the fluorophore at excitation wavelength (μ_{axf}) and/or the lifetime (τ) of the fluorescing agent. The absorption coefficient due to the fluorophore at emission wavelength (μ_{amf}) can be determined from the absorption coefficient due to the fluorophore at excitation wavelength (μ_{axf}), upon relating the two terms based on their extinction coefficients (ε_{am} and ε_{ax}).

$$\frac{\mu_{amf}}{\mu_{axf}} = \frac{2.3 \times \varepsilon_{am} \times C}{2.3 \times \varepsilon_{ax} \times C} \quad (5.17)$$

where, C is the concentration of ICG, $\varepsilon_{am} = 22,000 \text{ M}^{-1}\text{cm}^{-1}$, and $\varepsilon_{ax} = 130,000 \text{ M}^{-1}\text{cm}^{-1}$. The isotropic scattering coefficient at either wavelength (μ'_{sx} and μ'_{sm}) is obtained from FDPM measurements on infinite-medium phantoms [107].

In general, μ_{axf} is the reconstruction parameter when optical contrast studies are performed using a single fluorescing contrast agent at a constant fluorescence lifetime, but with varying concentrations in the target and background. During the reconstruction of the absorption coefficient due to the fluorophore at excitation wavelength (μ_{axf}), the non-fluorescing optical properties, namely the absorption coefficient due to the chromophores (μ_{axi} and μ_{ami}) and the isotropic scattering coefficients (μ'_{sx} and μ'_{sm}) can be considered homogeneous for the entire phantom, since μ_{axf} is insensitive to the variation in the non-fluorescing optical properties [108].

Fluorescence lifetime, τ is the reconstructing parameter when the lifetime of a single fluorescing dye varies with the local environment of the tissue medium, thus providing an optical contrast in the fluorescence lifetime between the target and the background tissue. Fluorescence lifetime, τ is the reconstructing parameter also when two different fluorescing contrast agents of varying fluorescence lifetime have an affinity to either the target or the background tissue medium, thus providing an optical contrast in the fluorescence lifetime. Reconstruction of τ is usually coupled with the reconstruction of the quantum efficiency, ϕ since both these parameters are characteristics of a given fluorescing contrast agent that vary with the tissue environment, and thus they cannot be evaluated independently.

In the current study, the reflection coefficient (R_x and R_m) are assumed known (described in Section 3.2.1) and if required, these parameters can be reconstructed using the same algorithm with modifications to incorporate the new reconstructing parameter. Reconstructions assuming the reflection coefficient as an unknown parameter have been demonstrated by other researchers in the field of optical tomography [109-110].

5.2.1.3 Jacobian sensitivity matrices by adjoint formulation

The third step in the formulation of the inverse problem is to relate the measurements to the unknown optical parameters algebraically via a system of linear equations ($Ax=b$), instead of using partial differential equations. This is obtained by generating Jacobian sensitivity matrices that are used to quantify the effect of local changes in the optical properties on the detected or measured fluence. The Bayesian AEKF inversion approach is based on regularized nonlinear least-squares optimization, which involves the repeated computation of these large Jacobian matrices (\sim order of magnitude of $10^3 \times 10^3$). Various researchers have used a first-order finite-difference method [71], a second-order finite difference method [108], or an approximate adjoint method [16-17, 84] in order to evaluate these computationally intense Jacobian matrices. Here, the complete adjoint formulation of the complex coupled diffusion equations is incorporated in order to evaluate the sensitivity matrix [111]. Adjoint method for coupled diffusion equations has been used earlier by Lee *at al.* [17, 84], incorporating approximations to the formulation (described in Section 3.4.3). The adjoint formulation

of the coupled diffusion equations is published by Fedele *et al.* [111] and described here for completeness.

The adjoint formulation is performed using tensor and vectorized notations of the coupled diffusion equations. Representing the coupled diffusion equations and the partial current boundary conditions in a matrix form (in tensor and vector notations):

$$-\underline{\underline{\nabla}}^T (\underline{\underline{D}} \underline{\underline{\nabla}} \underline{\underline{\Phi}}) + \underline{\underline{k}} \underline{\underline{\Phi}} = \underline{\underline{S}} \quad (5.18)$$

$$n^T (\underline{\underline{D}} \underline{\underline{\nabla}} \underline{\underline{\Phi}}) + \underline{\underline{b}} \underline{\underline{\Phi}} = 0 \quad (5.19)$$

where $\underline{\underline{\nabla}} = \begin{bmatrix} \underline{\underline{\nabla}} & 0 \\ 0 & \underline{\underline{\nabla}} \end{bmatrix}$, $\underline{\underline{D}} = \begin{bmatrix} \underline{\underline{D}}_x I & 0 \\ 0 & \underline{\underline{D}}_m I \end{bmatrix}$, $\underline{\underline{\Phi}} = \begin{bmatrix} \underline{\underline{\Phi}}_x \\ \underline{\underline{\Phi}}_m \end{bmatrix}$, $\underline{\underline{k}} = \begin{bmatrix} k_x & 0 \\ -S_m & k_m \end{bmatrix}$, $\underline{\underline{S}} = \begin{bmatrix} S_x \\ 0 \end{bmatrix}$, $\underline{\underline{n}} = \begin{bmatrix} \underline{\underline{n}} & 0 \\ 0 & \underline{\underline{n}} \end{bmatrix}$, and

$$\underline{\underline{b}} = \begin{bmatrix} b_x & 0 \\ 0 & b_m \end{bmatrix}.$$

Each of the individual terms in the matrix is defined as

$$D_{x,m} = \frac{1}{3[\mu_{ax,mi} + \mu_{a,mf} + \mu_{sx,m}]} \quad (\text{Diffusion coefficient at either wavelength}) \quad (5.20)$$

$$k_{x,m} = \frac{i\omega}{c} + \mu_{ax,mi} + \mu_{ax,mf} \quad (\text{Decay coefficient at either wavelength}) \quad (5.21)$$

$$S_m = \frac{\phi \mu_{axf}}{1 - i\omega\tau} \quad (\text{Emission source term}) \quad (5.22)$$

$$b_{x,m} = \frac{1 - R_{x,m}}{2(1 + R_{x,m})} \quad (\text{Boundary term at either wavelength}) \quad (5.23)$$

An infinitesimally small perturbation in the unknown parameter, p will cause a perturbation in the fluence ($\delta\Phi$) at both the wavelengths

$$p \rightarrow p + \delta p \Rightarrow \underline{\Phi} \rightarrow \underline{\Phi} + \delta \underline{\Phi} \quad (5.24)$$

This variation in fluence reflects in Equations (5.18) and (5.19) as

$$-\underline{\underline{\nabla}}^T \left(\underline{\underline{D}}(p + \delta p) \underline{\underline{\nabla}}(\underline{\Phi} + \delta \underline{\Phi}) \right) + \underline{\underline{k}}(p + \delta p)(\underline{\Phi} + \delta \underline{\Phi}) = \underline{\underline{S}} \quad \text{on } \Omega \quad (5.25)$$

$$n^T \left(\underline{\underline{D}}(p + \delta p) \underline{\underline{\nabla}}(\underline{\Phi} + \delta \underline{\Phi}) \right) + \underline{\underline{b}}(p + \delta p)(\underline{\Phi} + \delta \underline{\Phi}) = \underline{\underline{0}} \quad \text{on } \partial\Omega \quad (5.26)$$

The above equations can be expanded using Taylor's series and approximated to their first order terms. However, even after performing the first order approximations the computation becomes cumbersome if Equation (5.25) has to be solved for each spatially discretized parameter, p . Hence, the adjoint method is applied to solve for the unknown

parameter. Here, a matrix $\underline{\underline{\Psi}}$ is chosen as the adjoint or Green matrix of the coupled system such that it satisfies the adjoint system of equations that are defined as

$$-\underline{\underline{\nabla}}^T (\underline{\underline{D}}^T \underline{\underline{\nabla}} \underline{\underline{\Psi}}) + \underline{\underline{k}}^T \underline{\underline{\Psi}} = \underline{\underline{\Delta}}_d \quad \text{on } \Omega \quad (5.27)$$

$$n^T (\underline{\underline{D}}^T \underline{\underline{\nabla}} \underline{\underline{\Psi}}) + \underline{\underline{b}}^T \underline{\underline{\Psi}} = \underline{\underline{0}} \quad \text{on } \Gamma \quad (5.28)$$

where

$$\underline{\underline{\Psi}} = \begin{bmatrix} \Psi_{xx} & \Psi_{xm} \\ \Psi_{mx} & \Psi_{mm} \end{bmatrix} \quad (5.29)$$

and the Dirac-delta function is

$$\underline{\underline{\Delta}}_d = \begin{bmatrix} \Delta_d & 0 \\ 0 & \Delta_d \end{bmatrix} \quad (5.30)$$

Equation (5.25) is multiplied by $\underline{\underline{\Psi}}^T$ and integrated over the entire domain Ω , followed by integration by parts and applying the boundary condition given in Equation (5.26). Integrating by parts was performed the second time and Equations (5.27) and (5.28) are applied. Upon rearranging the terms, the variation in fluence (that is, fluence sensitivity) can be represented by three integral terms,

$$\underline{\underline{\delta\Phi}} = -\int_{\Omega} (\underline{\underline{\nabla}} \underline{\underline{\Psi}})^T \left(\frac{\partial \underline{\underline{D}}}{\partial p} \delta p \underline{\underline{\nabla}} \underline{\underline{\Phi}} \right) - \int_{\Omega} \underline{\underline{\Psi}}^T \left(\frac{\partial \underline{\underline{k}}}{\partial p} \delta p \underline{\underline{\Phi}} \right) - \int_{\Gamma} \underline{\underline{\Psi}}^T \left(\frac{\partial \underline{\underline{b}}}{\partial p} \delta p \underline{\underline{\Phi}} \right) \quad (5.31)$$

The above equation can be separated into sensitivity equations for excitation and emission fluence. The sensitivity of the excitation fluence is given by

$$\partial\Phi_x = \int_{\Omega} \nabla\Psi_{xx} \frac{\partial D_x}{\partial p} \delta p \nabla\Phi_x - \int_{\Omega} \Psi_{xx} \frac{\partial k_x}{\partial p} \delta p \Phi_x - \int_{\Gamma} \Psi_{xx} \frac{\partial b_x}{\partial p} \delta p \Phi_x \quad (5.32)$$

and the sensitivity of the emission fluence is given by

$$\begin{aligned} \partial\Phi_m = & \left[-\int_{\Omega} \nabla\Psi_{mm} \frac{\partial D_m}{\partial p} \delta p \nabla\Phi_m - \int_{\Omega} \Psi_{mm} \frac{\partial k_m}{\partial p} \delta p \Phi_m - \int_{\Gamma} \Psi_{mm} \frac{\partial b_m}{\partial p} \delta p \Phi_m \right] \\ & + \left[-\int_{\Omega} \nabla\Psi_{xm} \frac{\partial D_x}{\partial p} \delta p \nabla\Phi_x - \int_{\Omega} \Psi_{xm} \frac{\partial k_x}{\partial p} \delta p \Phi_x - \int_{\Gamma} \Psi_{xm} \frac{\partial b_x}{\partial p} \delta p \Phi_x \right] + \left[\int_{\Gamma} \Psi_{mm} \frac{\partial S_m}{\partial p} \delta p \Phi_x \right] \end{aligned} \quad (5.33)$$

The sensitivity of the excitation fluence depends on the sensitivity of the diffusion coefficient (D_x), decay coefficient (k_x), and the boundary term (b_x) at the excitation wavelength. However, the sensitivity of the emission fluence is contributed by three different terms, each given in a square bracket in Equation (5.33). The first term reflects the sensitivity of the diffusion coefficient (D_m), decay coefficient (k_m), and boundary terms (b_m) at the emission wavelength that contribute to the sensitivity of Φ_m . The second term reflects the sensitivity of diffusion coefficient (D_x), decay coefficient (k_x), and boundary terms (b_x) at the excitation wavelength, and the third term reflects the contribution from the sensitivity in the emission source term (S_m). If D_m , k_m , and b_m are assumed to be insensitive to the unknown parameter, p then the first term in Equation

(5.33) goes to zero. Similarly the second term goes to zero when D_x , k_x , and b_x are assumed to be insensitive to p . Also assuming that D_m is spatially smooth, we have $\nabla D_m = 0$, and the third term of Equation (5.33) can be simplified into an identical form of the approximate adjoint method (see Equation (3.21)) that has been employed by other researchers [16-17, 84].

When the unknown parameter, p is μ_{axf} , then the derivatives of the boundary terms with respect to the μ_{axf} are neglected.

$$\frac{\partial b_x}{\partial p} \approx 0 \ \& \ \frac{\partial b_m}{\partial p} \approx 0 \quad (5.34)$$

The sensitivity of the fluence at either wavelengths, given by Equations (5.32) and (5.33), is solved by employing the Galerkin formulation of the finite element method, similar to that employed for the forward model (Section 5.1). Having formulated the Jacobian sensitivity matrices in the finite-element domain, the sensitivity matrices are used along with the measurements in order to compute the unknown parameter, p , using the AEKF numerical inversion technique.

5.2.1.4 Inversions using the approximate extended Kalman filter algorithm

The fourth and last step in the formulation of the inverse problem is to develop the approximate extended Kalman filter (AEKF) algorithm required to solve for the

reconstructing parameter, employing acquired measurements and the Jacobian sensitivity matrices.

The Kalman filter is a linear state estimator used in process control for estimating a state recursively, based on its previous observations. This Bayesian estimator assumes that the state variables and the observations are normally distributed random variables and the estimator determines the mean value of the conditional probability function of unknown parameters Y , using the given measurements Z , $p[Y|Z]$. The advantages of this Bayesian estimator include (i) use of measurement error (error between measurement repetitions) and model error (due to the mathematical simplifications of the diffusion equation) to weight the updates in each iteration and regularize the matrix inversion, and (ii) estimation of parameter error values (or the confidence in the parameter value), apart from the estimation of the parameter value itself, and using these parameter error values to damp and regularize the inversions. In a clinical perspective, the second feature may help determine the confidence in a reconstructed image apart from just reconstructing an image.

The approximate extended Kalman filter (AEKF) is a stochastic method based on the statistically stronger criterion of minimizing the variance of the parameter error, given estimates of measurement, model, and initial parameter estimation errors, rather than simply minimizing the output error. It offers several advantages for inverting low SNR data, including (i) physically-based weighting of parameter updates that explicitly accounts for spatially variant measurement and model error covariances (\mathbf{R} and \mathbf{Q} , respectively), (ii) co-estimation of the spatially variant parameter error covariance (\mathbf{P})

that can be used as a measure of final parameter uncertainty, and (iii) enhanced convergence by damping on the inverse of the evolving parameter error covariance. The measurement error covariance matrix (\mathbf{R}) is estimated from repeated measurements from each individual source-detector pair, such that \mathbf{R} is spatially variant. Model error may arise due to the simplifications in the forward model formulation, and unlike the unbiased portion of the measurement error variance, it is not possible to empirically determine the model error covariance \mathbf{Q} for unknown domains. The parameter error is defined as the error in the spatially distributed (unknown) parameter values and it is also difficult to determine the parameter error covariance \mathbf{P} for unknown domains. The details of how the measurement error covariance (\mathbf{R}), model error covariance (\mathbf{Q}), and parameter error covariance (\mathbf{P}) are evaluated in the current studies will be described in Section 6.2.3. Prior studies with the AEKF have verified that the use of actual spatially variant measurement errors and recursively updated parameter errors increase the accuracy and stability of reconstructions of fluorescence absorption from noisy data [16]. While the AEKF is a first-order approximation of the full extended Kalman filter for time-series estimation [112], it is the exact minimum variance estimation for linearized estimation in steady-state 3-D tomography problems.

This minimum-variance AEKF algorithm regularizes the inversion using estimates of measurement error covariance \mathbf{R} , model error covariance \mathbf{Q} , and recursively updated co-estimates of parameter error covariance \mathbf{P} , as shown in the following pseudo-code:

AEKF algorithm

Loop

1. $\mathbf{x} \leftarrow f_s(\mathbf{y})$
2. $\mathbf{J} \leftarrow \frac{\partial \mathbf{x}}{\partial \mathbf{y}}$
3. $\mathbf{K} \leftarrow (\mathbf{J}^T \cdot (\mathbf{Q} + \mathbf{R})^{-1} \cdot \mathbf{J} + \mathbf{P}^{-1})^{-1} \cdot \mathbf{J}^T \cdot (\mathbf{Q} + \mathbf{R})^{-1}$
4. $\mathbf{y} \leftarrow \mathbf{y} + \mathbf{K} \cdot (\mathbf{z} - \mathbf{x})$
5. $\mathbf{P} \leftarrow \mathbf{P} - \mathbf{K} \cdot \mathbf{J} \cdot \mathbf{P}$

Until Convergence

Here, \mathbf{x} represents distributed predictions of the measurable state variables (that is, logarithmic AC ratio, $\ln(\text{ACR})$ and relative phase shift, RPS), and \mathbf{z} represents a vector of the corresponding measurements, for all source-detector fiber pairs used in the reconstruction. The forward simulator f_s is as described in Section 5.1. The Jacobian \mathbf{J} is calculated using the full-coupled adjoint sensitivities as described in Section 5.2.1.3 [111]. The discrepancies between measurements and predictions ($\mathbf{z} - \mathbf{x}$) are weighted by a gain matrix \mathbf{K} in order to update the uncertain parameters \mathbf{y} and the parameter error covariance \mathbf{P} . The AEKF algorithm is carried out *recursively*, meaning that each batch of measurements are used to continuously update the unknown parameter \mathbf{y} and the parameter error covariance \mathbf{P} , without storing individual batch of measurements in each loop (shown in the above pseudo-code). This recursive AEKF algorithm is carried out *iteratively* till the reconstructions converge. Details of the convergence criterion are described in Section 5.4.

Thus the four aspects involved in the formulation of the inverse problem (apart from solving the forward problem) include the choice of the measurement type, the

choice of the reconstructing parameter, the adjoint formulation of the Jacobian sensitivity matrices, and the performance of the AEKF algorithm. These four aspects are implemented accordingly, in order to obtain the spatial distribution of the unknown parameter (here, optical property maps) in the 3-D tissue volumes. Apart from the four aspects described in the above section, various other aspects include the choice of measurement error covariance (\mathbf{R}), model error covariance (\mathbf{Q}), and parameter error covariance (\mathbf{P}). These aspects are embedded in the image reconstructions presented in the result sections. Details of the implementation of the formulated inversion technique are described in the following section.

5.3 Implementation of the inversion methodology

Implementation of the inversion technique involves various *a priori* steps in order to organize the data in the desired format and consider the sources of error at each step of the AEKF implementation. In this section, the steps incorporated to successfully solve large 3-D tomography problems using the AEKF algorithm are described.

5.3.1 Parameter distribution using pseudo-beta transforms

Distribution of parameters is given by the probability distribution function of the parameters. One assumption of the AEKF is that the parameters are normally distributed. In the absence of *a priori* information about the tissue or medium of interest, one can assume the parameters to be independently and identically distributed (i.i.d.) random variables. But, when *a priori* information of the tissue is available in

terms of the distribution of parameters, then the information can be used to initialize the parameter covariance matrix, \mathbf{P} . However, a normally distribution implies that there are infinite lower and upper bounds for the parameter values. This is unrealistic for the parameter distribution in a real tissue. In order to overcome this problem, the probability-distributed functions can be transformed from a normal distribution to a pseudo-beta distribution [71]. Unlike the normal distribution, the pseudo-beta distribution has a lower bound, upper bound, and a skew factor that captures the skew in the mode of the distribution of the actual parameter of interest in the tissue medium.

The equations representing the transformation from normal distribution of parameter, Y , to pseudo-beta distribution of parameter, ξ and vice-versa are given by

$$\xi = \ln \left[\frac{(B_{upper} - B_{lower}) F_{skew}}{Y - B_{lower}} - F_{skew} \right] \quad (5.35)$$

$$Y = (e^{\xi} + F_{skew})^{-1} (B_{upper} - B_{lower}) F_{skew} + B_{lower} \quad (5.36)$$

where, B_{lower} , B_{upper} are the lower and upper bounds of the pseudo-beta distribution, respectively, and the term F_{skew} determines its skewness. In a typical case of a real tissue, when the absorption coefficient due to the fluorophore (μ_{axf}) is the unknown parameter to be reconstructed, the skewness in the pseudo-beta transform is typically towards the lower bound. This is due to the fact that μ_{axf} has a small value for normal

tissue and a higher value at the diseased tissue region, due to the enhanced absorption optical contrast in the diseased tissue region with respect to the normal background tissue region. Hence, for the current studies F_{skew} is chosen to be 0.2 when the unknown parameter was μ_{axf} . In the case of lifetime studies, where τ is the unknown parameter, the skew factor could be towards the upper bound or lower bound depending on the nature of the dye. In other words, when the dye exhibits a greater lifetime in the target over the background (i.e. in the diseased site over the normal tissue), the distribution of parameters skews towards the lower bound, and vice-versa.

5.3.2 Jacobian sensitivity matrix for referenced measurements

In the case of absolute unreferenced measurements, the Jacobian sensitivity matrix can be used directly without further modifications. However, absolute measurements are impractical in optical tomographic studies, since the unknown source strength and instrument effects (Section 4.4) need to be accounted for. Hence, the Jacobian matrix needs to be calculated for referenced measurements, which are obtained using either of the two referencing schemes (Φ_m/Φ_x or $\Phi_m/\Phi_{m,ref}$), as described in Section 4.4. Also, the Jacobian matrix should be modified in order to account for the pseudo-beta transformation of the unknown parameter, \mathbf{Y} .

Initially, the Jacobian matrix at each wavelength is evaluated using Equations (5.32) and (5.33), respectively. Assuming that the unknown parameter is μ_{axf} , the Jacobian (J) at either wavelength (x or m) is defined as

$$J_{x,m} = \frac{\partial \Phi_{x,m}}{\partial \mu_{axf}} \quad (5.37)$$

The measurements can be incorporated as fluence or logarithm of fluence, where the latter better reflects the acquired measurements in terms of amplitude (I_{AC}) and phase shift (θ) acquired from actual experiments. Hence the Jacobian formulation is modified accordingly in order to incorporate $\ln(\Phi)$ for the measurement type. Also, since the Kalman filter uses the beta-transformed parameter, ξ over the normally distributed parameter, \mathbf{Y} , the Jacobian is re-evaluated to determine how Φ_m (fluence at emission wavelength) changes with respect to ξ (beta-transformed parameter), instead of how Φ_m changes with respect to \mathbf{Y} (normally distributed parameter). Finally, referencing of emission measurements using either of the two referencing schemes (Φ_m/Φ_x or $\Phi_m/\Phi_{m,ref}$), is included in the Jacobian matrices. All these modifications are carried out in three steps as shown below.

Step 1: Re-defining the Jacobian for logarithmic measurements

$$J_m = \frac{J_m}{\Phi_m} = \left(\frac{\partial \Phi_m}{\partial \mu_{axf}} \right) \cdot \frac{1}{\Phi_m} \quad (5.38)$$

$$J_m = \frac{\partial(\ln \Phi_m)}{\partial \mu_{axf}} \quad (5.39)$$

Step 2: Converting the Jacobian to determine the change of measurements with respect to ξ ,

$$\frac{\partial(\ln \Phi_m)}{\partial \xi} = \left(\frac{\partial(\ln \Phi_m)}{\partial \mu_{axf}} \right) \cdot \left(\frac{\partial \mu_{axf}}{\partial \xi} \right) \quad (5.40)$$

where, the derivative of μ_{axf} with respect to ξ is obtained by solving Equation (5.36) (Section 5.3.1).

Step 3: Incorporating the referenced measurements obtained using either of the referencing schemes. When the first referencing scheme (Φ_m / Φ_x) is employed, where the measurements at emission wavelength are referenced to the measurements at excitation wavelength, the final Jacobian matrix is derived as

$$(J_m)_{\ln ref} = \frac{\partial(\ln \Phi_m)}{\partial \xi} - \frac{\partial(\ln \Phi_x)}{\partial \xi} \quad (5.41)$$

Using the second referencing scheme ($\Phi_m / \Phi_{m,ref}$), where the emission measurements are referenced with respect to the emission measurement obtained at a reference location, the final Jacobian matrix is derived as

$$J = (J_m)_{\ln ref} = \frac{\partial(\ln \Phi_m)}{\partial \xi} - \frac{\partial(\ln \Phi_{m,ref})}{\partial \xi} \quad (5.42)$$

The Jacobian matrix calculated from the above equation is a matrix of complex numbers, containing a real and imaginary part and is used in the AEKF algorithm as shown in the pseudo-code in Section 5.2.1.4. However, the final estimated parameter (which is either absorption coefficient or lifetime) is required to be a real number, which may not be the case upon solving the complex equation, $\Delta\Phi_m = \text{function}(J)\Delta Y$. The problem can be overcome by separating the real and imaginary parts of both the Φ_m and J to form a composite matrix for $(\Phi_m)_{reim} = \text{function}(J_{reim})\Delta Y$, where

$$(\Phi_m)_{reim} = \begin{bmatrix} \text{Re } \Delta\Phi_m \\ \text{Im } \Delta\Phi_m \end{bmatrix} \text{ and } J_{reim} = \begin{bmatrix} \text{Re } J \\ \text{Im } J \end{bmatrix} \quad (5.43)$$

or

$$J_{reim} = \begin{bmatrix} \frac{\partial \ln(ACR)}{\partial \xi} \\ \frac{\partial RPS}{\partial \xi} \end{bmatrix} \quad (5.44)$$

Separation of the real and imaginary terms has an advantage, in that the amplitude and phase information are preserved when the logarithm of fluence is used as the measurement type. Based on the estimated measurement precision and accuracy of the amplitude (I_{AC}) and phase shift (θ) data, either both the amplitude (I_{AC}) and phase shift (θ) or one of them can be used as known measurements during image reconstructions without any major modifications to Equation (5.44), in order to solve for the unknown parameter distribution \mathbf{Y} .

5.3.3 Computationally efficient version of the AEKF algorithm

The AEKF algorithm (Section 5.2.1.4) has been successfully implemented for 3-D optical tomographic fluorescence measurements using different phantom geometries [16]. However, high memory requirements, computational overhead, and sub-optimal updates due to the non-linearities in this AEKF recursive estimation technique, limit the algorithm in terms of the resolution of discretization in large 3-D geometries. Zhang *et al.* modified the AEKF algorithm by using data decomposition such that the memory requirements are reduced [113]. Of the three modified versions of the AEKF algorithms proposed in Zhang's work, one of the algorithms proved efficient and is employed in our current inversion algorithms. It is described briefly in this section.

In the AEKF algorithm applied to all measurements as a batch to solve large 3-D tomographic problems [16], the pseudo-code is as shown in Section 5.2.1.4. The current modified version of AEKF algorithm is a variation of the full AEKF pseudo-code involving decomposed data sets. Here, the Jacobian sensitivity matrix, J_i is updated using parameters from the previous measurement subset, such that the bias in the measurement subsets reflected in the overall sensitivity of emission fluence at the end of each measurement subset update. In addition, the parameter updates (**yupdate**) are calculated for each measurement subset, I ; the parameter error covariance, \mathbf{P} is also updated recursively for each data subset; and the parameter, \mathbf{y} is updated as a summation of the individual and independent updates from all the data subsets. However, in the modified version of AEKF algorithm (shown below), the estimation of \mathbf{P} was such that it was forced to remain uncorrelated unlike the formulation of \mathbf{P} in Section 5.2.1.4. This is

reflected in the pseudo-code (shown below) as the full diagonal of the parameter error covariance, \mathbf{P} . During the actual computations, only the diagonal elements of \mathbf{P} were stored and manipulated in the modified AEKF implementation. The modified variation of the actual AEKF pseudocode is as shown below:

Modified version of AEKF (data decomposed into subsets)

loop

$$1. \mathbf{x} \leftarrow f_s(\mathbf{y})$$

for all subsets i of measurements

$$2. \mathbf{J}_i \leftarrow \frac{\partial \mathbf{x}_i}{\partial \mathbf{y}}$$

$$3. \mathbf{K}_i = \mathbf{P} \cdot \mathbf{J}_i^T \cdot (\mathbf{R}_i + \mathbf{Q}_i + \mathbf{J}_i \cdot \mathbf{P} \cdot \mathbf{J}_i^T)^{-1}$$

$$4. \mathbf{yupdate}_i = \mathbf{K}_i \cdot (\mathbf{z}_i - \mathbf{x}_i)$$

$$5. \mathbf{P} = \text{full}(\text{diag}(\mathbf{P} - \mathbf{K}_i \cdot \mathbf{J}_i \cdot \mathbf{P}))$$

end

$$6. \mathbf{y} = \mathbf{y} + \sum_i \mathbf{yupdate}_i$$

until convergence

Based on studies performed by Zhang *et al.* [113] where actual experimental data was reconstructed, the above hybrid AEKF algorithm was not only computationally efficient and required less memory, but also gave equivalent qualitative image reconstructions. Hence, the above mentioned modified version of the AEKF algorithm is employed in the current studies.

5.3.4 Vectorization of the inverse formulation

The forward and inverse algorithm is coded using a highly vectorized method that is coded in Matlab (Mathworks Inc., Natick, MA). Vectorization improved the computational efficiency of the 3-D inversions at the expense of memory requirements. However, the memory requirements are optimized by decomposing the data into subsets [111]. Details of the vectorization implementation are beyond the scope of the current work and interested readers are encouraged to read the work published by Fedele *et al.* [111].

5.4 Flowchart of the optical tomography process

The entire optical tomography process, beginning from data acquisition until image reconstructions is presented as a flowchart in Figure 5.2. The flowchart depicts the actual process by which 3-D image reconstructions are carried out in the current work. Although the full AEKF algorithm is shown as an option in the flowchart, all the reconstructions were performed using the hybrid AEKF algorithm.

Three-dimensional image reconstructions are carried out iteratively until the inversions converged. In the current study, the reconstructions are determined to have converged when there was less than 1% additional decrease in root mean square output error (RSME). Based on the reconstruction details provided in the current major section and the experimental tools described in Section 4, the results obtained from various studies are described in the following major sections.

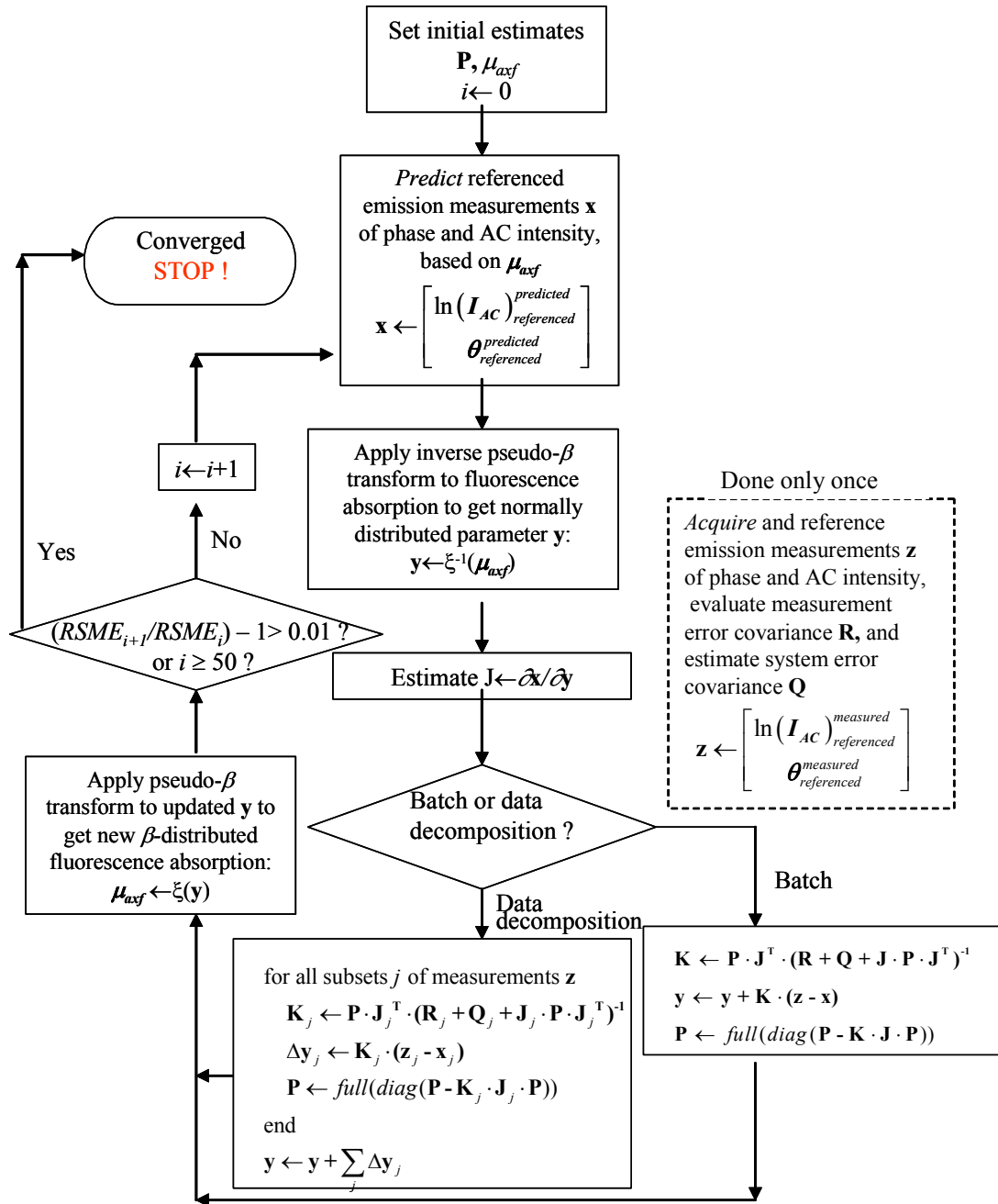


Figure 5.2 Flowchart of the image reconstruction algorithm.

6. DATA ANALYSIS AND EXPERIMENTAL PLAN

In the previous chapters, instrumentation set-up and details of the finite-element based forward and inverse problems towards 3-D fluorescence-enhanced optical tomography have been explained. Using the current imaging set-up and the AEKF inversion algorithm, experiments were performed under various conditions. Details of the general experimental parameters employed and an overall sketch of the experimental plan for the current studies are described herein.

6.1 Experimental parameters

Experiments were performed using 1% Liposyn solution filled in the large breast shaped phantom, in order to mimic the normal breast tissue. The 1% (by volume) Liposyn solution was prepared from a 20% (by volume) Liposyn stock solution (Abbott Laboratories, North Chicago, IL), by diluting the stock solution with de-ionized ultra-filtered water. The optical properties in terms of absorption and scattering coefficient of each batch of 1% Liposyn solution prepared was determined from FDPM measurements, which were performed using a point illumination\point collection measurement geometry in an infinite medium of Liposyn solution. Measurements acquired in terms of amplitude (I_{AC}), phase (θ), and DC values (I_{DC}), at both the excitation (~ 785 nm) and emission wavelengths (~ 828 nm), were used along with analytical solutions for diffusion

equation in infinite medium in order to evaluate the optical properties of the 1% Liposyn solution at both the wavelengths [107].

6.1.1 Fluorescence contrast agents

A fluorescing contrast agent was used to provide an enhanced absorption optical contrast in the target with respect to the background phantom. In the current experimental studies, one of the two fluorescing contrast agents were used, namely Indocyanine green (ICG) or 3-3' Diethylthiatricarbocyanine iodide (DTTCI).

ICG is a blood-pooling agent that was approved by the United States FDA (Food and Drug Administration) for systemic administration to investigate hepatic function [114] and retinal angiography [115]. ICG is soluble in water, but aggregates and quench over a period of 10 hours, reducing its fluorescence intensity. Sodium polyaspartate (MW 3000-8000) (Sigma-Aldrich Chemical Co., St. Louis, CO) stabilizes the dye by non-covalent interactions, thus prolonging the working time of ICG in water and Liposyn solution, without affecting its fluorescing optical properties [116]. The absorption and emission spectra of ICG (mol. wt. 775) diluted in de-ionized water was evaluated using the spectro-fluorometer (SPEX Fluorolog, Jobin Vyon, Edison, NJ) and is shown in Figure 6.1.

In general, the optical properties of any diluted fluorescing agent can be determined using the following relation:

$$\mu_{ax,m,f} = 2.3 \times \epsilon_{ax,m} \times C \quad (6.1)$$

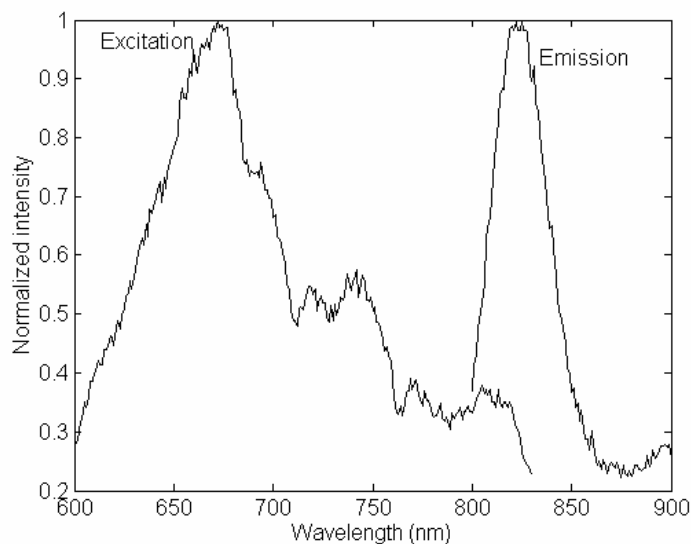


Figure 6.1 Excitation and emission spectra of ICG dissolved in water, plotted as normalized intensity versus the wavelength range. The excitation peak (between 600 nm to 800 nm) was obtained for a constant emission wavelength of 850 nm, and the emission peak (between 800 nm and 900 nm) was obtained for a constant excitation wavelength of 780 nm.

where, $\mu_{ax,m,f}$ is the absorption coefficient due to the fluorescing agent (suffix ' f ') at the excitation (suffix ' x ') and emission (suffix ' m ') wavelengths, respectively; $\epsilon_{ax,m}$ is the extinction coefficient at the excitation and emission wavelengths, respectively; and C is the concentration of the fluorescing agent (mol/l). The fluorescent properties of ICG are provided in Table 6.1 [117].

DTTCI was the other fluorescing agent that was used in our experimental studies. DTTCI is insoluble in water, but soluble in reagents such as ethanol, dimethyl sulfoxide (DMSO), and diethylene glycol. Based on the reagent it is dissolved in, the absorption and fluorescence spectra of the dye shift. The absorption and emission spectra of DTTCI

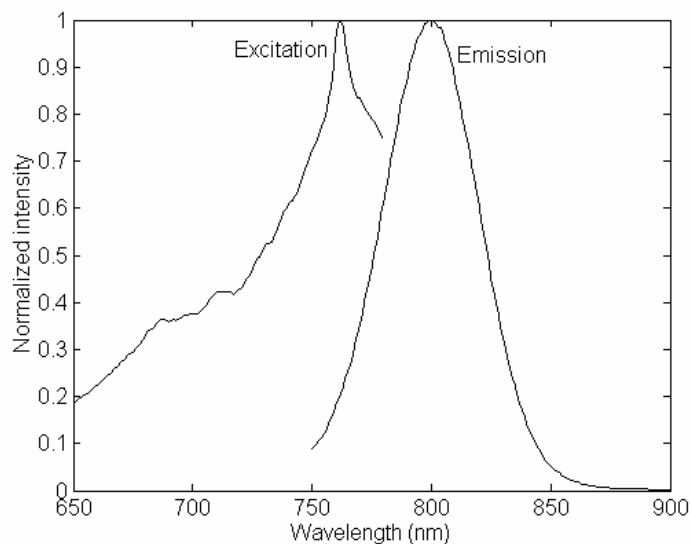


Figure 6.2 Excitation and emission spectra of DTTCI dissolved in DMSO, plotted as normalized intensity versus the wavelength range. The excitation peak (between 650 nm to 780 nm) was obtained for a constant emission wavelength of 800 nm, and the emission peak (between 750 nm to 900 nm) was obtained for the constant excitation wavelength of 730 nm.

Table 6.1 Fluorescent properties of ICG and DTTCI.

Fluorescing dye	Mol. wt.	Solubility	λ_{ex} (nm)	λ_{em} (nm)	τ (nsec)	ϕ	ϵ_{780}^{-1} (Mcm) ⁻¹	ϵ_{830}^{-1} (Mcm) ⁻¹
ICG	775	Water	780	830	0.56	0.016	130000	22000
DTTCI	544.52	DMSO, Ethanol	780	830	1.18	0.034	43000	5500

dissolved in DMSO was obtained using the spectro-fluorometer and is shown in Figure 6.2. The absorption coefficient at excitation and emission wavelengths was determined using Equation (6.1), using the appropriate extinction coefficient of DTTCI at both the wavelengths. The fluorescent properties of DTTCI are also provided in Table 6.1 [117].

6.2 Data analysis methodology

Experiments were performed under various conditions of target volume, target depth, target:background optical contrast ratio, and number of targets. For all the different experimental cases, the data was analyzed and 3-D images of the phantom were reconstructed in a similar fashion. The various steps involved in the data analysis process include:

- (i) Acquiring excitation and fluorescence measurements using the ICCD detection system.
- (ii) Determining the model match between experiments and simulations
- (iii) Estimating the measurement error covariance (\mathbf{R}), model error covariance(\mathbf{Q}), and parameter error covariance (\mathbf{P}) that was used in the AEKF inversion algorithm
- (iv) Performing 3-D image reconstructions using the hybrid version of the AEKF algorithm.

These four steps are described in the following section and a schematic of the entire data analysis process is given in Figure 6.3.

6.2.1 Acquisition of excitation and fluorescence measurements

Experiments were performed using the 3-D breast phantom filled with 1% Liposyn as the tissue-mimicking agent and using ICG or DTTCI for enhanced optical contrast. One or more targets of a given volume (based on the set experimental

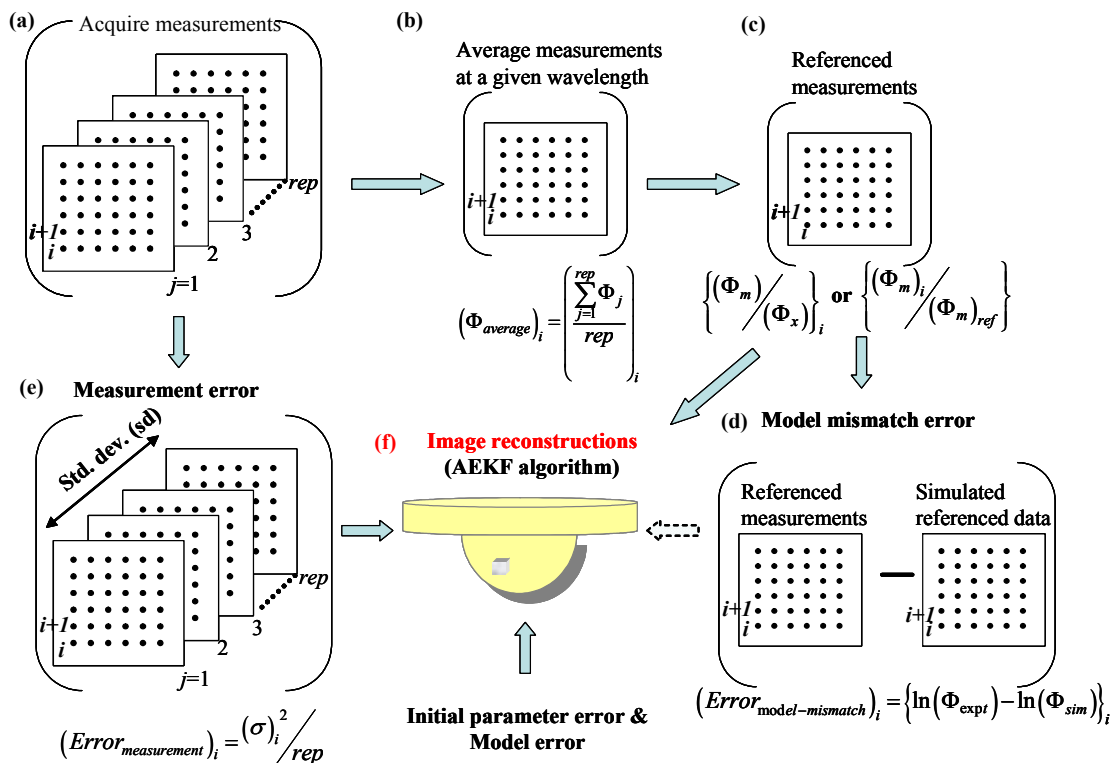


Figure 6.3 Schematic of the data analysis process (a) acquiring repeated measurements at each pixel (i), (b) averaging the data from repeated measurements at each pixel (i), (c) referencing the averaged data using either of the two referencing schemes at each pixel (i), (d) determining the model mismatch error between experiments and simulations at each pixel (i), (e) determining the measurement error from the repeated measurements at each pixel (i), and (f) performing image reconstructions using all the required input parameters as shown.

condition) were filled with 1% Liposyn and a greater concentration of the fluorescing agent in comparison to that present in the background. Fluorescence and excitation measurements were acquired using the ICCD detection system from different points of illuminations. The total data acquisition time for each experimental case was a function of (i) the exposure time of the camera (varying between 0.2 to 1 sec), (ii) the number of

repeated measurement acquired (5 in our case), (iii) the number of interfacing plates imaged (i.e. 1 or 2), and (iv) the number of point illuminations (sources) that were used to acquire fluorescence measurements from the interfacing plates (varying between 1 to 27). In comparison to our earlier imaging system employing PMTs for detecting single source-detector pair individually [15-17, 84], the current imaging system detecting multiple source-detector pairs using the ICCD camera is at least 4-7 times faster (based on the exposure time set on the CCD camera). Hence, rapid data acquisitions achieved using the ICCD imaging system is an added advantage during the clinical translation of the fluorescence-enhanced optical imaging technology.

6.2.2 Determination of model match and model mismatch errors

Five or ten sets of repeated FDPM measurements were acquired at each of the source-detector pairs (that is, at each collection fiber for a given point illumination of the excitation source) and at both the excitation and emission wavelengths. The means of $\ln(\text{ACR})$ (logarithmic AC ratio) and RPS (relative phase shift) obtained from these 5 or 10 sets of repeated measurements at each given source-detector fiber pair were used in the reconstruction vector \mathbf{z} , and are hereafter simply referred to as the ‘*measurements*.’ The referenced measurements obtained employing either of the two referencing schemes (Φ_m/Φ_x or $\Phi_m/\Phi_{m,ref}$) was compared to the simulated data obtained from the forward model for initial data sets (described in Section 7.3). The difference between the measurements and simulated data is thus an assessment of what is termed as “model mismatch error.”

which is determined in terms of the error in relative phase shift (RPS_{error}) and AC ratio (ACR_{error}) between measurements and simulations.

$$ACR_{error} = \ln(ACR)_{\text{expt}} - \ln(ACR)_{\text{sim}} \quad (6.2)$$

$$RPS_{error} = RPS_{\text{expt}} - RPS_{\text{sim}} \quad (6.3)$$

where, ACR and RPS are the referenced AC and phase shift obtained using one of the two referencing schemes (Φ_m/Φ_x or $\Phi_m/\Phi_{m,ref}$). The suffix *expt* represents experimental data, and *sim* represents simulated data obtained from the forward problem.

In addition to errors introduced by the computational forward model itself (e.g., discretization error, simplifications in the physics, errors in parameters and boundary conditions considered known, etc.), here the definition of model mismatch error also includes any biased portion of the measurement error. There is no method to evaluate the biased portion of the measurement error for unknown domains. Hawrysz *et al.* developed statistical correlations to estimate the biased measurement errors and incorporated these errors during 3-D image reconstructions [15]. However, in the current work, the biased portion of measurement error was assumed zero during reconstructions, although bias may exist in the current imaging system.

6.2.3 Estimation of measurement error covariance, model error covariance, and parameter error covariance

The measurement error covariance \mathbf{R} was estimated as a diagonal matrix from the variances of the means of 5 or 10 sets of repeated measurement from each individual source-detector fiber pair, so each \mathbf{R}_i is spatially variant and distinct. Measurement error variances (used on the diagonal of \mathbf{R}) were calculated for each source-detector pair as

$$(\text{Error}_{\text{measurement}})_i = \frac{\sigma_i^2}{\text{rep}} \quad (6.4)$$

where σ is the sample standard deviation in AC and phase shift of the ‘*rep*’ sets of repeated measurements from each source-detector pair (*i*), using the appropriate referencing method. The average measurement error variance for both AC and phase shift was determined for each experimental condition. The current assessment of measurement error did not include possible bias in measurement errors, and the biased portion was considered as a component of the model mismatch error.

Unlike the unbiased portion of the measurement error variance, it is not possible to accurately determine the model error covariance \mathbf{Q} for unknown domains. In previous work [16], the model error variance was approximated to be spatially invariant based on the average estimates of model error variance of both $\ln(\text{ACR})$ and RPS, where the model error variance of both $\ln(\text{ACR})$ and RPS was determined by comparing measurements with predictions from the forward model on several known phantoms. In some of the (preliminary) work presented here, the model error variance was

approximated to be spatially variant by scaling the inverse of the modulation depth (i.e. DC/AC) for $\ln(\text{ACR})$ and for RPS, in accordance with ranges of model errors observed on these and other data sets, so each \mathbf{Q}_i was also spatially variant and distinct. However, for most experimental studies, the model error variance \mathbf{Q} was empirically chosen to be one-fourth the mean of the measurement error covariance, \mathbf{R} .

$$\mathbf{Q} = \frac{1}{4} \text{mean}(\mathbf{R}_i) \quad (6.5)$$

The initial values of the parameter error covariance (\mathbf{P}) were arbitrarily set to constant value along the diagonal entries of the \mathbf{P} matrix.

$$\mathbf{P} = \text{constant} \quad (6.6)$$

where the *constant* was typically set to 0.001, 0.01, or 0.1. The measurement error covariance, \mathbf{R} and the model error covariance, \mathbf{Q} , were used along with the parameter error covariance, \mathbf{P} in the AEKF algorithm in order to perform 3-D image reconstructions in the current studies. Work is in progress to determine a more general method for estimating the parameter error covariance matrix as well as the model error covariance matrix.

6.2.4 Performance of image reconstructions using modified version of AEKF algorithm

Image reconstructions were performed using a finite-element based discretized breast phantom containing 6956 nodes and 34413 tetrahedral elements. Referenced measurements (obtained using one of the two referencing schemes) were used along with the estimates of measurement error covariance \mathbf{R} and model error covariance \mathbf{Q} (or model error variance), in order to reconstruct the 3-D optical property map of μ_{axf} , using the hybrid AEKF algorithm (Section 5.3.3). Reconstructions were performed using different initial guesses of μ_{axf} distribution and the parameter error covariance, \mathbf{P} . During all these reconstructions, the phantom was initially assumed to be homogeneous, and a constant value was set to the initial μ_{axf} distribution. Note that in all the reconstructions performed under varying experimental conditions, the reconstruction parameter was assumed constant and equal to the initial guess value of μ_{axf} in the cylindrical portion of the breast phantom, and reconstructions were only performed in the hemispherical portion of the breast phantom (3857 unknowns).

Inversions were carried out iteratively and the reconstructions were determined to have converged when (i) there was less than 1% additional decrease in root mean square output error (RSME), or when (ii) iterations had reached the maximum set limit (typically set to 50). The reconstructed unknown parameter's distribution was plotted in three-dimensional Tecplot 9.0 (Amtec Engineering Inc., Bellevue, WA), in order to determine the location of the target based on the μ_{axf} distribution. Quantitative analysis was also performed in order to determine the target size and location with better accuracy over the qualitative estimation from 3-D images.

To summarize the various parameters that were empirically chosen during 3-D image reconstructions, they included: (i) initial parameter error covariance matrix, \mathbf{P} , (ii) model error covariance matrix, \mathbf{Q} , and (iii) initial guess of the unknown reconstructing parameter.

Thus, employing the above described steps of the data analysis process, experiments were performed under various conditions. Details of the experimental plan in the current studies are described in the following section.

6.3 Experimental plan

The entire experimental plan is categorized into “preliminary studies” and “major studies” as shown in the flowchart (Figure 6.4). As a first step in the preliminary studies, the measurement precision and measurement accuracy were estimated, along with the effect of each referencing scheme (Φ_m/Φ_x or $\Phi_m/\Phi_{m,ref}$) as described earlier (Section 4.4). The feasibility of fluorescence-enhanced optical tomography using experimentally acquired measurements was demonstrated for the experimental cases when the target was present within the large phantom volume (Section 7), as a part of the preliminary studies. Feasibility studies were initiated using large target volumes of 1 cc and higher concentrations (micromolar) of the fluorescing agent (ICG). Having demonstrated the feasibility of performing fluorescence-enhanced optical tomography studies on large breast phantoms, further studies using smaller target volumes and lower ICG concentrations can be carried out. Following the feasibility studies on optical

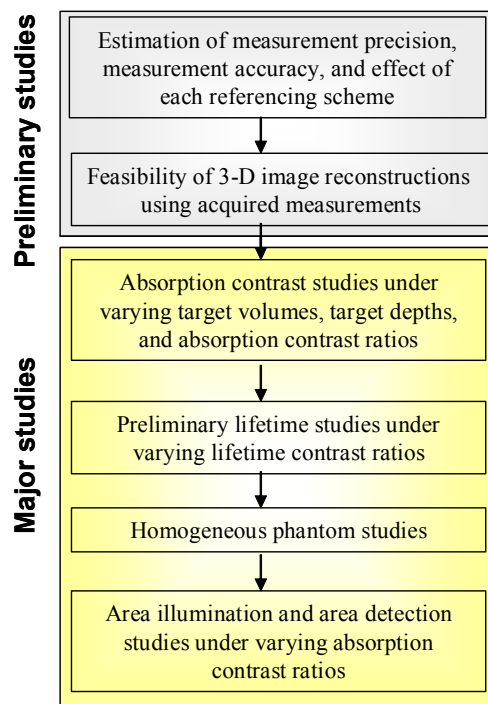


Figure 6.4 Outline of the broad research experimental plan.

tomography, experiments were performed under varying conditions, which are categorized as “major studies.”

The major studies in the experimental plan are divided into four categories. The first category involved absorption contrast studies, where the target:background optical contrast was based on the contrast in μ_{axf} . The second category involved lifetime contrast studies, where the target:background optical contrast was based on contrast in τ along with the contrast in μ_{axf} . Experiments were conducted under varying conditions of target volume, target depth, number of targets, and/or optical contrast ratios in each category. The third category involved homogenous phantom studies, where no target

was present within the large phantom and experiments were performed using uniformly distributed fluorescing agent in the entire phantom volume.

Apart from experimental studies performed using the current ICCD imaging system, studies were also performed on a parallel ICCD imaging system, which was based on the *area illumination and area detection* measurement geometry (fourth category), as a group effort. Details of each major study in the experimental plan are discussed below.

6.3.1 Absorption contrast studies

In the absorption contrast experiments, the varying parameters include the absorption contrast ratio (1:0 and 100:1), target depth (1-3 cms), target volume (0.5-1 cc), and number of targets (1-3) (see Figure 6.5).

In the *target depth studies*, the target depth was varied from 1 to 3 cms deep and experiments were performed under varying absorption optical contrast ratios of 1:0 and 100:1 (Section 8). Target depth studies were carried out using a single 1 cc volume target and micromolar concentrations of ICG, since these were the initial studies to determine how deep a large 1 cc volume target can be detected, before attempting to experiment using smaller volume targets and lower concentrations of the fluorescing agent (ICG). During the target depth studies, the feasibility of employing multiple simultaneous (dual, in our study) point illumination/point collection measurement geometry towards target detectability was also assessed.

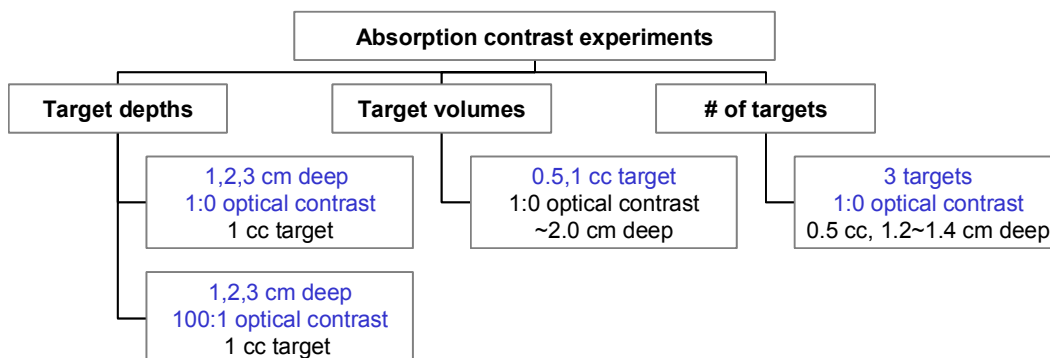


Figure 6.5 Experimental plan for absorption contrast studies.

Based on the results obtained from the target depth studies, the next parameter of interest was the target volume. In the *target volume studies*, the target volume was either 0.5 cc or 1 cc and was located up to 2 cm deep from the phantom surface, with an absorption optical contrast ratio of 1:0 (Section 9). The target depth and target volume studies focused on single 0.5 cc to 1 cc targets, and further studies involved the use of multiple targets.

In the *multiple target studies*, three targets of small volume (~ 0.5 - 0.6 cc) were located ~ 1.2 - 1.4 cm deep from the phantom surface, under an absorption optical contrast ratio of 1:0 (Section 9). Each study is explained in the following results and discussion sections (Sections 8 and 9). In all the absorption contrast studies, the lifetime contrast between the target and the background was maintained 1:1 or 1:0 based on the presence or absence of fluorescing agent in the background.

6.3.2 Lifetime contrast studies

In the lifetime studies, two fluorescing agents (ICG and DTTCl) that excite and emit fluorescent signals at similar wavelengths but differ in their lifetime and quantum efficiency were used. In these studies, the target volume and depth were fixed to 1 cc volume and 1 cm deep, respectively, with an absorption optical contrast ratio of 150:1 between the target and the background containing DTTCl and ICG or vice-versa (see Figure 6.4). A single target was used with a lifetime contrast of 2:1 and 1:2. Lifetime studies were preliminary in this work and were focused to demonstrate the extent of model match between experiments and simulations and not lifetime-based 3-D image reconstruction (Section 10). Future work will involve 3-D image reconstructions based on lifetime contrast along with more lifetime-based experiments with varying target volumes, depths, and number of targets (similar to the absorption contrast studies).



Figure 6.6 Experimental plan for lifetime contrast studies.

6.3.3 Homogenous phantom studies

Studies were also performed on homogeneous phantoms, containing no targets, in order to assess the ability of the optical imager and the reconstruction algorithm to locate no false targets (Section 11).

6.3.4 Area illumination and area detection studies

Unlike the experimental studies performed using point illumination and point detection measurement geometry in the current ICCD optical imager, experiments were performed by Thompson *et al.* using the area illumination and area detection geometry [51-52]. In his work, Thompson *et al.* demonstrated the model match between experiments and simulations, which were obtained by solving the forward problem using finite difference schemes (Section 12). In this study, the finite-element based forward problem of the coupled diffusion equations was developed for the area illumination and area detection ICCD imaging system, in order to demonstrate the model match between referenced measurements and simulations and eventually perform 3-D image reconstructions (performed by Dr. Roy).

Thus, the remaining major sections present the various studies described in the experimental plan and summarize the results obtained in each study.

7. MEASUREMENT PRECISION, ACCURACY, AND PRELIMINARY IMAGE RECONSTRUCTIONS

Determination of measurement precision and accuracy is important in understanding the quality of data that is generated using the current ICCD imaging system and also in verifying the mathematical model employed to predict the the light propagation in a scattering medium. In this chapter, measurement precision and accuracy of the fluorescence measurements are analyzed. The effect of both the referencing schemes (described in Section 4.4) with respect to the measurement accuracy is also assessed for determining a better way of referencing for all the future experimental studies. Finally, preliminary 3-D image reconstructions for two different experimental conditions with differing target:background absorption optical contrast is presented.

7.1 Measurement precision

Measurement precision assesses the repeatability or reproducibility of experimental data using the ICCD system under similar operating conditions. There are two approaches in determining the measurement precision, which include: (i) repeating an entire experiment performed under identical conditions and evaluating the precision with which the data was reproduced; or (ii) acquiring repeated data for a few point

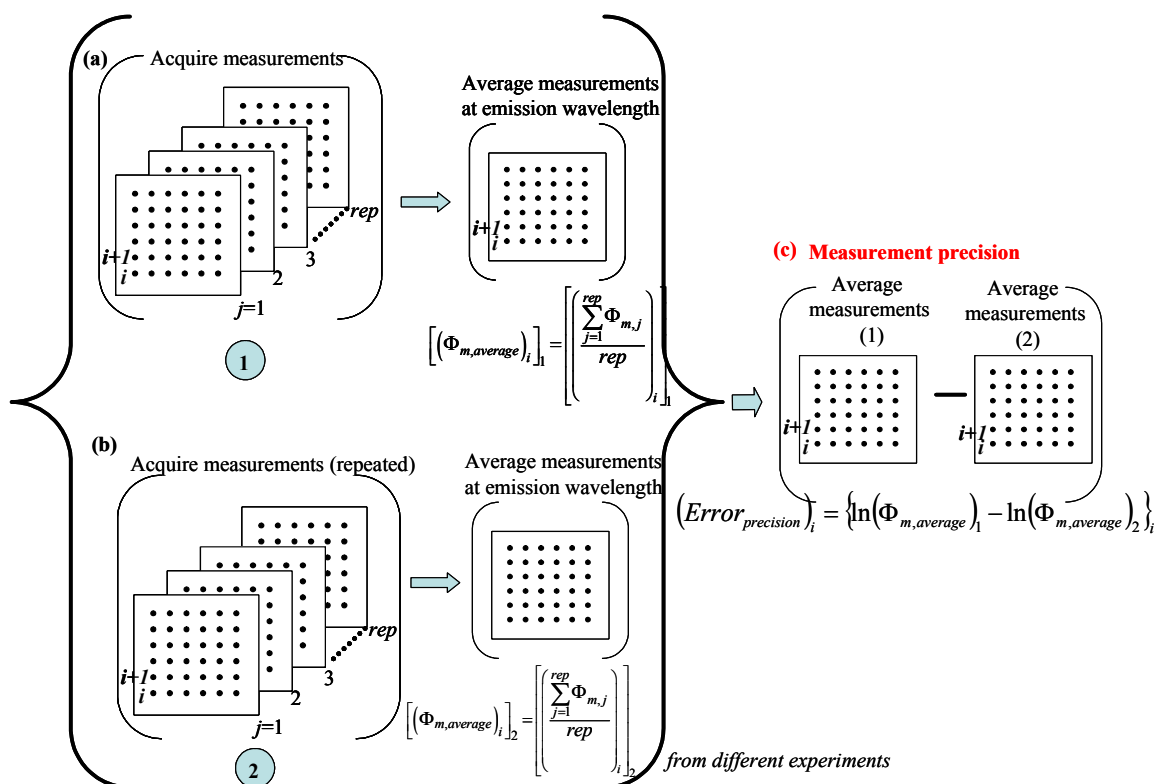


Figure 7.1 Schematic of the measurement precision analysis (a) acquiring repeated measurements and averaging the data at each pixel (i), (b) repeating the complete data acquisition procedure of (a) using the same point of illumination, and (c) determining the measurement precision between the two data sets (1,2) at each pixel (i).

source illuminations from different experimental studies. By employing the latter technique, a wide range of data sets at different experimental conditions can be obtained for evaluating the measurement precision of the ICCD detection system. In our case, the latter method was chosen for ease of acquiring the data, as well as using varied sample data sets. A schematic of the measurement precision analysis is given in Figure 7.1. Experiments performed absorption contrast studies were chosen as different data sets in order to determine the measurement precision. As a first step, fluorescence

measurements at each collection fiber location, i from the corresponding interfacing plate were acquired for different points of illumination, as repeated data sets of 5 or 10 (that is, $rep = 5$ or 10). The mean of these measurements in terms of AC and phase shift, or combined as fluence data $[(\Phi_{m,average})_i]_1$, were estimated from the 5 or 10 repeated data sets (Figure 7.1a). After acquiring measurements for different point illuminations, fluorescence measurements were also acquired the second time at one or two chosen points of illumination (Figure 7.1b), in order to repeat the data acquisition (5 or 10 repeated data sets) for these excitation sources. The means of measurements in terms of AC and phase shift, or combined as fluence data $[(\Phi_{m,average})_i]_2$, were also estimated for these measurements. The measurement precision was thus evaluated as the variance (σ^2) of the error (or difference) between the two average (or mean) fluence data at each measurement location (i), as

$$\left(Error_{precision} \right)_i = \sigma^2 \left\{ \ln(\Phi_{m,average})_1 - \ln(\Phi_{m,average})_2 \right\}_i \quad (7.1)$$

Measurement precision in terms of $\ln(AC)$ and phase shift (θ) is given by

$$\left(AC_{precision} \right)_i = \sigma^2 \left\{ \ln(AC_{average})_1 - \ln(AC_{average})_2 \right\}_i \quad (7.2)$$

$$\left(\theta_{precision} \right)_i = \sigma^2 \left\{ (\theta_{average})_1 - (\theta_{average})_2 \right\}_i \quad (7.3)$$

where, suffix 1 and 2 correspond to the first and second time that the same point of illumination was used to acquire the fluorescence measurements. In the measurement precision analysis, the data was not referenced, since the entire experiment was performed under similar conditions, with similar instrument effects during each experimental run. However, only those average measurements at each location (i) were considered whose modulation depth was > 0.05 . The measurement precision in $\ln(\text{AC})$ and phase shift (in degrees) for different detector measurements is shown in Figure 7.2 and 7.3 respectively. The mean (μ) and variance (σ^2) in the measurement precision of $\ln(\text{AC})$ and phase shift are provided in Figures 7.2 and 7.3, respectively.

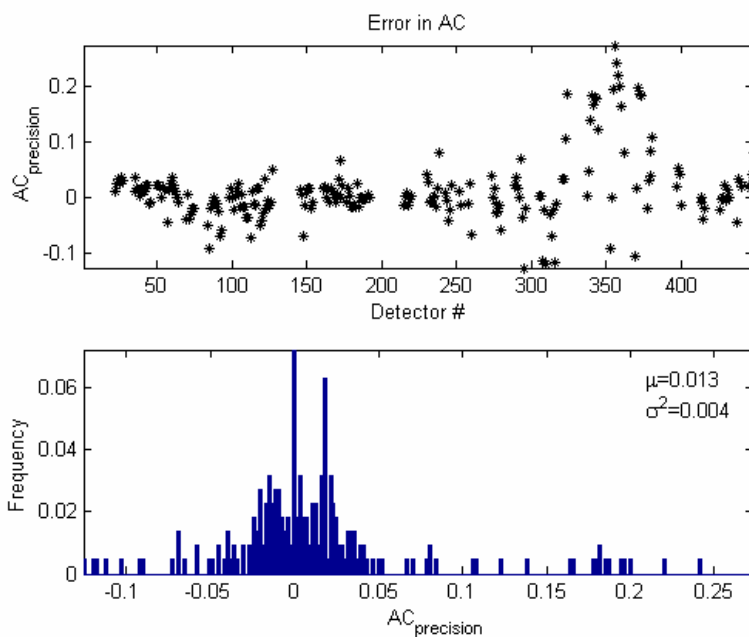


Figure 7.2 Measurement precision as variance between repeated AC measurements. Frequency (on y-axis) is defined as the probability distribution of the data points, μ is the mean and σ^2 is the variance of precision in AC.

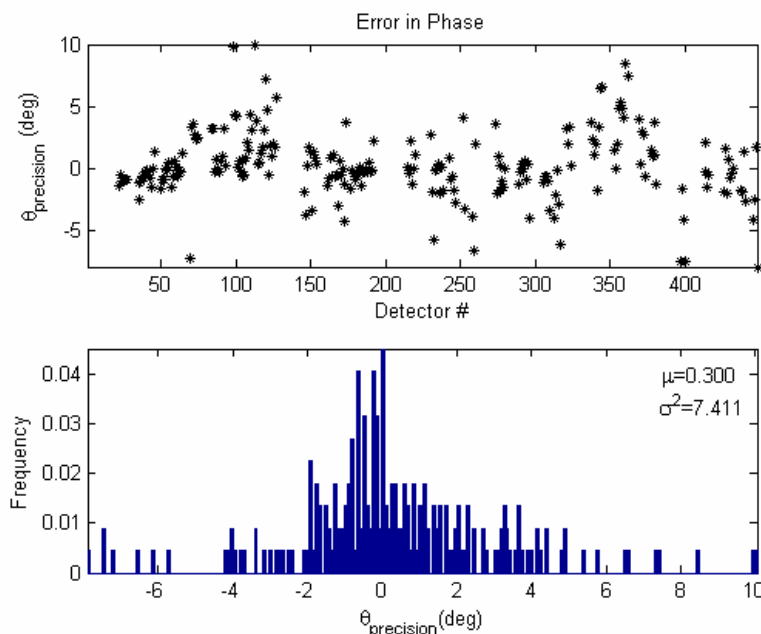


Figure 7.3 Measurement precision as variance between repeated phase measurements. Frequency (on y-axis) is defined as the probability distribution of the data points, μ is the mean (in deg) and σ^2 is the variance of precision in phase.

From the above figures, we observe that the mean of error in $\ln(AC)$ and phase shift are minimal. Here, only measurements with modulation depth > 0.05 were considered, since for very low modulation depths, the signal was at the noise floor and did not correspond to amplitude or phase data. Phase is a very sensitive parameter and fluctuates more than AC data. The variance of error was high for phase, since the deteriorating ICCD system started to show inconsistency in its performance upon its repeated use for various experiments. The range of modulation depths of acquired signal from the interfacing plate varied significantly, and this variation had a greater impact on the repeatability of the phase shift data over the AC data. The current ICCD imaging system lost its robustness during the course of the experimental studies, and

future work involves replacing the imaging system with a more robust and sensitive ICCD camera as a part of the future work.

7.2 Measurement accuracy (or model mismatch error) and effect of referencing schemes

The accuracy of the measurements with respect to a true model representing the light propagation is difficult to assess and hence the measurement accuracy in our case was in fact the “*model mismatch error*” that was determined by evaluating the difference between acquired referenced measurements and referenced simulated data (that is, model mismatch error), which was predicted from solving the forward problem (see Figure 7.4). The schematic provided in Figure 7.4 summarizes the model mismatch error analysis, which has been described in Section 6.2.2. The model mismatch error in terms of logarithmic AC ratio ($\ln(\text{ACR})$) and relative phase shift (RPS) are given by $\text{ACR}_{error} = \ln(\text{ACR})_{\text{expt}} - \ln(\text{ACR})_{\text{sim}}$ and $\text{RPS}_{error} = \text{RPS}_{\text{expt}} - \text{RPS}_{\text{sim}}$, respectively. Here, ACR and RPS are the referenced AC and phase shift obtained using one of the two referencing schemes (Φ_m/Φ_x or $\Phi_m/\Phi_{m,ref}$).

For the model mismatch error study, experiments were performed under conditions of imperfect uptake (100:1) and perfect uptake (1:0) of 1 μM ICG in the 1 cc target, which was located ~ 1 cm deep from the phantom’s hemispherical surface. Table 7.1 lists the optical properties of the target and the background, consisting of 1%

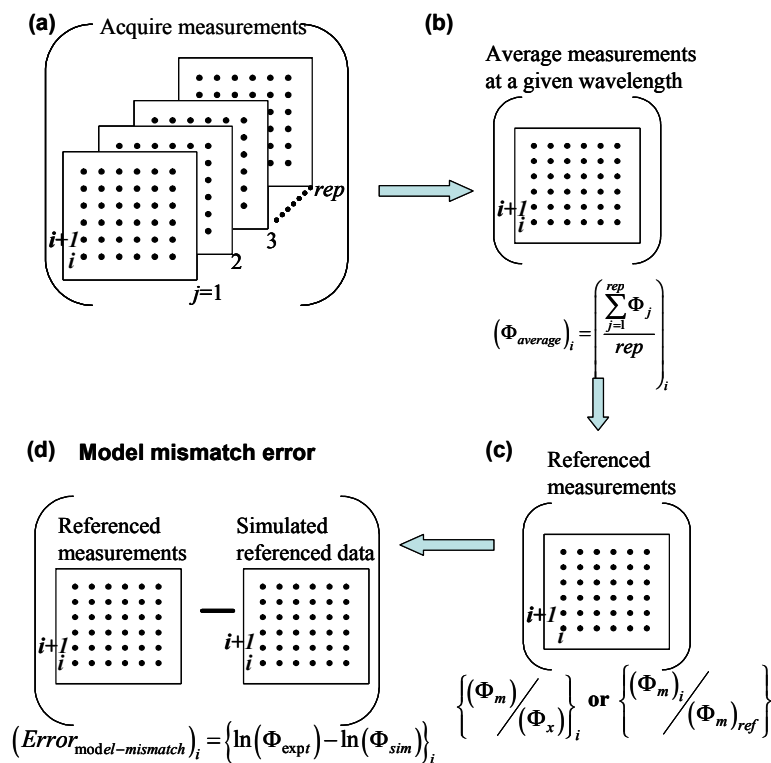


Figure 7.4 Schematic of the measurement accuracy analysis (a) acquiring repeated measurements (typically 5) at each pixel (i), (b) averaging the repeated measurements at each pixel (i), (c) referencing the averaged data at each pixel (i), and (d) determining the model mismatch errors between experimental and simulated data at each pixel or location (i).

Table 7.1 Optical properties of the target and the background in the 1:0 and 100:1 target:background absorption contrast experiments. One μM ICG was present in the single 1 cc target located 1 cm deep from the phantom surface. Reproduced with permission from ref [118]

Optical Properties (cm^{-1})		Perfect Uptake (1:0)		Imperfect Uptake (100:1)	
		Target	Background	Target	Background
Excitation	$\mu_{axf} + \mu_{axi}$	0.300+0.023	0.000 + 0.023	0.300+0.023	0.003 +0.023
	μ_{sx}	10.18	10.18	10.18	10.18
Emission	$\mu_{amf} + \mu_{ami}$	0.025+0.031	0.000 + 0.031	0.025+0.031	0.00025 + 0.031
	μ_{sm}	8.64	8.64	8.64	8.64

μ_{axf} , μ_{amf} – absorption coefficient due to the fluorophores at excitation and emission wavelengths, respectively
 μ_{axi} , μ_{ami} – absorption coefficient due to the chromophores at excitation and emission wavelengths, respectively
 μ_{sx} , μ_{sm} – reduced scattering coefficient at excitation and emission wavelengths

Liposyn solution and appropriate concentrations of ICG for both the perfect and imperfect uptake conditions [118].

A total of 768 measurements (using 7 point excitation sources) and 512 measurements (using 6 point excitation sources) were acquired at each of the excitation and emission wavelengths in the imperfect and perfect uptake experiments, respectively. On an average, the data acquisition time for the fluorescent signal was approximately 35 minutes for the 5 repeated data sets ($rep = 5$) acquired in each experimental case.

The effect of the two referencing schemes described in Section 4.4 (Φ_m/Φ_x or $\Phi_m/\Phi_{m,ref}$) on the measurement accuracy (or model match) was analyzed using both the experimental data sets.

7.2.1 Measurement accuracy using the first referencing scheme Φ_m/Φ_x

Model predictions poorly matched measurements when the excitation wavelength based referencing scheme (Equations (4.9) and (4.10)) was used for both the perfect (1:0) and imperfect (100:1) experimental data. A comparison plot of $\ln(\text{ACR})$ and RPS between measurements and predictions from the forward problem (for the imperfect uptake case) is shown in Figure 7.5a and 7.5b, respectively. Similar model mismatch in both the parameters ($\ln(\text{ACR})$ and RPS)) was observed for the perfect uptake experimental case as well. The predictions of both $\ln(\text{ACR})$ and RPS were highly biased (i.e. mean model mismatch error was far from zero) for both sets of

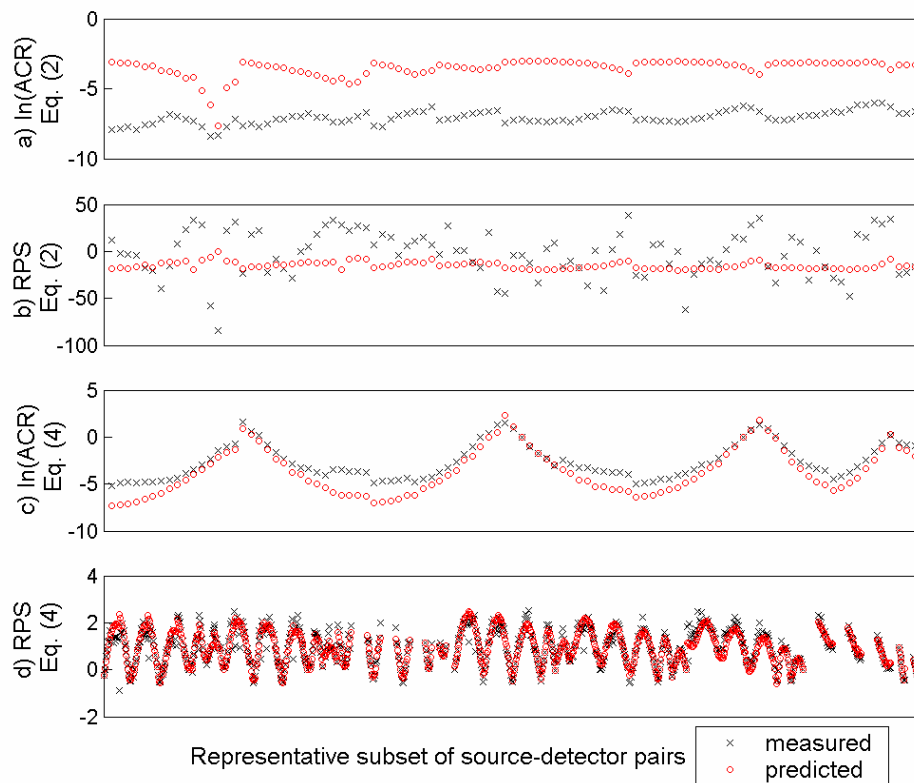


Figure 7.5 Comparison of model predictions with measurements for $\ln(\text{ACR})$ and RPS, shown for a representative subset of source-detector pairs in the imperfect uptake case, using first referencing scheme

$$\frac{\Phi_m}{\Phi_x} \quad (\text{a,b}) \quad \text{and} \quad \text{second referencing scheme} \quad \frac{\Phi_m}{\Phi_{m,\text{ref}}} \quad (\text{c,d}).$$

experimental data. In addition, the range of simulated RPS values was lower than that of the measured RPS values, resulting in high model mismatch error variance for RPS.

These large errors are believed to occur due to the unaccountable wavelength-dependency of the image intensifier under the current operating conditions. The characteristics of the image intensifier provided by the manufacturer were insufficient to accurately characterize the wavelength dependency of the image intensifier over the

voltage ranges it was operated at (for more details on the wavelength dependency of the image intensifier, see Appendix C). Hence, no good match was obtained between measurements and forward model predictions when the above referencing method, Φ_m/Φ_x (given by Equations (4.9) and (4.10)) was used.

7.2.2 Measurement accuracy using the second referencing scheme $\Phi_m/\Phi_{m,ref}$

Upon employing the second referencing scheme utilizing designated reference collection point at the emission wavelength, $\Phi_m/\Phi_{m,ref}$ (Equations 4.11 and 4.12), a better match between model predictions and acquired measurements was observed for both the experimental data sets (see Figure 7.5c and 7.5d for comparison plots in the imperfect uptake case). Similar model match in terms of $\ln(\text{ACR})$ and RPS was observed for the perfect uptake case as well. The histograms of the model mismatch error for the two experiments given in Figure 7.6 show that the RPS exhibited relatively low bias and variance. Model error for $\ln(\text{ACR})$ showed larger bias and variance than RPS (Figure 7.5c-d, Figure 7.6), but was less biased compared to that obtained when referencing to excitation light (Figure 7.5a). The large model mismatch errors in $\ln(\text{ACR})$ could possibly be due to an image retention effect in the image intensifier of the ICCD system that tended to affect the AC data but not the phase shift data. An additional source of error for both $\ln(\text{ACR})$ and RPS may arise from the assumption that the lengths of all the collection fibers were identical. However, the actual lengths in the current experimental

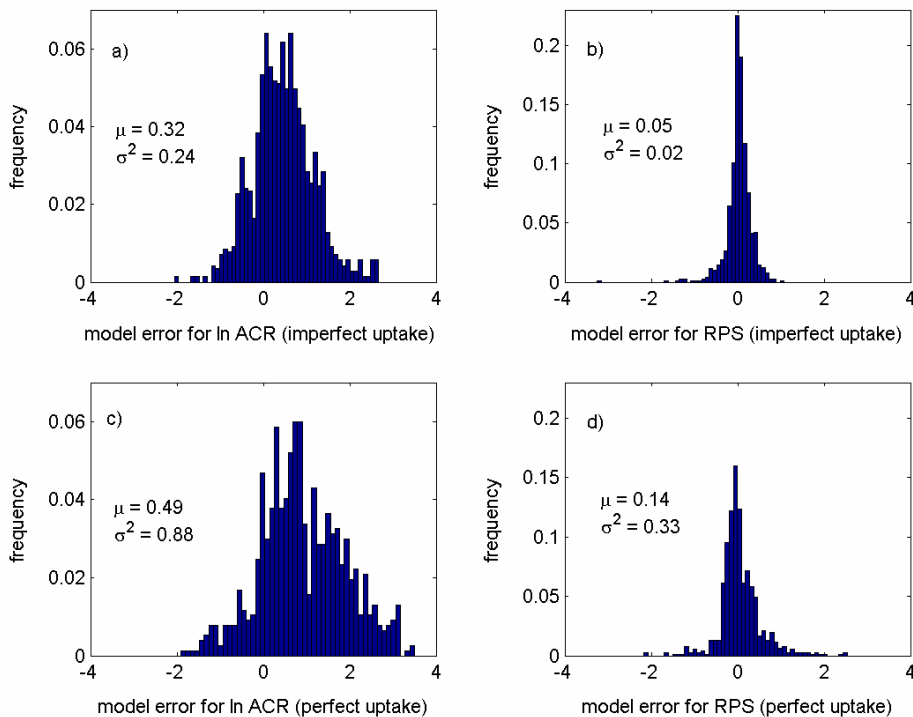


Figure 7.6 Histograms of model mismatch error for the two experiments, using the second referencing method $\Phi_m / \Phi_{m,ref}$, for a) ln(ACR), imperfect uptake, b) RPS, imperfect uptake (in radians), c) ln(ACR), perfect uptake, d) RPS, perfect uptake (in radians). Frequency is the probability distribution of the measurements, μ is the mean and σ^2 is the variance in ACR and RPS model mismatch errors.

set-up varied to a small extent. Because of the relatively unbiased model error and highly reduced model error variance for RPS using the second referencing method relative to the first referencing method, reconstructions were performed using the referenced data from the second referencing scheme.

If accurate determination of the wavelength dependence of the image intensifier becomes available, the first referencing method, Φ_m / Φ_x may ultimately prove to be the method of choice as observed by other researchers via experimental and simulated

studies [17, 92]. However, because of the reduced model mismatch error, especially in RPS, obtained using the second referencing method ($\Phi_m / \Phi_{m,ref}$) in comparison to the first referencing method (Φ_m / Φ_x), the remainder of the experiments reported here employed the second referencing scheme to determine the extent of model match as well as for to perform 3-D image reconstructions.

7.2.3 Effect of refractive index mismatch parameter on measurement accuracy

The refractive-index mismatch parameter in the boundary condition of the light propagation model, namely the diffusion equation, can possibly impact model prediction of measurements and therefore image recovery, as observed from earlier studies [104].

Here, the effect of incorporating different R_{eff} values in the partial current boundary condition of the forward problem was investigated in order to analyze the effect of R_{eff} value on the model match between referenced fluorescence measurements and referenced simulated measurements. Details of the refractive index mismatch parameter (R_{eff}) and its relation to the Fresnel's reflections and hence the boundary condition of the forward problem was described in Section 4.5.2.

Herein, solutions of the coupled diffusion equations with three different values of γ (or R_{eff}) in the partial current boundary conditions were used to study the effect of choosing refractive index parameter on forward model predictions. The three cases (Figure 7.7) include: (i) Case 1 in which the value of R_{eff} for an air-phantom interface

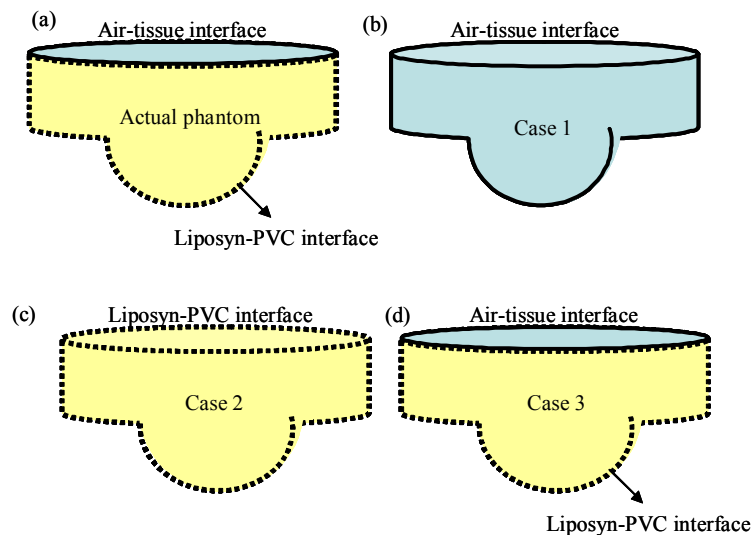


Figure 7.7 Different cases of R_{eff} approximations in the partial current boundary condition of the coupled diffusion equations (a) actual phantom with air-tissue interface at circular boundary surface, and Liposyn-PVC interface at the remaining boundary surfaces, (b) Case 1: approximating all boundary surfaces with air-tissue interface, (c) Case 2: approximating all boundary surfaces with Liposyn-PVC interface, and (d) Case 3: using the actual phantom case described in (a).

was chosen for all the interfaces of the phantom ($R_{eff} = 0.4311$) (Figure 7.7b); (ii) Case 2 in which the value of R_{eff} for the Liposyn-PVC interface was chosen for all six interfaces ($R_{eff} = 0.0282$) (Figure 7.7c); and (iii) Case 3 in which the values of R_{eff} corresponded to the actual phantom interfaces (Figure 7.7a and d) (used in Sections 7.2.1 and 7.2.2).

Histograms of the errors between experiments and simulations using the three cases are shown for the emission data for the perfect uptake case and the imperfect uptake case in Figures 7.8 and 7.9, respectively. From these histograms, we observe that there is a small variation in the predicted ACR and RPS values when different values of the refractive index parameter are considered, but the differences were not significant

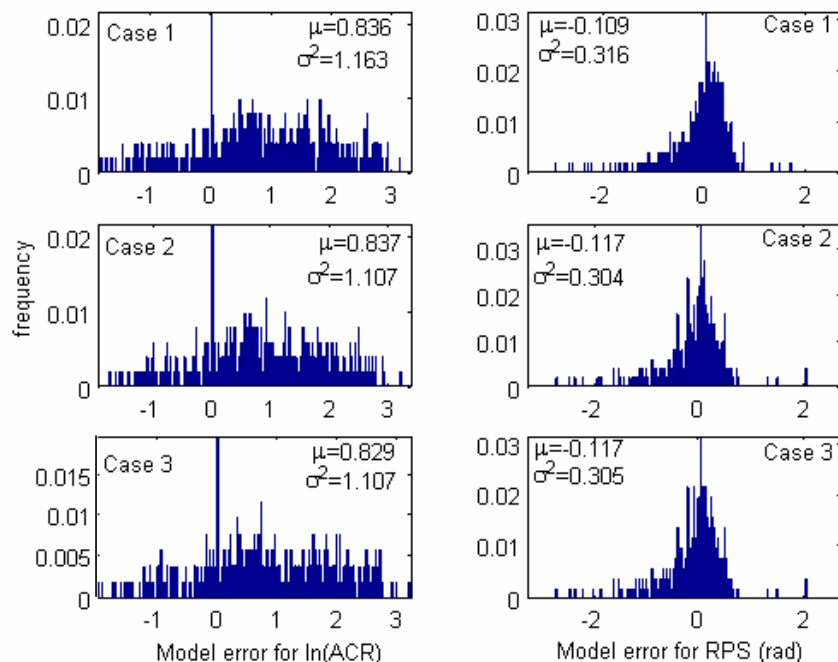


Figure 7.8 Effect of refractive index parameter in perfect uptake data at emission wavelength. (a), (b) correspond to Case 1; (c), (d) correspond to Case 2; and (e), (f) correspond to Case 3 of the three different R_{eff} cases. Frequency is the probability distribution of the data points, μ is the mean and σ^2 is the variance of ACR and RPS model mismatch errors.

enough to reduce the model mismatch between experiments and simulations at both the excitation and emission wavelengths. The results obtained in this study are in contradiction to those obtained from our phantom studies using slab geometry ($4 \times 8 \times 8$ cm^3 volume) [104]. In the slab-shaped phantom, the refractive index affected the simulations on transillumination side of the phantom. In other words, when the phantom was illuminated by a point source on the 8×8 cm^2 , the three cases of R_{eff} values affected the simulations on the opposite 8×8 cm^2 side (i.e. transillumination side) of the phantom (see Figure 7.10).

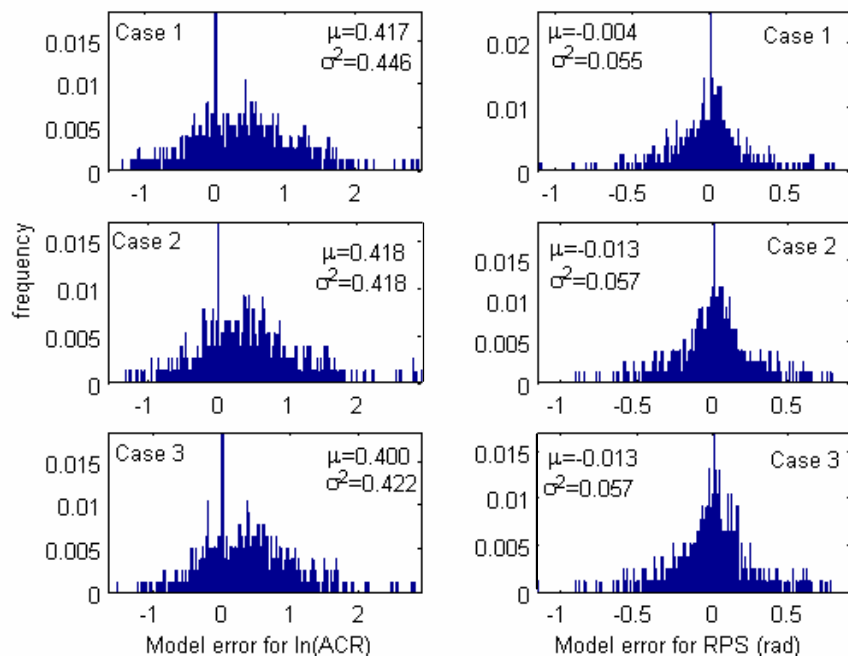


Figure 7.9 Effect of refractive index parameter in imperfect uptake data at emission wavelength. (a), (b) correspond to Case 1; (c), (d) correspond to Case 2; and (e), (f) correspond to Case 3 of the three different R_{eff} cases. Frequency is the probability distribution of the data points, μ is the mean and σ^2 is the variance of ACR and RPS model mismatch errors. Reproduced with permission from reference [119].

In our current cup-shaped phantom, there is no distinct transillumination side on the hemispherical surface, and the maximum depth of penetration is 10 cm against 4 cm penetration in the slab geometry. The illuminating source light reaches the noise floor before light reaches the opposite side of the illuminating point, making the refractive index an insignificant parameter for a noisy weak signal in a large curvilinear phantom. In addition, greater measurement errors could possibly mask the effect of the slight variations in the simulated data under the three different R_{eff} cases [119].

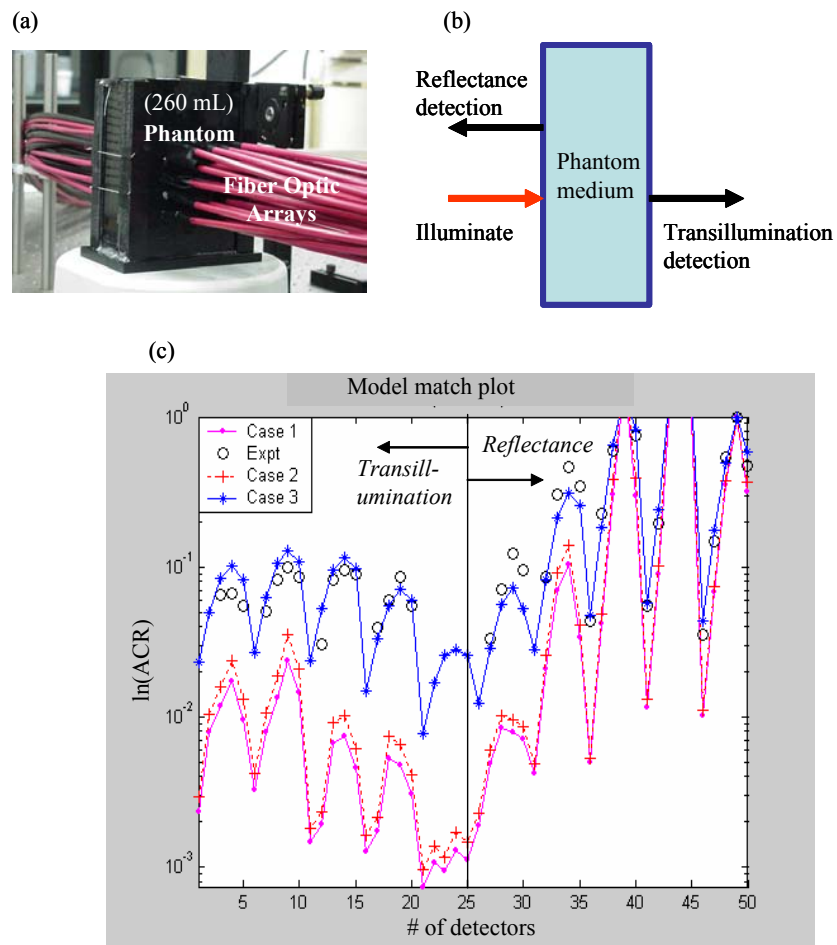


Figure 7.10 Model match of $\ln(\text{ACR})$ between experiments and simulations obtained using the three cases of the R_{eff} values in the slab phantom studies. Reproduced with permission from [104].

In summary, the effect of refractive index parameter depends on the shape and size of the phantom, especially in terms of its depth of penetration and sharp boundary edges. The greater the depth of the phantom and lesser the number of sharp boundaries, the smaller the effect of R_{eff} parameter in the boundary condition of the forward model.

Hence, for the breast phantom employed here, any reasonable choice of the R_{eff} value should not impact the simulated data from the forward model significantly.

7.3 Image reconstructions

For image reconstructions, individual referenced measurements with modulation depth < 0.025 were neglected, in order to minimize the propagation of errors into the inversion scheme while speeding up the reconstructions. This reduced the data sets to a total of 429 emission measurements for the imperfect uptake case and 207 emission measurements for the perfect uptake case. These referenced measurements (using the second referencing method, $\Phi_m / \Phi_{m,ref}$) were used along with the estimates of measurement error covariance \mathbf{R} and model error covariance \mathbf{Q} in order to reconstruct the 3-D optical property map of μ_{axf} , using the inversion algorithm described in Section 5.2. The measurement error covariance \mathbf{R} was evaluated from the measurement error in $\ln(\text{ACR})$ and RPS, plotted as histograms in Figure 7.11 [118]. The model error variance was approximated to be spatially variant by scaling the inverse of the modulation depth (i.e. DC/AC) for $\ln(\text{ACR})$ and for RPS, so each \mathbf{Q}_i (i measurements) is also spatially variant and distinct. Initial parameter error variance was empirically set to 0.1.

Low and spatially variable signal to noise ratios (SNR) in fluorescence emission data were thus accommodated by filtering out low SNR data at three levels (see Figure 7.12), as follows: (i) source level: point source locations were limited to those which elicit an average modulation depth greater than 0.1 for each interfacing plate, (ii)

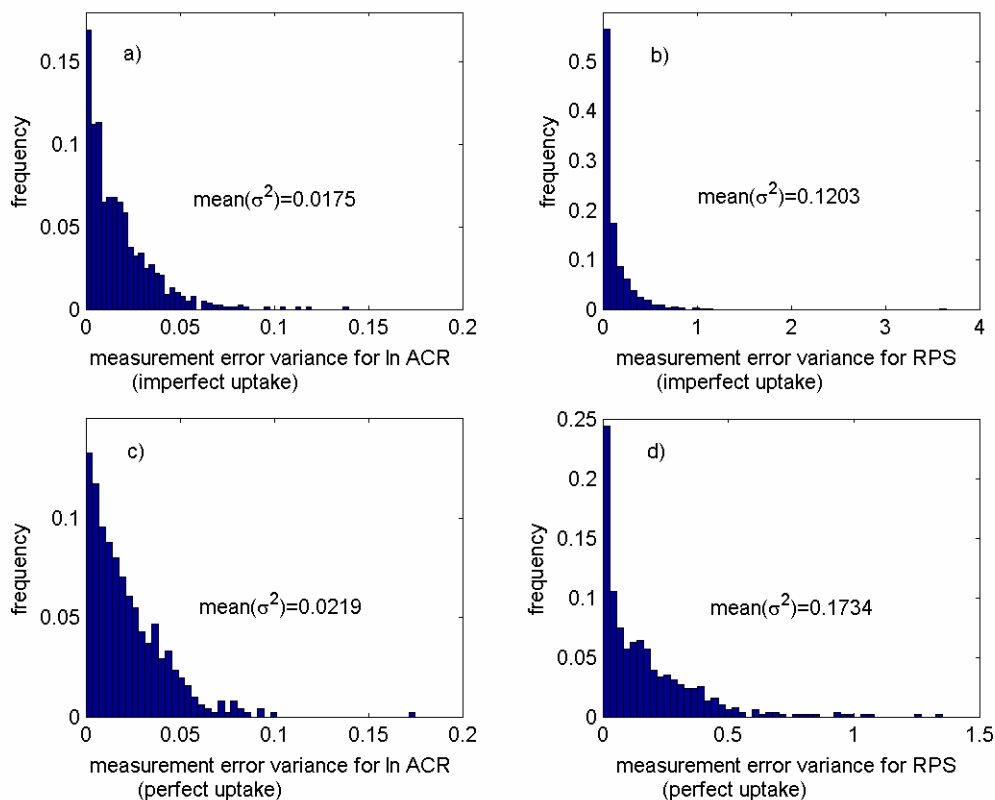


Figure 7.11 Histograms of measurement error variances for all measurements (referenced as shown in Equation (4) with modulation depth > 0.025 for a) $\ln(\text{ACR})$, imperfect uptake, b) RPS, imperfect uptake (in radians), c) $\ln(\text{ACR})$, perfect uptake, d) RPS, perfect uptake (in radians). Frequency is the probability distribution of the data points, μ is the mean and σ^2 is the variance of ACR and RPS measurement errors.

detector level: only those detected emission measurements with individual modulation depth greater than 0.025 were used in the inversion, and (iii) update level: parameter updates were weighted in a spatially-variant manner based on the observed variance and inverse modulation depth of each measurement. The model mismatch was larger for those source-detector pairs whose modulation depth was very small (< 0.025), as shown in Figure 7.13 (for the AC data). A similar trend was observed for the effect of

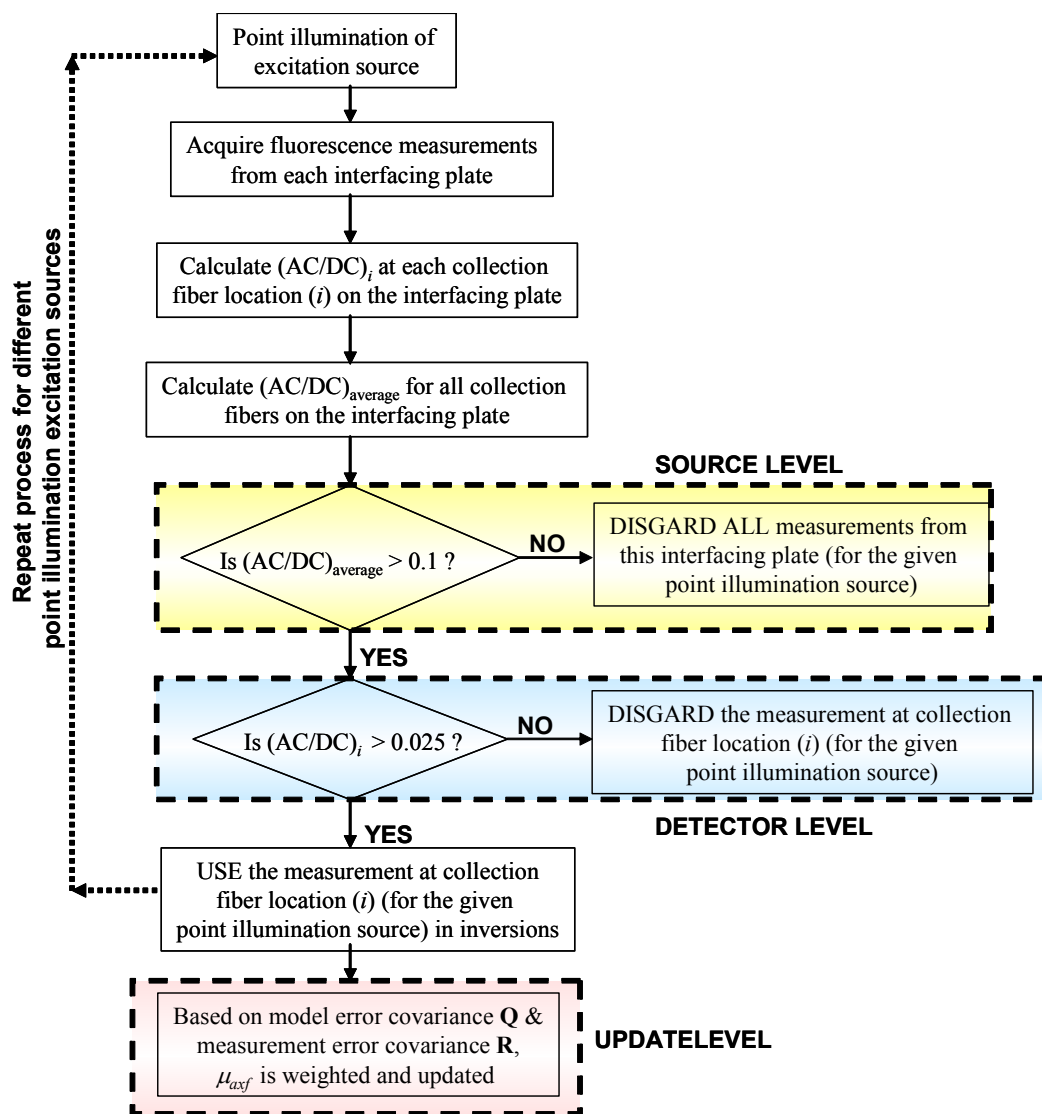


Figure 7.12 Flowchart for filtering out low signal-to-noise measurements at three levels: source level, detector level, and parameter update level.

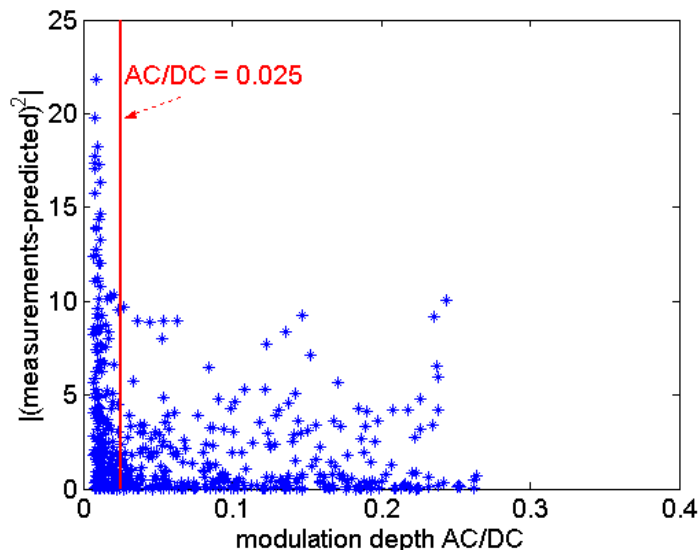


Figure 7.13 Model plot of the effect of modulation depth on model mismatch between experiments and simulations of AC data.

modulation depth on the model match of phase data. Hence, only those measurements were included in the reconstruction algorithm whose modulation depth was greater than 0.025 at the detector (that is, collection point) level. The advantages of pre-filtering the measurements for performing reconstructions include: (i) improvement in the convergence of the reconstructions and generation of minimal artifacts, since measurements with significant errors were excluded; and (ii) improvement in the computational efficiency, in terms of memory requirements (small matrices) and computational speed (fewer calculations for the Jacobian sensitivities and smaller matrices to invert).

For both the experimental data sets, the initial guess in μ_{axf} was 0.003 cm^{-1} for the entire phantom volume. Histograms of the differences in signal between model

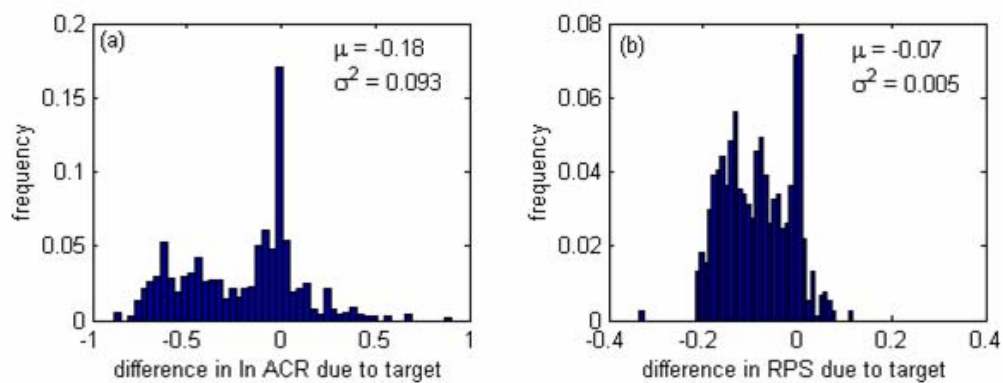


Figure 7.14 Histograms of differences in model predictions with and without the fluorescent target, assuming background fluorescence absorption of 0.003 cm^{-1} , for a) $\ln(\text{ACR})$, b) RPS (in radians). Frequency is the probability distribution of the data points, μ is the mean and σ^2 is the variance.

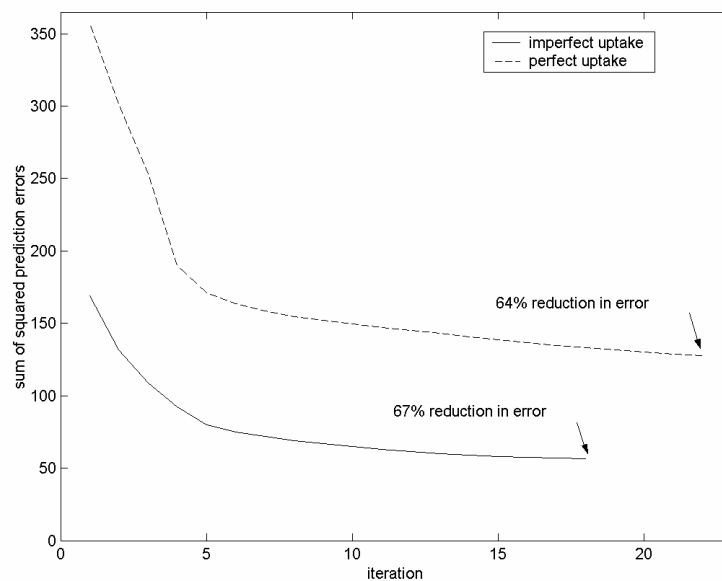


Figure 7.15 Convergence curves of sum of squared prediction errors for the two reconstructions.

predictions with and without the fluorescent target are shown in Figure 7.14, and are a measure of the signal information available for reconstruction of the target. Comparing these frequency distributions of the small signal change arising due to the presence of a target, with respect to the non-trivial model mismatch error (Figure 7.6) and measurement error (Figure 7.11), the overall signal-to-noise ratio (SNR) appears to be low for both the perfect (1:0) and imperfect (100:1) experimental data sets. Nonetheless, both reconstructions converged smoothly (Figure 7.15).

The target location was identifiable after the first iteration (4-7 minutes) and the inversions converged (exhibited less than a 1% decrease in model prediction error) after 22 iterations (1.4 hours) and 18 iterations (2 hours), for the imperfect and perfect uptake cases, respectively, on a 2.2 GHz Pentium IV. The iso-surfaces at 0.2 cm^{-1} for 3-D phantom containing the actual target (i.e. the known target in the actual experimental set-up), for the 3-D reconstructed phantom in the imperfect uptake case, and the 3-D reconstructed phantom in the perfect uptake case are plotted in Figures 7.16a,b,c, respectively. The figures are 3-D plots of the absorption coefficient due to the fluorophore (μ_{axf}) in the breast phantom, where iso-surface cut-off value was set to $\mu_{axf} = 0.2 \text{ cm}^{-1}$, in order to discriminate the region of interest (i.e., the target in this case) from the background. All nodes with estimates above the arbitrary cutoff of $\mu_{axf} > 0.2 \text{ cm}^{-1}$ were considered elevated. These nodes were then spatially clustered into distinct targets and each target was characterized by volume-integrated fluorescence absorption (volume-weighted averages of nodal μ_{axf} within each identified target), value-weighted centroid locations, and Euclidean distance of the identified centroid from the location of

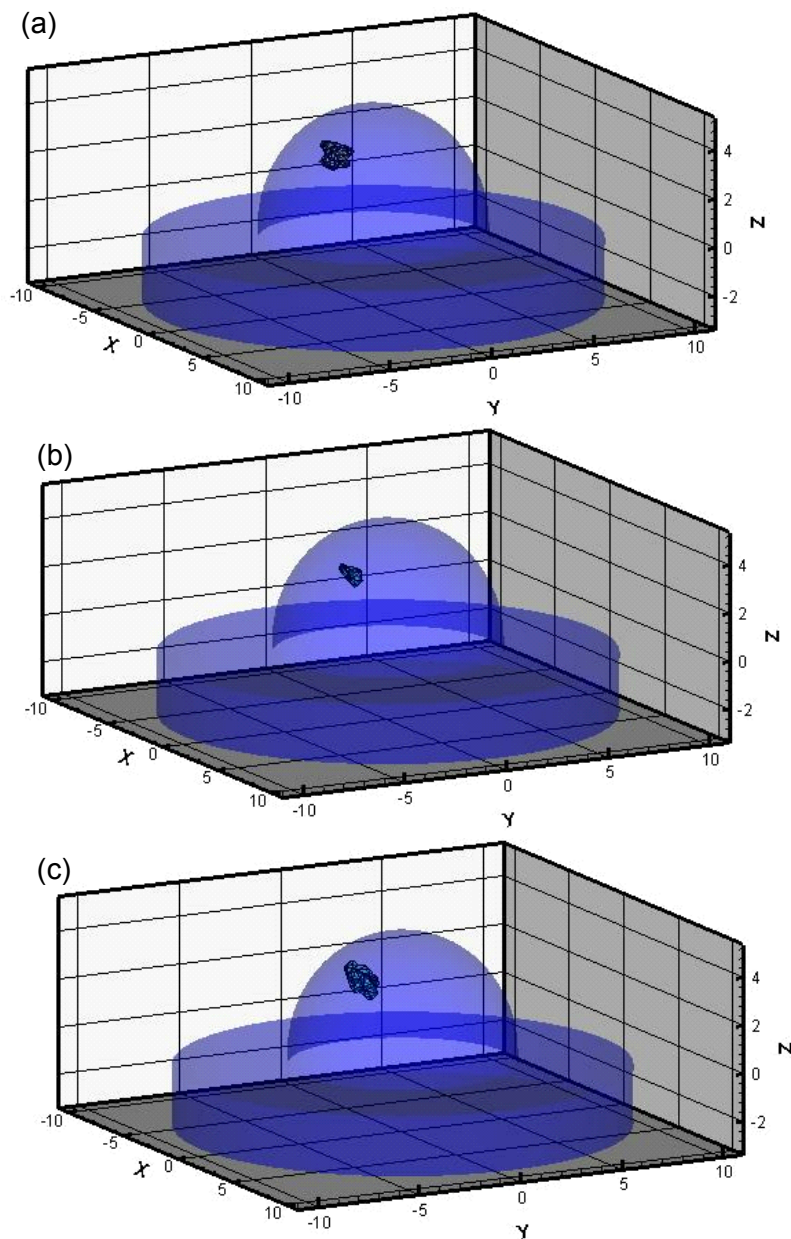


Figure 7.16 (a) The true fluorescence absorption distribution in the 3-D phantom containing the actual target. In both experiments, the value of the absorption coefficient due to fluorophore (μ_{axf}) in the actual target was 0.30 cm^{-1} . The background μ_{axf} value was 0.003 cm^{-1} and 0.000 cm^{-1} in the imperfect and perfect uptake case, respectively. (b) The fluorescence absorption distribution in the 3-D reconstructed phantom for the imperfect uptake case, with iso-surface shown at $\mu_{axf} = 0.2 \text{ cm}^{-1}$. (c) The fluorescence absorption distribution in the 3-D reconstructed phantom for the perfect uptake case, with iso-surface shown at $\mu_{axf} = 0.2 \text{ cm}^{-1}$.

Table 7.2 Centroid locations and integrated values of areas where fluorescence absorption (μ_{axf}) was greater than 0.2 cm^{-1} for the imperfect and perfect uptake experiments using a 1 cc target located $\sim 1 \text{ cm}$ deep from phantom surface.

Expt	Heterogeneity	Centroid			Distance off (cm)	Integrated μ_{axf} (cm^{-1})	Volume (cm^3)
		x (cm)	y (cm)	z (cm)			
Known phantom	Actual target	-2.50	-0.50	2.50	--	0.30	1.00
Imperfect uptake	Identified target	-2.04	-0.74	2.45	0.52	0.14	0.38
Perfect uptake	Identified target	-2.30	-0.73	2.60	0.32	0.43	0.69

the true centroid of the target. A single target was identified in both the imperfect and perfect uptake reconstructions (Figures 7.16b,c), located only 0.52 cm and 0.32 cm, respectively, away from the actual target location. These reconstructions are quantified in Table 7.2 for completeness. In Table 7.2, *volume* is defined as the sum of volumes associated with each node in the target. The volume information was used to estimate the volume-integrated fluorescence absorption of the reconstructed target. The Euclidean distance between the value-weighted centroids of the predicted and actual target location was also determined and termed as *distance-off*. The target volumes were underestimated in both cases, although this value is dependent on the arbitrarily chosen iso-surface value that defines the target boundary. The quantitative estimate of integrated fluorescence absorption was underestimated in the imperfect case, and overestimated in the perfect uptake case (Table 7.2). Choice of specific reference nodes affected the quantitative results and presence or absence of artifacts, although the target

was consistently identified. Most of this section is reproduced with permission from our published work in reference [118].

The discrepancies between the actual target (in terms of size and location) and the reconstructed targets in both the experimental cases could possibly be due to (i) sparse and noisy experimental data, (ii) measurement and model errors due to the experimental set-up and discretization of the phantom mesh, respectively, (iii) experimental error in terms of positioning the target at the specified location, and/or (iv) non-optimal choices for control variables in the inversion, such as initial parameter variance.

7.4 Summary

Measurement precision, measurement accuracy, and the effect of referencing schemes and the refractive-index mismatch parameters were analyzed for the current ICCD imaging system. Initial experiments performed using large breast-shaped tissue-mimicking phantoms exhibited a much better model match with a finite element implementation of the coupled diffusion equations when emission measurements were referenced to specified detectors at the emission wavelength rather than when they were referenced to excitation measurements at each detector location. Despite the low and spatially-variable signal to noise ratio (SNR), the 1 cc fluorescent target containing 1 μM ICG was identified in the correct location in the 3-D reconstructions of fluorescence absorption for both imperfect (100:1) and perfect uptake (1:0) cases, although the estimates were not quantitatively accurate.

Further experiments using the existing prototype imaging system were performed involving data acquisition and reconstructions using single and multiple targets at various depths, volumes, and levels of fluorescent contrast, in order to assess the robustness of the ICCD optical imager. Lifetime studies were also performed by exploiting the advantages of a frequency-domain imaging system over a CW system, where the enhanced phase contrast due to the differences in lifetime between the target and the background can be measured. Although it is encouraging that useful images can be reconstructed with low SNR, greater improvements in the data acquisition technology will be needed to further reduce the noise level.

8. DEPTH STUDIES USING SINGLE AND DUAL POINT ILLUMINATION GEOMETRIES

Fluorescence-enhanced optical tomography is typically performed using point illumination and point collection measurement geometry. For large phantoms with greater volumes or penetration depths, single point illumination may be insufficient to illuminate greater volumes and also provide a strong fluorescent signal. In this section, use of multiple point illumination geometry is proposed for acquiring higher number of strong fluorescent measurements, due to greater volume illumination. As a preliminary study, use of two point illuminations was attempted, in order to acquire surface measurements and perform three-dimensional reconstructions. Experiments were performed using different target depths (1-3cm deep) and contrast ratios (1:0 and 100:1), in order to evaluate the effect of using double point illumination measurement geometry in comparison to the widely used single point illumination measurement geometry. Three-dimensional reconstructions performed from measurements acquired using the dual point illumination geometry are presented for the first time along with the reconstructions performed from measurements acquired using the single point illumination geometry.

The current studies performed at varying target depths will also help determine the maximum depth of the target which can be reconstructed accurately, and thus analyze the limitations of the imaging system in terms of depth reconstruction.

8.1 Dual point illuminating imaging system

For small animal studies involving rats or for phantom studies (which are either small in volume or less deep), sufficient fluorescence generation and collection across the depth of the entire phantom is possible with sequential illumination at single boundary points. Consequently three-dimensional reconstruction of the target location and size is feasible with the point illumination measurement geometry [13-17, 84]. However, in studies involving large phantoms of greater volumes and penetration depths, single point illumination of the phantom surface may be insufficient to generate a fluorescent signal that arises throughout the entire phantom with a sufficient signal-to-noise ratio (SNR). Weak fluorescent signals are usually dominated by noise, thus impacting the measurement precision and accuracy, and eventually hindering the accurate reconstruction of the target location and size.

Here, we explore the feasibility of using simultaneous multiple point illumination measurement geometry in order to increase the volume of illumination, and the total number of fluorescent measurements with robust SNR. As a preliminary study towards applying the multiple point illumination geometry, initial studies are performed using dual point illumination geometry for different experimental conditions. In the past, researchers employed dual excitation sources that were 180° out-of-phase (destructive interfering photon density waves) for 2-D spatial localization of an absorbing (or fluorescing) target located in a 3-D phantom [120-124]. However, in the current work, surface fluorescence measurements obtained from dual excitation sources that are in-

phase (0° phase difference between the two modulating point sources) are used to reconstruct the target location and size in three dimensions.

8.1.1 Instrumentation for the dual point illuminating imaging system

The instrumentation of the dual point illuminating (or dual point excitation source) imaging system is similar to that described in Section 4.2, with a slight modification that the modulated excitation light source was split into two equal intensity (1:1 ratio of the normalized intensities) in-phase (0° phase difference between the two modulating point sources) light sources, using a 50:50 beam splitter (20Q20BS.2, Newport Corp., CA), in order to generate constructively interfering point sources. The schematic of the dual point illuminating imaging system is illustrated in Figure 8.1.

8.1.2 Experimental parameters

Experiments were performed under target:background absorption contrast ratios of 1:0 and 100:1 using a single 1 cc target ($1 \times 1 \times 1 \text{ cm}^3$) located 1 to 3 cm deep from the phantom surface. Measurements were acquired using both the single point and dual point illumination geometry. The list of experiments performed for the depth study are provided in Table 8.1, which includes the details about the total number of measurements acquired and the number of point illumination (or excitation source) combinations used for different experimental conditions. In the case of dual point illumination geometry, the number of source combinations corresponded to the total number point source pairs that illuminated the phantom; and in the case of single point

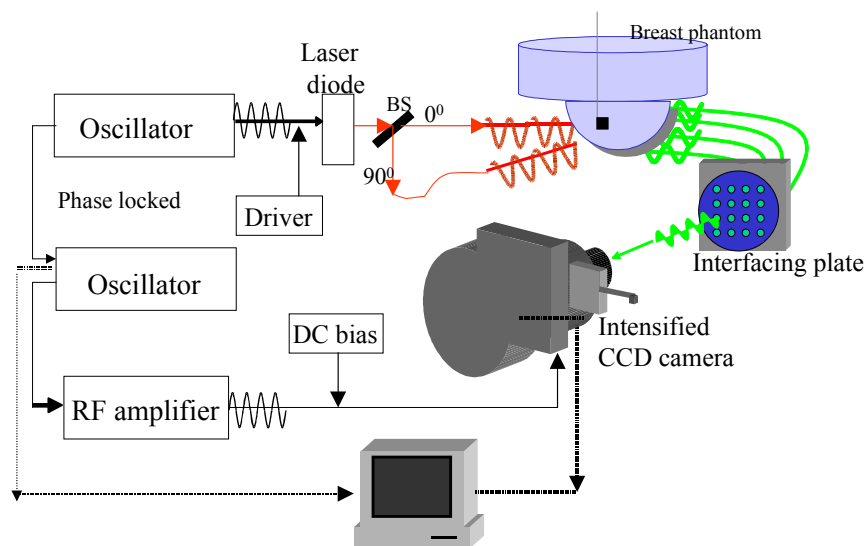


Figure 8.1 Instrument setup for dual point illuminating ICCD imaging system.

point illumination geometry, the number of source combinations corresponded to the total number of single point sources that illuminated the phantom.

Fluorescent measurements were acquired at single and dual point illumination configurations, where the average fluorescent signal of each interfacing plate, quantified in terms of the average modulation depth (AC/DC) was greater than 0.1 (value chosen based on the modulation depth of noise floor observed during experimentation). For all the target depth experiments, the point sources used in the single point illuminating imaging system were used in different combinations to obtain dual point illuminations, thus increasing the total number of measurements. The optical properties of the target and the background for different experimental cases are provided in Table 8.2.

Table 8.1 Experimental conditions towards target depth studies at various absorption optical contrasts and using two different measurement geometries.

Expt	Absorption optical contrast	Target depth (cm)	Measurement geometry	# of acquired measurements	# of source combinations	# of measurements used in reconstructions
1	1:0	1	Dual sources	832	13	439
2	1:0	1	Single sources	320	5	126
3	1:0	2	Dual sources	1408	22	773
4	1:0	2	Single sources	512	8	188
5	1:0	3	Dual sources	1152	18	-
6	1:0	3	Single sources	576	9	-
7	100:1	1	Dual sources	1216	19	964
8	100:1	1	Single sources	704	11	401
9	100:1	2	Dual sources	1600	25	1163
10	100:1	2	Single sources	896	14	480
11	100:1	3	Dual sources	1280	20	1025
12	100:1	3	Single sources	768	12	480

Table 8.2 Optical properties of target and background for different contrast ratio experiments and for all the target depth studies. One μM of ICG was used in the target, with 0 and 0.001 μM ICG in the background, for the perfect and imperfect uptake cases, respectively, and for all the target depths.

Optical Properties (cm^{-1})		Perfect Uptake (1:0)		Imperfect uptake (100:1)	
		Target	Background	Target	Background
Excitation	$\mu_{axf} + \mu_{axi}$	0.300+0.0248	0.000+0.0248	0.300+0.0248	0.003+0.0248
	μ_{sx}	10.88	10.88	10.88	10.88
Emission	$\mu_{amf} + \mu_{ami}$	0.050+0.0322	0.000+0.0322	0.050+0.0322	0.0005+0.0322
	μ_{sm}	9.82	9.82	9.82	9.82

The acquired fluorescence measurements of AC and phase shift from collection fibers mounted on each interfacing plate and for each excitation source combination were referenced with respect to the collection fiber location that exhibited maximum amplitude value (using the second referencing scheme, $\Phi_m / \Phi_{m,ref}$, given by Equations (4.18) and (4.19)). It was assumed that the collection fibers were of equal length and that the two split point sources in the dual point illuminating imaging system were of equal intensity (in terms of amplitude and DC values) and in-phase (phase shift was equal for both the modulating point illuminating sources).

8.1.3 Image reconstructions using single and dual point illumination geometries

The hybrid AEKF algorithm was used to perform image reconstructions for all the different experimental conditions. For the dual point illuminating imaging system, the excitation source term in the partial current boundary condition was modeled as two point excitation sources of equal amplitude and in-phase. In other words, the two point excitation sources were modeled as (1,0) for (I_{AC}, θ) at both the illuminating locations. For the single point illuminating imaging system, the excitation source term was modeled with amplitude of unity and phase delay of 0° , that is (1,0) for (I_{AC}, θ) .

The model match between referenced measurements and simulations from the forward problem of the coupled diffusion equations were determined for the dual and single point illuminating imaging systems and for all the experimental cases. Here, the model error covariance, \mathbf{Q} used in the AEKF algorithm was empirically chosen to be equal to one-fourth the mean of the measurement error covariance, \mathbf{R} (diagonal terms of

the measurement error). The parameter error covariance, \mathbf{P} , which is used to damp the parameter updates of μ_{axf} in the recursive reconstruction algorithm, was empirically chosen to be a constant value (= 0.001, 0.01, or 0.1). The measurement error covariance, \mathbf{R} and the model error covariance, \mathbf{Q} , were used along with the referenced measurements in order to determine the unknown parameter, μ_{axf} (absorption coefficient due to the fluorophore) and the parameter error covariance, \mathbf{P} . Only a subset of measurements were considered for reconstructions, after filtering the measurements at the source and detector level, as described earlier (Section 7.3)

8.2 Results and discussion: Perfect uptake case

8.2.1 Effect on volume illuminated and signal strength

An absolute fluorescent modulation depth (AC/DC) image of an interfacing plate (with multiple collection fibers) is illustrated in Figure 8.2 for both the single and dual point excitation source cases. From the figure, we observe that more collection fibers on the interfacing plate “lit up” when the phantom surface was illuminated using dual point excitation sources in comparison to a single point excitation source, thus increasing the total number of acquired fluorescence measurements. The above observation also implies that the total volume illuminated within the phantom increased when dual points were used instead of single points for excitation illumination. The signal strength at collection fibers located close to the dual points of excitation illumination was higher in comparison to the signal arising from a single point of excitation illumination (see

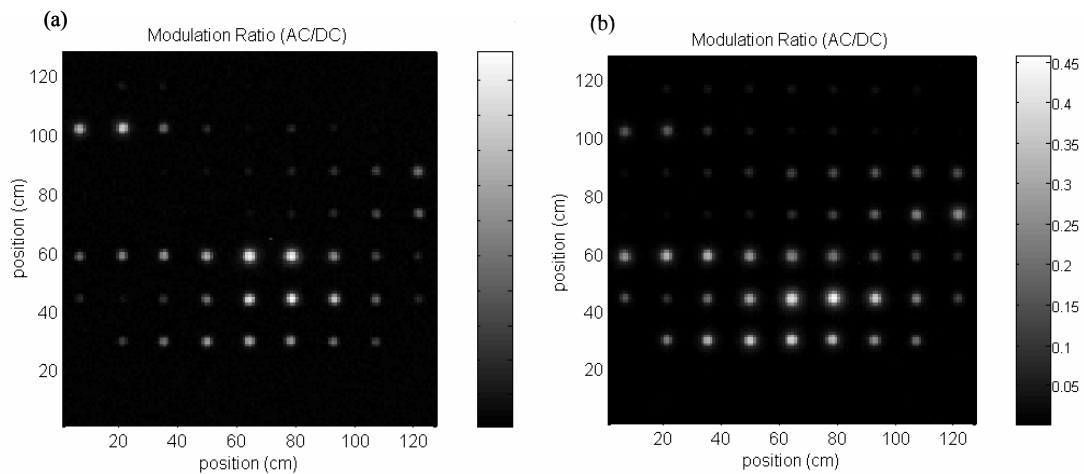


Figure 8.2 Modulation depth of an interfacing plate for (a) single point illumination and (b) dual point illumination, for perfect uptake of 2cm deep and 1cc volume target.

Figure 8.2). Also, more measurements above the set noise floor were acquired in the dual point illumination imaging system (see Table 8.1, column 5).

8.2.2 Model match between experiments and simulations

A good match was observed between referenced measurements and simulated predictions of logarithmic AC ratio ($\ln(\text{ACR})$) and relative phase shift (RPS) for target depths of 1 and 2 cm in both the illumination geometries. However, the bias and variance in the error between experiments and simulations was much lower when dual point excitation illuminations were used instead of single point excitation illuminations (Table 8.3).

Table 8.3 Model mismatch error in $\ln(\text{ACR})$ and RPS for different target depths with 1:0 absorption optical contrast ratio

Target depth (cm)	Measurement geometry	$\ln(\text{AC Ratio})$		Relative phase shift (RPS) (radians)	
		Mean	Variance	Mean	Variance
1	Dual sources	-0.353	0.926	-0.272	0.277
	Single sources	-0.803	1.630	-0.569	0.481
2	Dual sources	-0.485	0.975	-0.135	0.483
	Single sources	-1.057	2.142	-0.517	0.845
3	Dual sources	-1.386	0.710	-0.198	1.335
	Single sources	-1.509	0.851	-0.146	0.966

The observed mismatch for the 1 and 2 cm target depth cases could possibly be due to: (i) the assumption of equal source strengths in the case of dual point excitation sources; (ii) the assumption of equal fiber lengths for all the collection fibers in dual and single point illuminating imaging systems, which is an approximation of the referencing scheme employed; (iii) the degree of discretization in the finite element mesh; (iv) the experimental error in target location; and/or (v) the precision error in the normalized location of the source and collection fibers on the curvilinear phantom surface.

In the case of the 3 cm deep target, the model mismatch was significantly greater for either of the illumination geometries. Apart from the reasons stated above, the major reason for the loss in accuracy is due to excitation light leakage through the optical filters in the presence of weak fluorescence signal from deeply embedded targets, thus contaminating the measured emission signal, and hence increasing the model mismatch. In general, during the fluorescence-enhanced imaging process the strong excitation signal, which is at least 3-4 orders of magnitude greater than the fluorescent signal, cannot be completely rejected using a stack of optical filters without further attenuating

the transmission of the weak fluorescent signal. Future work will involve employing customized filters for optimal excitation light rejection in order to detect deeply embedded targets.

8.2.3 Measurement error

The measurement error in $\ln(AC)$ (reduced when dual point illumination was employed over single point illumination at target depths of 1 and 2 cm (Table 8.4). However, the measurement error was high, particularly in phase (given in radians), for the 3 cm deep target case, in either of the illumination geometries. Excitation light leakage limits precise measurements of weak fluorescent signal, which is reflected in the measurement error data when the target is 3 cm deep.

8.2.4 Image reconstructions

Reconstructions were performed for the experimental cases of 1 and 2 cm deep targets, using individual fluorescence measurements obtained from the dual and single point illumination imaging systems. Reconstructions were not performed on the 3 cm deep target case, since the imaging system was limited by excitation leakage (or noise), as reflected from the model mismatch and measurement error data shown in Table 8.3 and 8.4, respectively.

The referenced fluorescence measurements were reconstructed as blind data, without prior knowledge of the target location, size and optical contrast with respect to the background although the optical properties were known during the actual

Table 8.4 Measurement error (in terms of mean of variance) in $\ln(AC)$ and phase shift (θ) for different target depths with 1:0 absorption contrast ratio.

Target depth (cm)	Measurement geometry	Mean[$\sigma^2(\ln(AC))$]	Mean[$\sigma^2(\theta)$] (radians)
1	Dual sources	0.00154	0.237
	Single sources	0.00217	0.098
2	Dual sources	0.00221	0.007
	Single sources	0.00302	0.042
3	Dual sources	0.00436	0.896
	Single sources	0.00466	0.603

experiment. As an initial guess, the unknown parameter (μ_{axf}) to be reconstructed was assumed to be homogeneous with a low value of 0.003 cm^{-1} for the entire phantom. The reconstruction process was carried out recursively (within each iteration) until the system converged to less than 1% root mean square output error (RMSE). The reconstructions for both the single and dual point illuminating imaging systems gave comparable image quality for either of the two target depth cases (1 and 2 cm). The convergence curves for the dual and single point illuminating imaging systems for both the target depths are shown in Figure 8.3. The actual image of the phantom with the 1 cm deep target is shown in Figure 8.4a and the reconstructed images are shown in Figures 8.4b and 8.4c for the single and dual point illuminating imaging systems, respectively. Similar reconstruction images are provided for the 2 cm deep target case in Figure 8.5 [125].

The target was identified from the reconstructed spatially distributed fluorescence absorption coefficient μ_{axf} . A cutoff value of fluorescence absorption coefficient was selected to distinguish between the background and the target based on

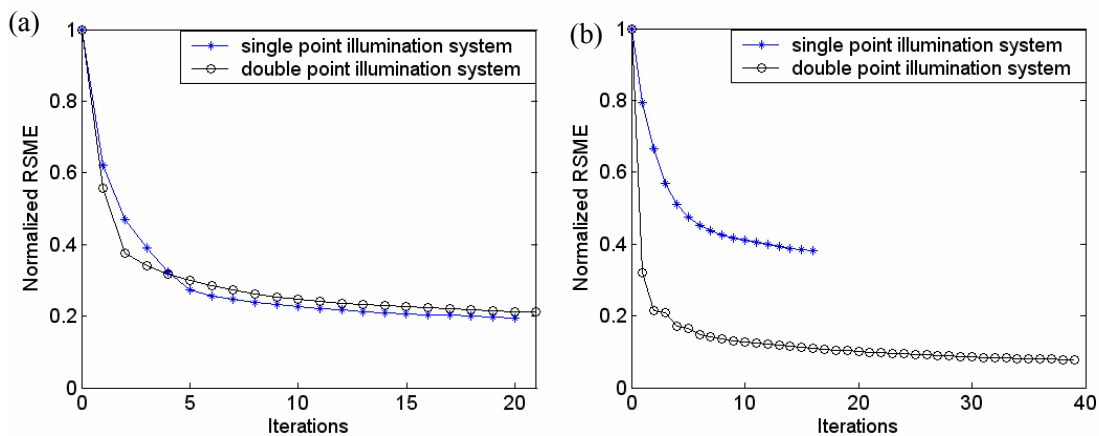


Figure 8.3 Convergence curves from 3-D image reconstructions using the dual and single point illumination geometries for (a) 1 cm target depth, and (b) 2 cm target depth cases under 1:0 absorption optical contrast ratio.

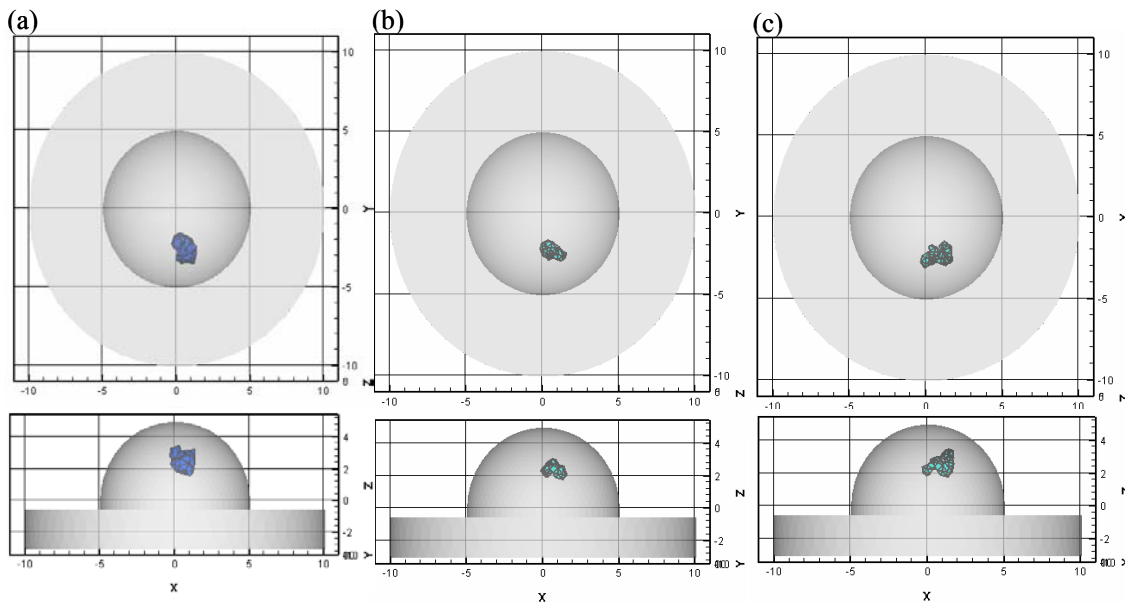


Figure 8.4 Actual and reconstructed targets in x-y and x-z planes: (a) actual 1 cc target located 1 cm deep under 1:0 absorption optical contrast ratio, (b) reconstructed target using single point illumination measurement geometry, and (c) reconstructed target using dual point measurement geometry. All the reconstructions were performed with the initial guess of $\mathbf{P}=0.001$, and $\mu_{\text{axf}}=0.003 \text{ cm}^{-1}$.

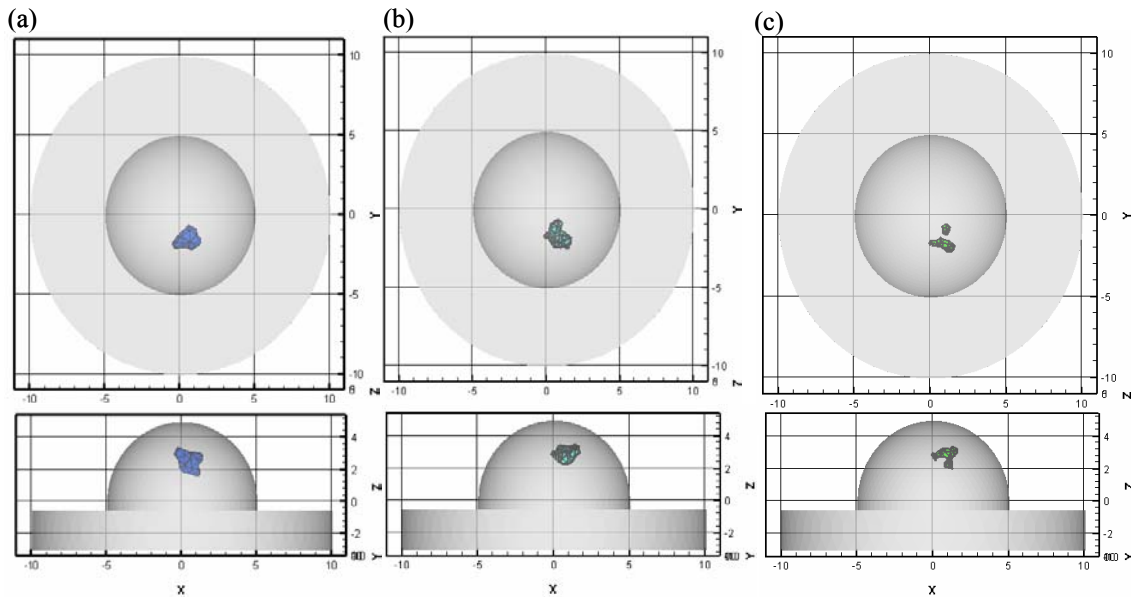


Figure 8.5 Actual and reconstructed targets in x-y and x-z planes: (a) actual 1 cc target located 2 cm deep under 1:0 absorption optical contrast ratio, (b) reconstructed target using single point measurement geometry, and (c) reconstructed target using dual point measurement geometry. All the reconstructions were performed with the initial guess of $\mathbf{P}=0.001$, and $\mu_{axf}=0.003 \text{ cm}^{-1}$.

Table 8.5 Reconstructed image quality for the 1 cm-target depth case with 1:0 absorption optical contrast ratio, using both the point illumination geometries.

Point illumination geometry	μ_{axf} cut-off value (cm^{-1})	Centroid			Integrated μ_{axf} (cm^2)	Volume (cm^3)	Distance off (cm)
		X(cm)	Y(cm)	Z(cm)			
Actual case ^a	--	0.5	-2.5	2.5	0.3	1.0	--
Dual	0.2	0.8	-2.3	2.6	0.4	0.8	0.3
Single	0.2	0.6	-2.3	2.5	0.3	0.6	0.2

^aActual case: Details of actual target location

Table 8.6 Reconstructed image quality for the 2 cm-target depth case with 1:0 absorption optical contrast ratio, using both the point illumination geometries.

Point illumination geometry	μ_{axf} cut-off value (cm ⁻¹)	Centroid			Integrated μ_{axf} (cm ²)	Volume (cm ³)	Distance off (cm)
		X(cm)	Y(cm)	Z(cm)			
Actual case	--	0.5	-1.5	2.5	0.3	1.0	--
Dual	0.4	0.8	-1.7	2.8	0.4	0.7	0.5
Single	0.2	0.8	-1.8	3.0	0.5	0.9	0.6

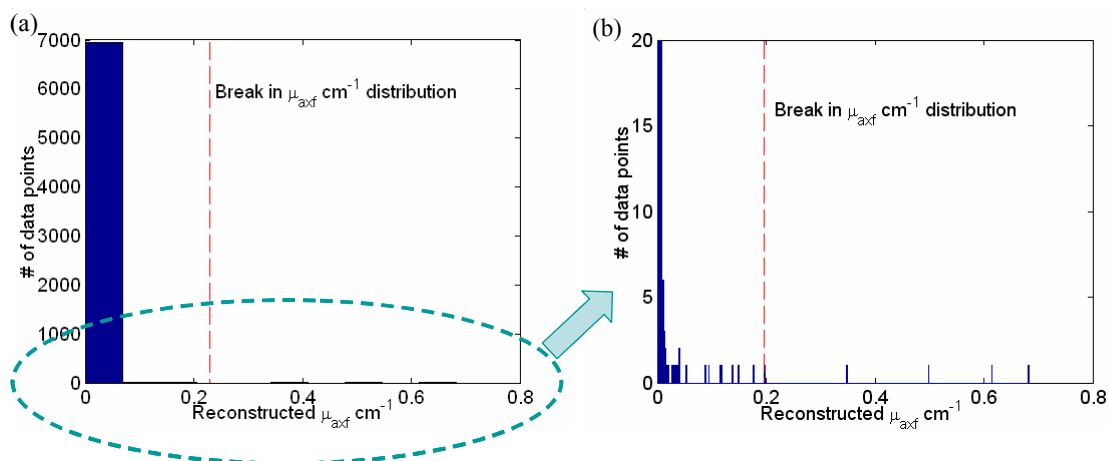


Figure 8.6 (a) Histogram of the reconstructed parameter, μ_{axf} (absorption coefficient due to the fluorophore) cm⁻¹ in the experimental case containing the 1 cc target located ~ 1 cm deep with 1:0 absorption optical contrast ratio and using single point illumination geometry, (b) Histogram of the same experimental case zoomed in the y-axis and plotted using 500 bins.

the break between modes in the histogram of the reconstructed μ_{axf} . A sample plot of the histogram obtained for the 1 cm deep target case and single point illumination geometry is illustrated in Figure 8.6. Details of the reconstructed target location, target volume, and integrated fluorescence absorption for 1 cm and 2 cm target depth cases are tabulated in Tables 8.5 and 8.6, respectively. The iso-surface cut-off value can be chosen at any of the breaks between the modes (see Figure 8.6), however in our case it was chosen from the significant break observed between modes. In addition, since the current studies are focused towards assessing the feasibility of detecting deeply located targets and not providing quantitatively accurate reconstructed target volumes, the choice of the iso-surface is chosen as described above. Future studies will involve evaluation of a more accurate method to determine the iso-surface cut-off values and also the reconstructed target details.

8.3 Results and discussion: Imperfect uptake case

8.3.1 Model match between experiments and simulations

For experiments with target:background absorption contrast ratios of 100:1, fluorescence is also present in the background. Hence, the overall signal strength was higher than that observed for the experiments containing no fluorescence in the background (perfect uptake case). Thus, the differences in the signal strength between the dual and single point illumination was smaller compared to the overall signal strength, and hence effect of illumination geometry on the signal strength was not assessed in the imperfect uptake studies.

Table 8.7 Model mismatch error in $\ln(\text{ACR})$ and RPS for different target depths with 100:1 absorption optical contrast ratio.

Target depth (cm)	Measurement geometry	$\ln(\text{AC Ratio})$		Relative phase shift (RPS) (radians)	
		Mean	Variance	Mean	Variance
1	Dual sources	-0.017	0.459	-0.048	0.977
	Single sources	0.253	0.357	-0.026	0.910
2	Dual sources	-0.124	0.625	0.001	1.090
	Single sources	0.220	0.712	-0.128	0.993
3	Dual sources	-0.280	0.860	-0.089	0.109
	Single sources	0.065	0.781	-0.154	0.093

A good model match was observed between experiments and simulations, for all the target depths and measurement geometries, as shown in Table 8.7. In most cases, the dual point illuminating imaging system provided minimal model mismatch errors (computed using Equations (6.2) and (6.3)) compared to the single point illuminating imaging system, especially in the logarithmic AC ratio (or $\ln(\text{ACR})$) data. In general it was observed that the dual source illumination geometry tended to degrade the model match in relative phase shift (RPS) data, probably due to the deteriorating ICCD camera, which lacks sensitivity to acquire good phase data. Similar results were obtained from the measurement precision studies (Section 7.1), in which there was more error in the phase shift data over the acquired AC data.

Unlike the perfect uptake case (1:0) for the 3 cm deep target, in which no model match was observed between experiments and simulations, a good model mismatch was observed in the imperfect uptake case (100:1) for the 3 cm deep target (see Figure 8.7)

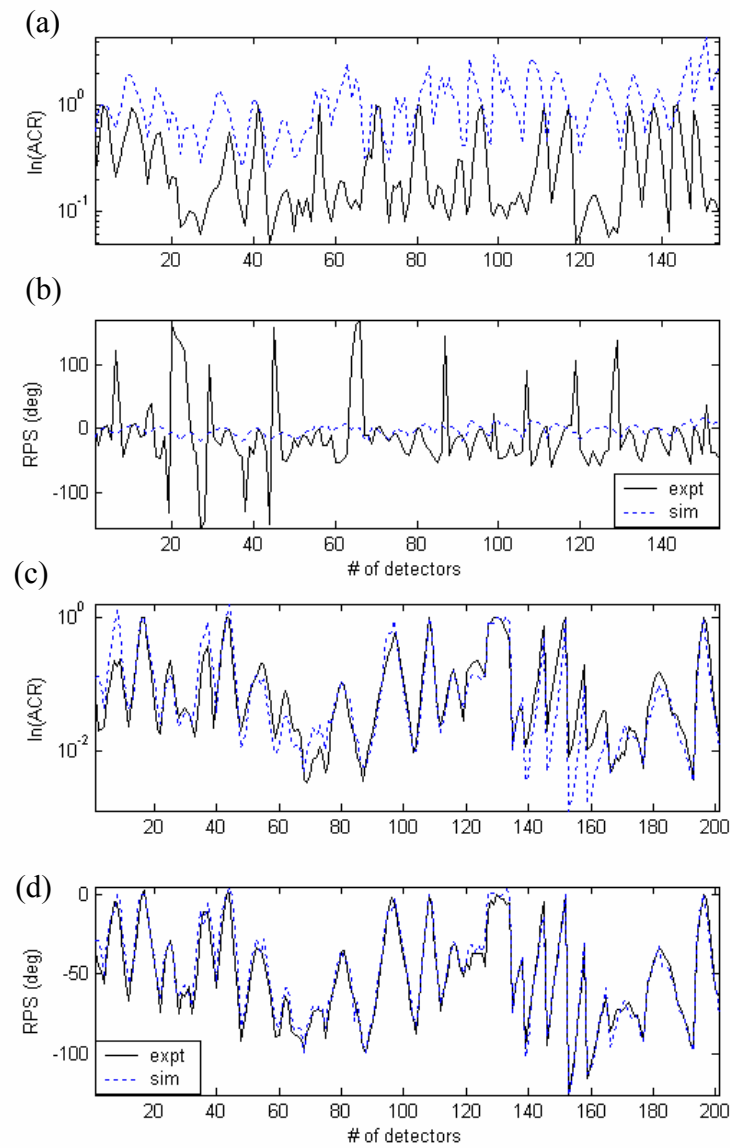


Figure 8.7 Model match between experiments and simulations of the 3 cm deep target using the single point illumination measurement geometry (a) $\ln(\text{ACR})$ for 1:0 case, (b) RPS for 1:0 case, (c) $\ln(\text{ACR})$ for 100:1 case, and (d) RPS for 100:1 case. The model match is plotted for a subset of the total number of acquired measurements.

although the perturbation caused by the deeply located target is probably minimal. The good model match for the imperfect uptake case could probably arise from the negligible perturbation caused by deeply located targets even in simulated data, occurring due to the exponential attenuation of the fluorescent light signal generated from the deeply located target. Thus, although a good model match is observed, it is uncertain if the 3 cm deep target can be reconstructed. However, reconstructions will still be attempted using the measurements acquired from the 3 cm deep target under imperfect uptake conditions. Future work may involve the assessment of the effect of perturbation from deeply located targets.

8.3.2 Measurement error

Measurement error for the imperfect uptake experimental cases was obtained for all the different target depth conditions (see Table 8.8). Unlike the trend of measurement errors increasing with the increase in target depth observed for the perfect uptake contrast ratio case, here we observe that the measurement error was of the same order of magnitude in $\ln(AC)$ data at different target depths. The reasons for such a varied behavior of the acquired data with and without fluorescence in the background are not known. However, from the various experiments performed so far, inconsistency in the current deteriorating ICCD camera was observed. Although, attempts were made to reconstruct the data obtained for all the target depths (1-3 cm) to observe the impact of such high measurement error, especially in phase shift, on the reconstructed target's location and size, and on the presence of artifacts, if any.

Table 8.8 Measurement error (in terms of mean of variance) in $\ln(AC)$ and phase shift for different target depths with 100:1 absorption optical contrast ratio of a single 1 cc target located from 1-3 cm deep.

Target depth (cm)	Measurement geometry	Mean[$\sigma^2(\ln(AC))$]	Mean[$\sigma^2(\theta)$] (radians)
1	Dual sources	0.00290	0.567
	Single sources	0.00379	0.542
2	Dual sources	0.00200	0.604
	Single sources	0.00291	0.524
3	Dual sources	0.00210	0.341
	Single sources	0.00307	0.232

8.3.3 Image reconstructions

Three-dimensional reconstructions were performed under similar conditions in terms of modulation cut-off parameter, and initial estimate of the unknown parameter ($\mu_{axf} = 0.003 \text{ cm}^{-1}$). Reconstructions were performed with different initial guess in the \mathbf{P} value (0.001, 0.01, and 0.1) that was chosen empirically. Here, reconstructed images under varying target depths are presented for both the single and dual source systems only for those initial \mathbf{P} values that gave better reconstruction target quality.

Convergence plots using the dual and single point illuminating imaging systems for various target depths (1 to 3-cm deep) are given in Figure 8.8. The actual and reconstructed phantom for different target depths using dual and single point illuminating imaging systems is given in Figure 8.9, 8.10, and 8.11 respectively. Details of the reconstructed target for all the experimental cases are provided in Table 8.9.

From the reconstruction results for all the three target depth cases, we observe that the dual point illuminating imaging system consistently generated artifacts unlike the single point illuminating imaging system, where no significant artifacts were observed. This shows that dual point illumination geometry may not be appropriate

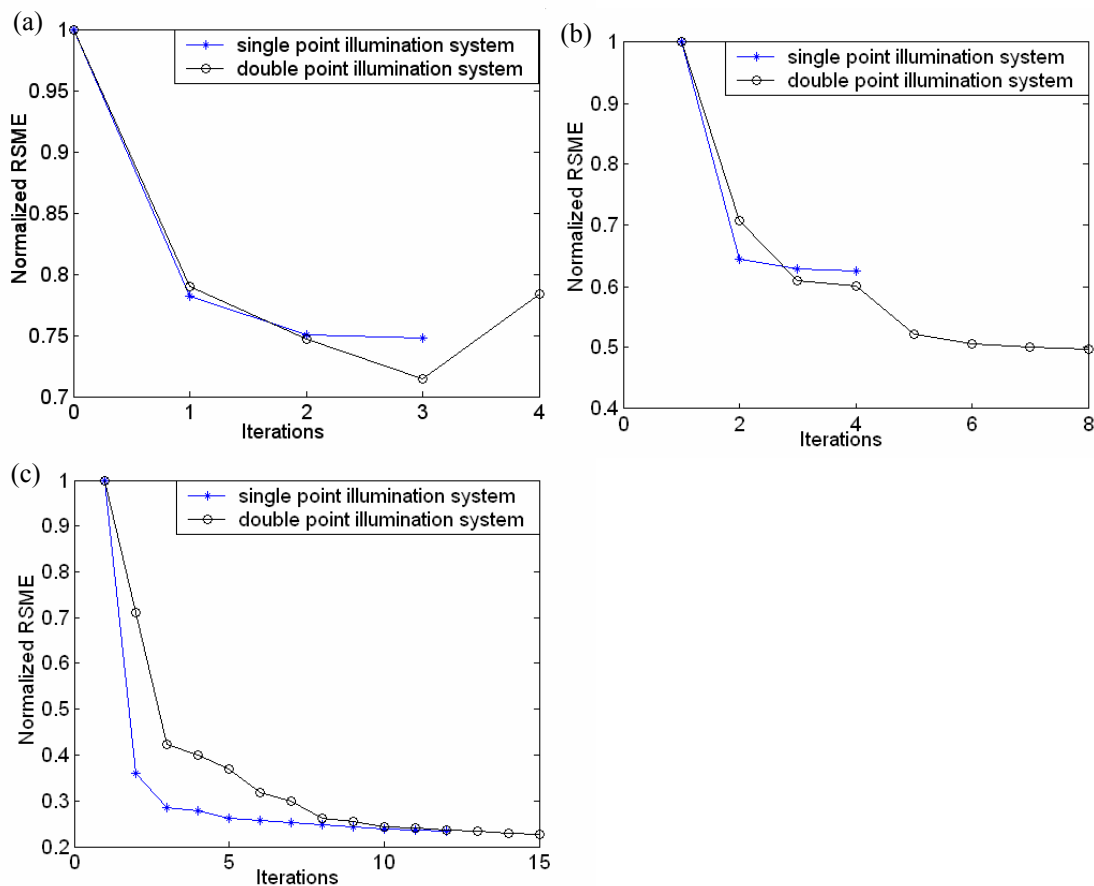


Figure 8.8 Convergence plots for (a) 1-cm deep target case, (b) 2-cm deep target case, and (c) 3-cm deep target case with 100:1 absorption contrast ratios, using both the illumination geometries. Reconstructions were performed with initial guess in $\mu_{axf}=0.003 \text{ cm}^{-1}$.

when fluorophores are present in the background. In the 3-cm target depth case, although the target's centroid in the x-y direction was very close to the true centroid the reconstructed target was observed to be closer to the phantom surface in the z-axis. In other words, reconstruction of deeply located targets is feasible but limited in detecting the true depth of the target.

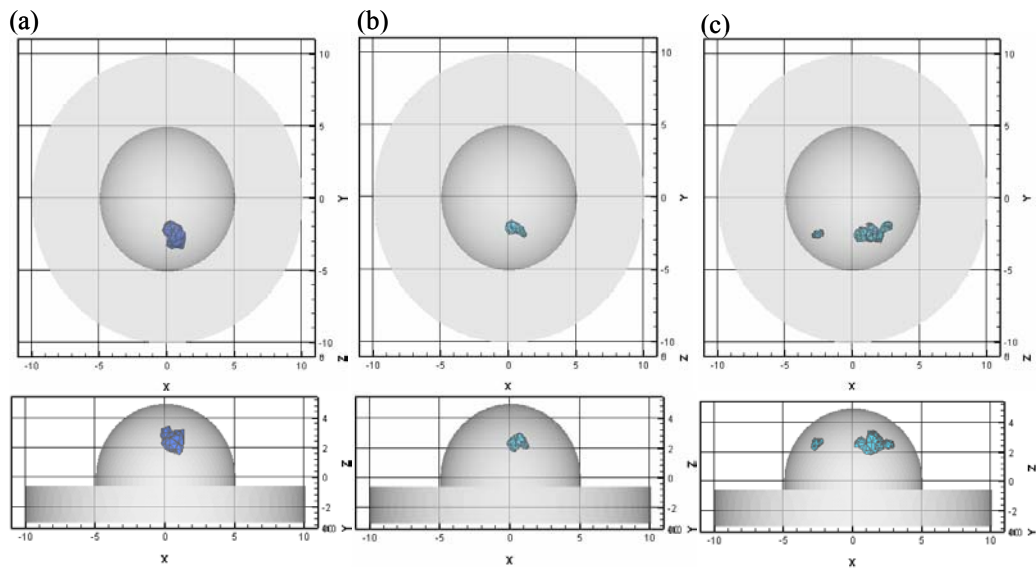


Figure 8.9 Actual and reconstructed targets in x-y and x-z planes for: (a) actual 1 cc target located ~ 1 cm deep under 100:1 absorption optical contrast ratio cases, (b) reconstructed target using single point illumination measurement geometry, when initial guess of $P=0.01$, and (c) reconstructed target using dual point illumination measurement geometry, when initial guess of $P=0.001$.

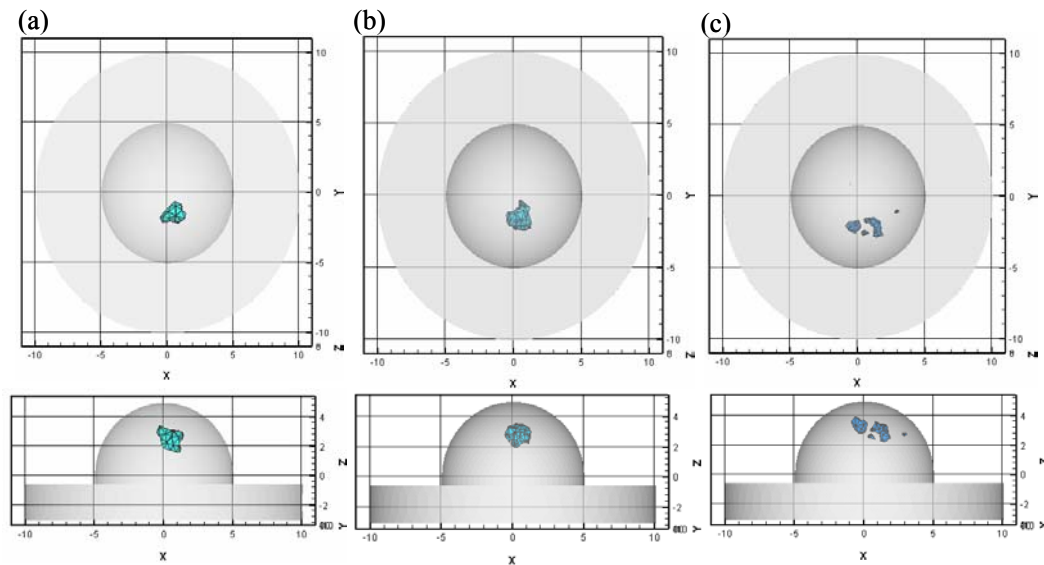


Figure 8.10 Actual and reconstructed targets in x-y and x-z planes for: (a) actual target 1 cc target located ~ 2 cm deep under 100:1 absorption optical contrast ratio cases, (b) reconstructed target using single point illumination measurement geometry, when initial guess of $P=0.01$, and (c) reconstructed target using dual point illumination measurement geometry, when initial guess of $P=0.001$.

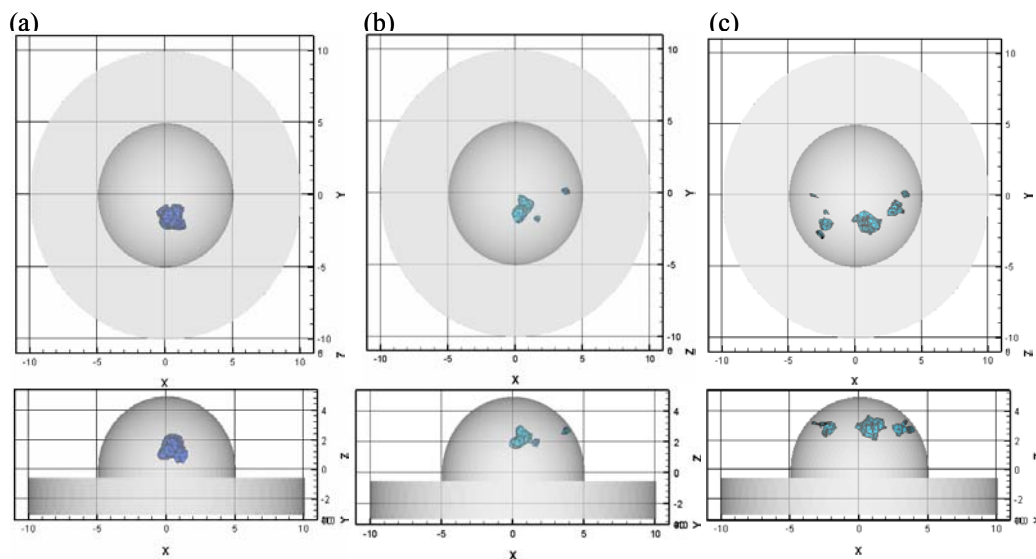


Figure 8.11 Actual and reconstructed targets in x-y and x-z planes for: (a) actual target 1 cc target located ~ 3 cm deep under 100:1 absorption optical contrast ratio cases, (b) reconstructed target using single point illumination measurement geometry, when initial guess of $\mathbf{P}=0.01$, and (c) reconstructed target using dual point illumination measurement geometry, when initial guess of $\mathbf{P}=0.001$.

Table 8.9 Reconstructed targets under different target depths for 100:1 absorption optical contrast ratio cases. The cut-off μ_{axf} was chosen based on the break between modes in the histogram of the reconstructed

μ_{axf} .

Target depth (cm)	Point illumination geometry	μ_{axf} cut-off (cm^{-1})	Centroid		Integrated μ_{axf} (cm^{-1})	Volume (cm^3)	Distance off (cm)
			True value [x y z] cm	Reconstructed [x y z] cm			
1	Dual	0.015	[0.5 -2.5 2.5]	[0.7 -2.4 2.7]	0.05	1.67	0.34
	Single	0.05	[0.5 -2.5 2.5]	[0.5 -2.1 2.4]	0.06	0.42	0.37
2	Dual	0.1	[0.5 -1.5 2.5]	[0.5 -1.8 3.2]	0.23	1.02	0.75
	Single	0.05	[0.5 -1.5 2.5]	[0.4 -1.5 2.9]	0.17	1.46	0.38
3	Dual	0.1	[0.5 -1.5 1.5]	[0.5 -1.5 3.0]	0.25	2.56	1.45
	Single	0.05	[0.5 -1.5 1.5]	[1.0 -1.0 2.2]	0.24	0.98	0.98

8.4 Summary

From the perfect uptake (1:0 contrast ratio) studies performed under 1- and 2- cm target depth conditions using both the point illumination measurement geometries, it was observed that the dual point illumination system not only provided adequate signal strength, increased the total phantom volume illuminated and total number of fluorescence measurements, but it also reduced the model mismatch and measurement errors in comparison to the single point illumination system. Three-dimensional reconstructions for the dual point illumination measurement geometry, performed for the first time, successfully reconstructed the target with results comparable to the reconstructions using the single point illumination geometry. Thus, 3-D image reconstruction using the simultaneous, in-phase, dual point illumination system is feasible. Future implementations will test this geometry for more than two simultaneous point excitation source illuminations. Advantages of simultaneous multiple point illumination geometry include (i) greater volume illumination, (ii) higher signal strength, and (iii) increased total number of measurements in large volume phantoms.

In terms of depth studies under perfect uptake conditions, the ICCD imaging system was not sensitive in detecting weak fluorescent signals against strong excitation light (which is 3-4 orders of magnitude higher). Also, the weak fluorescent signal was contaminated with excitation light leakage due to the inability of optical filters to completely reject the excitation light and efficiently transmit the weak fluorescent signal. The effect of various filter combinations was studied (see Appendix E) and it was concluded that stacking optical filters in order to achieve greater rejection of 785 nm

light as well as efficient transmission of 830 nm light was not possible. Currently, there are no optical filters available that can provide good rejection and transmission efficiencies. Future work in depth analysis will involve the use of customized optical filters (of blocking OD >10 at 785 nm and transmission > 90% at 830 nm) as well the replacement of the current CCD camera and the image intensifier.

In the imperfect uptake contrast (100:1) studies, artifacts were observed when reconstructing measurements acquired at different target depths using the dual point illumination geometry. The presence of fluorescence in the background as well as the increased measurement error in the acquired phase shift, obtained using the dual point illumination geometry, caused artifacts during reconstruction. However, due to the inconsistent performance of the ICCD system, it may be too early to conclude the feasibility of dual point illumination geometry for imperfect uptake studies, where fluorophores are also present in the background.

Unlike in the perfect uptake contrast studies, the limitation for detecting deeper targets was not excitation light leakage, but decrease in the perturbation of the fluorescing target due to the presence of fluorescence in the background. The target volume constituted less than 1% of the total phantom volume, and perturbation from such a small region tended to fade with increased depth. Thus, when the 3 cm deep target was located very close to the true location its x-y direction under 100:1 contrast conditions, the perturbation was so weak that the reconstructions failed to locate the depth of the target.

In summary, the target depth studies demonstrated the ability of the ICCD imaging system to precisely detect single 1 cc targets located up to 2 cm deep under both perfect and imperfect uptake cases. Hence, further absorption contrast studies were directed towards detecting smaller volume targets located up to 2 cm deep from the phantom surface.

9. SMALL VOLUME AND MULTIPLE TARGET STUDIES

Work presented this far was focused on using single 1 cc targets located at various depths from the phantom surface and at different target:background absorption optical contrast ratios (1:0 and 100:1), in order to assess the feasibility of detecting deeply embedded targets. However, for early stage tumor diagnosis in a clinical situation, there is a need to detect single and multiple smaller volume targets that are located in deep tissues of large volume. Also, from a clinical perspective, assessment of the multifocality of the disease is significant, since the diseased tissues spread metastatically in most cases. Hence, the current chapter is focused in determining the detectability of single and multiple smaller volume (0.5- 0.6 cc) targets, which mimic a clinically relevant scenario of small or early stage tumors as well as the multifocality of the disease.

9.1 Experimental parameters

From our depth studies using single 1cc volume targets, we observed that the targets were located very close to their true location with minimal artifacts under perfect uptake (1:0) conditions, over the imperfect uptake (100:1) case. Since the current ICCD system performed well under perfect uptake (1:0) conditions, preliminary experiments using single and multiple small volume (0.5-0.6 cc) targets was performed under perfect uptake conditions, and using ICG as the fluorescing contrast agent. Details of the

Table 9.1 Experimental parameters for small volume and multiple target studies.

Expt	Absorption contrast ratio	[ICG] in target (μM)	# of targets	Target volume (cm^3)	Target depth (cm)	Target shape	Illumination geometry
1	1:0	1	1	0.5	2.0	Cuboid 0.5x1x1cc	Dual point & Single point
2	1:0	2.5	3	0.5-0.6 each	1.2-1.4	Spherical ~ 0.95 cm dia	Single point

experimental conditions are provided in Table 9.1.

9.2 Single small volume target study (Experiment # 1)

Here, a single 0.5 cc volume target of cuboid shape ($1 \times 1 \times 0.5 \text{ cm}^3$) was located ~2 cm deep from its centroid to the hemispherical surface of the phantom. Fluorescence measurements were acquired in the frequency-domain using both the single point illumination and dual point illumination measurement geometries. In order to determine the extent of excitation light leakage, measurements were also acquired without any fluorescence in the entire phantom (by removing the fluorescing target from the non-fluorescing 1% Liposyn background). The average modulation depth of the excitation light leakage (averaged over an interfacing plate for each source illumination) was determined as 0.225 from the no-fluorescence measurements and was used to differentiate between measurements that correspond to true fluorescence signal originating from the fluorescing target and the measurements that correspond to excitation light leakage from the background. Hence measurements were filtered at two

stages (Figure 9.1): (i) source level: point source illuminating locations were limited to those which elicit an average modulation depth (AC/DC) greater than 0.225 for each interfacing plate, and (ii) detector level: only those detected emission measurements (i) with individual modulation depth, $(AC/DC)_i$, greater than 0.025 were used in the inversions.

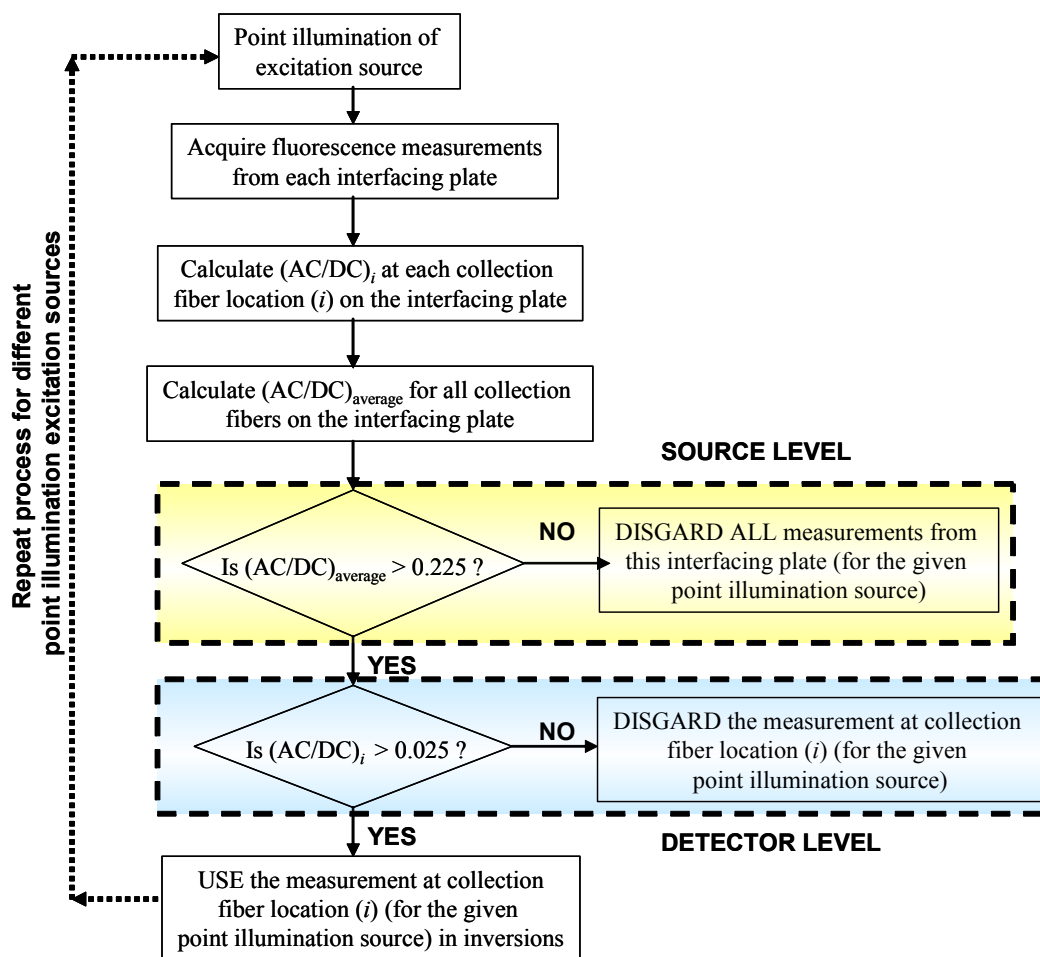


Figure 9.1 Measurement filtration process to remove data representing excitation leakage (at source level) or noise (at detector level).

Details of the total number of measurements acquired and the actual number of measurements used in the inversions are provided in Table 9.2. From the table, we observe that in the case of single point illumination geometry very few measurements remain after the two-step filtration process, in comparison to the measurements from the dual point illumination geometry. Hence reconstructions were attempted only from the measurements acquired using the dual point illumination geometry.

9.2.1 Model match and measurements errors

The model match between experiments and simulations for the above experimental case is given in Figure 9.2 and the errors in $\ln(\text{ACR})$ and RPS were evaluated. The measurement errors were also evaluated from the 5 repeated measurements ($rep = 5$), as a mean of variance in logarithmic AC and phase shift measurements. The values were determined to be 0.0027 and 0.337 for logarithmic AC and phase shift (in radians), respectively.

9.2.2. Image reconstructions

Image reconstructions were performed with different initial guesses of the parameter error covariance, \mathbf{P} (0.001, 0.01, and 0.1) and an initial guess of the reconstructing parameter ($\mu_{axf} = 0.001 \text{ cm}^{-1}$), where the value was randomly chosen. The convergence criterion remained the same (that is less than 1% root mean square output error (RSME) or a maximum of 50 iterations). For all the initial guesses of \mathbf{P} , the reconstructions terminated after the 2nd iteration, since the error between consecutive

Table 9.2 Acquired measurements for the single 0.5 cc target experimental case (Expt #1).

Illumination geometry	# of source combinations used	# of measurements acquired	# of source combinations after filtering	Measurements used in reconstructions
Dual point	16 pairs	1024	9 pairs	343
Single point	9 single	576	2 single	68

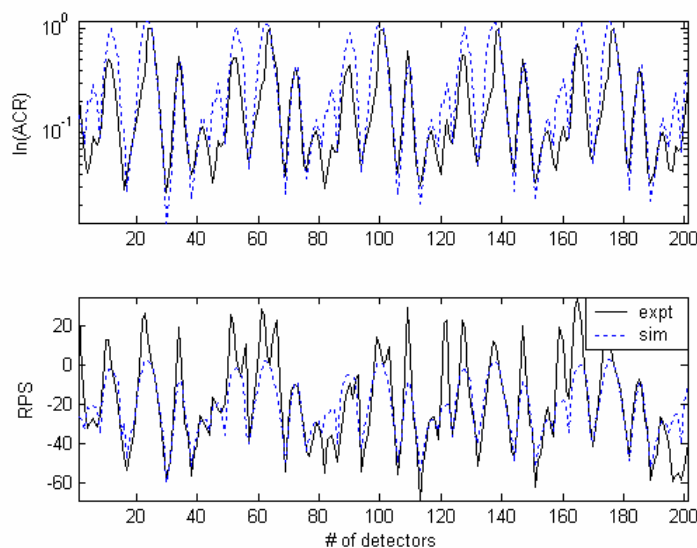


Figure 9.2 Model match between experiments and simulations in terms of $\ln(\text{ACR})$ and RPS (in degrees), plotted for a subset of total acquired measurements. The mean and variance of errors in $\ln(\text{ACR})$ were estimated as -0.305 and 0.422, respectively, and the mean and variance of errors in RPS (in radians) were estimated as 0.068 and 0.149, respectively.

iterations started to increase (see Figure 9.3). Hence, reconstructions were performed using the convergence criterion of iterating until a maximum of 20 iterations were reached, and not based on the decrease in RMSE. The mean output error, evaluated as

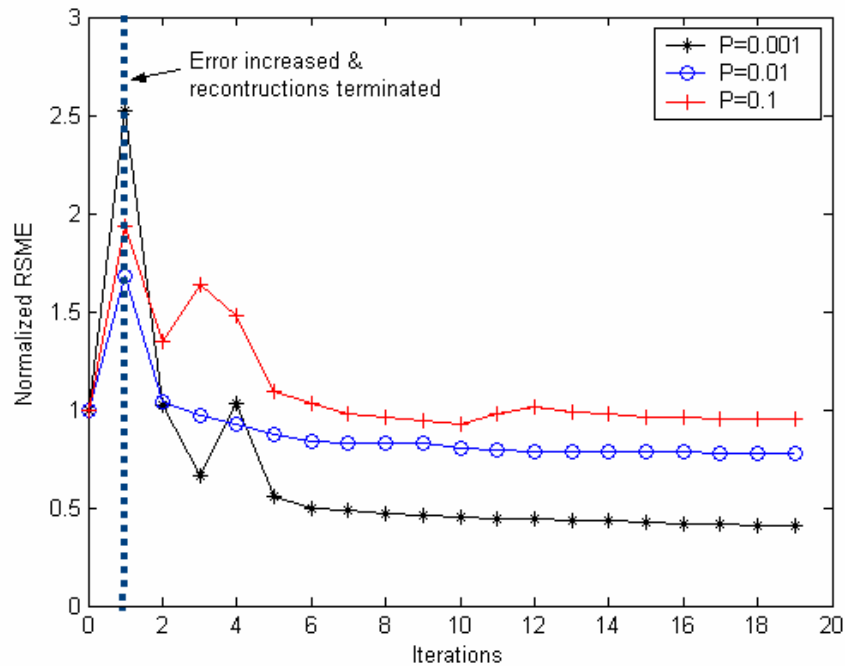


Figure 9.3 Convergence plot for the single 0.5 cc target experimental case under perfect uptake case. Based on the convergence criterion, the reconstructions terminated after the 2nd iteration (dotted vertical line) due to an increase in the errors, and the reconstructions were carried out until 20 iterations were reached.

the root mean square error (RMSE) for the 20 iterations are shown in Figure 9.3 for different **P** values.

Reconstructed images were analyzed for the different initial **P** cases and both the convergence criteria used during reconstructions. From all the reconstructions performed under varying initial **P** values and different convergence criteria, it was observed that the target volume as well the reconstructed μ_{axf} value increased with an increase in the initial guess of the **P** value. Based on our different experimental studies,

in most experiments with a perfect uptake optical contrast condition, $\mathbf{P}=0.001$ provided a reasonably good reconstructed image of the phantom even in the current experimental case. Hence, contour slices of the true and reconstructed phantom obtained using both the convergence criteria are presented in Figure 9.4 for the initial guess of $\mathbf{P}=0.001$. With an increase in the initial guess of \mathbf{P} , the reconstructing parameter μ_{axf} reached the upper bound value ($\mu_{axf} = 0.8 \text{ cm}^{-1}$) set in the pseudo-beta transforms during image reconstructions, although in most reconstructions, the centroid of the reconstructing target was close to the true centroid. Future work will involve in determining a better method of choosing the initial guess of \mathbf{P} , and thus remove the arbitrary approach that is employed in the current reconstructions.

From the contour slices of the reconstructed image shown in Figure 9.4, we observe that the target was reconstructed successfully without any artifacts using the first convergence criterion, when the reconstructed terminated after 2nd iteration. When the reconstructions were carried out for 20 iterations, there were artifacts around the reconstructed target, making it difficult to accurately locate the target from the contour slices. Evaluating the target volume and centroid location from experimental data using an iso-surface cut-off value for μ_{axf} based on the break between modes in the histogram (Figure 9.5) of the reconstructed μ_{axf} (see Table 9.3). Based on the results obtained, we observe that the choice of the convergence criterion also plays an important role in reconstructing the correct target volume and location.

From the above experimental study, we observe that the reconstructed target's centroid was $\sim 1 \text{ cm}$ off from the true centroid location of the target. The excitation

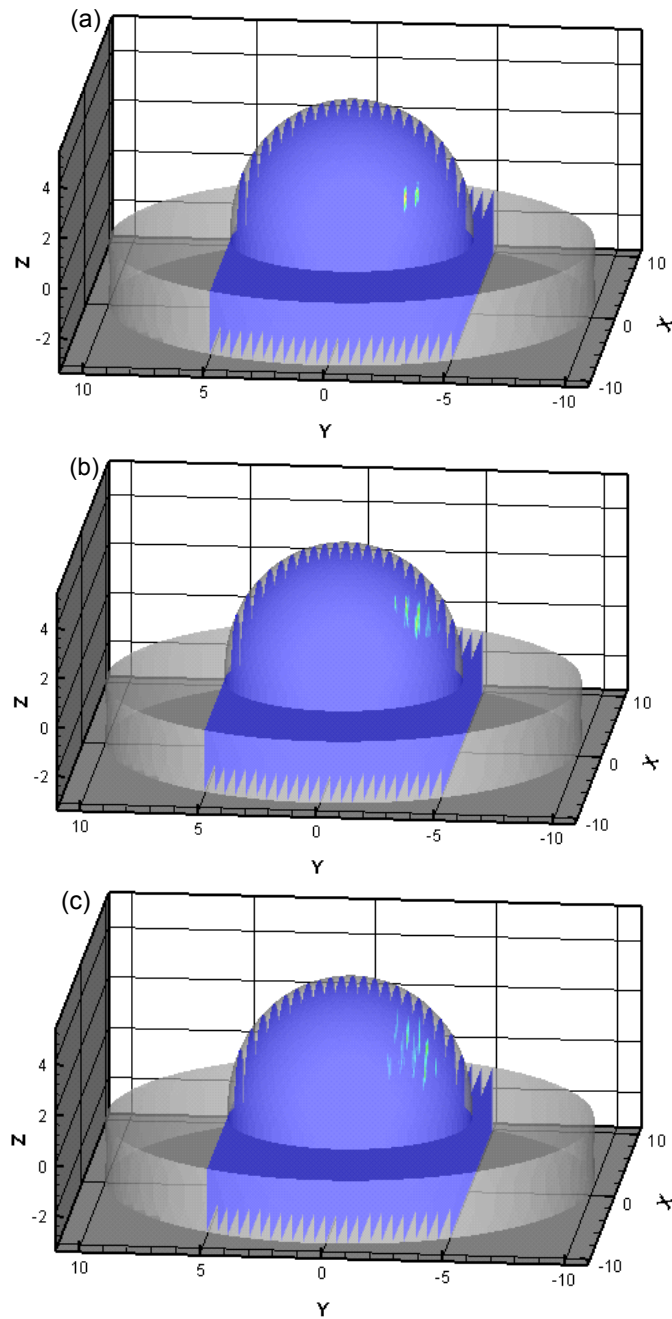


Figure 9.4 Contour slices in the y-plane of the (a) actual phantom containing a single 0.5 cc target, with no ICG in the background (b) reconstructed phantom using the first convergence criterion of $< 1\%$ RMSE or a maximum iterations of 50, and (c) reconstructed phantom using the second convergence criterion of maximum 20 iterations. In both the reconstruction cases, $P=0.001$, $\mu_{axf}=0.001 \text{ cm}^{-1}$.

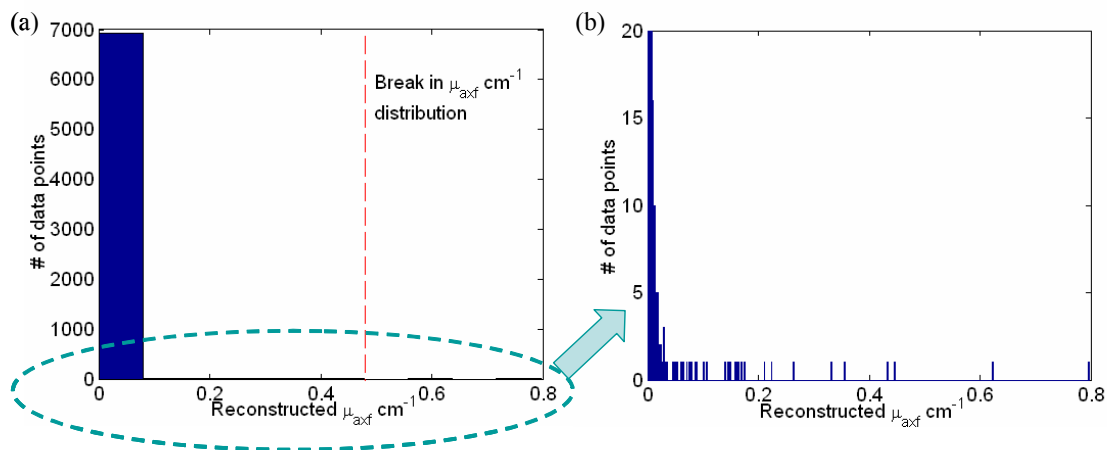


Figure 9.5 (a) Histogram of the reconstructed parameter, μ_{axf} (absorption coefficient due to the fluorophore) cm^{-1} for the experimental case containing a 0.5 cc target at 1:0 absorption optical contrast ratio and located ~ 2 cm deep, (b) Histogram of the same experimental case zoomed in the y-axis and plotted using 500 bins.

Table 9.3 Details of the reconstructed images using both the convergence criteria (for $P=0.001$) for a single 0.5 cc target located 2 cm deep under perfect uptake case.

Convergence criterion	μ_{axf} cut-off value (cm^{-1})	Centroid			Integrated μ_{axf} (cm^2)	Volume (cm^3)	Distance off (cm)
		X(cm)	Y(cm)	Z(cm)			
Actual case ^a	--	-0.5	-2.5	1.55	0.15	0.5	--
< 1% RSME or max. 50 iterations	0.4	-0.6	-3.0	2.4	0.35	0.57	1.0
20 iterations	0.5	-0.6	-3.2	1.9	0.18	0.25	0.78

^aActual case: Details of actual target location and its optical properties during experiments

leakage of the imaging system was high, limiting the current ICCD camera from collecting weak fluorescent signal from small and deeply embedded targets. Hence

further measurements using small volume targets located deeper than 2 cm were not attempted using the current ICCD imaging system.

9.3 Multiple small volume target study (Experiment # 2)

In this study, three small volume (0.5-0.6 cc) targets were located between 1.2-1.4 cm deep from the hemispherical surface of the phantom. Only the single point illumination measurement geometry was applied, since the current experiment was first of its kind towards multiple small volume target study. For the current study, 0.5-0.6 cc spherical targets (custom made from Pyrex glass at Chemistry Glass Blowing Shop, Texas A&M University) with an aspect ratio of one were employed, unlike the previous studies employing cuboid shaped 0.5 cc targets ($1 \times 1 \times 0.5 \text{ cm}^3$), whose aspect ratio was not equal to one. For small volume targets with aspect ratio not equal to one, the orientation of the target with respect to the point of excitation source illumination plays an important role in acquiring fluorescence measurements with adequate signal strength. Hence, for multiple small volume target studies, spherical targets were used in order to avoid any possible decrease in the total number of fluorescence measurements acquired with adequate signal strength. The targets used in the experiments are shown in Figure 9.6.

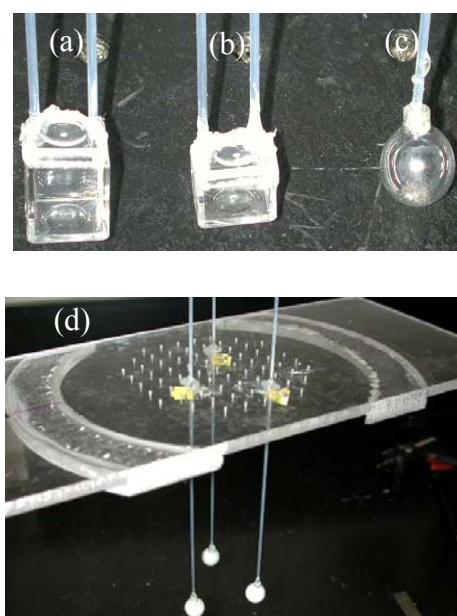


Figure 9.6 Actual targets used in the experimental studies (a) $1 \times 1 \times 1 \text{ cm}^3$ target made from clear plastic. It was used in depth studies, (b) $0.5 \times 1 \times 1 \text{ cm}^3$ target made from clear plastic. It was used in single small volume target study, and (c) $\sim 0.5 \text{ cm}$ radius spherical target made from Pyrex glass. (d) Suspension of the three targets in multiple target detection experiment, using optical fibers for support. The plate holding the targets helps position the targets precisely in the xyz coordinates.

Table 9.4 Acquired measurements for the multiple target experimental case (Expt # 2).

Illumination geometry	# of source combinations used	# of measurements acquired	# of source combinations after filtering	# of measurements used in reconstructions
Single point	25 single	1728	10 single	286

Excitation leakage was observed in the current study as well, and hence the fluorescence measurements were filtered at two stages, similar to that performed in the previous study (see Section 9.2). Details of the total number of measurements acquired and that used during reconstructions after filtering are provided in Table 9.4.

9.3.1 Model match and measurement errors

A reasonably good model match was observed between referenced experiments and simulations. Comparison plots of $\ln(\text{ACR})$ and RPS between experiments and simulations are provided in Figure 9.7, along with the mean and variance in the model mismatch errors. Measurement errors were also evaluated from the five repeated measurements ($rep=5$). The mean of the variance in repeated measurements was observed to be 0.002 and 0.092 in logarithmic AC and phase shift (in radians), respectively.

9.3.2 Image reconstructions

Image reconstructions were performed using the AEKF algorithm and employing the similar finite element mesh (6956 nodes) as in the previous reconstructions cases. The initial guess of the reconstructing parameter (μ_{axf}) was chosen as 0.001 cm^{-1} and the reconstructions were performed for different initial guesses of \mathbf{P} (0.001, 0.01, and 0.1), but presented for a single case of \mathbf{P} value. Here the upper and lower bound limits of μ_{axf} , $[\mu_{axf,lower}, \mu_{axf,upper}]$ and μ_{amf} , $[\mu_{amf,lower}, \mu_{amf,upper}]$ were set to $[0, 1.5] \text{ cm}^{-1}$ and $[0.009, 0.21] \text{ cm}^{-1}$, respectively, during the pseudo-beta transforms, since the concentration of the fluorophores in the targets were 2.5 times higher than their concentration in earlier experiments, thus increasing the upper bounds limits of μ_{axf} and μ_{amf} above the

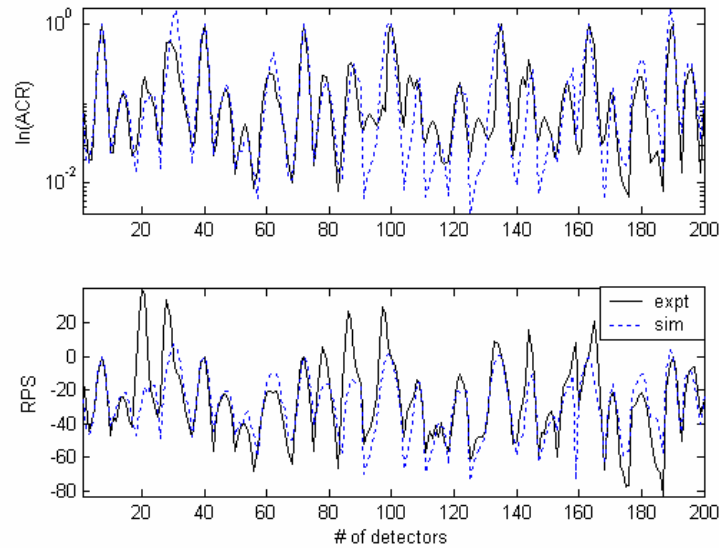


Figure 9.7 Comparison plots between referenced measurements and simulations (using coarse finite element mesh) in terms of $\ln(\text{ACR})$ and RPS (in degrees), plotted for a subset of the total measurements acquired. The mean and variance of errors in $\ln(\text{ACR})$ were 0.108 and 0.558, respectively. Similarly, the mean and variance of errors in RPS (in radians) were 0.062 and 0.080, respectively.

previously set upper limits of 0.8 cm^{-1} and 0.11 cm^{-1} , respectively. The reconstructions converged and convergence plot is shown in Figure 9.8. Note that in all these reconstructions, the reconstruction parameter was assumed constant in the cylindrical portion of the breast phantom and the reconstructions were only performed in the hemispherical portion of the breast phantom.

Discretization of the finite element mesh affected the reconstruction of all the three small volume targets. When a coarsely discretized phantom with 6956 nodes (termed as *coarse mesh*) was employed, one of the three targets was not completely

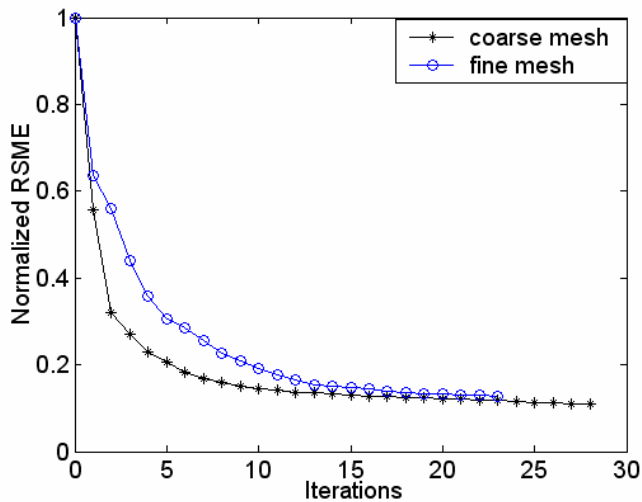


Figure 9.8 Convergence plots of the multiple target experiment, using coarse and fine mesh during image reconstructions.

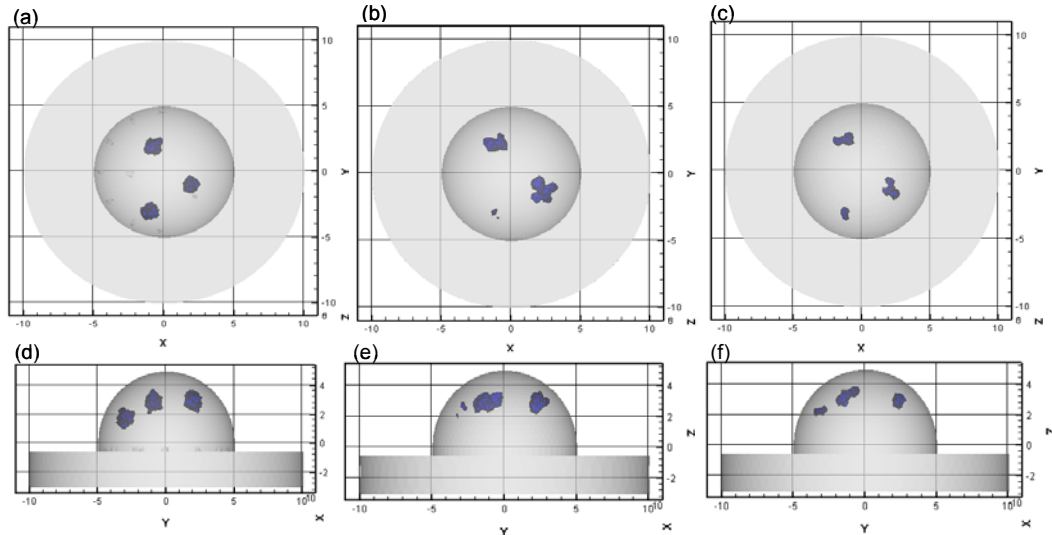


Figure 9.9 y-x and y-z planar views of the actual breast phantom (a,d), reconstructed breast phantom using coarse mesh (b,e) and reconstructed breast phantom using fine mesh (c,f). Three targets of 0.5~0.6 cc volume were used in the actual breast phantom of ~1087 cc volume and illuminated using single point illumination geometry. All the reconstructions were performed using initial guess of $\mathbf{P}=0.001$ and $\mu_{axf}=0.001 \text{ cm}^{-1}$.

reconstructed and appeared as an artifact (see Figure 9.9b), although the reconstructions converged. However, when a fine discretized phantom with 18105 nodes (termed as *fine mesh*) was employed and reconstructions were performed under similar initial conditions as that used for the coarsely discretized phantom, the three targets were distinctly located without any artifacts, although the perturbation of the fluorescent signal originated from the three small targets, which contributed to less than 0.6 % of the hemispherical portion of the breast phantom volume (262 cm^3) (see Figure 9.9c) [126]. This result could possibly be attributed to the level of finite element mesh discretization, wherein the distance between two consecutive nodes in the mesh, if equivalent to the radius of the target, could reduce the probability of reconstructing the target. In addition, the reconstructed target that appears more as an artifact in a coarsely discretized phantom was located farther away from all the point illuminations (or sources), thus contributing towards a weaker fluorescent signal during image reconstructions in either of the discretized phantoms. It is noteworthy that these breast phantom studies that attempt to mimic the multifocality of lesions within the breast are preliminary and future work will assess the significance of discretization for detecting small volume targets.

Quantitative details of the image quality of the reconstructed images are tabulated in Table 9.5 and 9.6 for the coarse and fine mesh used during reconstructions, respectively. Each target's volume and location were evaluated by setting an iso-surface cut-off value for μ_{axf} based on the break between modes in the histogram of the reconstructed μ_{axf} (Figure 9.10), in each quadrant of the hemispherical phantom that

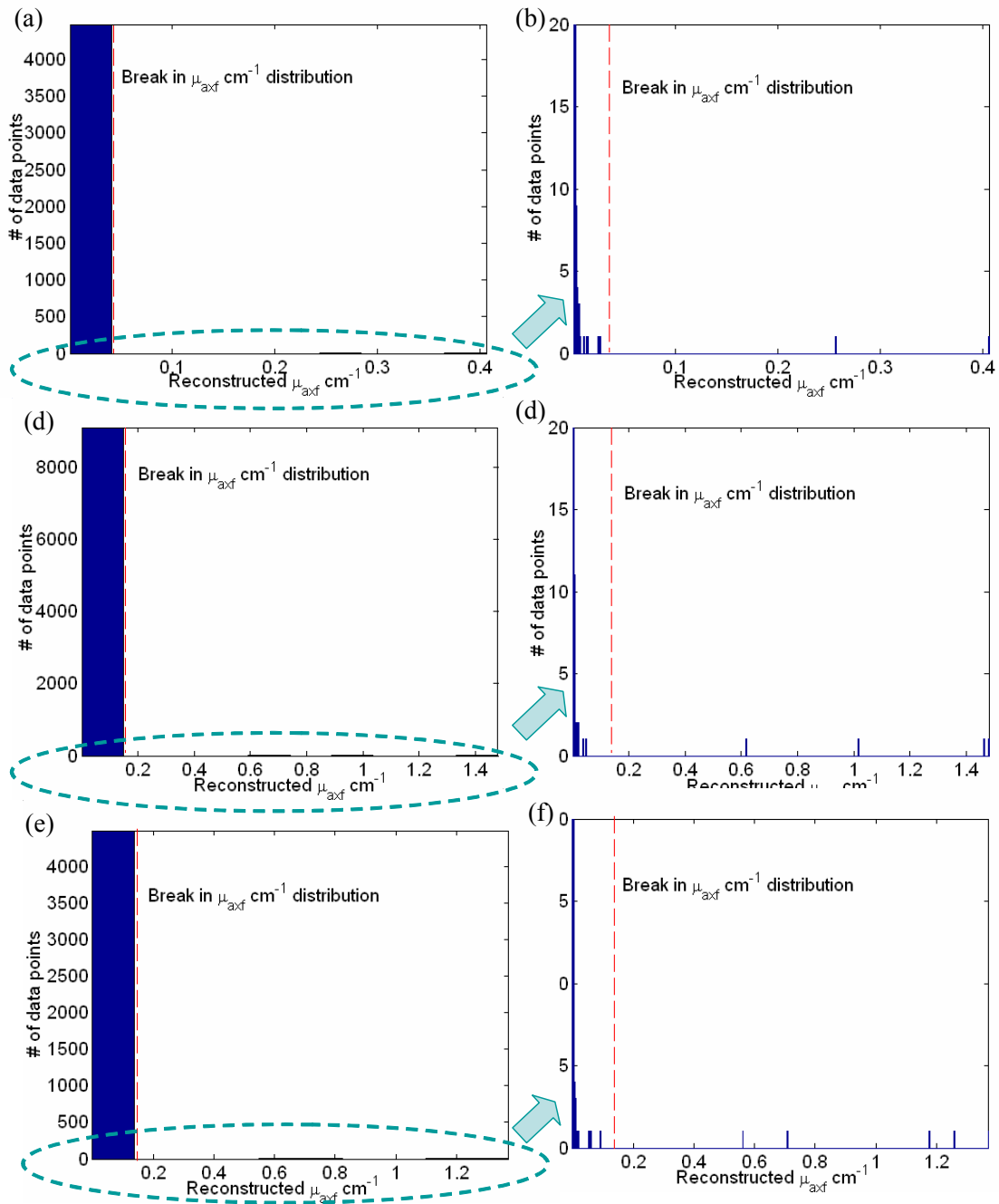


Figure 9.10 Histograms of reconstructed parameter, μ_{axf} (absorption coefficient due to the fluorophores) for the multiple small volume target experiment, under perfect uptake conditions. μ_{axf} distribution obtained in the finely discretized phantom is plotted separately for regions (a,b) $x < 0$ & $y < 0$, (c,d) $y > 0$, and (e,f) $x > 0$ & $y < 0$. (b,d,f) are the same histograms of (a,c,e), respectively, but zoomed in y-axis and plotted using 500 bins.

Table 9.5 Details of the reconstructed images in the multiple small volume target study, using the coarsely discretized phantom (for $P=0.001$).

Target	True centroid (cm)	Region of interest	Max μ_{axf} region (cm^{-1})	μ_{axf} cut-off value	Volume (cm^3)	Integrated μ_{axf} (cm^2)	Distance off (cm)	Reconstructed centroid (cm)
1	[-1 -3 1.8]	$x < 0$ & $y < 0$	0.11	0.03	0.42	0.03	0.50	[-1.1 -3.0 2.3]
2	[-1 2 2.9]	$y > 0$	1.07	0.22	0.30	0.25	0.28	[-1.1 2.2 2.8]
3	[2 -1 3]	$x > 0$ & $y < 0$	1.08	0.4	0.24	0.24	0.12	[2.1 -1.1 3.0]

Table 9.6 Details of the reconstructed images in the multiple small volume target study, using the finely discretized phantom (for $P=0.001$).

Target	True centroid (cm)	Region of interest	Max μ_{axf} region (cm^{-1})	μ_{axf} cut-off value	Volume (cm^3)	Integrated μ_{axf} (cm^2)	Distance off (cm)	Reconstructed centroid (cm)
1	[-1 -3 1.8]	$x < 0$ & $y < 0$	0.41	0.02	0.13	0.02	0.61	[-1.3 3.1 2.3]
1	[-1 -3 1.8]	$x < 0$ & $y < 0$	0.41	0.05	0.07	0.02	0.59	[-1.3 -3.1 2.3]
2	[-1 2 2.9]	$y > 0$	1.48	0.2	0.15	0.18	0.35	[-1.4 2.3 3.0]
3	[2 -1 3]	$x > 0$ & $y < 0$	1.37	0.2	0.18	0.19	0.33	[2.1 -1.3 3.2]

showed a possible target in the reconstructed images (see Figures 9.9b,c). From Table 9.6, we observe that even a small variation in the iso-surface cut-off value for μ_{axf} impacted the evaluated target volume, but not the reconstructed centroid of the target location.

In addition, the reconstructed images were plotted by setting the iso-surface cut-off values based on the contour levels of the μ_{axf} distribution, whereas the quantitative analysis of the target volume was based on the break between modes in the histograms of the μ_{axf} distribution. It was not possible to plot the reconstructed images based on the individual iso-surface cut-off values for each of the three targets, and hence the target size appearing in the reconstructed images (Figures 9.9b,c) do not match with the quantitatively evaluated target volume given in Table 9.5 and 9.6.

9.4 Summary

Tomographic studies using small volume single and multiple targets have been demonstrated from two experimental studies performed under perfect uptake conditions. From these studies we infer the following:

- (i) A single 0.5 cc target located 2-cm and deeper could not be precisely reconstructed in terms of its location. Although a single target was reconstructed without any artifacts, the target was reconstructed closer to the phantom surface (in terms of its depth) in comparison to its true location, similar to our observations in depth studies, when a 1 cc target was located 3 cm deep under imperfect uptake conditions.

- (ii) Owing to the faint fluorescent signal collected at the tissue surface from small volume targets located in non-fluorescing background, the “noise” floor attributed to excitation light leakage through conventional optical interference filters, remains the limiting factor in detecting deeply embedded small volume targets. For example, the excitation light that reaches the end of a fiber optic is *at least* 3-4 orders of magnitude higher than the fluorescent signal collected in our studies. Rejection of excitation light with interference filters with “typical” optical densities of 4-5 will result in a high “noise” floor and limit the sensitivity of detecting deep or weakly fluorescing lesions, as observed from our depth studies (Section 8). While FDPM measurements alleviate the “noise floor” owing to ambient light [12] in comparison to time-domain, or CW measurements, excitation light leakage remains a limitation of the technique.
- (iii) Discretization may be significant in locating small volume targets, as observed from the multiple small volume target study. A finely discretized phantom located the targets more distinctly over a coarsely discretized phantom although at the cost of computational time and memory requirements during image reconstructions. Hence, development of alternate methods such as adaptive finite element meshing and boundary element methods are currently in progress (at PML and University of Vermont), in order to overcome the discretization problems.
- (iv) The current studies performed towards detecting single small volume targets and multiple small volume targets that mimic the multi-focality of lesions in a clinical situation, were carried out under perfect uptake conditions only. Future work will

involve similar experiments under imperfect uptake conditions, where fluorophores are also present in the background.

Following the absorption contrast studies performed under varying target depths (1-3 cm deep), target volumes (0.5-1 cc), absorption optical contrast ratios (1:0 and 100:1), and number of targets (1-3), fluorescence lifetime contrast experiments were carried out in the following major section.

10. PRELIMINARY LIFETIME STUDIES

Studies performed so far were related to the target:background optical contrast in the absorption coefficient due to the fluorophore (μ_{axf}) between the target and the background using a single fluorescing agent (ICG). Here, experiments were performed with a contrast in the lifetime of the fluorescing dye between the target and the background, along with the absorption contrast. Two different fluorescing agents with varying fluorescence lifetime (ICG and DTTCI) were used in the target and the background. Details of the lifetime-based experiments and data analysis performed are described in this chapter.

Before performing the lifetime studies, the effect of using DTTCI as the fluorescing contrast agent was analyzed, since the dye was unstable, unlike ICG which was stabilized using polyaspartic acid.

10.1 Effect of the unstable DTTCI on lifetime studies

The ability to acquire fluorescence measurements with adequate signal using the unstable DTTCI dye was assessed by performing an absorption contrast study using DTTCI. Here 1 μM of DTTCI in 1% Liposyn was used in the 1cc target, which was located ~ 1 cm deep from the phantom surface, in order to perform experiments under perfect uptake conditions (similar to that performed using ICG as the fluorescing dye as described in Section 7). Fluorescence measurements were acquired from many single

point excitation sources from the hemispherical surface of the phantom. Some of measurements were repeated at the end of data acquisition in order to determine any decrease in the fluorescent intensity, which may occur due to the unstable nature of DTTCI. No significant decrease in the fluorescent intensity was observed during the entire time of data acquisition (which was less than one hour). Also, a good model match was observed between the referenced measurements and simulations from the forward model. The reconstructions performed using μ_{axf} as the unknown parameter converged in 30 iterations and the target was located successfully without any artifacts, as shown in Figure 10.1. From this preliminary study, we can conclude that DTTCI can be applicable for performing absorption contrast studies and thus even the lifetime studies, since the dye remained stable during the entire data acquisition time. However, if the total data acquisition time increases enormously, the instability in the dye may affect the acquired fluorescence measurements, and hence the image reconstructions.

10.2 Experimental parameters for lifetime studies

Experiments were performed using ICG and DTTCI, alternately in the target and the background, providing a fluorescence lifetime contrast along with the absorption contrast. In all the lifetime-based studies, 1 cc volume target filled with either of the two dyes and 1% Liposyn solution was located approximated 1 cm deep from the hemispherical phantom surface, and the background phantom was filled with the second

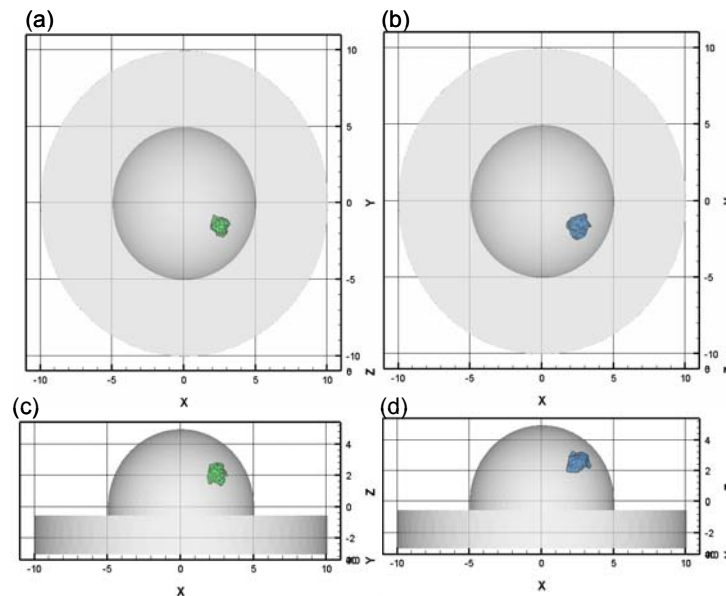


Figure 10.1 x-y and x-z planar views of the actual breast phantom (a,c), and the reconstructed breast phantom using coarse mesh (b,d). A single target of 1.0 cc volume was used in the actual breast phantom of $\sim 1087 \text{ cm}^3$ volume and illuminated using single point illumination geometry. Reconstructions shown here are for μ_{axf} as unknown parameter performed with initial guess of $\mathbf{P}=0.001$, $\mu_{axf}=0.001 \text{ cm}^{-1}$. The iso-surface cut-off value was chosen as $\mu_{axf}=0.1 \text{ cm}^{-1}$.

Table 10.1 Experimental conditions in lifetime studies using ICG and DTTCI fluorescing contrast agents.

Expt	Illumination geometry	$\phi \cdot \mu_{axf}$ contrast	τ contrast	# of sources used	# of measurements acquired	# of measurements used in reconstructions
DTTCI in target	Single sources	150:1	2:1	24	1856 = (15+14)*64	1068
ICG in target	Single sources	150:1	1:2	24	1728 = (15+14)*64	1044

dye and 1% Liposyn solution. Details of the measurement illumination geometry, the fluorescence yield ($\phi \bullet \mu_{axf}$) and lifetime contrast ratios used, and the number of fluorescence measurements acquired are given in Table 10.1. The quantum efficiency of the two dyes was different and thus, by considering the optical contrast in terms of fluorescence yield (instead of μ_{axf} alone), there is consistency in comparing the total number of fluorescence molecules emitted from the target to that from the background. Optical properties of the target and the background phantom in each experiment are also tabulated (see Table 10.2).

10.3 Model match and measurement errors

The referenced fluorescence measurements were compared to the simulations from the forward model and the comparison plots for both the experimental cases are provided in Figures 10.2 and 10.3, respectively.

Table 10.2 Optical properties in the fluorescence lifetime contrasted experimental studies.

Parameter	DTTCI in target		ICG in target	
	Target	Background	Target	Background
μ_{axi} (cm ⁻¹)	0.023	0.023	0.023	0.023
μ_{axf} (cm ⁻¹)	0.211	0.003	0.448	0.002
μ_{ami} (cm ⁻¹)	0.029	0.029	0.029	0.029
μ_{amf} (cm ⁻¹)	0.027	0.0005	0.076	0.0003
μ_{sx} (cm ⁻¹)	9.99	9.99	9.99	9.99
μ_{sm} (cm ⁻¹)	9.67	9.67	9.67	9.67
τ (sec)	1.18x10 ⁻⁹	0.56x10 ⁻⁹	0.56x10 ⁻⁹	1.18x10 ⁻⁹
ϕ	0.034	0.016	0.016	0.034

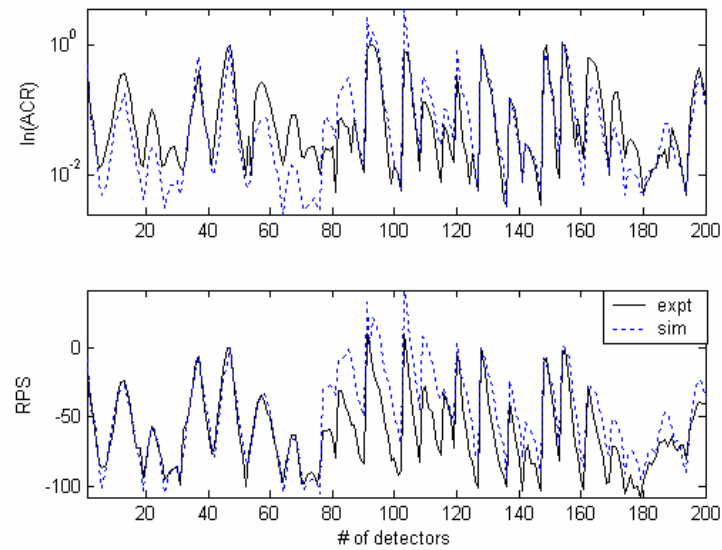


Figure 10.2 Comparison plot of $\ln(\text{ACR})$ and RPS (in deg) for the experiment with 150:1 absorption optical contrast and 2:1 lifetime optical contrast (i.e. DTTCI in target). A random subset of the total number of detections is presented here.

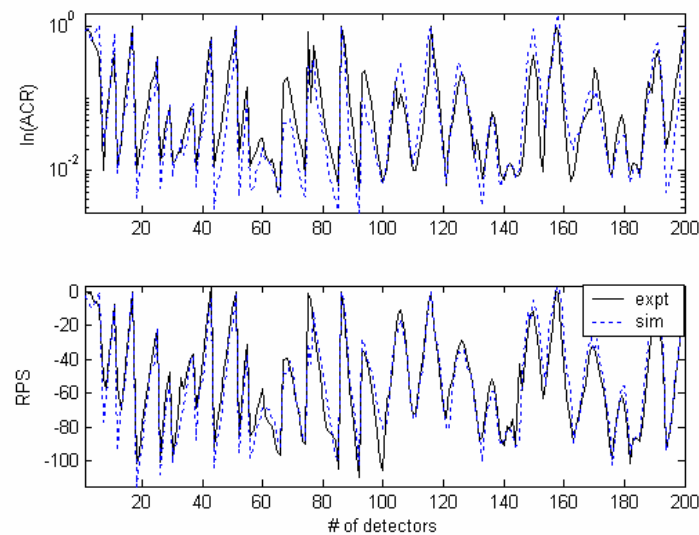


Figure 10.3 Comparison plot of $\ln(\text{ACR})$ and RPS (in deg) for the experiment with 150:1 absorption optical contrast and 1:2 lifetime optical contrast (i.e. ICG in target). A random subset of the total number of detections is presented here.

Table 10.3 Mean and variance of errors in the model match comparison of $\ln(\text{ACR})$ and RPS in both the lifetime studies.

Experiment	$\phi \bullet \mu_{axf}$ contrast	τ contrast	$\ln(\text{ACR})$		RPS (radians)	
			Mean	Variance	Mean	Variance
DTTCI in target	150:1	2:1	0.132	0.686	-0.131	0.043
ICG in target	150:1	1:2	0.157	0.585	-0.032	0.031

Table 10.4 Measurement error (mean of variance) in $\ln(\text{ACR})$ and RPS for both the lifetime studies.

Experiment	$\phi \bullet \mu_{axf}$ contrast	τ contrast	Mean[$\sigma^2(\ln(\text{AC}))$]	Mean[$\sigma^2(\theta)$] (radians)
DTTCI in target	150:1	2:1	0.0026	0.022
ICG in target	150:1	1:2	0.0021	1.231

From the plots, we observe a good model match in RPS compared to the model match in RPS when there was no lifetime contrast. This is due to the enhanced phase contrast obtained from the lifetime difference between the target and the background, which in turn improved the strength of the measured signal. The mean and variance of errors in terms of $\ln(\text{ACR})$ and RPS are given in Table 10.3.

The measurement error was also evaluated and provided in Table 10.4. In comparison to absorption contrast studies under imperfect uptake conditions of a target located $\sim 1\text{cm}$ deep, the measurement error was relatively smaller, especially in phase.

The phase contrast increases due to the lifetime contrast present between the target and the background, probably accounting for the decrease in the measurement error as well.

10.4 Image reconstructions using μ_{axf} as the reconstructing parameter

Reconstructions on lifetime studies can be performed using two different approaches: (i) reconstructing on both μ_{axf} and fluorescence parameters (τ and ϕ) simultaneously, or (ii) reconstructing on μ_{axf} and fluorescence parameters (τ and ϕ), sequentially. Currently, the AEKF reconstruction algorithm is set to work using only the μ_{axf} as the unknown parameter assuming that the rest of the optical parameters as known quantities. Hence, as an initial step in lifetime studies, we assumed that the second approach of sequentially reconstruction of μ_{axf} and $(\tau+\phi)$ is feasible and thus perform reconstructions on μ_{axf} . In these reconstructions, with μ_{axf} as the unknown parameter, the fluorescing lifetime and the quantum efficiency was assumed constant and equal to the lifetime of the fluorescing agent present in the background. Reconstructions were performed with an initial guess in $\mu_{axf} = 0.001 \text{ cm}^{-1}$ and different initial guesses of \mathbf{P} (0.001, 0.01, and 0.1). The measurements were filtered at only at individual detector level, where only measurements whose modulation depth was greater than 0.025 were included during reconstructions (see last column of Table 10.1). Since fluorescence was present in the target and the background (similar to imperfect uptake case), measurements could not be filtered based on the excitation light leakage.

The reconstructions converged in both the experimental cases and the convergence plots for reconstructions for initial guess of $\mathbf{P}=0.001$ are presented in Figure 10.4. In the experimental case, where DTTCI was located in the target, the target was reconstructed very close to its true location with no artifacts as shown in Figure 10.5. However, in the case where ICG was present in the target and DTTCI was present in the background, many artifacts were observed in the reconstructed phantom, enhancing the difficulty in locating the target visually (see Figure 10.6). Quantitative estimates of the target volume and location are provided in Table 10.5 for both the experimental conditions.

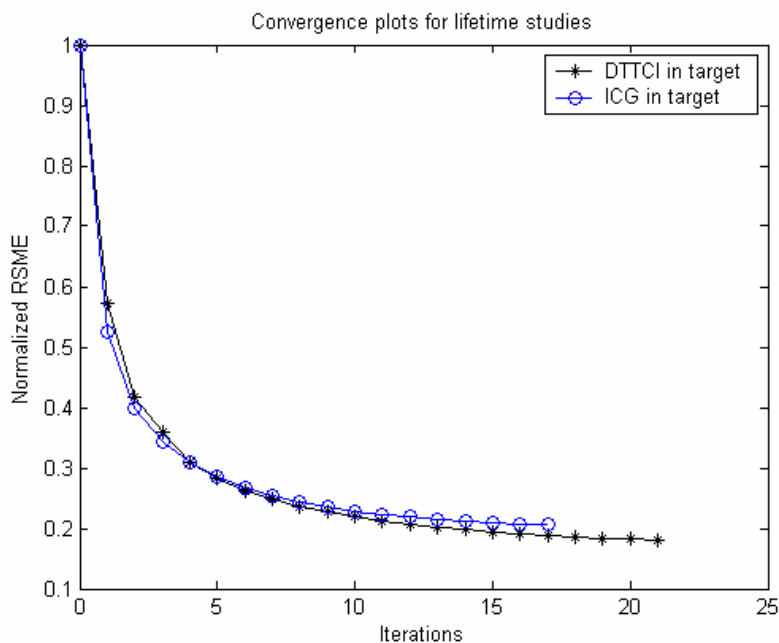


Figure 10.4 Convergence plots in reconstructions performed using μ_{axf} as the unknown parameter in both the lifetime studies. During reconstructions, initial guess of μ_{axf} and \mathbf{P} was assumed equal to 0.001 cm^{-1} and 0.001 , respectively.

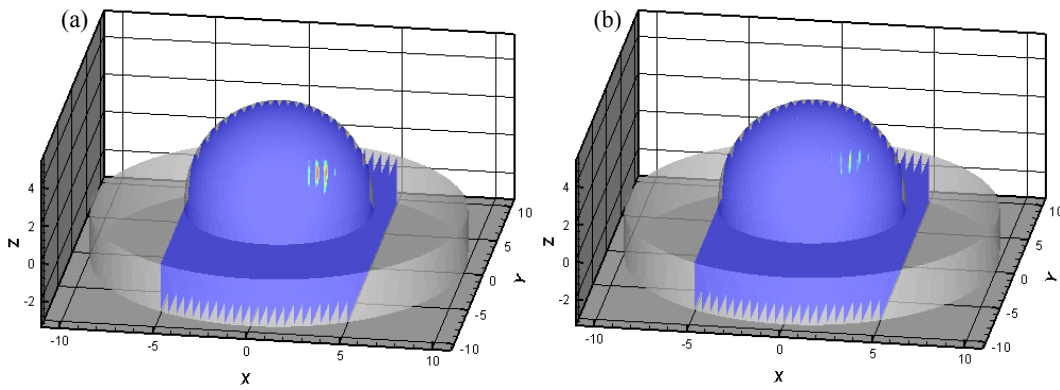


Figure 10.5 Contour slices in the x-plane (between $\langle -5, 5 \rangle$ cm) of the (a) actual phantom, and (b) reconstructed phantom when DTTCI was present in the target and ICG was present in the background. During reconstructions, $\tau = 0.56$ nsec, $\phi = 0.016$ was assumed constant for the entire phantom.

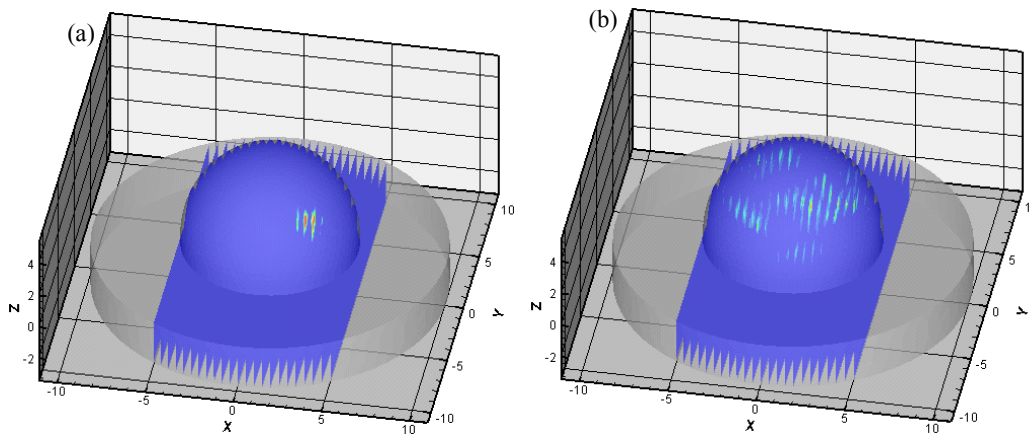


Figure 10.6 Contour slices in the x-plane (between $\langle -5, 5 \rangle$ cm) of the (a) actual phantom, and (b) reconstructed phantom when ICG was present in the target and DTTCI was present in the background. During reconstructions, $\tau = 1.18$ nsec, $\phi = 0.034$ was assumed constant for the entire phantom.

Table 10.5 Image quality of the actual and reconstructed phantoms for both the lifetime experiments, when $\mathbf{P} = 0.001$ and $\mu_{axf} = 0.001 \text{ cm}^{-1}$ are the initial guesses during reconstructions.

Experimental case	μ_{axf} cut-off value (cm^{-1})	Centroid			Integrated μ_{axf} (cm^2)	Volume (cm^3)	Distance off (cm)
		X(cm)	Y(cm)	Z(cm)			
Actual case for 2:1 τ contrast	--	2.5	-1.5	2.2	0.21	1.0	--
Reconstructed 2:1 τ contrast	0.15	2.4	-1.4	2.7	0.13	0.13	0.53
Actual case for 1:2 τ contrast	--	2.5	-1.5	2.2	0.45	1.0	--
Reconstructed 1:2 τ contrast	0.01	0.5	-1.2	2.9	0.08	4.1	2.13

10.5 Summary

From these preliminary reconstructions with μ_{axf} as the reconstructing parameter, we observe that when the lifetime contrast was 2:1 in the real system, the measurements reconstructed to locate the target very close to its true location. Hence, using the reconstructed μ_{axf} values as the initial guess for μ_{axf} distribution, we could possibly reconstruct on τ and ϕ . Thus the second approach for reconstructing μ_{axf} and $(\tau+\phi)$ seems feasible when the lifetime was greater in the target over the background (2:1). However, from the reconstructions with 1:2 lifetime contrast, the artifacts mask the location of the target, thus making the sequential reconstruction approach not feasible. Although, more work needs to be performed in terms of (i) performing more experiments under varying experimental conditions and validating our preliminary conclusions from the current studies, and eventually (ii) modifying the AEKF algorithm to accommodate both the

reconstruction approaches required to perform reconstructions on μ_{axf} and $(\tau + \phi)$ of the fluorescing agents.

Here, preliminary lifetime studies were performed in order to determine the model match and also evaluate the measurement errors during experimentation, for future reconstruction studies on lifetime.

11. HOMOGENEOUS PHANTOM STUDIES

Experimental studies presented thus involved the presence of single or multiple targets of varying volume, depth, and optical contrast ratio (both in absorption coefficient due to the fluorophore, μ_{axf} and fluorescence lifetime, τ). All these studies were performed in order to indicate the true positive rate (that is, detect targets when they are actually present) of the ICCD imaging system. In the current study, experiments were performed under homogeneous (or no target) conditions of the phantom in order to evaluate the false positive rate (that is, detect the absence of targets) of the ICCD imaging system.

Homogenous phantom studies performed under two different experimental conditions will be described herein in terms of their model match comparisons and 3-D image reconstructions.

11.1 Homogeneous phantom study (Experiment # 1)

The first homogeneous phantom study (experiment # 1) was carried out in the absence of targets. The entire phantom was filled with 0.01 μM fluorescing agent (ICG) in 1% Liposyn solution (Figure 11.1). The optical properties of the homogeneous background are given in Table 11.1. Fluorescence measurements were acquired along the entire hemispherical surface of the phantom using single point illumination and point collection measurement geometry and the details are provided in Table 11.2.

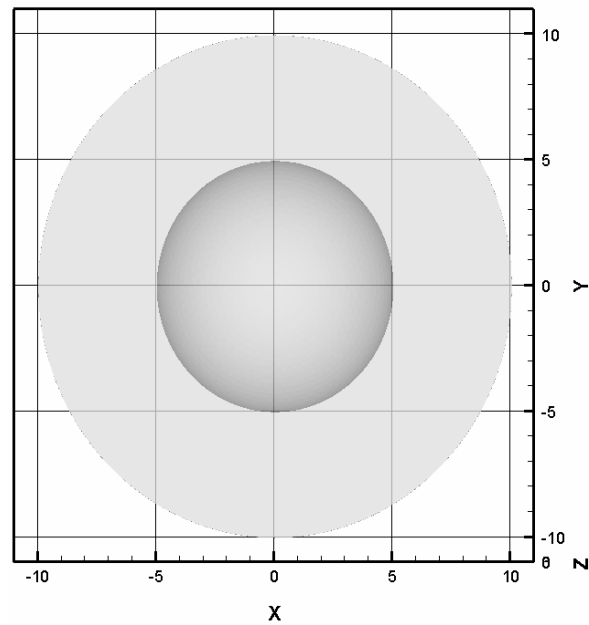


Figure 11.1 x-y plot of the homogeneous phantom study (Experiment # 1) in the absence of targets.

Table 11.1 Optical properties of the background phantom during the homogeneous phantom study (Experiment # 1).

Optical Properties	Background (Expt # 1)
$\mu_{axf} + \mu_{axi} \text{ (cm}^{-1}\text{)}$	0.003+0.023
$\mu_{sx} \text{ (cm}^{-1}\text{)}$	9.99
$\mu_{amf} + \mu_{ami} \text{ (cm}^{-1}\text{)}$	0.0005+0.029
$\mu_{sm} \text{ (cm}^{-1}\text{)}$	9.67
$\tau \text{ (nsec)}$	0.56
ϕ	0.016

Table 11.2 Experimental conditions of the homogeneous phantom study (Experiment # 1).

Expt	# of source combinations	# of acquired measurements	# of measurements used in reconstructions
1	23	1472	787

11.1.1. Model match and measurement errors

A good model match was observed between fluorescence measurements and simulations as shown in Figure 11.2. The corresponding model mismatch errors and the measurement errors (obtained from five repeated measurements, $rep=5$), are provided in Table 11.3 and 11.4, respectively.

11.1.2. Image reconstructions

Image reconstructions were performed assuming initial guess of 0.001 cm^{-1} and 0.001 for μ_{axf} and parameter error covariance (\mathbf{P}) constant for the entire phantom. As mentioned in earlier major sections, there is no definite method yet in choosing the initial \mathbf{P} , and work is continuously in progress to determine a better way to estimate the initial guess for parameter error covariance (\mathbf{P}). In these reconstructions, measurements whose modulation depth was < 0.025 were not included during inversions (see last column of Table 11.2). The convergence curves and the reconstructed image, which is presented as contour slices along the y-axis, are shown in Figures 11.3 and 11.4, respectively.

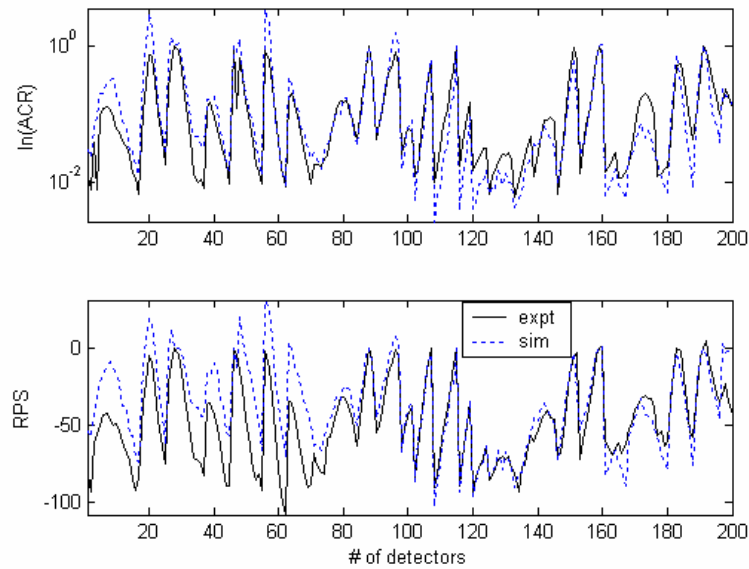


Figure 11.2 Model match between experiments and simulations in terms of $\ln(\text{ACR})$ and RPS (in deg) for Expt # 1 in the homogeneous studies, plotted for a subset of measurements from the total number of acquired measurements.

Table 11.3 Model mismatch errors in $\ln(\text{ACR})$ and RPS for the homogeneous phantom study (Experiment # 1).

Expt	Measurement geometry	$\ln(\text{AC Ratio})$		Relative phase shift (RPS) (radians)	
		Mean	Variance	Mean	Variance
1	Single sources	0.126	0.590	-0.114	0.120

Table 11.4 Measurement errors for the homogeneous phantom study (Experiment # 1).

Expt	Measurement geometry	$\text{Mean}[\sigma^2(\ln(\text{AC}))]$	$\text{Mean}[\sigma^2(\theta)]$ (radians)
1	Single sources	0.0030	0.053
2	Single sources	0.0026	0.041

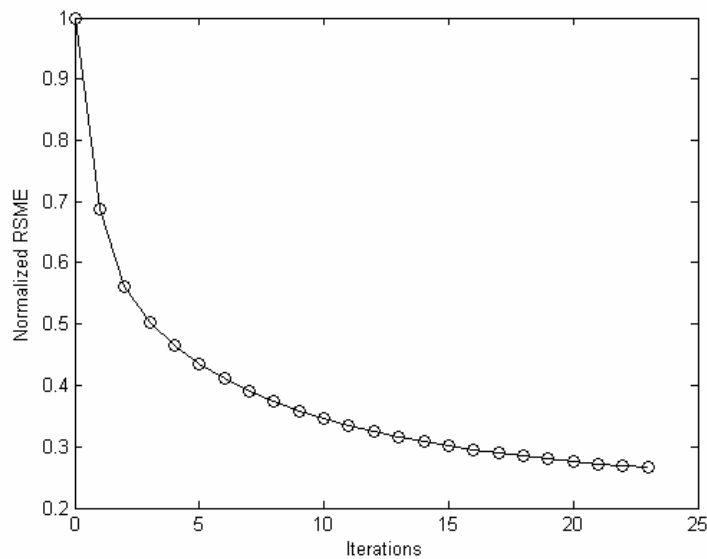


Figure 11.3 Convergence plot for homogeneous phantom study (Experiment # 1).

From the contour-sliced plot, we observe that the reconstructed parameter, μ_{axf} (absorption coefficient due to the fluorophores) was not homogeneous (or uniform) throughout the entire phantom, but was higher at different regions in the phantom.

Although the regions of higher μ_{axf} values were not confined to a particular location, such that the confined location can be considered as a potential target, these higher μ_{axf} valued regions were observed almost throughout the hemispherical portion of the phantom where fluorescence measurements were acquired. However, it is not certain that each region of increased μ_{axf} values (also termed as *artifact*) with respect to the background is a potential target. In order to validate that the observed artifact may not be a potential target, a second experiment under different experimental conditions was carried out and is presented in the following section.

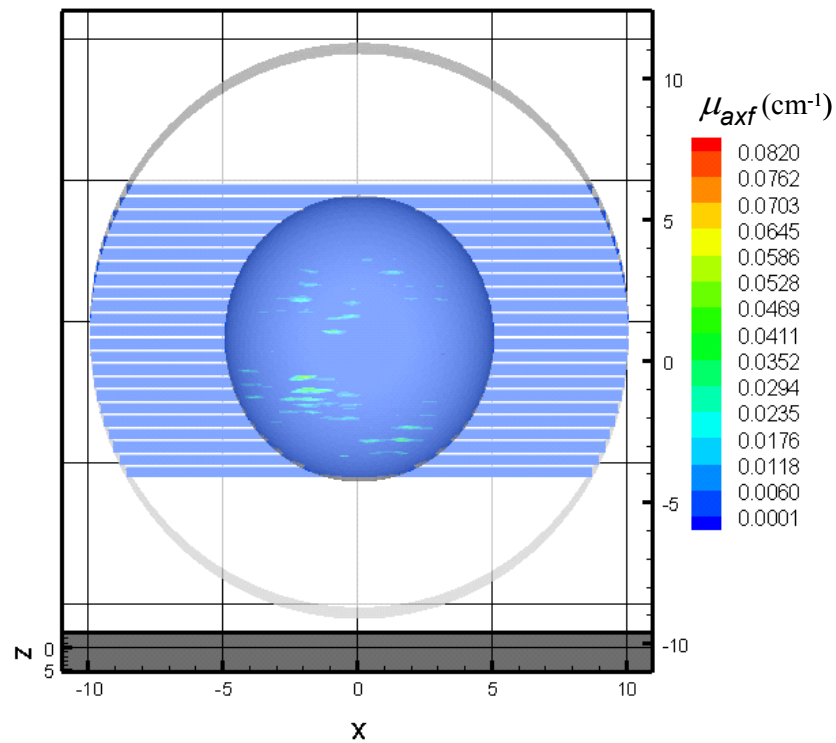


Figure 11.4 Contour slices in y-plane of the reconstructed image corresponding to the homogeneous phantom (Experiment # 1).

11.2 Homogenous phantom study (Experiment # 2)

Unlike the homogeneous phantom study (experiment # 1) in which no target was present during the experiment, the current phantom study involved a single 1 cc target located in a single quadrant of the hemispherical portion of the breast phantom (~ 1 cm deep from the hemispherical surface with its centroid at $\langle 2.5, -1.5, 2.2 \rangle$ cm) (see Figure 11.5).

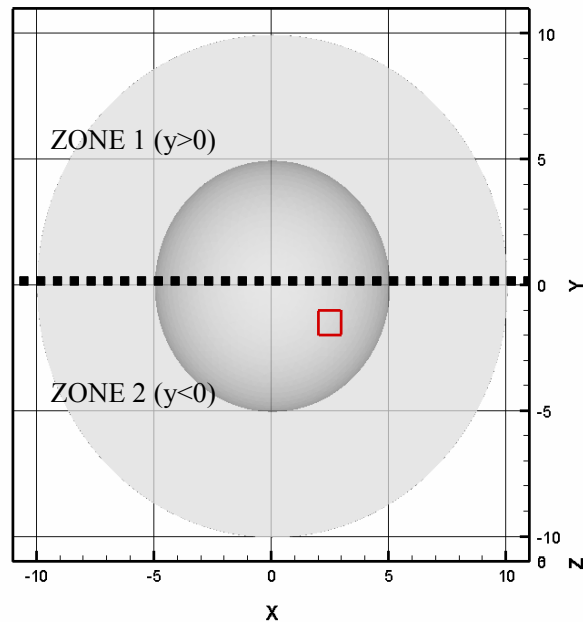


Figure 11.5 x-y plot of the homogeneous phantom study (Experiment # 2), containing a single 1 cc target (red square) located in zone 2 ($y < 0$) region. Zone 1 ($y > 0$), which is the region above the dotted line, is considered homogeneous. Zone 2 ($y < 0$), which is the region below the dotted line, is considered heterogeneous (that is, target present case).

Although an optical contrast was present between the target and the background, the fluorescence measurements acquired farther away from the target's location did not include the perturbation signal generated by the fluorescently contrasted target. The intensity of the perturbation fluorescent signal diminished as it propagated within deep tissues (maximum penetration of 10 cm in the current breast phantom), before it was detected at the tissue surface, because of the exponentially attenuating nature of the propagated light. In other words, the fluorescence measurements acquired from zone 1 ($y > 0$ cm) (see Figure 11.5) may not reconstruct the target located in zone 2 ($y < 0$ cm), because the points of illumination and detection in zone 1 were located farther away

from the target. Hence, the phantom can be considered as a homogeneous phantom in zone 1.

The current homogeneous study was performed in order to analyze: (i) if the fluorescence measurements acquired only from zone 1 reconstructed a homogeneous phantom or was indeed capable of locating the target located in zone 2; and (ii) if the fluorescence measurements acquired from both zone 1 and 2 showed any artifacts apart from possibly detecting the true target location. This study may possibly help in differentiating between artifacts and truly reconstructed targets.

11.2.1. Experimental parameters

Herein, the homogeneous background was filled with 0.01 μM fluorescing agent (ICG) in 1% Liposyn solution. The 1 cc volume target, located in the zone 2 region (see Figure 11.5) was filled with a fluorescing agent (DTTCI), with an optical contrast of 150:1 in its fluorescence yield ($\phi \bullet \mu_{axf}$) (same experiment as described in Section 10.2). The optical properties of the target and the homogeneous background are given in Table 11.5. Note that the background optical properties in the current experimental study (experiment # 2) were similar to the optical properties of the previous homogeneous phantom study (experiment # 1). Fluorescence measurements were acquired using the single point illumination geometry. The details are provided in Table 11.6.

Table 11.5 Experimental conditions of homogeneous phantom studies (Experiment # 2).

Expt	Expt type	# of source combinations	# of acquired measurements	# of measurements used in reconstructions
2	Zone 1 alone	13	832	484
2	Entire phantom (zone 1 + zone 2)	24	1856	1068

Table 11.6 Optical properties of the target and the background in the homogeneous phantom study (Experiment # 2).

Optical Properties	Target	Background
$\mu_{axf} + \mu_{axi} \text{ (cm}^{-1}\text{)}$	0.211+0.023	0.003+0.023
$\mu_{sx} \text{ (cm}^{-1}\text{)}$	9.99	9.99
$\mu_{amf} + \mu_{ami} \text{ (cm}^{-1}\text{)}$	0.027+0.029	0.0005+0.029
$\mu_{sm} \text{ (cm}^{-1}\text{)}$	9.67	9.67
$\tau \text{ (nsec)}$	1.18	0.56
ϕ	0.034	0.016

11.2.2. Model match and measurement errors

A good model match was observed between experiments and simulations for the fluorescence measurements acquired in zone 1 (Figure 11.6). The corresponding model mismatch errors and measurements errors were evaluated for the fluorescence measurements in zone 1 and are given in Tables 11.7 and 11.8, respectively. A good model match was also observed when all the fluorescence measurements acquired from

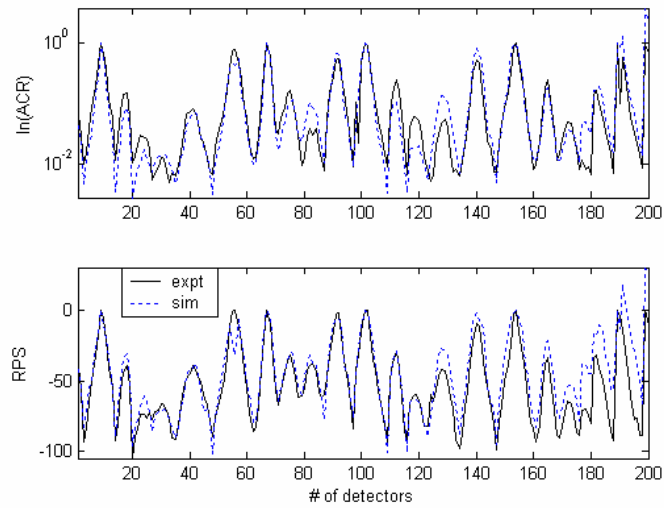


Figure 11.6 Model match between experiments and simulations in terms of $\ln(\text{ACR})$ and RPS for zone 1 of the homogeneous phantom study (Expt # 2), plotting a subset of measurements from the total number of acquired measurements.

Table 11.7 Model mismatch errors in $\ln(\text{ACR})$ and RPS for zone 1 of homogeneous phantom study (Experiment # 2).

Expt	Measurement geometry	$\ln(\text{AC Ratio})$		Relative phase shift (RPS)	
		Mean	Variance	Mean	Variance
2 (zone 1 only)	Single sources	0.178	0.607	-0.110	0.042

Table 11.8 Measurement errors for zone 1 of homogeneous phantom study (Experiment # 2).

Expt	Measurement geometry	Error in $\ln(\text{AC})$	Error in θ
2 (zone 1 only)	Single sources	0.0026	0.041

both zone 1 and 2 were analyzed together (see Figure 10.2), and the corresponding model mismatch errors and measurements errors were presented earlier (Section 10.2).

11.2.3. Image reconstructions

Image reconstructions for experiment # 2 were performed under two different cases: (i) case 1, in which fluorescence measurements were acquired only from zone 1 of the breast phantom; and (ii) case 2, in which fluorescence measurements were acquired from the entire phantom (zone 1 and zone 2). In both the cases (case 1 and 2), reconstructions were performed using similar initial guesses in μ_{axf} (0.001 cm^{-1}) and \mathbf{P} (0.001) as in the reconstructions in experiment # 1. In these reconstructions as well, measurements whose modulation depth was < 0.025 were not included during inversions (see last column of Table 11.5).

Case 1: Reconstructions from case 1 converged (Figure 11.7) and the reconstructed images are plotted as contour slices in y-axis, as shown in Figure 11.8a. Similar to the artifacts observed in the previous homogenous phantom study (experiment # 1), artifacts (or regions of higher μ_{axf} values) were observed in case 1 of the current homogeneous phantom study (experiment # 2). In addition, the artifacts appear throughout zone 1 of the phantom, whose fluorescence measurements were used in case 1 of the image reconstructions.

Case 2: The reconstructions for case 2 converged (Figure 11.7) and a distinct confined region of higher μ_{axf} values was observed at the true location of the target (see Figure 11.8b), unlike many regions of higher μ_{axf} values (or artifacts) that were observed in case

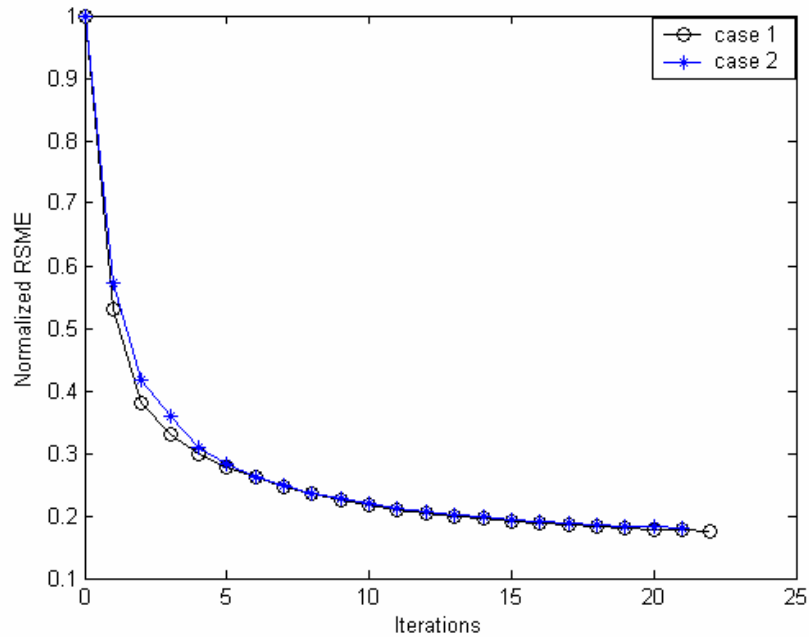


Figure 11.7 Convergence curves for the homogeneous phantom study (Experiment # 2) for both cases using initial $\mathbf{P}=0.001$ and initial $\mu_{axf}=0.001\text{ cm}^{-1}$. Case 1 was reconstructed using data only from zone 1 and case 2 was reconstructed.

1 (see Figure 11.8a). In addition, the maximum value of the reconstructed μ_{axf} in case 2 (0.4736 cm^{-1}) was almost 10 times higher than the maximum value of μ_{axf} in case 1 (0.0456 cm^{-1}). The fluorescence measurements acquired from the boundary surface locations closer to the true target location in case 2 caused an enhanced perturbation of the fluorescence signal, thus masking the presence of any artifacts that were observed in case 1. However, the enhanced perturbation does not imply that the artifacts observed in case 1 of the reconstructions disappeared, but were in fact masked due to the contour level range of the acquired image. This can be demonstrated from Figure 11.9, where the reconstructed images from case 1 and case 2 were plotted with respect to their actual

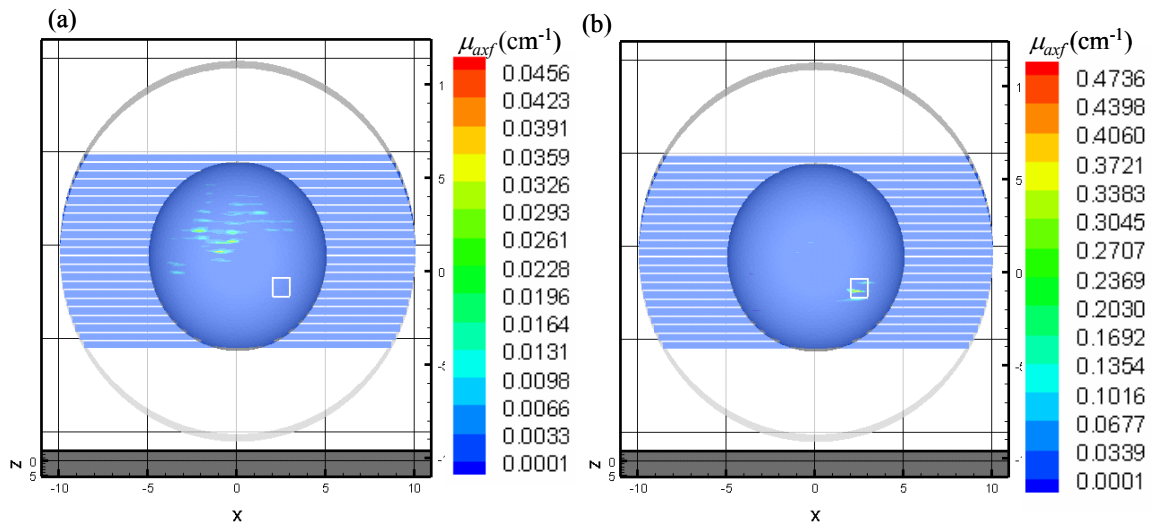


Figure 11.8 Contour slice in y -plane of the reconstructed μ_{axf} distribution in experiment # 2 for (a) case 1, where only measurements from zone 1 were used in the reconstructions, and (b) case 2, where measurements from entire phantom were used in the reconstructions.

reconstructed contour limits ($[0.001, 0.0456] \text{ cm}^{-1}$ and $[0.001, 0.4736] \text{ cm}^{-1}$, respectively), and with respect to the contour limits observed in the alternate case (that is, contour limits from case 1 reconstructions were applied to case 2 reconstructions and vice-versa). From the contour plots in Figure 11.9, we observe that artifacts in zone 1 appear or disappear based on the contour limits set to the reconstructed images. Hence differentiation of the artifacts from truly reconstructed targets is limited by the image assessing technique.

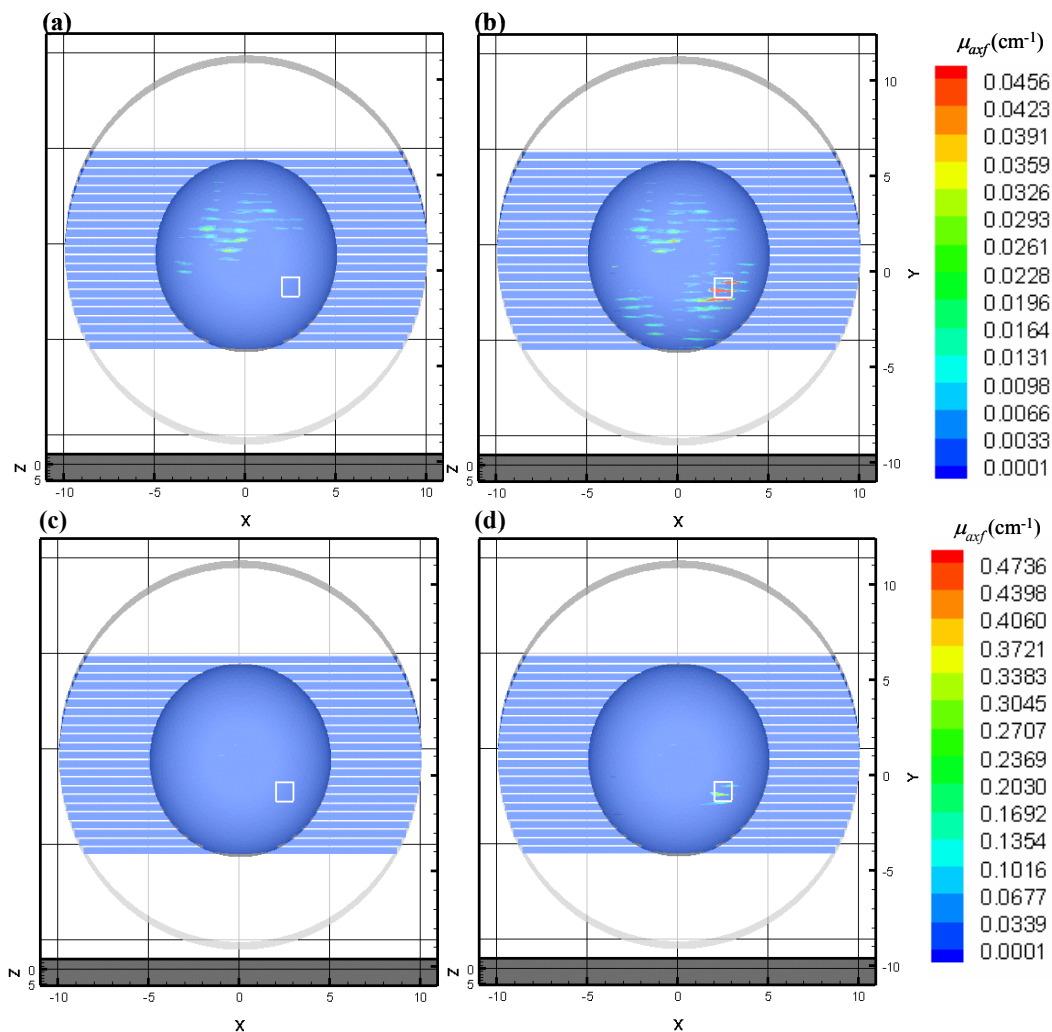


Figure 11.9 Contour slices in y-plane of reconstructed μ_{axf} distribution in experiment # 2 for reconstruction case 1 (a,c), and reconstruction case 2 (b,d). The contour limits for (a,b) was $[0.0001 \ 0.0456] \text{ cm}^{-1}$ and contour limits for (c,d) was $[0.0001 \ 0.4736] \text{ cm}^{-1}$.

11.3. Summary

From the two different homogeneous experimental studies (experiment # 1 and 2), we observe that artifacts (or regions of higher μ_{axf} values) are present throughout the regions from where fluorescence measurements were acquired. However, in the

presence of a true target, these widely spread artifacts are masked due to the enhanced perturbation generated by the true target. Yet, the method of differentiating artifacts from true targets in a reconstructed image is an image assessment problem. Based on the raw reconstructed images, it is incorrect to conclude about the target locations before assessing the quality of images. In addition, in real clinical situations, it is difficult to compare the images using the two reconstruction cases as mentioned above. Thus, image quality assessment is very crucial in differentiating between true and false targets, and may be implemented as a part of the future work.

12. PLANAR SOURCE STUDIES

Fluorescence-enhanced optical tomography studies presented so far involved the use of large volume tissue-mimicking phantoms, where single or dual point illumination and multiple point collection measurement geometry was employed in order to acquire fluorescence measurements from the phantom surface and thus perform 3-D image reconstructions under varying experimental conditions. Alternately, in this study, area illumination and area detection measurement geometry was employed in order to perform image reconstructions from reflectance fluorescence measurements acquired a large volume cubical phantom.

The studies performed using the area illumination/area detection measurement geometry towards tomographic reconstructions was carried out for the first time at Photon Migration Laboratory. The dual point illumination geometry when extended to multiple point illumination geometry through closely placed optical fibers mimic the area (or planar) illumination geometry (see Figure 12.1). The advantages of area illumination/area detection measurement geometry include the following: (i) no optical fibers are required to illuminate or collect the light signal from the phantom surface, but the phantom surface can be illuminated directly via an expanded laser beam, (ii) dense measurements can be obtained rapidly from the region of interest via the ICCD camera, without the use of optical fibers that could possibly limit the density of measurements, and (iii) successful 3-D reconstructions using the current measurement geometry has

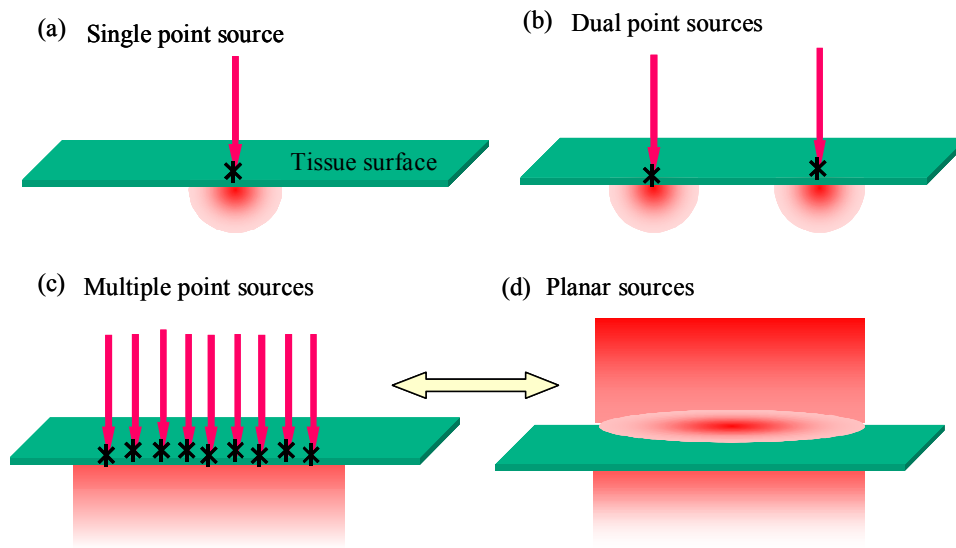


Figure 12.1 Different measurement geometries (a) Sequential point illumination of single excitation sources using optical fibers, (b) Simultaneous point illumination of two excitation sources using optical fibers, (c) Simultaneous point illumination of multiple excitation sources using optical fibers, and (d) Area illumination using an expanded beam of excitation source. (c) and (d) are equivalent, if each point of illumination in the area illumination is assumed to be an individual optical fiber.

greater potential for designing a hand-held probe towards clinical studies such as sentinel lymph node mapping, where only reflectance measurements can be acquired.

The current work is a group effort, with experimental work performed by Dr. A. Thompson [51-52], and image reconstructions performed by Dr. Ranadhir Roy [127]. As a part of my project, the finite-element based forward model that was developed for our major studies using the breast phantom was modified for the current imaging system and the model match between experiments and simulations was assessed before image reconstructions were performed.

Herein, the instrumentation details, experimental procedure, and model match studies will be described. Preliminary 3-D image reconstructions performed by Dr. Roy will also be provided in order to demonstrate the feasibility of the new measurement geometry imaging technique for future clinical applications.

12.1 Phantom details and instrumentation

Large cubical phantoms of $8 \times 8 \times 8 \text{ cm}^3$ volume were used to perform fluorescence-enhanced optical tomography using fluorescence measurements from the top surface of the phantom using the area illumination and area detection measurement geometry. Here, the measurement geometry did not involve any optical fibers to illuminate or collect the light signal. An expanded beam of NIR light was launched over a given area on the top surface of the cubical phantom and the emitted fluorescent signal from the same illuminated area was imaged directly using an ICCD detection system. The phantom was filled with 1% Lipsoyn solution and a 1 cc cubical cuvette was used to represent the target. ICG was used as the fluorescing agent and experiments were performed under varying conditions of target depth (1 and 2 cm deep), and target:background optical contrast ratios (1:0, 100:1, 50:1, and 10:1).

The instrumentation set-up was similar to that used for the breast-phantom system, with modifications to incorporate the current measurement geometry (see Figure 12.2). Modulated light at 100 MHz was launched from a 70-mW laser diode (Model DL7140-201, Thorlabs Inc., Newton, NJ) onto the top surface of the cubical phantom as

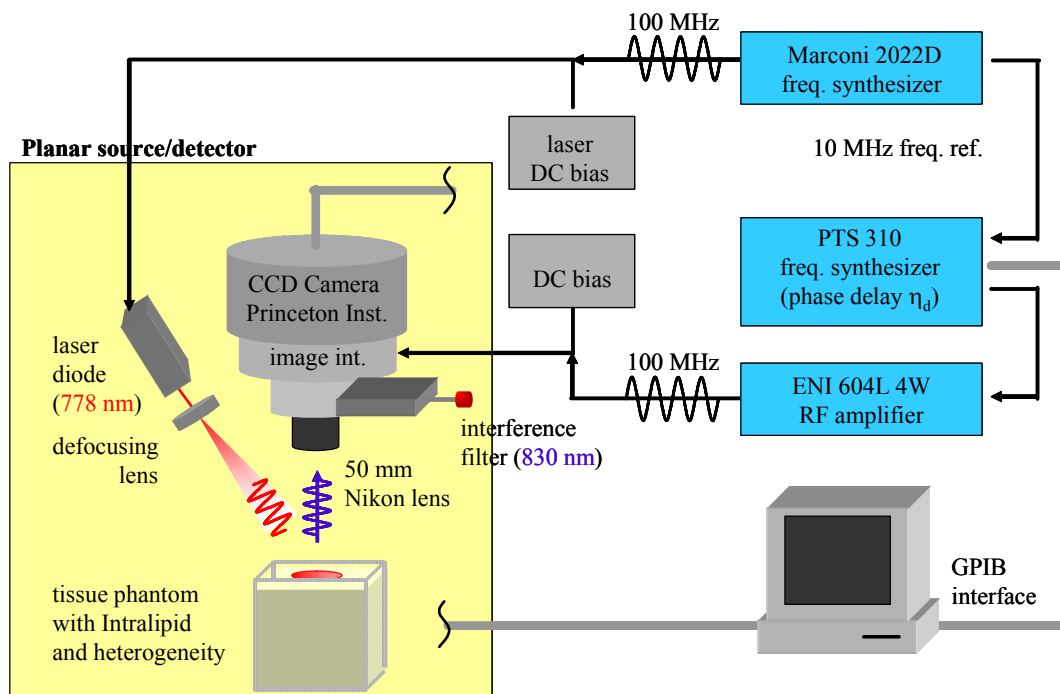


Figure 12.2 Instrumentation set-up for area illumination/area detection measurement geometry, using a cubical phantom of 8x8x8 cc volume.

an expanded beam of ~ 4 cm diameter. The emitted fluorescent signal around the area of illumination was acquired via a 50-mm AF Nikon lens by the photocathode of the image intensifier (Model FS9910C, ITT Night Vision, Roanoke, VA). The photons at the photocathode were converted to electrons, amplified at the photocathode, and reconverted back to photons of a particular wavelength at the phosphor screen. The photons were in turn imaged by the CCD camera (Model S1512B, Series AT200, Photometrics Ltd., Tucson, AZ), which was lens coupled to the phosphor screen of the image intensifier. The laser diode and the photocathode of the image intensifier were modulated at same frequency of 100MHz (*homodyne detection scheme*) using two

different oscillators, which were phase locked using a 10 MHz reference signal. Steady-state images were acquired in a similar manner as in the breast-phantom imaging system, by introducing phase delays between the two oscillators and thus performing FFT in order to obtain amplitude and phase at each detection point. The CCD array was discretized into a 128x128 pixelated 2-D array and the acquired data was stored at these discrete points, although the data represented the entire detected area (~ 4cm diameter). Detailed description of the instrumentation is provided elsewhere [51-52,100] and the experimental work was performed by Dr. Thompson at PML.

12.2 Forward problem formulation

The coupled diffusion equations were used to represent the excitation and emission of the fluorescent signal during light propagation in a turbid medium. The finite-element formulation for the current system was similar to that described in Section 5, except for the formulation of the excitation source term in the coupled diffusion equations (Equations (3.1) and (5.9)).

Representation of the source term in Equation (5.9) can change based on the measurement geometry employed. Point illumination excitation source was represented as

$$S = \sum_{i=1}^n S \delta(\vec{r} - \vec{r}_s) \quad (12.1)$$

where, r_s is the positional vector of the illuminating point, δ is the dirac delta function representing the excitation source as a single point and n is the total number of point illuminations ($n=1$ for single point illumination, and $n=2$ for dual point illumination). For the area illumination geometry, the area of the planar source is discretized into a number of triangular elements and each source element (S_{el}) can be represented as a linear approximation of the source values at the nodes corresponding to the surface element.

$$S_{el} = \sum_{i=1}^3 L_i S_i \quad (12.2)$$

where, L_i is the x-y-z coordinates and S_i is the source value at each node (i) of the triangular element. Based on the type of elements used to discretize the phantom surface the number of nodes (i) corresponding to each element varies. If the discretization were fine, then the source area could possibly be approximated as the summation of multiple point sources as shown in Equation (12.1), where n is the total number of nodes representing the entire discretized source area. The effect of representing the source terms using either of the two methods was also analyzed and presented in Section 12.4.1.

12.3 Experimental parameters

Experiments were performed under varying target:background optical contrast ratios (1:0, 100:1, 50:1, and 10:1) and target depths (1-2 cm deep) using 1cc volume

target and ICG as the fluorescing contrast agent. From all these experimental studies, only a single case is presented here as an example, in order to demonstrate model match between measurements and predictions from the finite-element based forward model, and hence present 3-D image reconstructions performed using the current measurement geometry. The optical properties of the experiment performed under target:background contrast ratio of 100:1 using a single 1cc volume target located ~ 1 cm deep from the top surface of the phantom, is given in Table 12.1.

The data acquisition time varied with the integration time of the CCD camera (0.2 to 1 sec), number of phase delays acquired (here, 32), and the total number of repetitions (10 in this case) of each steady-state images. The CCD camera used for the current studies was a full frame transfer system, meaning that a single 512x512 array is sequentially used for data acquisition and storage. Thus the integration time set on the CCD camera does not reflect directly in estimating the total data acquisition time. Also the data acquisition rate for each source illumination using the current 16-bit full frame CCD camera is slow in comparison to the data acquisition rate for a single source illumination using the 12-bit frame transfer CCD camera that was used in breast phantom studies. However, since the focus of the current study was to demonstrate the feasibility of tomographically imaging using the area illumination/area detection geometry, the data acquisition rate was not highly significant.

Table 12.1 Optical parameters for imperfect uptake absorption contrast ratio (100:1) experiment using ICG as the contrast agent.

Parameter	Target	Background
$\mu_{axi}(\text{cm}^{-1})$	0.023	0.023
$\mu_{axf}(\text{cm}^{-1})$	0.30	0.0030
$\mu_{ami}(\text{cm}^{-1})$	0.027	0.027
$\mu_{amf}(\text{cm}^{-1})$	0.051	0.00051
$\mu'_{sx}(\text{cm}^{-1})$	10.5	105
$\mu'_{axi}(\text{cm}^{-1})$	9.7	9.7
$\tau(\text{sec})$	0.56×10^{-9}	0.56×10^{-9}
ϕ	0.016×0.68	0.016

Here, fluorescent images were acquired for a single area illumination of the expanded excitation source and the acquired fluorescent measurements (total of 3194 measurements) were referenced with respect to the detection pixel in the 128x128 array that has the maximum AC intensity. Finite-element mesh using tetrahedral elements of varying degrees of discretization was generated (see Figure 12.3) and the simulated data from different meshes were compared to referenced measurements in order to evaluate the effect of discretization on the model mismatch. Simulations using finite difference based forward model were performed in earlier studies [46-47,101] and its discretization details are provided along with the discretization details of two different finite-element based meshes (that vary in their degree of discretization) in Table 12.2. A study was also performed to assess the effect of representing the planar area source as multiple

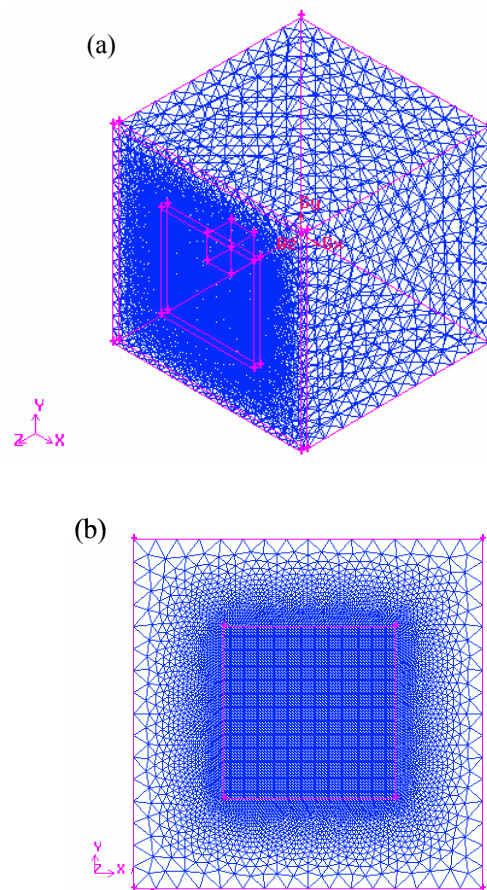


Figure 12.3 Discretized cubical phantom using tetrahedral finite elements (Mesh 1 of Table 12.2) (a) Entire phantom (b) top surface of the phantom, where the interior square is the region of area illumination and area detection.

Table 12.2 Finite-element (FE) and finite difference (FD) mesh details for the cubical phantom (8x8x8 cc volume).

Parameter	Finite element Mesh 1	Finite element Mesh 2 (fine)	Finite difference mesh
Nodes	24356	28007	4276737
Total elements	136587	156616	4194304
Surface elements	17578	20736	163840
Interior elements	119009	135880	4030464

point sources in the finite-element formulation of the forward model (using one of the finite-element meshes).

12.4 Results and discussion

The acquired fluorescence measurements using the above described imaging system were compared with respect to the simulations obtained from the Fortran-based forward model that was developed as a part of my project. The effect of formulating the excitation source term in the area illumination geometry was assessed along with the effect of 3-D finite element mesh discretization and the results are described in the following section.

12.4.1 Effect of area source versus multiple point sources

Approximation of the area (planar) source term (given by Equation (12.2)) by multiple point sources (Equation (12.1)) during the finite-element based forward model formulation are compared with the referenced measurements in order to assess the effect of the source term formulation. The results are presented for Mesh 2 of the finite-element discretization, where the distance between adjacent nodes in the region of interest (region of illumination and detection) was 0.0625. The simulated $\ln(\text{ACR})$ and RPS using either of the two source formulations were compared to the referenced measurements, as shown in Figure 12.4. From these plots, we observe that the model mismatch error in $\ln(\text{ACR})$ and RPS was similar for either of the two source formulations. The model mismatch errors are provided in the Table 12.3 (first two

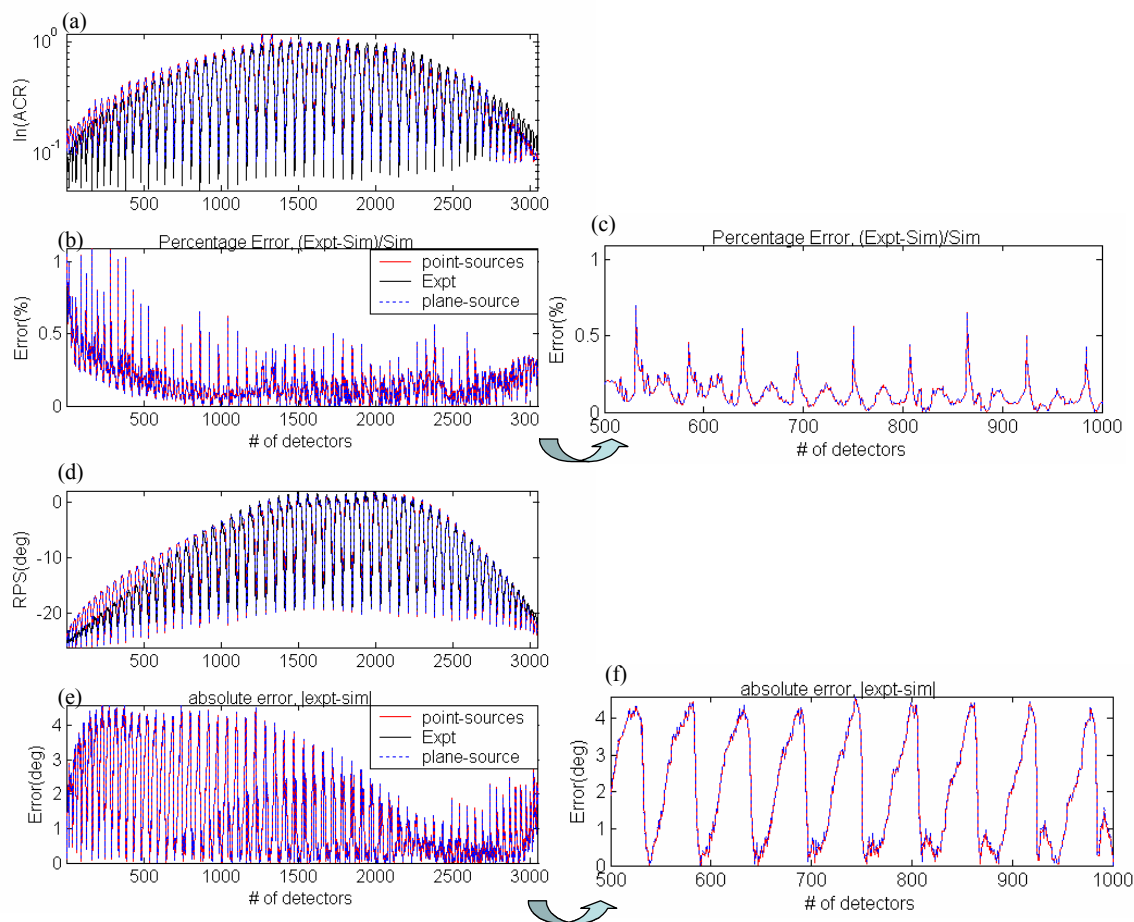


Figure 12.4 Effect of plane source versus multiple point sources in forward model simulations, in comparison to the experimental data, in terms of (a) $\ln(\text{ACR})$, (b) Relative error in ACR (%), (c) Zoomed ACR error plot for a subset of detectors, (d) RPS (deg), (e) Absolute error in RPS (deg), and (f) Zoomed ACR error plot for a subset of detectors.

rows). There was no significant effect in model match when the area source was approximated by multiple point sources, probably due to fine level of discretization in the region of interest. Hence, further studies on model match were performed using the multiple point source approximation of the area-illuminated source.

12.4.2 Effect of finite-element discretization on the model match

The referenced measurements were compared to the simulations obtained using the two different meshes (Mesh 1 and Mesh 2, given in Table 12.2). In both the finite element meshing schemes, the level of discretization in the region of interest was identical and equal to 0.0625 as the distance between consecutive nodes. The difference was in the level of discretization in the region around the region of interest and also along the depth of the phantom. Simulations using either of the two meshes were compared to measurements (see Figure 12.5). Here, the simulated data was obtained using multiple point source formulation in the finite-element forward solution.

From the comparison plots, it is observed that simulations using Mesh 2 (with finer discretization over Mesh 1) provided a better model match with respect to the referenced measurements (given by $\ln(\text{ACR})$ and RPS) over the model match using Mesh 1. The mean and variance of model mismatch errors are given in Table 12.3 in order to quantitatively compare the effect of discretization. Here, the model match errors using the FD mesh are also provided as a comparison between FE and FD approaches of the forward model formulation. From these results, we observe that discretization of the mesh plays significant role in reducing model mismatch errors between experiments and simulations, although at the cost of computational time in solving for the forward model. In comparison to the FD mesh (4276737 unknowns), which has more than 150% of unknowns compared to the fine FE mesh (Mesh 2 containing 28007 unknowns), the model match errors are not significantly lower using a uniformly discretized finer FD mesh. Thus, employing a FE mesh with lesser number of

Table 12.3 Model mismatch errors in $\ln(\text{ACR})$ and RPS between measurements and simulations obtained using two different finite-element meshes and a finite-difference mesh.

Simulated mesh	Source formulation	$\ln(\text{ACR})$		RPS (in radians)	
		Mean	Variance	Mean	Variance
FE Mesh 2	Planar source	0.16	0.02	1.43	1.78
FE Mesh 2	Multiple point sources	0.16	0.02	1.42	1.76
FE Mesh 1	Multiple point sources	0.26	0.04	2.17	4.03
FD mesh	Multiple point sources	0.18	0.04	1.07	0.72

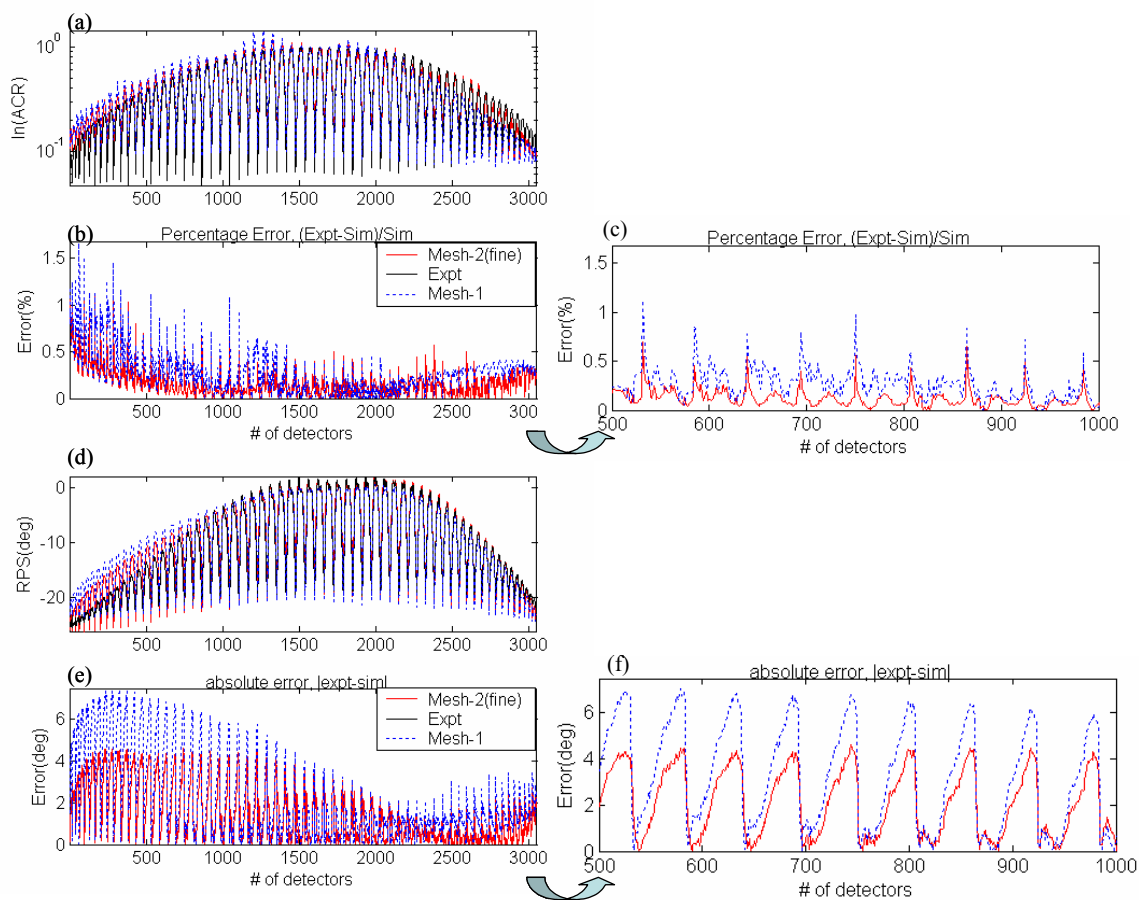


Figure 12.5 Model match comparison plots between two finite-element meshes (of varying discretization) and the experimental data, in terms of (a) $\ln(\text{ACR})$, (b) Relative error in ACR (%), (c) Zoomed ACR error plot for a subset of detectors, (d) RPS (deg), (e) Absolute error in RPS (deg), and (f) Zoomed RPS error plot for a subset of detectors.

unknowns in comparison to the FD mesh, not only reduces the computational time, but also reduces the ratio of the number of measurements to the number of unknowns, thus reducing the ill-posedness of the inverse problem.

12.5 Image reconstructions

Three-dimensional image reconstructions were performed by Dr. Roy using constrained truncated Newton's method [89-90]. The rate of convergence during the iterative image reconstruction scheme and the accuracy of the reconstructions were improved by incorporating a modified penalty/Barrier method developed by Polak [128] for constrained optimization problems. The modified Barrier method was shown to have a finite convergence as opposed to an asymptotic one, providing expeditious recovery of parameter maps. Details of the reconstruction algorithm are beyond the scope of this dissertation, and hence only preliminary image reconstructions are presented here to demonstrate the feasibility of reconstruction using the current measurement geometry.

Three-dimensional image reconstructions for the experimental case described in the Section 12.3 are given in Figure 12.6. From the contour slices of the 3-D cubical phantom in the y-plane, we observe qualitatively that the 1 cc volume target was reconstructed close to its true location, with minimal artifacts around the target.

Preliminary studies using the planar illumination geometry were successful and demonstrated for the first time at PML [51-52,102,127]. Work is in progress in performing model match and 3-D image reconstructions on various data sets that were acquired under different experimental conditions [101,47].

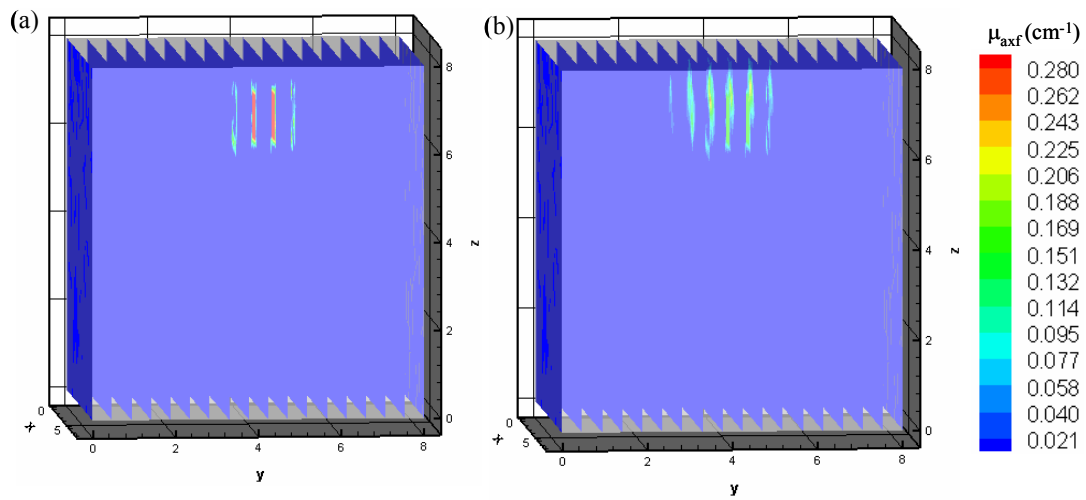


Figure 12.6 (a) Contour slices along the y-plane of actual cubical phantom, representing the true location of the 1cc target located 1cm deep from the top surface. (b) Contour slices along the y-plane of the reconstructed phantom, representing the reconstructed location of the target.

13. CONCLUSIONS AND FUTURE WORK

Future diagnostic and prognostic breast imaging with NIR must be focused towards molecular targeting of single and multiple lesions. To realize these future goals, simultaneous development of (i) fluorescence-enhanced optical imaging systems using clinically relevant phantom systems and different possible measurement geometries, and (ii) reconstruction algorithms to solve for the highly ill-posed inversion problem, where sparse surface measurements are used to determine the 3-D interior optical property maps must be undertaken.

A novel fluorescence-enhanced optical imaging system was developed using clinically relevant breast-shaped phantoms (~ 1087 cc) and a gain-modulated intensified CCD (ICCD) camera for rapid data acquisitions. The feasibility for 3-D optical tomographic imaging of single and multiple, fluorescently contrasted lesions from boundary surface measurements of re-emitted fluorescent light generated by micromolar concentrations of a non-specific contrast agent (ICG) are demonstrated.

Boundary surface referenced measurements of amplitude and phase shift in the frequency-domain were used along with the coupled diffusion equations in order tomographically reconstruct 3-D images of μ_{axf} (absorption coefficient due to the fluorophores) using approximate extended Kalman filter (AEKF) algorithm. Single 1 cc volume targets were located with good precision up to 2 cm deep from the phantom surface under absorption contrast ratios of 1:0 and 100:1. Single and multiple small volume (0.5-0.6 cc) targets located ~ 1.2 -1.5 cm deep under perfect uptake absorption

contrast ratio (1:0) were also detected in the breast phantom without any artifacts. These studies demonstrate for the first time the feasibility of tomographically reconstructing large 3-D phantoms of clinical relevance, and using different geometries.

Phantom studies performed using clinically relevant breast volumes (using point illumination/point collection geometry) foresee a direct translation into clinical diagnostic imaging of the breast tissue by molecularly targeting the metastatic spread of lesions or early stage lesions using the systemic, *i.v.* (intravenous) injected fluorescent contrast agent. The technology also holds a promise for assessing the multi-focality of lesions using targeted agents. The feasibility of employing dual point illumination measurement geometry in breast phantoms can be easily translated into simultaneous multiple point illumination geometry for clinical feasibility trials, prior to which the sensitivity and specificity of this imaging modality must be assessed using different phantom models.

The preliminary semi-infinite phantom studies using area illumination/area collection geometry presented herein has paved an opportunity in performing prognostic imaging of the sentinel lymph and also locating nodes for surgical resection. Although the initial clinical feasibility trials are undergoing using a non specific and blood pooling contrast agent (ICG), parallel feasibility studies are currently performed to develop and assess the performance of tumor-specific contrast agents through small animal studies [129].

Unlike established, conventional imaging modalities such as nuclear, magnetic resonance imaging (MRI), positron emission tomography (PET), and computed

tomography (CT), NIR optical imaging with fluorescent contrast requires the simultaneous introduction of both the contrast agent (drug) and the imaging system (device) into the clinic. Indeed, the Food and Drug Administration (FDA) requires the simultaneous approval of a combinational Investigational New Drug (IND) and an Investigational Device Exemption (IDE) application for clinical translation. The current optical imaging studies using clinically relevant sized phantoms have demonstrated the feasibility of the fluorescence-enhanced imaging technology using ICG as the contrast agent, which is FDA approved for the indications of assessing hepatic function and retinopathy.

However, several limitations hinder the rapid translation to the clinic. First and foremost, owing to the faint fluorescent signal collected at the tissue surface, the “noise” floor attribute-able to propagated excitation light that leaks through conventional optical interference filters remains the critical factor for determining the maximum depth and minimal contrast required for detection of lesions. For example, the excitation light that reaches the end of a fiber optic is *at least* 3-4 orders of magnitude higher than the fluorescent signal collected in our studies. Rejection of excitation light with interference filters with “typical” optical densities of 4-5 will result in a high “noise” floor and limit the sensitivity of detecting deep or weakly fluorescing lesions. While FDPM measurements alleviate the “noise floor” owing to ambient light [12], the modulated excitation light leakage remains a limitation of the technique. Furthermore, 3-D inversion of data from large volumes remains computationally intensive, despite recent advances in algorithm development and implementation (16,111,118). Finally, the

development of NIR excitable probes conjugated to targeting and reporting agents are paramount for fluorescence enhanced optical tomography.

Hence future work needs to be performed in overcoming the current limitations and modifying the current fluorescence-enhanced optical imaging system for clinical applications.

13.1 Future work

Future work towards translating fluorescence-enhanced optical imaging into the clinic includes: (i) modifications in the current optical imager towards a robust imaging system; (ii) improvement in reconstruction algorithm towards computationally efficient and arbitrary-free data analysis; (iii) analysis of specificity and sensitivity of the optical imager towards the evaluation of receiver operator characteristic (ROC) statistics; and (iv) development of non-toxic, patient-safe, tumor-specific contrast agents towards enhanced optical contrast and detection of early stage tumors. A schematic of the future work with efforts towards the clinical translation of the fluorescence-enhanced optical imaging technology is given in Figure 13.1.

13.1.1. Modifications in the current optical imaging system

The current optical imager has limitations in terms of (i) excitation light leakage, (ii) outdated CCD camera and image intensifier models, (iii) sparse point illumination locations on the phantom surface, and (iv) slow data acquisition rates due to the use of two interfacing plates. Since the feasibility of fluorescence-enhanced optical

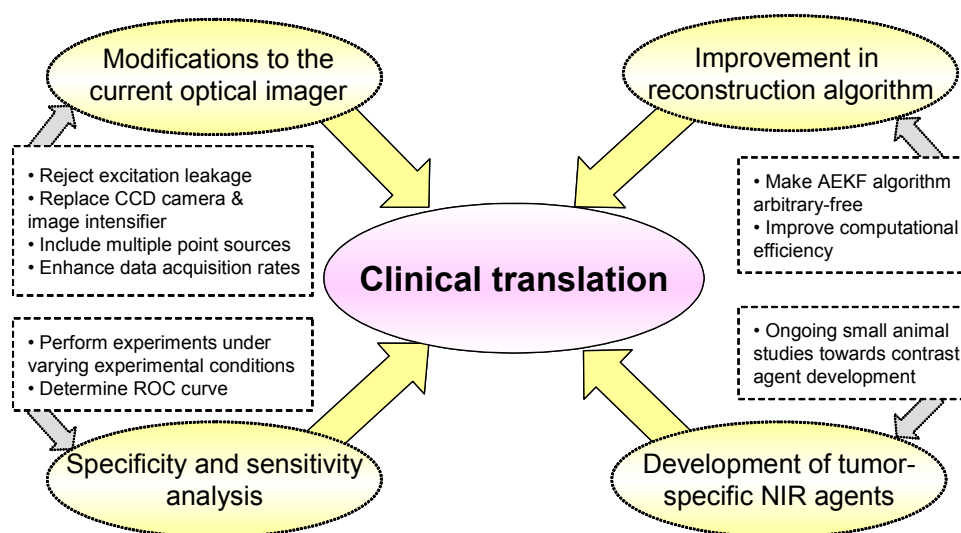


Figure 13.1 Flowchart of the future direction of the current work towards clinical translation of the technology.

tomography has been demonstrated for the first time in the current work, future work towards the clinical translation of the technology requires modifications in the current imaging set-up in order to acquire precise measurements from deeply located targets at further enhanced data acquisition rates. These modifications include:

- (i) Development of alternate techniques to overcome the excitation leakage in order to improve the ability of detecting weak fluorescent signals generated from deeply located small volume targets. Initial efforts will involve the development of customized interference filters, which can reject the excitation light completely, without affecting the transmission efficiency of the weak fluorescent signal. The ability to collect signal from 100 femtomoles of ICG at tissue depths of 4 cm and greater [12] needs to be effectively translated to clinical breast imaging.

- (ii) Replacement of the current 12-bit CCD camera of the ICCD detection system with a new latest generation 16-bit CCD camera due to its deterioration on prolonged use as well as its inefficiency in providing precise measurements. The new 16-bit frame transfer CCD camera acquires data at the same speed as the current 12-bit bit frame transfer CCD camera, but with an improved resolution and precision in the acquired images.
- (iii) Replacement of the current Gen III image intensifier with the latest image intensifier (filmless tube) in order to alleviate the problem of image retention as well as improve the amplification of the weak fluorescent signal.
- (iv) Inclusion of more source fibers on the phantom surface, in order to increase the density of acquired measurements as well as the probability of detecting small volume targets.
- (v) Feasibility studies employing dual point illumination geometry were demonstrated in the current work and are encouraging towards employing multiple point illumination measurement geometry. The illumination of excitation light from multiple points interrogates a relatively large portion of the tissue volume also increasing the probability of detecting small volume targets. Dense multiple point illuminations mimic the area illumination geometry, whose reconstructions have already been demonstrated as a preliminary step. The employment of multiple point illumination geometry can be achieved using different techniques: (a) custom-built optical switch wherein the laser diode source light is split into required number of multiple sources and launched onto the phantom surface (Figure 13.2a), or (b) expanded laser diode

light, where the expanded beam is focused onto a fiber optic bundle that launches the excitation light onto the phantom surface (Figure 13.2b). Of the two multiple point illumination techniques, the latter technique is more practical and easy to implement, since the source strength can be characterized using the already development methods that were demonstrated in the area illumination studies [51-52].

(vi) The current optical imager uses two interfacing plates to image all the 128 collection fibers located around the hemispherical surface of the breast phantom. The data acquisition rates can be enhanced by positioning all the 128 collection fibers on to a single interfacing plate or by using a fiber bundle containing 128 collection fibers, without compensating for the image resolution. Replacing the current 12-bit CCD camera with the new 16-bit CCD camera will maintain the image resolution even for greater areas of detection. In addition, the use of a fiber bundle can overcome the problem of signal loss caused by proximity focused imaging of the interfacing plate.

Based on all the suggested modifications to the current optical imaging system, the future imaging system could possibly resemble the schematic provided in Figure 13.3.

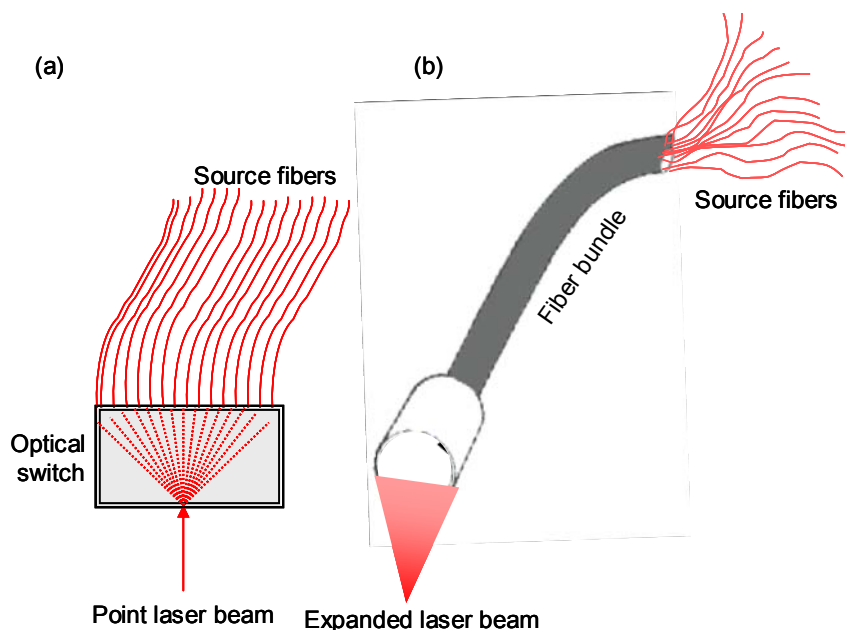


Figure 13.2 Different methods to illuminate the phantom surface using simultaneous multiple point excitation sources using (a) an optical switch that splits the input laser beam into multiple optical fibers, or using (b) expanded laser beam focused onto a fiber bundle of optical fibers.

13.1.2. Improvement in reconstruction algorithm

The AEKF algorithm employed for reconstructions uses arbitrary methods to determine the model error covariance (\mathbf{Q}) and the initial parameter error covariance (\mathbf{P}). Work is currently in progress to determine alternate and more robust methods of estimating these covariance matrices and thus make the reconstruction algorithm applicable to various experimental conditions. New approaches that may further improve computational efficiency, such as adaptive meshing and use of the boundary element method are also currently under investigation at PML and at University of Vermont (collaborators).

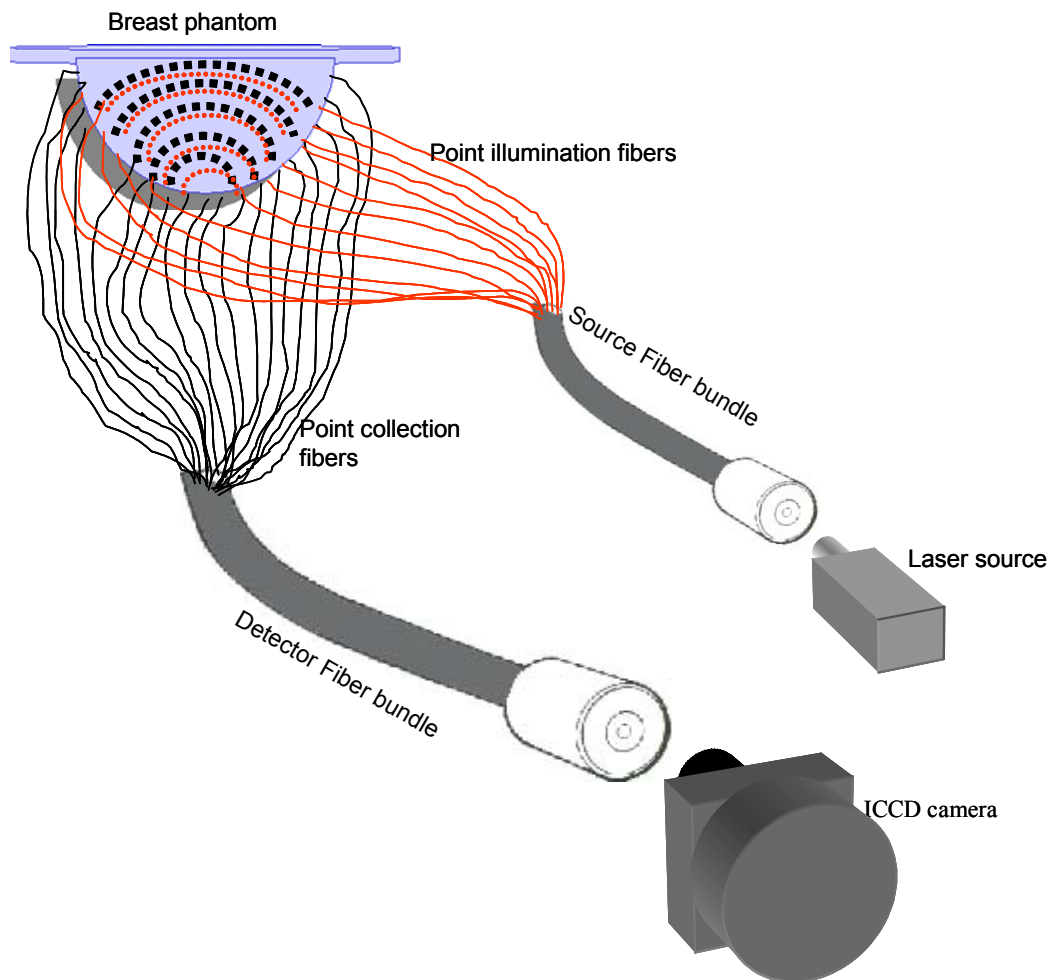


Figure 13.3 Future set-up of the ICCD imaging system towards clinical translation of the technology.

13.1.3. Analysis of specificity and sensitivity of the optical imager

The success of any imaging modality in clinic depends on its sensitivity and specificity, or in other words, the receiver operator characteristic (ROC) curves. The accuracy and precision of the images in terms of the target location/size will be analyzed

under various experimental conditions and the overall sensitivity and specificity of the developed 3D imaging system will be evaluated in terms of the receiver operator characteristic (ROC) statistics. ROC analysis will provide a means to assess the current imaging system and tomographic algorithm with respect to the currently available imaging modalities.

13.1.4. Development of tumor-specific contrast agents

With the demonstration of clinically relevant phantom studies, there is an increased motivation for innovations in NIR agent development. Small animal studies using mice are currently carried out at MD Anderson Cancer Center as a collaborative effort with Photon Migration Laboratory (PML), towards development of NIR contrast agents that have a greater affinity to the tumor cells.

In summary, future development critically depends upon overcoming the current limitations and implementing the suggested modifications in order to enable clinical translation of the technology for detecting early stage and small volume lesions located at greater depths using lower concentrations of the fluorophores.

REFERENCES

1. R. Weissleder, U. Mahmood, "Molecular imaging," *Radiology* **219**, 316-333 (2001).
2. M. A. Franceschini, K. T. Moesta, S. Fantini, G. Gaida, E. Gratton, H. Jess, W. W. Mantulin, M. Seeber, P. M. Schlag, M. Kaschke, "Frequency-domain techniques enhance optical mammography: Initial clinical results," *Proceedings of National Academy of Science USA* **94**, 6468-6473 (1997).
3. S. Fantini, S. A. Walker, M. A. Franceschini, M. Kaschke, P. M. Schlag, K. T. Moesta, "Assessment of the size, position, and optical properties of breast tumors *in vivo* by noninvasive optical methods," *Applied Optics* **37**, 1982-1989 (1998).
4. K. T. Moesta, S. Fantini, H. Jess, S. Totkas, M. A. Franceschini, M. Kaschke, P. M. Schlag, "Contrast features of breast cancer in frequency-domain laser scanning mammography," *Journal of Biomedical Optics* **3**, 129-136 (1998).
5. D. Grosenick, H. Wabnitz, H. H. Rinneberg, K. T. Moesta, P. M. Schlag, "Development of a time-domain optical mammograph and first *in vivo* applications," *Applied Optics* **38**, 2927-2943 (1999).
6. S. B. Colak, M. B. van der Mark, G. W. 't Hooft, J. H. Hoogenraad, E. S. van der Linden, F. A. Kuijpers, "Clinical Optical Tomography and NIR Spectroscopy for Breast Cancer Detection," *IEEE Journal of Selected Topics in Quantum Electronics* **5**, 1143-1158 (1999).

7. B. W. Pogue, S. P. Poplack, T. O. McBride, W. A. Wells, K. S. Osterman, U. L. Osterberg, K. D. Paulsen, "Quantitative hemoglobin tomography with diffuse near-infrared spectroscopy: Pilot results in the breast," *Radiology* **218**, 261-266 (2001).
8. H. Jiang, Y. Xu, N. Iftimia, J. Eggert, K. Klove, L. Baron, L. Fajardo, "Three-dimensional optical tomographic imaging of breast in a human subject," *IEEE Transactions on Medical Imaging* **20**, 1334-1340 (2001).
9. D. J. Hawrysz, E. M. Sevick-Muraca, "Developments toward diagnostic breast cancer imaging using near-infrared optical measurements and fluorescent contrast agents," *Neoplasia* **2**, 388-417 (2000).
10. K. Licha, "Contrast agents for optical imaging," *Top Curr Chem* **222**, 1-29 (2002).
11. M. Gurfinkel, S. Ke, X. Wen, C. Li, E. M. Sevick-Muraca, "Near-infrared fluorescence optical imaging and tomography," *Disease Markers* (in press) (2003).
12. J. P. Houston, A. B. Thompson, M. Gurfinkel, E. M. Sevick-Muraca, "Sensitivity and depth penetration of continuous wave *versus* frequency-domain photon migration near-infrared fluorescence contrast-enhanced imaging," *Photochemistry and Photobiology* **77**, 420-430 (2003).
13. V. Ntziachristos, R. Weissleder, "Experimental three-dimensional fluorescence reconstruction of diffuse media by use of a normalized Born approximation," *Optics Letters* **26**, 893-895 (2001).
14. V. Ntziachristos, R. Weissleder, "Charge-coupled-device based scanner for tomography of fluorescent near-infrared probes in turbid media," *Medical Physics* **29**, 803-809 (2002).

15. D. J. Hawrysz, M. J. Eppstein, J. Lee, E. M. Sevick-Muraca, "Error consideration in contrast-enhanced three-dimensional optical tomography," *Optics Letters* **26**, 704-706 (2001).
16. M. J. Eppstein, D. J. Hawrysz, A. Godavarty, E. M. Sevick-Muraca, "Three-dimensional near-infrared fluorescence tomography with Bayesian methodologies for image reconstruction from sparse and noisy data sets," *Proceedings of National Academy of Science USA* **99**, 9619-9624 (2002).
17. J. Lee, E. M. Sevick-Muraca, "3-D Fluorescence enhanced optical tomography using references frequency-domain photon migration measurements at emission and excitation measurements," *Journal of Optical Society of America A* **19**, 759-771 (2002).
18. M. R. Styzt, O. Fieder, "Three-dimensional medical imaging modalities: An overview," *Critical Reviews in Biomedical Engineering* **18**, 1-25 (1990).
19. S. Akashi-Tanaka, T. Fukutomi, T. Watanabe, N. Katsumata, T. Nanasawa, K. Matsuo, K. Miyakawa, H. Tsuda, "Accuracy of contrast-enhanced computed tomography in the prediction of breast cancer after neoadjuvant chemotherapy," *Int. J. Cancer (Radiat. Oncol. Invest.)* **96**, 66-73 (2001).
20. A. Szymanski-Exner, N. T. Stowe, K. Salem, R. Lazebnik, J. R. Haaga, D. L. Wilson, J. Gao, "Noninvasive monitoring of local drug release using x-ray computed tomography: Optimization and *in vitro/in vivo* validation," *Journal of Pharmaceutical Sciences* **92**, 289-296 (2003).

21. M. D. Schnall, "Application of magnetic resonance imaging to early detection of breast cancer," *Breast Cancer Research* **3**, 17-21 (2001).
22. S. G. Orel, M. D. Schnall, "MR imaging of the breast for the detection, diagnosis, and staging of breast cancer," *Radiology* **220**, 13-30 (2001).
23. W. A. Kaiser, E. Zeitler, "MR imaging of the breast: Fast imaging sequences with and without Gd-DTPA," *Radiology* **170**, 681-686 (1989).
24. S. H. Heywang, A. Wolf, E. Pruss, T. Hilbertz, W. Eiermann, W. Permaneter, "MR imaging of the breast with Gd-DTPA: Use and limitations," *Radiology* **171**, 95-103 (1989).
25. S. Aime, C. Cabella, S. Colombatto, S. Geninatti, E. Gianolio, F. Maggioni, "Insights into the use of paramagnetic Gd(III) complexes in MR-molecular imaging investigations," *Journal of Magnetic Resonance Imaging* **16**, 394-406 (2002).
26. A. R. Padhani, "Dynamic contrast-enhanced MRI in clinical oncology: Current status and future directions," *Journal of Magnetic Resonance Imaging* **16**, 407-422 (2002).
27. A. Teifke, A. Hlawatsch, T. Beier, T. W. Vomweg, S. Schadmand, M. Schmidt, H-A Lehr, M. Thelen, "Undetected malignancies of the breast: Dynamic contrast-enhanced MR imaging at $1.0T^1$," *Radiology* **224**, 881-888 (2002).
28. P. A. Dayton, K. W. Ferrara, "Targeted imaging using ultrasound," *Journal of Magnetic Resonance Imaging* **16**, 363-377 (2002).

29. H. Leong-Poi, J. Christiansen, A. L. Klibanov, S. Kaul, J. R. Lindner, "Noninvasive assessment of angiogenesis by ultrasound and microbubbles targeted to α_v -integrins," *Circulation* **107**, 455-460 (2003).
30. M. H. Chaudhari, F. Forsberg, A. Voodarla, F. N. Saikali, S. Goonewardene, L. Needleman, G. C. Finkel, B. B. Goldberg, "Breast tumor vascularity identified by contrast enhanced ultrasound and pathology: Initial results," *Ultrasonics* **38**, 105-109 (2000).
31. D. Gopalan, J. B. Bomanji, D. C. Costa, P. J. Ell, "Nuclear medicine in primary breast cancer imaging," *Clinical Radiology* **57**, 565-574 (2002).
32. L. Kostakoglu, H. Agress Jr., S. J. Goldsmith, "Clinical role of FDG PET in evaluation of cancer patients," *Radiographics* **23**, 315-340 (2003).
33. J. Dose, C. Bleckmann, S. Bachmann, K. H. Bohuslavizki, J. Berger, L. Jenicke, C. R. Habermann, F. Janicke, "Comparison of fluorodeoxyglucose positron emission tomography and 'conventional diagnostic procedures' for the detection of distant metastases in breast cancer patients," *Nuclear Medicine Communications* **23**, 857-864 (2002).
34. J. Czernin, M. E. Phelps, "Positron emission tomography scanning: Current and future applications," *Annu. Rev. Med.* **53**, 89-112 (2002).
35. N. Avril, C. A. Rose, M. Schelling, J. Dose, W. Kuhn, S. Bense, W. Weber, S. Zeigler, H. Graeff, M. Schwaiger, "Breast imaging with positron emission tomography and fluorine-18 fluorodeoxyglucose: Use and limitations," *J. Clin Oncol* **18**, 3495-3502 (2000).

36. C. Rose, J. Dose, N. Avril, "Positron emission tomography for the diagnosis of breast cancer," *Nuclear Medicine Communications* **23**, 613-618 (2002).
37. F. Berger, S. S. Gambhir, "Recent advanced in imaging endogenous or transferred gene expression utilizing radionuclide technologies in living subjects: Applications to breast cancer," *Breast Cancer Research* **3**, 28-35 (2002).
38. E. M. Sevick-Muraca, A. Godavarty, J. P. Houston, A. B. Thompson, R. Roy, "Near-infrared imaging with fluorescent contrast agents" in *Handbook of Biomedical Fluorescence*, eds. Brian W. Pogue and Mary-Ann Mycek, (Marcel Dekker Inc., New York, 2003).
39. H. W. Lim, N. A. Soter, *Clinical Photomedicine* (Dekker, New York, 1993).
40. S. Achilefu, R. B. Dorshow, J. E. Bugaj, R. Rajagopalan, "Novel receptor-targeted fluorescent contrast agents for in vivo tumor imaging," *Investigation Radiology* **35**, 479-485 (2000).
41. C. H. Tung, U. Mahmood, R. Weissleder, "In vivo imaging of proteolytic enzyme activity using a novel molecular reporter," *Cancer Research* **60**, 4953-4958 (2000).
42. R. Weissleder, C. H. Tung, U. Mahmood, A. Bogdanov, "In vivo imaging of tumors with protease-activated near-infrared fluorescent probes," *Nature Biotechnology* **17**, 375-378 (1999).
43. T. A. Giambernardi, G. M. Grant, G. P. Taylor, R. J. Hay, V. M. Maher, J. J. McCormick, R. J. Klebe, "Overview of matrix metalloproteinase expression in cultured human cells," *Matrix Biol* **16**, 483-496 (1998).

44. E. M. Sevick-Muraca, J. P. Houston, M. Gurfinkel, "Fluorescence-enhanced, near infrared diagnostic imaging with contrast agents," *Current Opinions* **6**, 642-650 (2002).
45. C. Bremer, V. Ntziachristos, R. Weissleder, "Optical-based molecular imaging: Contrast agents and potential medical applications," *Eur. Radiol.* **13**, 231-243 (2003).
46. B. Chance, J. S. Leigh, H. Miyake, D. S. Smith, S. Nioka, R. Greenfeld, M. Finander, K. Kaufmann, W. Levy, M. Young, P. Cohen, H. Yoshioka, R. Boretsky, "Comparison of time-resolved and -unresolved measurements of deoxyhemoglobin in brain," *Proceedings of National Academy of Science USA* **85**, 4791-4975 (1988).
47. R. M. P. Doornbos, R. Lang, M. C. Aalders, F. W. Cross, H. J. C. M. Sterenborg, "The determination of *in vivo* human tissue optical properties and absolute chromophore concentrations using spatially resolved steady-state diffuse reflectance spectroscopy," *Physics in Medicine and Biology* **44**, 967-981 (1999).
48. S. R. Arridge, W. R. B. Lionheart, "Nonuniqueness in diffusion-based optical tomography," *Optics Letters* **23**, 882-884 (1998).
49. G. Balgi, J. S. Reynolds, R. H. Mayer, R. Cooley, E. M. Sevick-Muraca, "Measurements of multiply scattered light for on-line monitoring of changes in size distribution of cell-debris suspensions," *Biotechnology Progress* **15**, 1106-1114 (1999).

50. R. C. Straight, R. E. Benner, R. W. McClane, P. M. N. Y. Go, G. Yoon, J. A. Dixon, "Application of charge-coupled device technology for measurement of laser light and fluorescence distribution in tumors for photodynamic therapy," *Photochemistry and Photobiology* **53**, 787-796 (1991).
51. A. B. Thompson, E. M. Sevick-Muraca, "Near-infrared fluorescence contrast-enhanced imaging with intensified charge-coupled device homodyne detection: Measurement precision and accuracy," *Journal of Biomedical Optics* **8**, 111-120 (2003).
52. A. Thompson, D. J. Hawrysz, E. M. Sevick-Muraca, "Near-infrared fluorescence contrast-enhanced imaging with area illumination and area detection: The forward imaging problem," *Applied Optics* **42**, 4125-4136 (2003).
53. S. Folli, G. Wagnieres, A. Pelegrin, J. M. Calmes, D. Braichotte, F. Buchegger, Y. Chalandon, N. Hardman, D. G. Heusser, J. C. Givel, G. Chapuis, A. Chatelain, H. van Den Bergh, J. P. Mach, "Immunophotodiagnosis of colon carcinomas in patients injected with fluoresceinated chimeric antibodies against carcinoembryonic antigen," *Proceedings of National Academy of Science USA* **89**, 7973-7977 (1992).
54. J. C. Finlay, D. L. Conover, E. L. Hull, T. H. Foster, "Porphyrin bleaching and PDT-induced spectral changes are irradiance dependent in ALA-sensitized normal rat skin in vivo," *Photochemistry and Photobiology* **73**, 54-63 (2001).
55. A. Ishimaru. *Wave propagation and scattering in random media* (Academic Press, New York, 1978).

56. A. Ishimaru, "Diffusion of light in turbid media," *Applied Optics* **28**, 2210-2215 (1989).
57. E. M. Sevick, C. L. Burch, "Origin of phosphorescence signals reemitted from tissues," *Optics Letters* **19**, 1928-1930 (1994).
58. M .S. Patterson, B. W. Pogue, "Mathematical model for time-resolved and frequency-domain fluorescence spectroscopy in biological tissues," *Applied Optics* **33**, 1963-1974 (1994).
59. C. L. Hutchinson, J. R. Lakowicz, E. M. Sevick-Muraca, "Fluorescence life-time based sensing in tissues: A computational study," *Biophys. J.* **68**, 1574-1582 (1995).
60. S. L. Jacques, "Light distributions from point, line, and plane sources for photochemical reactions and fluorescence in turbid biological tissues," *Photochemistry and Photobiology* **67**, 23-32 (1998).
61. A. D. Kim, A. Ishimaru, "Optical diffusion of continuous-wave, pulsed, and density waves in scattering media and comparisons with radiative transfer," *Applied Optics* **37**, 5313-5319 (1998).
62. K. M. Yoo, F. Liu, R. R. Alfano, "When does the diffusion approximation fail to describe photon transport in random media?" *Phys Rev Lett* **64**, 2647-2649 (1990).
63. R. C. Haskell, L .O. Scassand, T-T. Tsay, T-C. Feng, M. S. Mc Adams, B. J. Tromberg, "Boundary conditions for the diffusion equation in radiative transfer," *Journal of Optical Society of America A* **11**, 2727-2741 (1994).

64. M. Keijzer, W. M. Star, P. R. M. Storchi, "Optical diffusion in layered media," *Applied Optics* **27**, 1820-1824 (1988).
65. M. S. Patterson, B. Chance, B. Wilson, "Time resolved reflectance and transmittance for the non-invasive measurement of tissue optical properties," *Applied Optics* **28**, 2331-2336 (1989).
66. A. H. Hielscher, S. L. Jacques, L. Wang, F. K. Tittel, "The influence of boundary conditions on the accuracy of diffusion theory in time-resolved reflectance spectroscopy of biological tissues," *Physics in Medicine and Biology* **40**, 1957-1975 (1995).
67. T. J. Farrell, M. S. Patterson, B. Wilson, "A diffusion theory model of spatially resolved, steady-state diffuse reflectance for the noninvasive determination of tissue optical properties *in vivo*," *Medical Physics* **9**, 879-888 (1992).
68. Y. Yao, Y. Wang, Y. Pei, W. Zhu, R. L. Barbour, "Frequency-domain optical imaging of absorption and scattering distributions by a Born iterative method," *Journal of Optical Society of America A* **14**, 325-342 (1997).
69. D. Y. Paithankar, A. U. Chen, B. W. Pogue, M. S. Patterson, E. M. Sevick-Muraca, "Imaging of fluorescent yield and lifetime from multiply scattered light reemitted from random media," *Applied Optics* **36**, 2260-2272 (1997).
70. B. W. Pogue, M. S. Patterson, H. Jiang, K. D. Paulsen, "Initial assessment of a simple system for frequency domain diffuse optical tomography," *Physics in Medicine and Biology* **40**, 1709-1729 (1995).

71. M. J. Eppstein, D. E. Dougherty, T. L. Troy, E. M. Sevick-Muraca, "Biomedical optical tomography using dynamic parameterization and Bayesian conditioning on photon migration measurements," *Applied Optics* **38**, 2138-2150 (1999).
72. S. R. Fulton, P. E. Ciesielski, W. H. Schubert, "Multigrid methods for elliptic problems. A review," *Weather Rev.* **114**, 943-959 (1986).
73. J. C. Adams, "MUDPACK Multigrid portable FORTRAN software for the efficient solution of linear elliptic partial differential equations," *Appl. Math. Comp.* **34**, 113-146 (1989).
74. K. D. Paulsen, H. Jiang, "Spatially varying optical property reconstruction using a finite element diffusion equation approximation," *Medical Physics* **22**, 691-701 (1995).
75. M. Schqeiger, S. R. Arridge, D. T. Delpy, "Application of the finite element for the forward and inverse models in optical tomography," *J. Math. Imag. Vision.* **3**, 263-283 (1993).
76. R. Roy, E. M. Sevick-Muraca, "Truncated Newton's optimization scheme for absorption and fluorescence optical tomography: Part I Theory and Formulation," *Optics Express* **4**, 353-371(1999).
77. E. L. Hull, M. G. Nichols, T. H. Foster, "Localization of luminescent inhomogeneities in turbid media with spatially resolved measurements of cw diffuse luminescence emittance," *Applied Optics* **37**, 2755-2765 (1998).

78. M. A. O’Leary, D. A. Boas, B. Chance, A. G. Yodh “Reradiation and imaging of diffuse photon density waves using fluorescent inhomogeneities,” *J. of Luminescence* **60 & 61**, 281-286 (1994).
79. J. Wu, Y. Wang, L. Perleman, I. Itzkan, R. R. Dasari, M. S. Feld, “Time-resolved multichannel imaging of fluorescent objects embedded in turbid media,” *Optics Letters* **20**, 489-491 (1995).
80. V. Chernomordik, D. Hattery, I. Gannot, A. H. Gandjbakhche, “Inverse method 3-D reconstruction of localized *in vivo* fluorescence – application to Sjogren syndrome,” *IEEE J. on Selected Topics on Quantum Electronics* **54**, 930-935 (1999).
81. J. C. Schotland, “Continuous-wave diffusion imaging,” *Journal of Optical Society of America A* **14**, 275-279 (1997).
82. E. M. Sevick-Muraca, D. L. Heintzleman, J. Lee, T. L. Troy, D. Y. Paithankar, “The role of higher order scattering in solutions to the forward and inverse optical imaging problems in random media,” *Applied Optics* **36**, 9058-9067 (1997).
83. M. A. O’Leary, D. A. Boas, X. D. Li, B. Chance, A. G. Yodh, “Fluorescence lifetime imaging in turbid media,” *Optics Letters* **21**, 158-160 (1996).
84. J. Lee, E. M. Sevick-Muraca, “Fluorescence-enhanced absorption imaging using frequency-domain photon migration: tolerance to measurement error,” *Journal of Biomedical Optics*, **6**, 58-67 (2001).

85. J. Chang, H. L. Graber, R. L. Barbour, "Improved reconstruction algorithm for luminescence when background luminophore is present," *Applied Optics* **37**, 3547-3552 (1998).
86. H. Jiang, "Frequency-domain fluorescent diffusion tomography: A finite-element-based algorithm and simulations," *Applied Optics* **37**, 5337-5343 (1998).
87. M. J. Eppstein, D. E. Dougherty, D. J. Hawrysz, E. M. Sevick-Muraca, "Three-dimensional optical tomography," in *Optical Tomography and Spectroscopy of Tissue III*, B. Chance, R. R. Alfano, B. J. Tromberg eds., Proc. Soc. Photo-Opt. Instrum. Eng. **3497**, 97-105 (1999).
88. R. Roy, E. M. Sevick-Muraca, "Truncated Newton's optimization scheme for absorption and fluorescence optical tomography: Part II Reconstruction from synthetic measurements," *Optics Express* **4**, 372-382 (1999).
89. R. Roy, E. M. Sevick-Muraca, "Active constrained truncated Newton method for simple-bound optical tomography," *Journal of Optical Society of America A* **17**, 1627-1641 (2000).
90. R. Roy, E. M. Sevick-Muraca, "Three-dimensional unconstrained and constrained image-reconstruction techniques applied to fluorescence, frequency-domain photon migration," *Applied Optics* **40**, 2206-2215 (2001).
91. R. Roy, E. M. Sevick-Muraca, "A numerical study of gradient-based nonlinear optimization methods for contrast-enhanced optical tomography," *Optics Express* **9**, 49-65 (2001).

92. R. Roy, A. Godavarty, E. M. Sevick-Muraca, "Fluorescence-enhanced, optical tomography using referenced measurements of heterogeneous media," *IEEE Transactions on Medical Imaging* **22**, 824-836 (2003).
93. J. Chang R. L. Barbour, H. Graber, R. Aronson, "Fluorescence optical tomography," in *Experimental and Numerical Methods for Solving Ill-Posed Inverse Problems: Medical and Nonmedical Applications*, R. L. Barbour, M. J. Carvlin, M. A. Fiddy, eds., *Proc. Soc. Photo-Opt. Instrum. Eng.* **2570**, 59-72 (1995).
94. J. Chang, H. L. Graber, R. L. Barbour, "Imaging of fluorescence in highly scattering media," *IEEE Transactions on Biomedical Engineering* **44**, 810-822 (1997).
95. J. Wu, L. Perelman, R. R. Dasari, M. S. Feld, "Fluorescence tomographic imaging in turbid media using early-arriving photons and Laplace transforms," *Proceedings of National Academy of Science* **94**, 8783-8788 (1997).
96. Y. Yang, N. Iftimia, Y. Xu, H. Jiang, "Frequency-domain fluorescent diffusion tomography of turbid media and in vivo tissues," in *Optical Tomography and Spectroscopy of Tissue IV*, B. Chance, R. R. Alfano, B. J. Tromberg, eds., *Proc. Soc. Photo-Opt. Instrum. Eng.* **4250**, 537-545 (2001).
97. D. T. Delpy, M. Cope, "Quantification in tissue near-infrared spectroscopy," *Phil. Trans. R. Soc. Lond. B.* **352**, 649-659 (1997).

98. J. C. Hebden, H. Veenstra, H. Dehghani, E. M. C. Hillman, M. Schweiger, S. R. Arridge, D. T. Delpy, "Three-dimensional time-resolved optical tomography of a conical breast phantom," *Applied Optics* **40**, 3278-3287 (2001).
99. ITT Industries Night Vision, <http://www.ittnv.com/military/generationgap.html>, browsed in January 2002.
100. J. S. Reynolds, T. L. Troy, E. M. Sevick-Muraca, "Multipixel techniques for frequency-domain photon migration imaging," *Biotechnology Progress* **13**, 669-680 (1997).
101. P. C. Schneider, R. M. Clegg, "Rapid acquisition, analysis, and display of fluorescence lifetime-resolved images for real-time applications," *Review of Scientific Instruments* **68**, 4107-4119 (1997).
102. A. B. Thompson, *Detection of a new optical imaging modality for detection of fluorescence-enhanced disease*, PhD Dissertation, Texas A&M University, College Station, May 2003.
103. A. Kienle, M. S. Patterson, "Improved solution of the steady-state and the time-resolved diffusion equations for reflectance from a semi-infinite turbid medium," *Journal of Optical Society of America A* **14**, 246-254 (1997).
104. A. Godavarty, D. J. Hawrysz, R. Roy, E. M. Sevick-Muraca, M. J. Eppstein, "Influence of the refractive index-mismatch at the boundaries measured in fluorescence-enhanced frequency-domain photon migration imaging," *Optics Express* **10**, 653-662 (2002).

105. O. C. Zeinkiewicz, R. L. Taylor. *The Finite Element Methods In Engineering Science* (McGraw-Hill, New York, 1989).
106. J. N. Reddy. *An Introduction to the Finite Element Method* 2ed. (McGraw-Hill, New York, 1993).
107. Z. Sun, Y. Huang, E. M. Sevick-Muraca, "Precise analysis of frequency domain migration measurement for characterization of concentrated colloidal suspensions," *Review of Scientific Instruments* **73**, 383-393 (2002).
108. M. J. Eppstein, D. E. Dougherty, D. J. Hawrysz, E. M. Sevick-Muraca, "Three-dimensional Bayesian optical image reconstruction with domain decomposition," *IEEE Transactions on Medical Imaging* **20**, 147-163 (2000).
109. M. A. Bartlett, H. Jiang, "Effect of refractive index on the measurement of optical properties in turbid media," *Applied Optics* **40**, 1735-1741 (2001).
110. B. W. Pogue, S. Geimer, T. O. McBride, S. Jiang, U. L. Osterberg, K. D. Paulsen, "Three-dimensional simulation of near-infrared diffusion in tissue: Boundary condition and geometry analysis for finite-element image reconstructions," *Applied Optics* **40**, 588-600 (2001).
111. F. Fedele, J. P. Laible, M. J. Eppstein, "Coupled complex adjoint sensitivities for frequency-domain fluorescence tomography: Theory and vectorized implementation," *J. of Computational Physics* **187**, 597-619 (2003).
112. M. J. Eppstein, D. E. Dougherty, "Simultaneous estimation of transmissivity values and zonation," *Water Resources Research*, **32**, 3321-3336 (1996).

113. C. Zhang, M.J. Eppstein, A. Godavarty, and E.M. Sevick-Muraca, "A hybrid approach to Bayesian image reconstruction", in *Optical Tomography and Spectroscopy of Tissue V*, B. Chance, R. R. Alfano, B. J. Tromberg, E. M. Sevick-Muraca, eds., Proc. Soc. Photo-Opt. Instrum. Eng. **4955**, 591-599 (2003).
114. C. M. Leevy, F. Smith, J. Longueville, "Indocyanine green clearance as a test for hepatic function: Evaluation by dichromatic ear densitometry," *JAMA* **200**, 236-240 (1967).
115. K. Kogure, N. J. David, U. Yamanouchi, E. Choromokos, "Infrared absorption angiography of the fundus circulation," *Arch. Ophthalmol.* **83**, 209-214 (1970).
116. R. Rajagopalan, P. Uetrecht, J.E. Bugaj, S.A. Achilefu, and R.B. Dorshow, "Stabilization of the optical tracer agent indocyanine green using noncovalent interactions." *Photochemistry and Photobiology* **71**, 347-350 (2000).
117. E. M. Sevick-Muraca, G. Lopez, T. Troy, J. S. Reynolds, C. L. Hutchinson, "Fluorescence and absorption contrast mechanisms for biomedical optical imaging using frequency-domain techniques," *Photochemistry and Photobiology* **66**, 55-64 (1997).
118. A. Godavarty, M. J. Eppstein, C. Zhang, S. Theru, A. B. Thompson, M. Gurfinkel, E. M. Sevick-Muraca, "Fluorescence-enhanced optical imaging in large tissue volumes using a gain modulated ICCD camera," *Physics in Medicine and Biology* **48**, 1701-1720 (2003).
119. A. Godavarty, E. M. Sevick-Muraca, M. J. Eppstein, C. Zhang, "Fluorescence-enhanced tomographic imaging in large phantoms using gain-modulated ICCD

- camera,” in *Lasers in Surgery: Advanced Characterization, Therapeutics, and Systems XIII*, L. S. Bass, N. Kollias, R. S. Malek, A. Katzir, U. K. Shah, B. J. Wong, E. A. Trowers, T. A. Woodward, W. T. de Riese, D. S. Robinson, H-D. Reidenbach, K. D. Paulsen, K. W. Gregory, eds., Proc. Soc. Photo-Opt. Instrum. Eng. **4949**, 433-443 (2003).
120. J. M. Schmitt, A. Knüttel, J. R. Knutson, “Interference of diffusive light waves,” *Journal of Optical Society of America A* **9**, 1832-1843 (1992).
121. A. Knüttel, J. M. Schmitt, J. R. Knutson, “Spatial localization of absorbing bodies by interfering diffusive photon-density waves,” *Applied Optics* **32**, 381-389 (1993).
122. A. Knüttel, J. M. Schmitt, R. Barnes, J. R. Knutson, “Acousto-optic scanning and interfering photon density waves for precise localization of an absorbing (or fluorescent) body in a turbid medium,” *Review of Scientific Instruments* **64**, 638-644 (1993).
123. B. Chance, K. Kang, L. He, J. Weng, E. Sevick, “Highly sensitive object location in tissue models with linear in-phase and anti-phase multi-element optical arrays in one and two dimensions,” *Proceedings of National Academy of Science USA* **90**, 3423-3427 (1993).
124. Y. Chen, C. Mu, X. Intes, B. Chance, “Adaptive calibration for object localization in turbid media with interfering diffuse photon density waves,” *Applied Optics* **41**, 7325-7333 (2002).

125. A. Godavarty, C. Zhang, M. J. Eppstein, E. M. Sevick-Muraca, "Fluorescence-enhanced optical imaging of large phantoms using single and simultaneous dual point illumination geometries," *Medical Physics* (submitted) (2003).
126. A. Godavarty, A. B. Thompson, R. Roy, M. J. Eppstein, C. Zhang, E. M. Sevick-Muraca, "Progress towards diagnostic imaging of breast cancer using fluorescence-enhanced optical tomography," *Journal of Biomedical Optics* (submitted) (2003).
127. R. Roy, A. B. Thompson, A. Godavarty, E. M. Sevick-Muraca, "Fluorescence-enhanced optical tomography using area illumination and area detection methodology," *Science* (2003) (manuscript in preparation).
128. R. Polyak, "Modified barrier functions (theory and methods), *Mathematical programming*," **54**, 177-222 (1992).
129. S. Ke, X. Wen, M. Gurfinkel, C. Charnsangavej, Z. Fan, S. Wallace, E. M. Sevick-Muraca, C. Li, "Near-infrared optical imaging of epidermal growth factor receptors (EGFr) in a breast cancer xenograft," *Cancer Research* (accepted) 2003.

APPENDIX A

SOURCE AND DETECTOR LOCATIONS ON BREAST PHANTOM

Table A.1 Illumination fiber x-y-z locations on the hemispherical surface of the breast phantom.

Source	x (cm)	y(cm)	z(cm)
1	-4.91	0.48	0.78
2	-3.13	3.82	0.78
3	0.48	4.91	0.78
4	3.82	3.13	0.78
5	4.91	-0.48	0.78
6	3.13	-3.82	0.78
7	-0.48	-4.91	0.78
8	-3.82	-3.13	0.78
9	-3.44	2.83	2.27
10	-0.44	4.43	2.27
11	2.83	3.44	2.27
12	4.43	0.44	2.27
13	3.44	-2.83	2.27
14	0.44	-4.43	2.27
15	-2.83	-3.44	2.27
16	-4.43	-0.44	2.27
17	-3.52	0.35	3.54
18	0.35	3.52	3.54
19	3.52	-0.35	3.54
20	-0.35	-3.52	3.54
21	-1.44	1.75	4.46
22	1.75	1.44	4.46
23	1.44	-1.75	4.46
24	-1.75	-1.44	4.46
25	0.78	0.08	4.94
26	-0.78	-0.08	4.94
27	0.00	0.00	5.00

Table A.2 Collection fiber x-y-z locations on the hemispherical surface of the breast phantom.

Detector	x (cm)	y (cm)	z (cm)
1	-5.00	0.00	0.00
2	-4.90	0.98	0.00
3	-4.62	1.91	0.00
4	-4.16	2.78	0.00
5	-3.54	3.54	0.00
6	-2.78	4.16	0.00
7	-1.91	4.62	0.00
8	-0.98	4.90	0.00
9	0.00	5.00	0.00
10	0.98	4.90	0.00
11	1.91	4.62	0.00
12	2.78	4.16	0.00
13	3.54	3.54	0.00
14	4.16	2.78	0.00
15	4.62	1.91	0.00
16	4.90	0.98	0.00
17	5.00	0.00	0.00
18	4.90	-0.98	0.00
19	4.62	-1.91	0.00
20	4.16	-2.78	0.00
21	3.54	-3.54	0.00
22	2.78	-4.16	0.00
23	1.91	-4.62	0.00
24	0.98	-4.90	0.00
25	0.00	-5.00	0.00
26	-0.98	-4.90	0.00
27	-1.91	-4.62	0.00
28	-2.78	-4.16	0.00
29	-3.54	-3.54	0.00
30	-4.16	-2.78	0.00
31	-4.62	-1.91	0.00
32	-4.90	-0.98	0.00
33	-4.76	0.00	1.55
34	-4.66	0.93	1.55
35	-4.39	1.82	1.55
36	-3.95	2.64	1.55
37	-3.36	3.36	1.55
38	-2.64	3.95	1.55
39	-1.82	4.39	1.55
40	-0.93	4.66	1.55
41	0.00	4.76	1.55
42	0.93	4.66	1.55
43	1.82	4.39	1.55
44	2.64	3.95	1.55

45	3.36	3.36	1.55
46	3.95	2.64	1.55
47	4.39	1.82	1.55
48	4.66	0.93	1.55
49	4.76	0.00	1.55
50	4.66	-0.93	1.55
51	4.39	-1.82	1.55
52	3.95	-2.64	1.55
53	3.36	-3.36	1.55
54	2.64	-3.95	1.55
55	1.82	-4.39	1.55
56	0.93	-4.66	1.55
57	0.00	-4.76	1.55
58	-0.93	-4.66	1.55
59	-1.82	-4.39	1.55
60	-2.64	-3.95	1.55
61	-3.36	-3.36	1.55
62	-3.95	-2.64	1.55
63	-4.39	-1.82	1.55
64	-4.66	-0.93	1.55
65	-4.05	0.00	2.94
66	-3.97	0.79	2.94
67	-3.74	1.55	2.94
68	-3.36	2.25	2.94
69	-2.86	2.86	2.94
70	-2.25	3.36	2.94
71	-1.55	3.74	2.94
72	-0.79	3.97	2.94
73	0.00	4.05	2.94
74	0.79	3.97	2.94
75	1.55	3.74	2.94
76	2.25	3.36	2.94
77	2.86	2.86	2.94
78	3.36	2.25	2.94
79	3.74	1.55	2.94
80	3.97	0.79	2.94
81	4.05	0.00	2.94
82	3.97	-0.79	2.94
83	3.74	-1.55	2.94
84	3.36	-2.25	2.94
85	2.86	-2.86	2.94
86	2.25	-3.36	2.94
87	1.55	-3.74	2.94
88	0.79	-3.97	2.94
89	0.00	-4.05	2.94
90	-0.79	-3.97	2.94
91	-1.55	-3.74	2.94
92	-2.25	-3.36	2.94

93	-2.86	-2.86	2.94
94	-3.36	-2.25	2.94
95	-3.74	-1.55	2.94
96	-3.97	-0.79	2.94
97	-2.94	0.00	4.05
98	-2.72	1.12	4.05
99	-2.08	2.08	4.05
100	-1.12	2.72	4.05
101	0.00	2.94	4.05
102	1.12	2.72	4.05
103	2.08	2.08	4.05
104	2.72	1.12	4.05
105	2.94	0.00	4.05
106	2.72	-1.12	4.05
107	2.08	-2.08	4.05
108	1.12	-2.72	4.05
109	0.00	-2.94	4.05
110	-1.12	-2.72	4.05
111	-2.08	-2.08	4.05
112	-2.72	-1.12	4.05
113	-1.55	0.00	4.76
114	-1.43	0.59	4.76
115	-1.09	1.09	4.76
116	-0.59	1.43	4.76
117	0.00	1.55	4.76
118	0.59	1.43	4.76
119	1.09	1.09	4.76
120	1.43	0.59	4.76
121	1.55	0.00	4.76
122	1.43	-0.59	4.76
123	1.09	-1.09	4.76
124	0.59	-1.43	4.76
125	0.00	-1.55	4.76
126	-0.59	-1.43	4.76
127	-1.09	-1.09	4.76
128	-1.43	-0.59	4.76

APPENDIX B

EVALUATION OF ELECTRICAL AND OPTICAL POWER OF THE LASER LIGHT

B.1. Evaluation of the electrical power of the laser light (AC and DC values)

The mathematics involved in determining the AC power and DC current that should be supplied to the laser diode in order to obtain a required modulation depth and a chosen maximum power for the system is described herein. The general electrical signal into laser mount set-up, TCLDM9 (Thorlabs Inc, NJ) is schematically given in Figure B.1. Here, I_{max} is the current corresponding to the desired maximum optical power of the laser diode; I_{th} is the threshold current of the laser diode; I_{AC} is the amplitude of the RF signal supplied by the frequency synthesizer; and I_{DC} is the constant DC supplied by the laser driver (LDC500). The depth of modulation, n of the optical output based on the input DC and AC intensities is given by

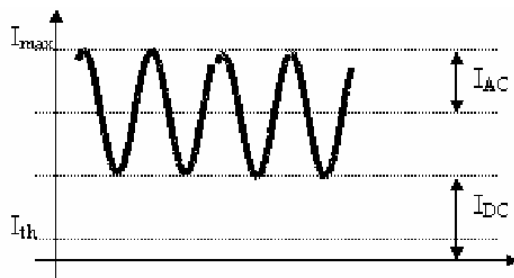


Figure B.1 Electrical signal into the laser diode mount.

$$n = \frac{I_{AC}}{I_{AC} + (I_{DC} - I_{th})} \quad (\text{B.1})$$

Also, from Figure B.1, we also have the following relation

$$I_{\max} = 2 \bullet I_{AC} + I_{DC} \quad (\text{B.2})$$

For a desired modulation depth, n , equations (B.1) and (B.2) are rearranged to obtain the AC current.

$$I_{AC} = \frac{n(I_{\max} - I_{th})}{(n+1)} \quad (\text{B.3})$$

The AC current in terms of the RF input power (P_{RF}) to the laser mount having a resistor of $R = 50 \Omega$ is calculated as

$$P_{RF} = (I_{AC})^2 R \quad (\text{B.4})$$

The RF power is supplied to the laser diode using a frequency synthesizer (-127 dBm to + 13 dBm range) and an amplifier of +37dBm (ENI-403LA model, Rochester, NY) if required, in terms of decibels of power input.

$$'x' \text{ dBM} = 10 \log_{10} \left(\frac{P_{RF}}{1} \right) \quad (\text{B.5})$$

where, P_{RF} is the RF power in mW. In the current studies, for the given (i) threshold current of the laser diode (190 mA), (ii) maximum desired power (P_{max}) of 467 mW (i.e. $I_{max} = 600$ mA), and (iii) desired modulation depth of 98%, the RF power and DC current were estimated as 30.6 dBm and 197.9mA, respectively. The laser diode driver provided 197.9 mA current and 30.6 dBm RF power (which was achieved by amplifying the signal from the frequency synthesizer).

B.2. Evaluation of the optical power of the laser light

The actual amount of light that was launched by the laser diode is given by its optical power, which is different from the electrical power supplied by the laser diode driver and the oscillators (as DC and AC power, respectively). The optical power was evaluated based on the characteristics of the laser diode and operation mode of the laser diode mount. Here, the optical power ($P_{optical}$) is given by

$$P_{optical} = \left(\sqrt{2}I_{AC} + I_{DC} - I_{th} \right) \eta_{slope} \quad (\text{B.6})$$

where η_{slope} is the slope efficiency (W/A) of the laser diode that was estimated from the manufacturer specifications based on the formula

$$\eta_{slope} = \frac{P_{max} - P_{th}}{I_{max} - I_{th}} \quad (\text{B.7})$$

where P_{th} is the threshold power of the laser diode. The slope efficiency for the current laser diode was calculated to be ~ 0.69138 W/A. Thus the optical power ($P_{optical}$) was determined to be 153.63 mW.

APPENDIX C

WAVELENGTH DEPENDENCY OF ICCD IMAGING SYSTEM

Fluorescence-enhanced optical imaging studies involves data acquisition of light signal at two different wavelengths, the excitation light (785 nm) which is used to excite the fluorophores, and the fluorescent light (830 nm) which is emitted by the fluorophores. The components of the imaging system, such as the optical filters, image intensifier, and CCD camera, are usually wavelength-dependent with variation in the efficiency with respect to wavelength. Details of the wavelength-dependency of these components are described below.

C.1 Transmission efficiencies of the optical filters

Based on the kind of filter used, the transmission efficiency was evaluated as a function of the wavelength from the manufacturers' specifications.

C.1.1 Neutral density filters

The optical density (OD) of an absorptive neutral density filter varies with the wavelength of light that passes through it. A typical graph of the variation of the actual OD of a neutral density (ND) filter of given OD at a particular wavelength is shown in Figure C.1. However, in actual case, each filter is provided with a specification sheet

and the OD corresponding to that particular filter at required wavelength is evaluated accordingly. For the experiment performed in the homogeneous phantom case, neutral density filters of OD=3 and OD=2 at 546nm wavelength were used to collect the

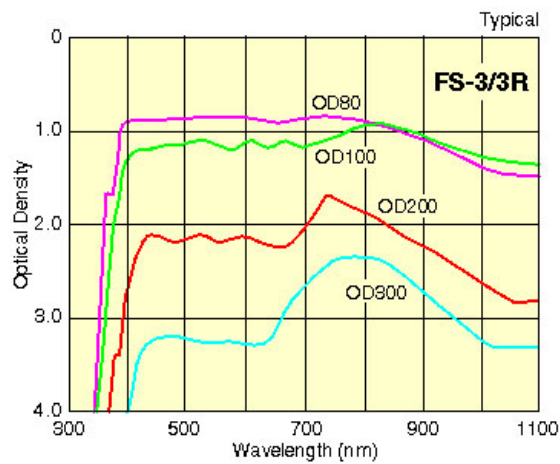


Figure C.1 Typical plot of optical density as a function of wavelength for different neutral density filters.

excitation signal and their corresponding OD values at 785nm were estimated to be 2.1 and 1.6, respectively.

C.1.2 Holographic Filter

The transmission of the holographic filter used for collecting the emission signal at 830nm is about 82.2%, as provided from Figure C.2 (obtained from the manufacturer).

C.1.3 Interference filters

An 830-nm interference filter was used during the emission experiments and the transmission of this filter was estimated by performing a transmission trace analysis using an absorptive spectrophotometer (Spectroscopy Lab, Dept of Veterinary Physiology and Pharmacology) (see Figure C.3). From this plot of transmission versus

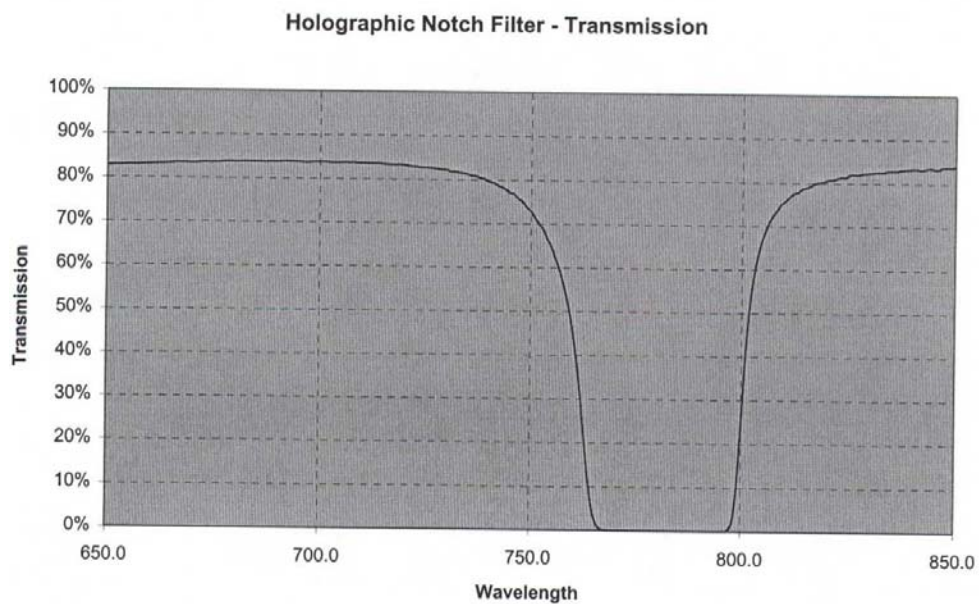


Figure C.2 Transmission curve of the holographic filter.

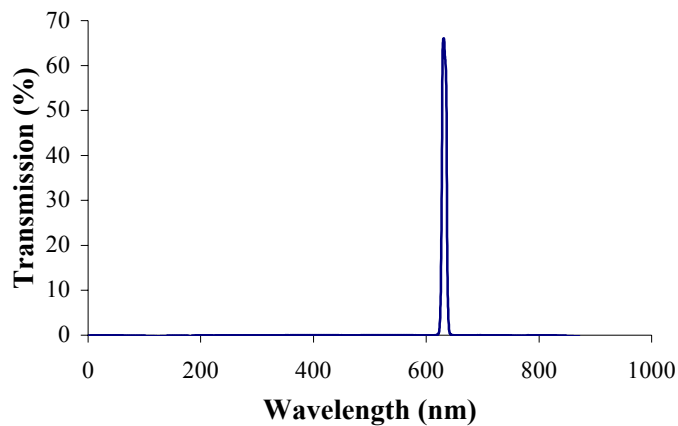


Figure C.3 Transmission curve for the 830 nm interference filter.

wavelength, the transmission was determined to be approximately 64% at the central wavelength of 831nm.

C.2 Compounded gain and quantum efficiency of the image intensifier

It was assumed that the compounded gain of the image intensifier was independent of the wavelength of light detected. The photo response of a typical FS9910C image intensifier was obtained from the manufacturer (ITT Night Vision) at wavelengths varying from 500nm to 830 nm and photocathode voltages varying from 900 to 150V. Quantum efficiency of the image intensifier was evaluated for the varying wavelengths and photocathode voltages from the photo response data provided by the manufacturer.

$$QE = QE_{\text{cons tan } t} * \frac{\text{Photorespo nse}(mA / W)}{\text{Wavelength (nm)}} \quad (\text{C.1})$$

$$QE_{\text{cons tan } t} = \frac{h \times c \times 100}{\varepsilon \times 1000 \times 10^{-9}} \quad (\text{C.2})$$

where, h is the Planck's constant (6.626×10^{-34} joules/sec); c is the speed of light (2.99×10^8 m/sec) and ε is the charge of the electron (1.602×10^{-19} coulombs). Hence, the quantum efficiency was plotted as a function of the wavelength at varying photocathode voltages in Figure B.4. Under the operating photocathode voltage of -65V and operating wavelengths of 785nm and 830 nm, the quantum efficiency of the image intensifier was extrapolated and approximated to about 30% and 27.8% respectively.

C.3 Quantum efficiency of the CCD camera

The quantum efficiency of the 12-bit CCD camera does vary with wavelength. However, in this case, the image from the phosphor screen of the image intensifier that impinges onto the CCD array is at constant wavelength and independent of the signal's wavelength at the photocathode of the image intensifier. Hence the effect of wavelength in this case was eliminated. Also, since light of constant wavelength impinged the CCD array for either wavelength of the detected signal, the gain term of the CCD output amplifier was eliminated.

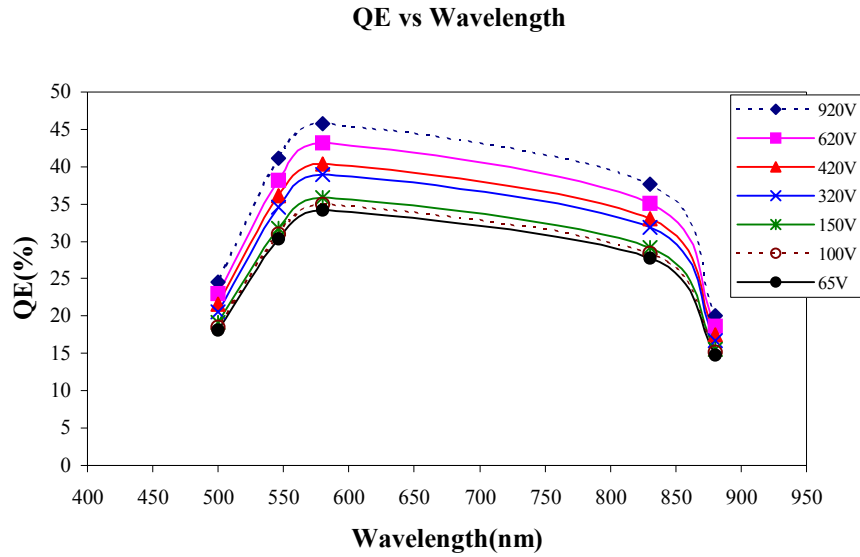


Figure C.4 Quantum efficiency of the image intensifier at varying wavelengths and photocathode voltages.

Hence, the wavelength-dependent factor (F) was estimated using the above parameters, when the referencing scheme involving data acquired from both the excitation and emission signals was involved (see Section 4.4.1). It was assumed that only the AC ratio would be affected by the wavelength dependent factor and phase remains independent of wavelength. Hence, the factor, F that needs to be accounted for determining the true AC ratio and relative phase shift data from experiments, was defined by F_{AC} and F_{θ} as

$$F_{AC} = \left(\frac{T_{ex}^{-OD}}{T_{em}^{-OD}} \right)_{ND} \times \left(\frac{t_{ex}}{t_{em}} \right) \times \left(\frac{1}{T_{holographic}} \right) \times \left(\frac{1}{T_{830-interference}} \right) \times \left(\frac{QE_{ex}}{QE_{em}} \right)_{II} \times \left(\frac{QE_{ex}}{QE_{em}} \right)_{CCD} \quad (B.3)$$

$$F_{\theta} = 1 \quad (\text{B.4})$$

where, the suffix *em* and *ex* correspond to the emission and excitation wavelength, respectively; *T* is the transmission of the respective filters such as neutral density (ND), holographic or 830-nm interference filter. *OD* represents the actual optical density of the ND filters; *t* is the exposure time of the camera while acquiring the images at either wavelength; and *QE* is the quantum efficiency of the image intensifier (*II*) or the CCD camera. Multiplying the above *F* values to the experimentally obtained AC ratio and relative phase shift would aid in accounting for the wavelength dependency of the system and hence eliminate the effect of various terms as mentioned earlier.

APPENDIX D

DETAILS OF THE CCD CAMERA

A 512×1024 frame transfer (TE/CCD-512-EFT Photometric CH12, Roper Scientific, Trenton, NJ) CCD camera that was thermoelectrically cooled to -35°C and has a 12-bit A/D (analog-to-digital) converter was coupled to the image intensifier in the current ICCD imaging system. A CC-100 coolant circulator (Princeton Instruments, Trenton, NJ) using water/ethylene glycol (50% solution) removed the heat from the thermoelectrically cooled CCD camera [1-2]. The CCD was usually N_2 purged throughout the whole process of image acquisition in order to prevent any moisture condensation when operating at such low temperatures of -35°C .

CCDs are typically composed of crystalline silica that is sensitive to light at a wavelength range of 400-1000 nm. The 512×512 array of photosensitive detectors or charge potential wells present in this camera convert the incident photons to electrons. The total accumulated charge in these potential wells (typically on the order of μm^2 area) is proportional to the product of light intensity and the charge integration time (or exposure time) of the camera. This accumulated charge is then read out from the parallel register into the serial register column wise as shown in Figure D.1. These charge packets are then shifted from the serial register to an output amplifier, which in turn generate a signal that was proportional to the charge of each pocket. The signal generated is proportional to the type of A/D converter, and in this case, we use a 12-bit

A/D converter in which the charge is represented by 4096 (2^{12}) gray levels. The computer processes the digitized signals in order to display the images.

The rate of image acquisition depends on the architecture of the camera. Here, full frame transfer architecture is employed for this camera, facilitating a 512×512 array for acquiring the image and a 512×512 array for its storage, thus comprising a total of 512×1024 array. Actual photon exposure and exposure time occurs on the image array and the charge is then shifted rapidly to the storage array for readout; clearing the image array in order to acquire the next image and perform charge integration [3].

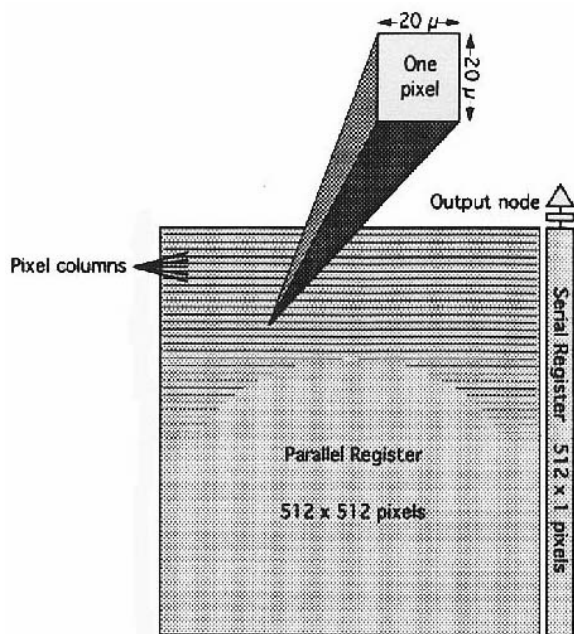


Figure D.1 CCD array.

Noise is typically introduced into the CCD system by the charge integration time (i.e. exposure time) and the readout rate (which is the rate-limiting step). This noise in turn affects the sensitivity of the camera. Photon noise (or shot noise), preamplifier noise and dark current noise are the primary sources of noise in a CCD camera [3].

- (i) *Photon or shot noise* is an unavoidable inherent tendency of the photons emitted from a steady state source to vary in intensity over a period.
- (ii) *Preamplifier or read noise* is generated by the on-chip output amplifier and can be reduced by careful choice of the operating conditions.
- (iii) *Dark current noise* is the thermally generated noise, which can be measured and accounted for, but cannot be isolated. However, it can be minimized by cooling the CCD to around -60°C .

The effect of noise on the performance of the CCD is described in terms of signal-to-noise ratio (SNR). Binning is a process, which improves the SNR and extends the dynamic range of the CCD imager, but at the expense of the spatial resolution. Binning is specified in terms of the binning factor, which is the number of pixels to be combined on the CCD. In our case, the 512×512 array is binned to 128×128 CCD array, meaning that it is binned twice using a binning factor of 2.

Typically, the primary source of noise that corrupts the phase-sensitive time-invariant measurements is identified from the SNR (signal-to-noise ratio) in the DC intensity and the mean DC intensity (I_{DC}) values. For a photon-noise-limited operation, SNR is proportional to the square root of the signal (DC intensity) [4]. If a linear trend is observed in the plot of I_{DC} SNR and mean I_{DC} , the operation of the ICCD homodyne

detection system is considered photon-noise-limited [5], stating that the system has no other form of noise present and the detection system has least noise arising from various sources. The current 12-bit CCD camera was deteriorating in its performance during each experiment and hence the current noise limitation study was not performed.

References

1. *TE/CCD Detector Operation manual*, Princeton Instruments, Inc., Trenton, NJ.
2. *CC-100 Coolant Circulator Operation Manual*, Princeton Instruments, Inc., Trenton, NJ.
3. *AT200 CCD Camera System Hardware Reference Manual*, Photometrics Ltd., Tuscon, AZ.
4. A. Frenkel, M. A. Sartor, M. S. Wlodawski, "Photon-noise-limited operation of intensified CCD cameras," *Appl Opt.* **36**, 5288-5294 (1997).
5. A. B. Thompson, E. M. Sevick-Muraca, "Near-infrared fluorescence contrast-enhanced imaging with intensified charge-coupled device homodyne detection: measurement precision and accuracy," *J. Biomed. Opt.* **8**, 111-120 (2003).

APPENDIX E

EFFECT OF OPTICAL FILTERS ON EXCITATION LIGHT LEAKAGE

Optical filters such as interference, long pass, and holographic were used for acquiring the fluorescence measurements after rejecting the excitation light at 785 nm. A single filter is insufficient in most cases to effectively reject the 785nm light completely, although its transmission efficiency for 830 nm light is typically above 80%. In this study, different filter combinations were attempted to determine a better combination of filters that can efficiently reject the excitation light.

Measurements were performed in the frequency-domain of the large homogeneous breast phantom containing 1% Liposyn solution, without any fluorescence in the background. Optical filters in different combinations in order to collect only the 830 nm fluorescence signal. However, since there was no fluorescence present in the background, the signal obtained corresponds to the excitation light leakage from the phantom which is illuminated using single point excitation sources. The different filter combinations that were used are listed in Table E.1 below.

Data acquired was plotted in terms of raw dc (mean of ac) values for all the detector locations in a single interfacing plate, as shown in Figure E.1. All the experiments using different filter combinations were performed under similar operating conditions, allowing the comparison of raw dc data in the current study. Since the data is very dense to infer a good filter combination, a single detector was considered (given

Table E.1. Filter combinations used to test for excitation leakage.

Expt	Filter combination	Abbreviation
1	1-Holographic filter + 1-830 nm interference filter	1-holo + 1-830
2	1- 830 nm interference filter	1-830
3	1- 830 nm interference filter + 1- 812 long pass filter	1-830 + 1-LP
4	1-Holographic filter + 1- 812 nm long pass filter	1-holo + 1-LP
5	1- 812 nm long pass filter	1-LP
6	1-Holographic filter + 1- 812 nm long pass filter + 1-815 nm long pass filter	1-holo + 2-LP
7	1-812 long pass filter + 1-815 nm long pass filter	2- LP
8	1-830 nm interference filter + 1-812 nm long pass filter + 1-815 nm long pass filter	1-830 + 2-LP
9	2-830 nm interference filter	2-830

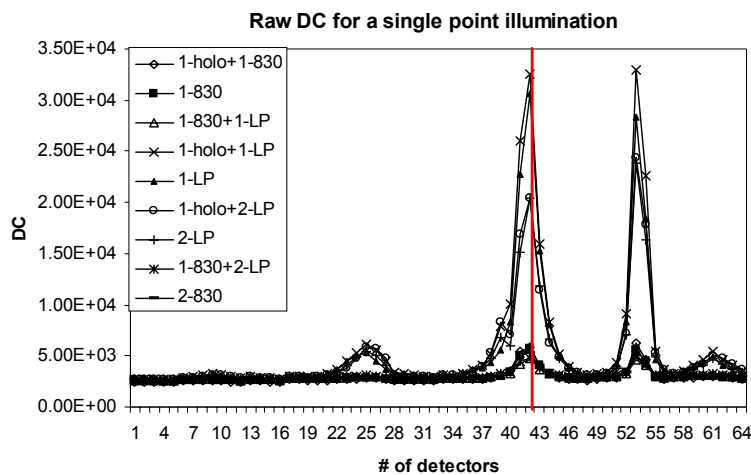


Figure E.1 Acquired fluorescence DC data (mean of AC data in the frequency-domain) for detectors located in a single interfacing plate using different filter combinations. The red vertical line represents a single detector location, whose DC values were considered in comparing the effect of different filter combinations (see Figure E.2), since the signal was strong at this detector location.

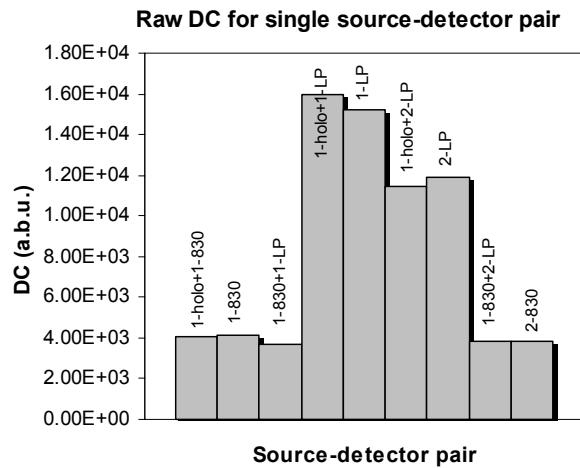


Figure E.2 Bar plot of the DC intensity at a single detector location (at the red line shown in Figure E.1), using different filter combinations.

by the vertical line in Figure E.1) to show the effect of different filters (see Figure E.2).

From Figure E.2, we observe that the filter combinations (i) 1-830 +1-LP, (ii) 1-830-+2-LP, and (iii) 2-830 provide the least excitation leakage in terms of raw DC data. Although the excitation leakage was minimal in these three filter combinations, it was not sufficient to efficiently reject the excitation light leakage completely. Also the transmission of the stacked filters dropped as the number of filters used was increased. This was concluded from the physics behind transmission (T) given by the formula

$$T = T_1 \times T_2 \times T_3 \times \dots \times T_n \quad (\text{E.1})$$

where, n is the total number of filters stacked. Hence, a better option to overcome excitation leakage will be to employ customized filters that have a blocking OD > 10 for 785 nm light, while maintaining the transmission efficiency at least 80%.

VITA

Anuradha Godavarty has completed her bachelor's degree in Chemical Engineering from University of Madras, India in May 1997, and her M.S. degree in Chemical Engineering from University of Tennessee, Knoxville in August 1999. She completed her PhD in Chemical Engineering from Texas A&M University in December 2003. After the completion of her doctoral program, she accepted a Post-Doctoral Associate position in the Department of Computer Science, at the University of Vermont (since September 2003), during which she will telecommute from her permanent residence. Dr. Godavarty's permanent address is 9619 Fountainebleau Blvd., Apt 216, Miami, Florida 33172 after her graduation.